Normandie Université

UNIVERSITÉ DE ROUEN NORMANDIE

THÈSE

Pour obtenir le diplôme de doctorat

Spécialité **PHYSIQUE**

Préparée au sein de l'**Université de Rouen Normandie**

Influence of hydrogen on precipitation in Al-Cu and Al-Zr aluminum alloys

Présentée et soutenue par

BOUKIR OMAR

Thèse soutenue le 02/12/2025

devant le jury composé de :

M. SAUVAGE XAVIER	Directeur de Recherche - URN - Université de Rouen Normandie	Directeur de thèse
MME ZAPOLSKY HELENA	Professeur des Universités - URN - Université de Rouen Normandie	Président du jury
M. DORIN THOMAS	Maître de Conférences - Université de Deakin	Membre du jury
M. DESCHAMPS ALEXIS	Professeur des Universités - Université de Grenoble Alpes	Rapporteur du jury
M. PUNDT ASTRID	Professeur des Universités - Université de Karlsruhe (ALLEMAGNE)	Rapporteur du jury

Thèse dirigée par **SAUVAGE XAVIER** (GROUPE DE PHYSIQUE DES MATERIAUX)

ED 591 PSIME

GPM Groupe de Physique des Matériaux

ACKNOWLEGMENTS

I would like to express my sincere gratitude to the members of my thesis committee for the time they devoted to reviewing this manuscript and for the insightful and constructive discussions we had.

I am deeply grateful to my PhD supervisor, Xavier Sauvage, for his constant encouragement, guidance, and support throughout this thesis. His mentorship has been invaluable, and I feel very fortunate to have benefited from his scientific expertise as well as his exemplary integrity and dedication to research.

I would also like to warmly thank Dr. Guillaume Hachet for his time, support, and substantial contributions, which played an important role in the progress of this work.

My sincere thanks go to all the people who contributed to this project. I would like to thank Kaveh Edalati (I^2CNER, Japan) for welcoming me into his laboratory for two months to carry out experiments as part of my thesis. I am also grateful for his personal support and kindness, which greatly helped me during my stay. I also thank Shivam Dangwal for his help with the experiments. I am grateful to Abdelali Oudriss (LaSIE Laboratory, La Rochelle) for performing the TDS experiments.

I would like to acknowledge the valuable scientific exchanges with David Embury, Williams Lefebvre, Juan Macchi, and many others, which enriched my understanding and broadened my perspective.

I also wish to thank my colleagues and all the members of the GPM Laboratory. Each of you contributed, in your own way, to making this experience truly enriching. I would also like to thank my friends for their support throughout this journey.

Finally, I would like to express my deepest gratitude to my family, whom I miss every day. Their love, support, and encouragement have been essential, and without them I would never have reached my personal goals.

TABLE OF CONTENTS

GENERAL INTRODUCTION **5**

CHAPTER I: Precipitation and Hydrogen in Aluminum Alloys - Literature Review **7**

1. General Context **8**

1.1. Hydrogen Embrittlement 8

1.2. Influence of Hydrogen on Phase Transformation 12

2. Precipitation in Aluminium Alloys **16**

2.1. Precipitation Mechanisms and Kinetics 16

2.1.1. Classical Nucleation Theory 16

2.1.2. Precipitate Growth 19

2.1.3. Coarsening 21

2.2. Role of Defects 22

2.3. Precipitation in the Al-Cu System 25

2.4. Precipitation in the Al-Zr System 29

2.5. Precipitation Strengthening Mechanisms 32

2.6. Age-hardening Behavior of Al-Cu and Al-Zr systems 36

2.6.1. Al-Cu system 36

2.6.2. Al-Zr system 38

3. Hydrogen in Aluminum and Its Alloys **38**

3.1. Hydrogen Solubility 38

3.2. Hydrogen Transport and Diffusion 41

3.3. Hydrogen Trapping 42

3.4. Hydrogen Charging Techniques 45

3.4.1. High-pressure Hydrogen Charging 45

3.4.2. Electrochemical (cathodic) Charging 47

3.4.3. Plasma Charging Methods 48

CHAPTER II: Materials and Methods **50**

1. Selected Al Alloys and Thermal Treatment **51**

2. Cold Rolling **52**

3. Hydrogen Charging Methods **53**

4. Characterization Techniques 55
4.1. Vickers Microhardness Testing 55
4.2. Transmission Electron Microscopy (TEM) 56
4.2.1. Fundamentals of TEM 56
4.2.2. TEM Imaging 59
4.2.3. STEM mode 60
4.2.4. Energy Filtered Transmission Electron Microscopy 62
4.2.5. TEM Sample Preparation 62
4.2.6. Determination of Precipitate Size and Number Density 63
4.3. Atom Probe Tomography (APT) 66
4.4. Thermal Desorption Spectroscopy (TDS) 70

CHAPTER III: Influence of hydrogen on the growth kinetics of Al_3Zr precipitates in the Al-0.2Zr alloy 75

1. Introduction 76

2. Microhardness Evolution During Aging 76
2.1. Aging In Air 76
2.2. Aging Under Hydrogen Atmosphere 78

3. Precipitates in the Al-0.2Zr alloy aged in Air 79
3.1. Precipitate Morphology and Structure (TEM) 79
3.2. Solid Solution and precipitate compositions (APT) 86

4. Effect of Hydrogen on Precipitation 90
4.1. Precipitate Morphology and Structure (TEM) 90
4.2. Solid solution and precipitate compositions (APT) 93

5. Discussion 94
5.1. Growth Rate of Al_3Zr Precipitates 94
5.2. Influence of Hydrogen on Zr Mobility 97

6. Conclusions 99

CHAPTER IV: Influence of hydrogen on precipitation in the Al-5Cu Alloy 101

1. Introduction 102

2. Hardness Evolution During Aging 102

3. Measurement of hydrogen concentration 105
4. Microstructural Characterization 107
4.1. As-quenched state 107
4.2. Precipitation at 140 °C 112
4.3. Influence of hydrogen on precipitation sequence 118
5. Relationship between microstructure and hardness 122
5.1. Precipitate Strengthening Models 122
5.2. Calculated Strengthening Contributions 125
5.3. Theoretical versus experimental hardness comparison 128
6. Hydrogen Trapping and its Effect on GP zones Transformations 130
7. Influence of deformation and hydrogen on precipitation 135
7.1. Microstructure characterization of the deformed Al-5Cu alloy 135
7.2. Influence of Hydrogen on Precipitation (chemical charging) 136
7.3. Influence of Hydrogen on Precipitation (aging under hydrogen environment) 142
7.3.1. Hardness Evolution 142
7.3.2. Microstructure characterization 144
7. Discussion 150
CONCLUSIONS AND PERSPECTIVES 153
1. Summary and key results 153
2. Perspectives 155
APPENDIX 157
REFERENCES: 163

GENERAL INTRODUCTION

The global transition toward renewable energy sources has positioned hydrogen as a key element for sustainable energy systems [1]. Today, hydrogen is primarily considered as a strategic energy carrier for storing renewable energy production from wind and solar sources through water electrolysis [2]. Subsequently, this stored hydrogen can be utilized to generate electricity *via* fuel cells, produce heat through combustion when mixed with natural gas, or for industrial processes, particularly in coke-free steel production aimed at reducing CO_2 emissions [3,4]. Moreover, recent studies highlight hydrogen's versatility and its potential to transform carbon dioxide into sustainable fuels [5].

In this energy ecosystem, hydrogen acts more as an energy carrier than a primary energy source, with the fundamental challenge lying in its efficient production, safe storage, and reliable transportation [6]. The transportation sector's quest for energy efficiency has driven the adoption of lightweight alloys in aerospace and automotive applications [7]. Among these materials, aluminum alloys offer particularly attractive properties, including favorable strength-to-weight ratios and excellent corrosion resistance [8].

However, like other metals and alloys, the integration of aluminum alloys in hydrogen environments presents a fundamental challenge: hydrogen-induced embrittlement (HE) [9]. This phenomenon results in a degradation of mechanical properties, particularly ductility and fracture toughness, leading to accelerated failure through crack initiation and propagation [10].

The mechanisms underlying hydrogen embrittlement have been studied and reviewed in several articles [11–14]. Various models have been developed, all considering the interaction between hydrogen and crystalline defects, including grain boundaries, dislocations, vacancies, and interfaces. However, these hydrogen-defect interactions remain incompletely described and the proposed models are largely phenomenological [15], due to the exceptionally high mobility and small size of hydrogen atoms, which make their direct quantification and spatial localization within microstructures extremely challenging [16].

Phase transformations in metallic alloys are governed by thermodynamic and kinetic [17]. However, the presence of crystalline defects significantly influences transformation kinetics and resulting microstructures [18]. Indeed, the mobility of substitutional solute elements is intrinsically coupled to the concentration and mobility of point defects, particularly vacancies, by the vacancy-diffusion mechanism [19]. Concurrently, the nucleation of secondary

phases and precipitates depends highly on interfacial energy contributions, as well as the crystallographic orientation relationships between different phases, which are fundamentally influenced by interfacial energy anisotropy [20].

Since hydrogen preferentially segregates to the same crystalline defects that control precipitation behavior, understanding the role of hydrogen in precipitation may provide an opportunity to indirectly probe hydrogen-defects interactions and yield new insights. To achieve this objective, two model systems are investigated in this work; an Al-Cu alloy with a well-known precipitation sequence (GP zones → θ" → θ' phase → θ), and Al-Zr, where Zr exhibits a high affinity with hydrogen.

This manuscript is organized into four chapters. Chapter I reviews the influence of hydrogen in phase transformations in metallic alloys. It also outlines the fundamental principles of precipitation theory and describes the precipitation sequences, crystal structure, and morphology that occur in the Al-Zr and Al-Cu systems. Besides, the chapter reviews experimental approaches for hydrogen charging, as well as its diffusion, solubility, and trapping in Al alloys.

Chapter II presents the aluminum alloys investigated in this study, detailing their chemical compositions. The experimental protocols for thermal treatments, plastic deformation (cold rolling), and hydrogen charging methods are detailed in this chapter. Then, it describes the characterization techniques used to analyze precipitation in the alloys. Transmission electron microscopy (TEM) was used to measure size, structure, and morphology evolution across different states. Complementary, atom probe tomography (APT), thermal desorption spectroscopy (TDS), and microhardness testing were used to measure the composition of precipitates and the solid solution, to assess hydrogen uptake, and to evaluate the hardness response, respectively.

Experimental results and discussions are presented in Chapters III and IV for the Al-Zr and Al-Cu alloys respectively. Chapter III provides detailed analysis of Al_3Zr precipitate and elucidates the influence of hydrogen on precipitate growth kinetics. Chapter IV systematically examines the well-established precipitation sequence in Al-Cu alloys, specifically the transformation pathway: GP zones → θ″ and θ″→ θ′. The chapter presents a comparative analysis of hydrogen effects on this precipitation sequence in both pre-deformed and undeformed Al-Cu alloy conditions.

CHAPTER I: Precipitation and Hydrogen in Aluminum Alloys - Literature Review

1. General Context 8
1.1. Hydrogen Embrittlement 8
1.2. Influence of Hydrogen on Phase Transformation 12
2. Precipitation in Aluminium Alloys 16
2.1. Precipitation Mechanisms and Kinetics 16
2.1.1. Classical Nucleation Theory 16
2.1.2. Precipitate Growth 19
2.1.3. Coarsening 21
2.2. Role of Defects 22
2.3. Precipitation in the Al-Cu System 25
2.4. Precipitation in the Al-Zr System 29
2.5. Precipitation Strengthening Mechanisms 32
2.6. Age-hardening Behavior of Al-Cu and Al-Zr systems 36
2.6.1. Al-Cu system 36
2.6.2. Al-Zr system 38
3. Hydrogen in Aluminum and Its Alloys 38
3.1. Hydrogen Solubility 38
3.2. Hydrogen Transport and Diffusion 41
3.3. Hydrogen Trapping 42
3.4. Hydrogen Charging Techniques 45
3.4.1. High-pressure Hydrogen Charging 45
3.4.2. Electrochemical (cathodic) Charging 47
3.4.3. Plasma Charging Methods 48

1. General Context

1.1.Hydrogen Embrittlement

Hydrogen interactions in metallic alloys have a significant impact on mechanical properties, microstructural evolution, and long-term performance of engineering components. The presence of hydrogen in aluminum alloys can originate from various sources, including environmental exposure, manufacturing processes (melting, casting, welding), and electrochemical reactions during service conditions [21,22]. Once introduced into the metallic structure, hydrogen diffuses easily and segregates at defects such as grain boundaries, dislocations, precipitate interfaces, and vacancies [21–23], due to its small atomic size and high mobility.

For aluminum alloys, hydrogen can have a significant impact on the mechanical properties, including crack propagation and embrittlement. One of the most significant impacts of hydrogen embrittlement (HE) is the reduction in ductility and toughness. The material becomes more brittle and less capable of deforming plastically before fracturing. This loss of ductility is evident from stress-strain curves where hydrogen-charged samples show a lower strain at fracture compared to uncharged samples (Figure **I-1**).

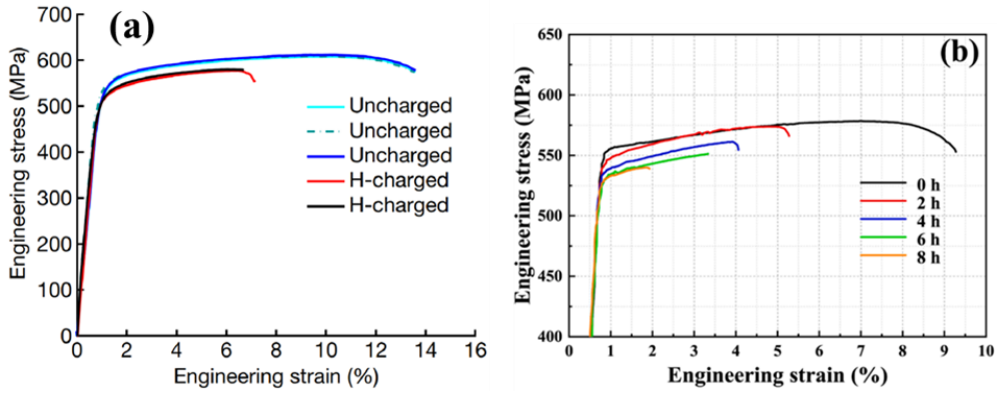


*Figure **I-1**: (a) Stress-strain curves for unloaded and H-loaded samples in maximum ageing condition (120°C - 24 h) [24]. (b) Engineering stress-strain of (Al-4Cu-1Li-0.36Mg wt.%) alloy for various H-charged time [25].*

Henry Holroyd and Scamans [26] examined the behavior of selected aluminum alloys under conditions of mechanical stress and exposure to humid environments. The findings indicate a significant sensitivity of crack propagation to environmental conditions like humidity and the presence of water, along with temperature, which affects the activation energy required for

crack growth. The study also suggests that the formation of aluminum hydride at the crack tip could enhance crack propagation under humid conditions.

Data from Abe *et al* [27], indicate that the Al-6Zn-1.2Mg alloy pre-charged with hydrogen exhibits a significant decrease in both the apparent activation energy and the time required for crack initiation at room temperatures up to about 35 °C (Figure **I-2**). The apparent activation energy decreased from 109 kJ/mol to 45 kJ/mol, but not at higher temperatures where it remained at around 100 kJ/mol [24].

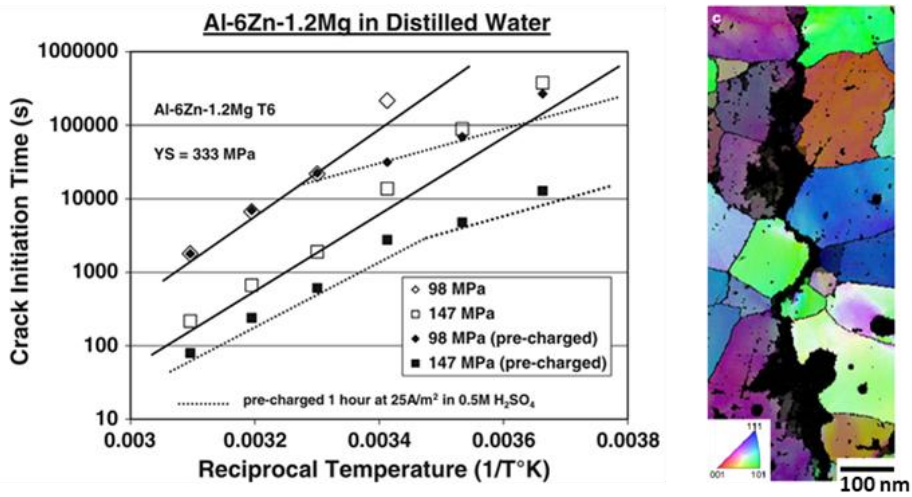


*Figure **I-2**: Intergranular crack initiation times for peak-aged Al-6Zn-1.2Mg exposed to distilled water with and without precharging with hydrogen [26], Backscattered electron imaging of an intergranular crack in H-loaded alloy (Al-6.2Zn-2.5Mg-2.13Cu-0.15Zr % wt) subjected to tensile fracture [24].*

Hydrogen-induced cracking typically follows a path along grain boundaries leading to intergranular cracking [24,26]. This is because hydrogen reduces the energy required for crack propagation, making the material more susceptible to fracturing even under lower external loads.

Hydrogen also affects the fatigue life of materials. The presence of hydrogen can lead to the early initiation of fatigue cracks and accelerate their growth during cyclic loading, thus reducing the lifespan of the metal under repetitive stress conditions [28,29].

It is generally accepted that the Hydrogen embrittlement (HE) in metallic materials is primarily driven by three key processes [30,31]:

Ingress and Diffusion: Hydrogen atoms enter the material from a hydrogen-rich environment and diffuse, even at room temperature, towards regions with high stress concentrations and microstructural traps.

Interaction with Defects: Hydrogen atoms interact with various microstructural defects including vacancies, solute atoms, dislocations, interfaces, and micro-voids or cracks [32]. These interactions are the basis of the embrittlement process and leads to various proposed embrittlement models (schematically summarized in Figure **I-3**).

Damage Nucleation and Evolution: Under applied stress**,** interaction of hydrogen with defects promote damage nucleation and crack propagation within the structure, enhancing the susceptibility to embrittlement.

Several mechanisms have been proposed to explain how hydrogen embrittlement occurs.

Hydrogen-Enhanced Decohesion (HEDE) [33]**:** This model suggests that hydrogen atoms reduce the cohesion force between metal atoms. This weakening effect is more pronounced along grain boundaries or at precipitate interfaces where hydrogen tends to accumulate. Hydrogen reduces the energy required to separate atoms, effectively facilitating the nucleation and propagation of cracks under tensile stress. This mechanism often results in a brittle fracture mode where cracks propagate along the weakened atomic bonds.

Hydrogen-Enhanced Localized Plasticity (HELP) [34]**:** This mechanism describes HE by enhancing localized plastic deformation. The presence of hydrogen lowers the energy barrier for dislocation movement, which can lead to an increase in localized plasticity at stress concentrations (*e.g.*, crack tips), promoting the initiation and growth of cracks.

Adsorption-Induced Dislocation Emission (AIDE) [35,36]: This model focuses on the role of hydrogen adsorbed on the material surface, which can weaken interatomic bonds and increase dislocation emission at crack edges.

So far, the effect of hydrogen on dislocation mobility is still controversial. Several studies have suggested that hydrogen forms atmospheres around dislocation cores, providing a shielding effect that reduces long-range elastic interactions between dislocations and obstacles. This reduction in interaction decreases the hindering effect of obstacles on dislocation motion, thus enhancing dislocation mobility [10,37,38], as demonstrated in α-iron where hydrogen reduces the critical stress for screw dislocation motion by 27-43% [39].

In contrast, according to Cottrell's theory, hydrogen atmosphere exerts a drag force on moving dislocations, impeding their movement [40]. Recent experiments based on transmission electron microscopy (TEM), have also provided interesting information on the interaction between hydrogen atoms and dislocations in pure aluminum [41]. A thin sheet of material was exposed to a hydrogen atmosphere, and after applying a cyclic load to pillar samples, the movement of dislocations was observed. The authors found that dislocations remained fixed after hydrogenation, which was totally different from vacuum loaded. They attributed this locking effect to the segregation of hydrogenated vacancies at the core of the dislocation. Through the interaction with hydrogen and vacancy, Zhu *et al* [42], based on atomistic modelling, have also demonstrated that in α-Fe, hydrogen-stabilized vacancies can lead to dislocation locking.

Hydrogen-Enhanced Strain-Induced Vacancies (HESIV) [23,43]**:** According to this mechanism, hydrogen is thought to stabilize vacancies clusters. The presence of hydrogen makes it energetically favorable for vacancies to form and cluster together. These clusters can grow into voids, which coalesce and contribute to the formation of microcracks. This mechanism is particularly relevant under conditions of high hydrogen concentration and mechanical strain, where the generation of vacancies is enhanced.

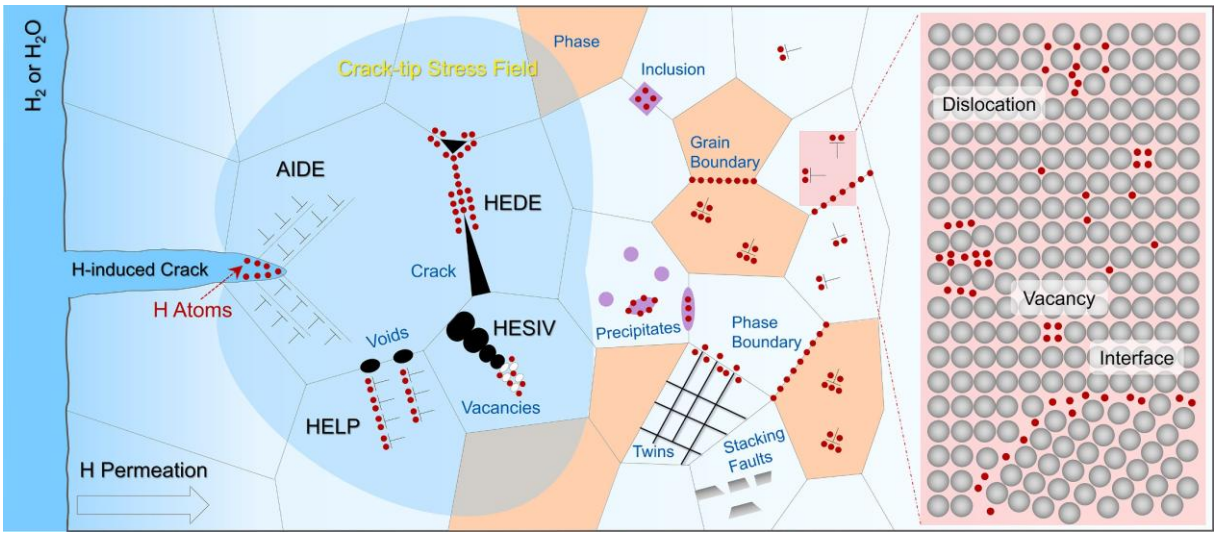


*Figure **I-3**: Schematic diagram illustrating the interaction between H atoms and some of the microstructural defects as well as commonly reported H embrittlement models (HEDE: H-enhanced decohesion, HELP: H-enhanced localized plasticity, AIDE: adsorption-induced dislocation emission, HESIV: H-enhanced strain-in- duced vacancies) [44].*

These mechanisms may coexist and interact, with localized plasticity potentially leading to increased dislocation activity that, in turn, enhances both decohesion and the formation of strain-induced vacancies, compounding the embrittlement process [44]. However, a major challenge in fully understanding and quantifying these interactions lies in the inherent difficulty of precisely localizing hydrogen atoms within the metallic structure, particularly at low concentrations.

Another important effect of hydrogen is its possible influence on phase transformations in metallic alloys. Hydrogen can modify thermal stability and kinetics of phases, and even promote the formation of hydride phases depending on the alloy system and thermodynamic conditions. Previous studies about the influence of hydrogen on phase transformations will be discussed in the following section.

1.2.Influence of Hydrogen on Phase Transformation

The influence of hydrogen on phase transformations in metallic alloys involves a complex interplay of thermodynamic, kinetic, and microstructural factors (Hydrogen-defect interactions) that can dramatically alter material properties.

In titanium alloys, Hydrogen acts as a β-stabilizer, significantly lowering phase transformation temperatures [45]. Hydrogen decreases the $\alpha + \beta \rightarrow \beta$ phase transformation point by more than 200°C when hydrogen content reaches 0.44 wt% [45]. Hydrogen dissolution causes lattice expansion and generates internal stresses that can trigger phase transformations [46,47]. In β-21S Titanium alloy, hydrogen concentrations beyond 23 at% generate sufficient internal stress to induce formation of metastable α″ martensite and ω phases [46]. In Ti-6Al-4V alloys, hydrogen dramatically alters precipitation sequences and morphologies. Hydrogenation leads to formation of intermetallic Ti_3Al phases at concentrations as low as 0.29 wt%, with dimensions and volume fractions increasing significantly with hydrogen content [48].

In titanium alloys, hydrogen is usually used to optimize heat treatment processes [49,50]. Biao Zhang *et al* [51], demonstrates that adding 0.3 wt% hydrogen to Ti-2Fe-0.1B alloy induces significant phase transformations, forming lamellar α_L and martensite α'structures while increasing the β-phase fraction from 4.95% to 30.1%. This hydrogen charging enhances yield strength at room temperature through lattice distortion, dislocation slip impediment, and solid solution strengthening, albeit at the cost of plasticity induced by hydrogen.

In steels, Mogilny *et al*. [52], showed that cathodic hydrogen charging in austenitic steels causes plastic deformation and triggers the γ→ε transformation. This transformation occurs in hydrogen-rich areas and influences the hydrogen distribution in the retained austenite. The γ→ε transformation reduces hydrogen embrittlement and depends on the degree of deformation during charging, when the γ→ε transformation is absent, hydrogen embrittlement is more severe.

Hydrogen is also known to form hydride phases in metallic alloys under specific thermodynamic and kinetic conditions. These phases can occur at high hydrogen pressure and/or temperature, or by electrochemical charging/corrosion that produces very high local hydrogen supersaturations [53,54].

Several distinct hydride phases have been documented in Al alloys, including AlH_3 (alane) [55] and hydrides formed with alloying elements. Figure **I-4**, illustrates hydride-forming and non-hydride-forming elements in the periodic table. For example, electrochemical hydrogen charging of an Al–Li–Cu alloy produced $LiAlH_4$ phase that nucleated from a grain-boundary phase AlLi [56]. Similarly to Li, Zr is also known to have a high affinity with hydrogen with enthalpy of hydride forming of -169 kJ/mol H_2 [57]. In Al–Zr system, during ball milling, hydrogen can be captured by Zr to form hydride phases whose stoichiometry depends on local hydrogen concentration and thermodynamic equilibrium conditions, ranging from ZrH to ZrH_2 [56]. However, recent studies have shown that hydrides containing aluminum and transition metals, such as Al_2CuH and Al_3FeH_4, can only be formed under extreme conditions (*e.g.*, 10 GPa pressure and high temperature) [58,59].

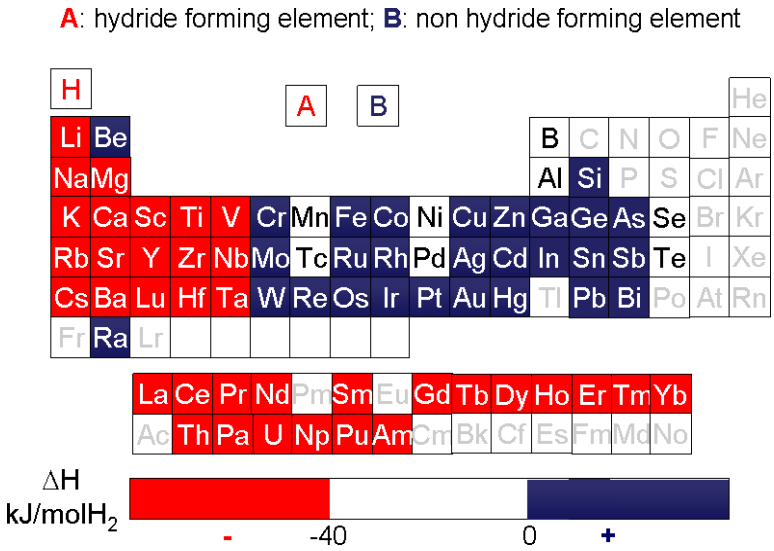


Figure I-4: Periodic table highlighting hydride-forming (A) and non-hydride-forming (B) elements [60].

Hydrogen-vacancy binding energy is relatively high (0.52–0.53 eV [61,62]), indicating that hydrogen has a strong attraction to vacancies. These interactions influence the precipitation or solutes mobility in aluminum alloys. This has been demonstrated experimentally and through *ab initio* calculations in Hachet's work [63,64]. In the AlMgSi alloy, even with a low concentration of hydrogen in solid solution, there is a significant effect on the mobility of alloying elements in the matrix. This was attributed to hydrogen-vacancy interactions leading to an increase in vacancy migration energy [63]. In an Al-5Cu alloy, during natural aging, the presence of hydrogen delays the hardening kinetics of the alloy which was attributed to slower growth of GP zones due to a reduced mobility of copper atoms (Figure **I-5**). This has been demonstrated experimentally and confirmed by ab initio calculations. This delay is attributed to the reduction in the probability of copper atom exchange with vacancies [64].

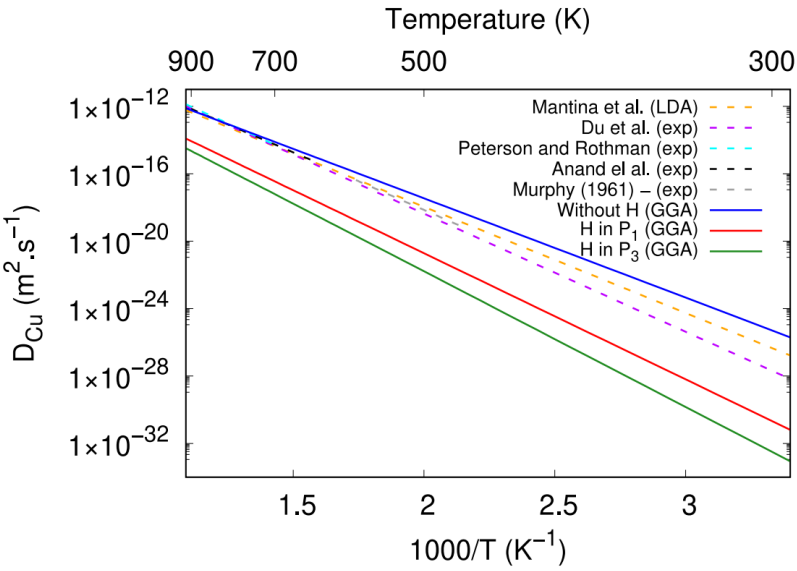


*Figure **I-5**: Calculated diffusion coefficient of Cu as a function of T with and without, P1 and P3 refer to specific positions of hydrogen atoms in relation to a vacancy [64].*

GP zones, which are metastable phases, eventually transform into the θ" metastable phase. This transformation may also be sensitive to the vacancy-hydrogen interactions, as well as to hydrogen-precipitate interface, and hydrogen-dislocation interactions. In this PhD work, we aim to investigate the influence of hydrogen on the full precipitation sequence (GP → θ" → θ' → θ) in the Al-Cu system.

In terms of solute-vacancy binding in aluminum, Cu has a binding energy of 0.02 eV, while Zr exhibits -0.28 eV (Figure **I-6**), indicating a repulsive interaction. As a result, the mobility of Zr in Al is low [65], but interestingly, it exhibits a high affinity for hydrogen. Therefore, the Al-Zr alloy was selected as another model system to investigate the influence of hydrogen on precipitation.

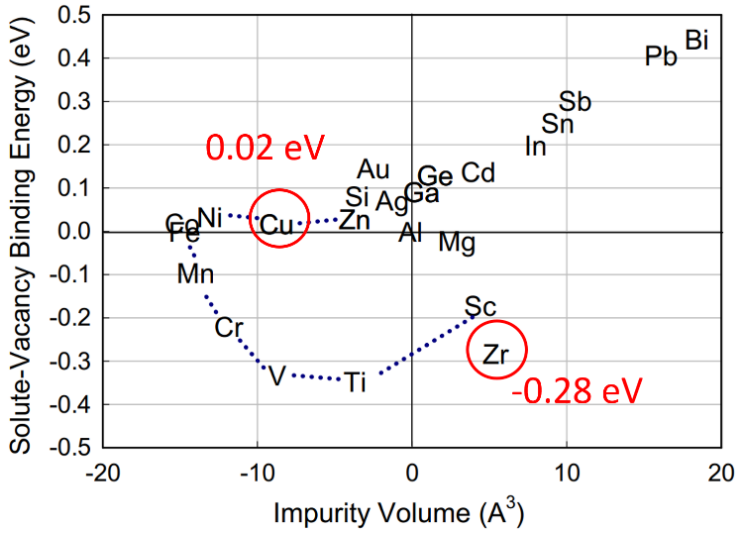


Figure I-6: Solute-vacancy binding energies in Al as a function of the solute impurity volume[66].

In the following, basic concepts of precipitation are introduced and the precipitation mechanisms in aluminum alloys are described, including a detailed review of precipitate types, structures, and properties in the Al-Cu and Al-Zr systems. Finally, hydrogen in aluminum (solubility, diffusion, trapping) and charging techniques will be reviewed in the last part of Chapter I.

2. Precipitation in Aluminium Alloys

2.1. Precipitation Mechanisms and Kinetics

2.1.1. Classical Nucleation Theory

Phase transformations are usually induced by temperature changes in alloys with a fixed bulk composition. These transformations can be categorized into several types, including precipitation reactions, eutectoid transformations, ordering reactions, massive transformations, and polymorphic changes [17]. Specifically focusing on precipitation, these can be described by reactions where metastable supersaturated solid solution transitions produce a more stable solid solution and one or several stable or metastable second phases. This process involves long-range diffusion, as phases with different compositions from the matrix form.

Nucleation and growth of precipitates represent fundamental phase transformation processes that control microstructural evolution in metallic alloys [17,67]. Understanding these mechanisms is crucial for controlling material properties, as precipitation significantly influences strength, and other mechanical properties [68].

Typically, the alloy is heated in a temperature range where a homogeneous solid solution is achieved. Subsequent quenching preserves this supersaturated state at room temperature, locking the solute atoms in a non-equilibrium, supersaturated state within the matrix. At this stage, the supersaturated matrix is unstable, creating a driving force for the nucleation of a new phase. This nucleation may be homogeneous or heterogeneous [17].

Homogeneous nucleation in solids occurs without any preferential nucleation sites [69], such as grain boundaries or dislocations. The free energy change associated with the nucleation process has the following three contributions [17,70]:

- The creation of a volume V of new phase, resulting in a volume free energy reduction of $V\Delta G_V$.
- The creation of an area A of interface, leading to a free energy increase of $A\gamma$, where γ is the interfacial energy.
- Misfit strain energy (ΔG_s) due to the transformed volume not fitting perfectly into the space originally occupied by the matrix.

Adding up all these contributions the total free energy changes as:

$$\Delta G = -V\Delta G_V + A\gamma + V\Delta G_s \qquad \text{I-1}$$

If the variation of γ with interface orientation is neglected and if nucleus are spherical, the volume and surface area are $V = \frac{4}{3}\pi r^3$ and $A = 4\pi r^2$, respectively. Thus, Eq I-1 becomes:

$$\Delta G = -\frac{4}{3}\pi r^3(\Delta G_v - \Delta G_s) + 4\pi r^2\gamma \qquad \text{I-2}$$

Where r is the Radius of the spherical nucleus. This representation makes it easier to analyze how the free energy changes with the size of the nucleus, it is shown as a function of r in Figure **I-7**.

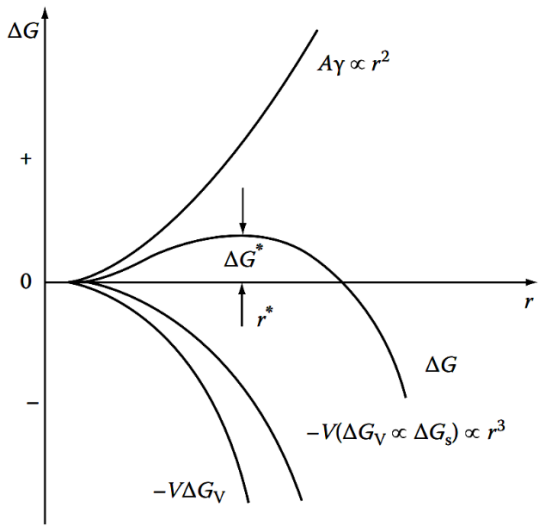


*Figure **I-7** : The variation of ΔG with r (a spherical nucleus) for a homogeneous nucleus. There is an activation energy barrier ΔG* [17].*

Taking the derivative of ΔG with respect to r and solving for r we can obtain the critical radius of the nuclei as follows:

$$r^* = \frac{2\gamma}{\Delta G_v - \Delta G_s} \qquad \text{I-3}$$

By substituting r^* into the expression for ΔG, we can obtain the activation energy barrier ΔG^* which represents the total free energy change when the nucleus is at the critical radius r^*.

$$\Delta G^* = \frac{16\pi\gamma^3}{3(\Delta G_v - \Delta G_s)^2} \qquad \text{I-4}$$

This barrier represents the energy needed to form a stable nucleus that can grow to form the new phase. The rate of homogeneous nucleation is influenced by ΔG^*, which defines the probability of surpassing the energy barrier needed to form a nucleus of critical size [17]. The nucleation rate is given by:

$$N_{homg} = \omega\, C_0 e^{\left(-\frac{\Delta G_m}{kT}\right)} e^{\left(-\frac{\Delta G^*}{KT}\right)} \qquad \text{I-5}$$

Where C_0 is the atom density, ω includes the vibrational frequency of atoms and the area of the critical nucleus, and ΔG_m is the activation energy for atomic migration.

Heterogeneous nucleation occurs at interfaces, grain boundaries, or dislocations, leading to significantly lower energy barriers [17,70]. When a nucleus forms at these defect sites, it

releases some free energy (ΔG_d) and thus reducing or even eliminates the activation energy barrier. The free energy change during heterogeneous nucleation is given by [17]:

$$\Delta G_{het} = -V(\Delta G_v - \Delta G_s) + A\gamma - \Delta G_d \qquad \text{I-6}$$

The energy barrier for each phase during precipitation is influenced by the balance between the driving force for phase transformation (volume free energy reduction) and the energy costs associated with creating new interfaces and accommodating lattice mismatches (interfacial and misfit strain energies) [17,70]. This balance determines the nucleation rate, the critical nucleus size, and the sequence of phase transformations in a supersaturated solid solution.

2.1.2. Precipitate Growth

After the nucleation step, precipitates grow by volume diffusion of the solutes, driven by concentration gradients around them. The rate of precipitate growth is influenced by the rate at which solute atoms are delivered to the interface and the rate at which these atoms rearrange at the interface. The rate of growth is governed by the volumetric diffusion of atoms. It is commonly accepted that interfacial processes occur faster than volume diffusion [17]. The complexity of precipitate growth arises from the intricate interaction between thermodynamic driving forces (supersaturation, interfacial energy), diffusion processes (solute mobility), interface kinetics, elastic strain effects, and morphological considerations [71].

The growth kinetics depend on the specific diffusion mechanism and the nature of the interface. For spherical particles, growth rates are controlled by the supply of solute atoms through bulk diffusion and the incorporation kinetics at the particle-matrix interface.

In diffusion-controlled growth, the growth rate depends on the concentration gradient and the mobility of solute atoms through the matrix to the growing precipitate interface (Figure **I-8**).

The concentration of solute at the interface C_i is controlled by the Gibbs-Thomson effect and can be expressed as a function of the precipitate radius r.[72,73]

$$C_i = C_e \exp\left(\frac{2\gamma V_m}{R\,T\,r}\right) \qquad \text{I-7}$$

where C_e is the equilibrium solute concentration in the matrix, and V_m is the molar volume of the product phase.

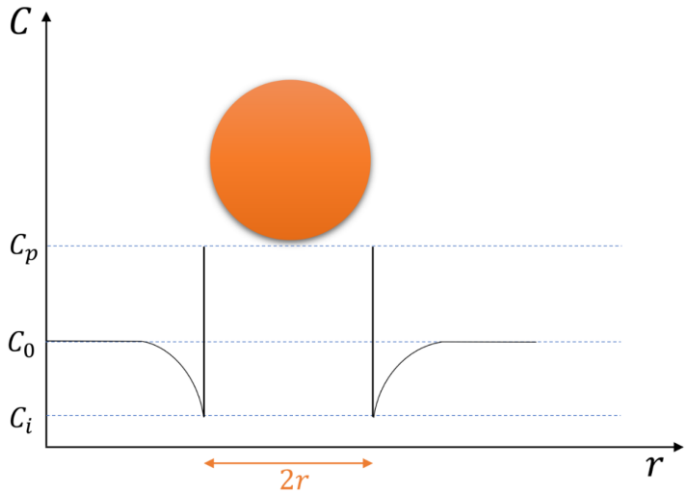


Figure I-8: Schematic composition profile through precipitate in the classical growth mode.

For a unique spherical particle, in an infinite volume, the solute concentration at the interface C_i is the equilibrium concentration C_e, if the effect of precipitate curvature is neglected. This assumption leads to the following equation [72–74]:

$$\frac{dr}{dt} = \frac{D}{R}\frac{C_0 - C_i}{C_p - C_i} \qquad \text{I-8}$$

integration through time yields to:

$$r(t) = \left(r_0^2 + 2Dt\frac{(C_0 - C_e)}{(C_p - C_e)}\right)^{1/2} \qquad \text{I-9}$$

where r is the precipitate radius, C_0 the nominal solute concentration, C_e is the solute concentration in matrix at equilibrium, and C_p is the solute concentration in precipitate, D is the diffusion coefficients for solute, which typically exhibits Arrhenius temperature dependence, reflecting the thermally activated atomic migration [75–77]. This dependence is expressed as:

$$D = D_0 \exp(-\frac{Q}{RT}) \qquad \text{I-10}$$

where D_0 and Q are constants.

This results in the characteristic parabolic growth law: $R \propto t^{1/2}$ [78,79]. In multicomponent alloys, the growth rate depends also on diffusive interactions between different solute species [80]. In real system, which are not infinite, the solute concentration in matrix progressively

decreases ($C_0 \neq$ const). Nevertheless, experimental growth rates are usually close to this theoretical model, as shown for Al-Zr alloys [72,73,81].

When the attachment kinetics at the precipitate-matrix interface becomes rate-limiting (solute atoms cannot easily cross the interface), interface-controlled growth dominates. This mechanism typically results in linear growth kinetics ($R \propto t$) [82,83], because the interface area and driving force remain relatively constant [84]. In such a situation, the growth rate is independent of precipitate size and depends primarily on interface properties and local supersaturation [85]. It has been shown experimentally in Co-20Fe alloys, where precipitates at grain boundaries initially exhibited interface-controlled growth with linear kinetics, then changed to diffusion control as precipitates grew larger [86].

Temperature significantly influences these mechanisms as it affects diffusion and interface mobility [87]. Higher temperatures generally favor diffusion control by increasing atomic mobility, whereas lower temperatures may favor interface control [88]. The supersaturation also influences the growth mechanism, high supersaturation reduces nucleation barriers, leading to diffusion-controlled growth, while low supersaturation may result in interface control [89,90].

2.1.3. Coarsening

Coarsening starts when the supersaturation of the system decreases and solute-driven growth from the matrix becomes slower. During this stage, precipitate growth is highly competitive, smaller precipitates progressively dissolve, supplying solute to larger precipitates, which continue to grow.

According to the Lifshitz Slyosov [91] and Wagner [92] theory, in the limit of pure coarsening of an infinitely dilute system, the average particle radius changes as:

$$r^3 - r_0^3 = \frac{8}{9}\frac{D\gamma V_p}{k_B T}\frac{C_e}{C_p - C_e}t \qquad \text{I-11}$$

Where r_0 is the particle radius at the onset of coarsening ($t = 0$), V_p is the atomic volume of the precipitate, and k_B is the Boltzmann's constant.

In some systems, precipitation occurs *via* metastable intermediate phases rather than directly to the equilibrium phase. Such intermediates form early because their lower interfacial energy reduces the nucleation barrier. Consequently, precipitation often follows a sequence of

metastable transformations that progressively evolve toward the stable phase. A classic example is the Al-Cu alloy, which will be described in the next section.

2.2.Role of Defects

Defects such as vacancies, dislocations, and grains boundaries influence the nucleation, growth, and distribution of precipitates within the material [93–97].

During the aging process, precipitates tend to form preferentially along dislocation lines. This phenomenon occurs because dislocations act as sites of high stress, reducing the activation energy for precipitate nucleation [98]. For example, in Al-Cu alloy, dislocations act as nucleation sites for θ' precipitates [99–102]. Figure **I-9**, shows an example of precipitates nucleated at dislocations [99].

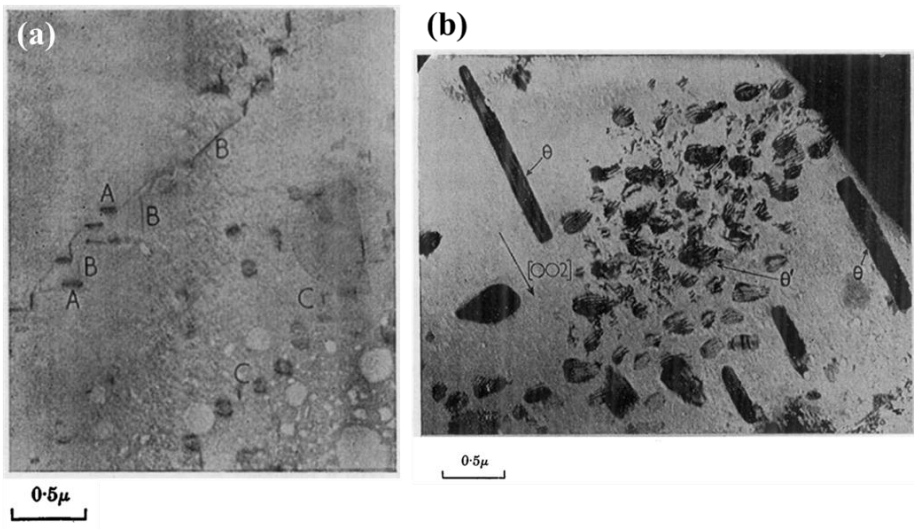


*Figure **I-9** :TEM Images for Al-3.7wt% Cu. (a) aged in bulk at 270°C. Note the precipitates A and the dislocations B. (b) aged at 320°C showing θ and θ' distribution, (110) as orientation [99].*

Studies by Suzuki *et al* 1970 [100], on an Al-4% Cu alloy, indicate that Small vacancy clusters grow by condensation of excess vacancies and then become coarser, leading to the reduction of the nucleation barrier of θ' phase and promoting its nucleation. Recently, Lu Jiang *et al* [103], highlight that dislocations are critical for the heterogeneous nucleation of θ' precipitates in Al-Cu alloys, affecting their distribution and density. Pre-stretching influences the distribution of precipitates through dislocations, leading to anisotropy.

Similarly, to dislocations, grain boundaries may act as preferential nucleation sites for precipitates, influencing precipitate morphology, and leading to the formation of precipitate-

free zones (PFZs) adjacent to these boundaries Figure **I-10**. This phenomenon was described in the early work of Turnbull and Nicholson [104–106]. The grain boundary precipitate free zone forms due to the depletion of vacancies and solute atoms near grain boundaries during the heat treatment. During quenching, grain boundaries act as sinks for vacancies, creating a vacancy profile adjacent to the grain boundary, the distribution of solute atoms also impacts PFZ formation [95]. Slow quenching or interrupted quenching at high temperatures can result in significant precipitation in the grain boundaries [104].

It is generally assumed that the PFZs cause numerous disturbances in the mechanical properties, localizing strain during deformation and facilitating crack initiation and propagation along grain boundaries [107–111], which contributes to grain boundary ductile fracture (GBDF) by facilitating the growth of microvoids initiated at the GB precipitates [108].

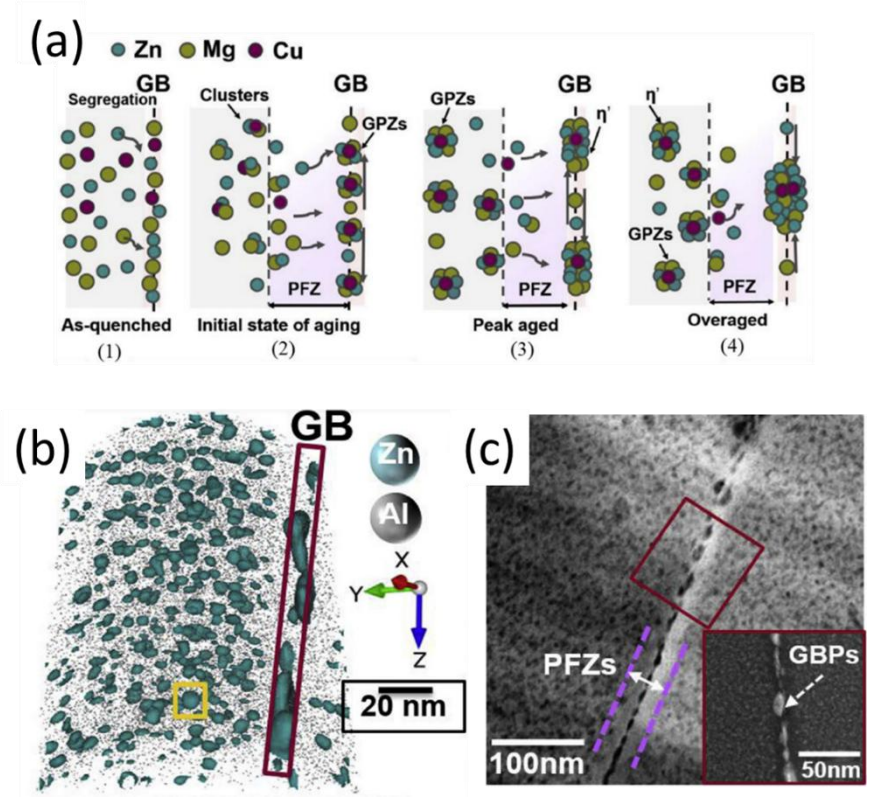


*Figure **I-10**: (a) Schematics of precipitation at grain boundaries and PFZ formation during annealing in a 7000 alloy: (1) after quenching, (2) first stage of aging (0.5h at 120°C), (3) at peak hardening, (4) over-aged. (b) and (c) Analysis performed on an Al-Zn-Mg-Cu alloy after 24 hours of aging at 120 °C, (b) by atom probe tomography (Precipitates highlighted in terms of 10 at% Zn iso-composition surfaces). (c) TEM image shows the size of precipitates and PFZ in the aged state [111].*

In the case of deformed Al-Zr alloy [112], Al_3Zr precipitation occurs mainly at grain boundaries or on dislocations. Figure **I-11**, shows TEM images of heterogeneous Al_3Zr precipitation in an Al-0.3%wt Zr alloy after aging at 450°C for 190h. Indeed, at this temperature, the supersaturation of Zr in the Al matrix is low, which reduces the driving force for nucleation, resulting mainly in heterogeneous precipitation at grain boundaries and dislocations where the nucleation barrier is significantly reduced.

Robson's work [72], demonstrates the same phenomenon of heterogeneity in the distribution of Al_3Zr precipitates. Al_3Zr precipitation was modeled for an industrial alloy (7050) to determine the influence of various alloying elements on Al_3Zr precipitation. It was found that at high temperatures (> 450°C), Al_3Zr precipitates form on dislocations and other structural defects.

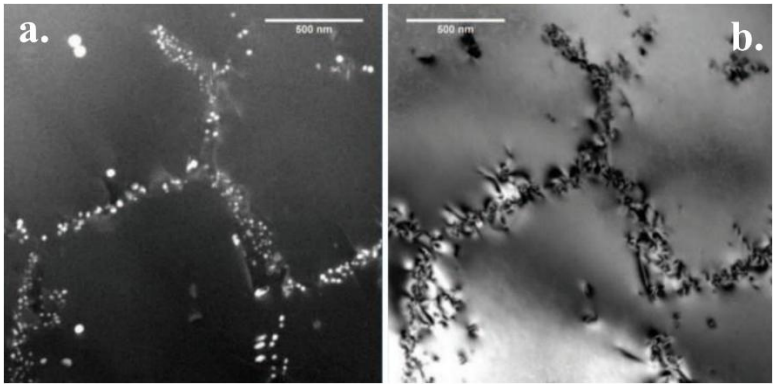


*Figure **I-11** :TEM images in dark (a) and bright fields (b) of heterogeneous Al_3Zr precipitation in an Al – 0.3%wt Zr alloy after solutionizing at 620°C for 288h and aging at 450°C for 190h [112].*

In addition to dislocations and grain boundaries, the concentration of vacancies directly influences the morphology and spatial distribution of precipitates. High concentrations of vacancies promote homogeneous precipitation with finely dispersed precipitates [113].

The excess vacancies generated during quenching from solution treatment enable diffusion processes at relatively low temperatures (room temperature to ~200°C) [114]. The entire precipitation sequence in 6xxx Al alloys is mainly controlled by quenched-in vacancies, which drive diffusion processes that would be kinetically impossible at these temperatures [114]. It has been shown that vacancy concentrations of at least 2×10^{-5} per atom are required for effective clustering [115].

Myhr *et al*. developed precipitation models incorporating the coupled nucleation, growth, and coarsening processes in Al alloys that successfully reproduce short aging times required to reach maximum strength during direct artificial aging (just after quenching) by accounting for

excess vacancy concentrations [116]. In contrast, prolonged natural aging reduces the vacancy concentrations to equilibrium levels, resulting in a slower response during subsequent artificial aging [116].

2.3.Precipitation in the Al-Cu System

Numerous studies have been conducted on the precipitation sequence in the Al-Cu alloy system [117–122]. The precipitation sequence is sensitive to the Cu content and aging temperature, as these factors influence the kinetics of each precipitation stage and the stability of the phases formed [123]. The sequence is as follows: supersaturated solid solution (s.s.s.) → Guinier-Preston (GP) → θ" phase (or GPII) → metastable θ' phase → stable θ phase.

The maximum solubility of copper in aluminum occurs at the eutectic temperature (Figure **I-12**) of 548°C, reaching approximately 5.65 wt% (2.4 at%) [124]. This solubility decreases dramatically with temperature reduction. At room temperature, the equilibrium solubility is extremely low, typically around 0.02-0.05 wt% Cu [124].

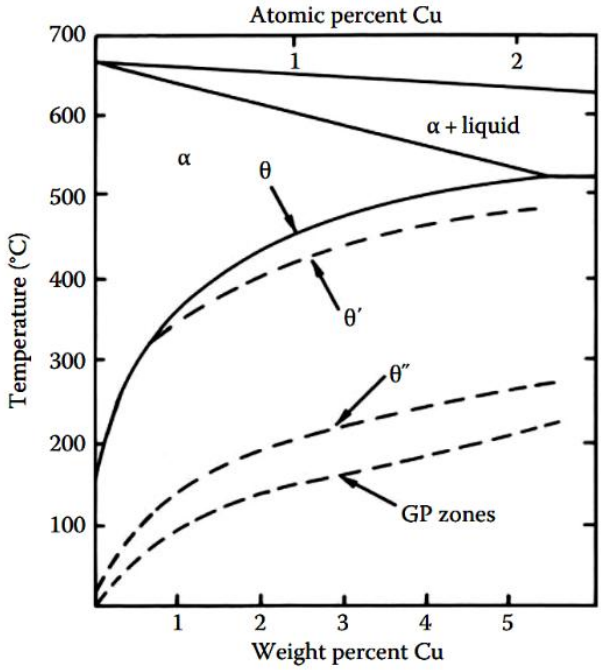


*Figure **I-12** : Equilibrium phase diagram of the Al-Cu system showing the solubility limits in equilibrium with the dashed lines are the solvus lines of GP zones, θ″ and θ′ [17].*

Figure **I-13**a illustrates the nucleation energy barrier for the formation of each metastable phase in the precipitation sequence (GP → θ″ → θ′ → θ). The GP zone formation exhibits the smallest nucleation barrier due to its fully coherent nature with the aluminum matrix and minimal

interfacial energy, while the direct transformation from supersaturated solid solution to the equilibrium θ phase ($\alpha_0 \rightarrow \alpha_4 + \theta$) requires overcoming a significantly higher energy barrier for nucleation. The free energy of the alloy thus decreases more rapidly *via* the progressive formation of intermediate metastable phases than by direct transformation to the equilibrium phase (Figure **I-13**b).

However, more than one phase can coexist at a given stage, as the transformation from one phase to another is not instantaneous and involves nucleation, growth, and dissolution occurring over time.

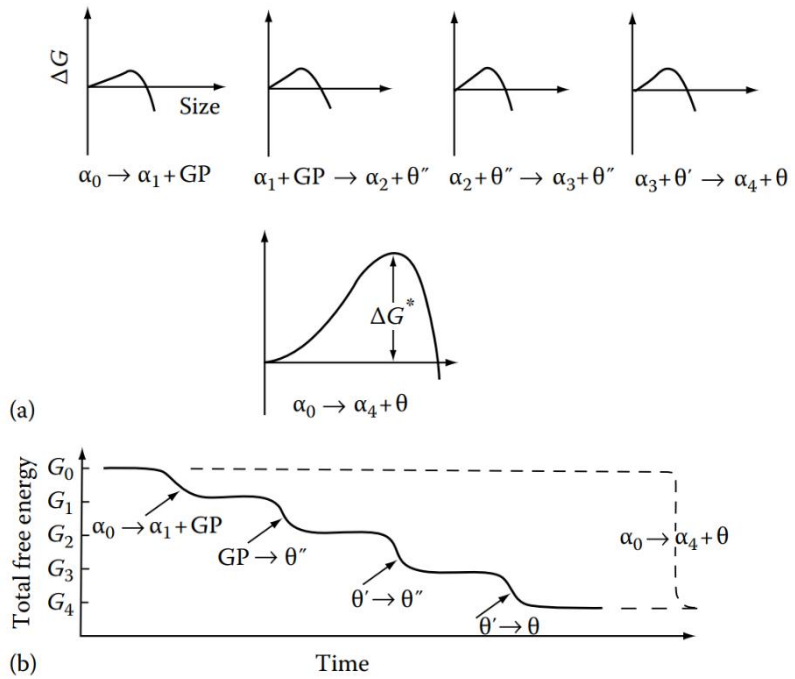


*Figure **I-13** : (a) activation energy barrier to the nucleation of each metastable phase. (b) Schematic diagram showing the total free energy of the system versus time [17].*

The crystal structures of GP-zones, θ″, θ′, and θ have been thoroughly investigated using various diffraction methods and microscopy, and are all illustrated in Figure **I-14-6**.

The size and volume fraction of GP zones vary depending on the alloy composition and the aging conditions [17,125]. GP zones were first discovered in 1938 by André Guinier and G.D. Preston through X-ray diffraction techniques [126–129]. Subsequent studies have been carried out to characterize the structure of GP zones [78-80]. In 2003 the ^{63}Cu NMR technique has been utilized to characterize GP zones in Al-Cu alloys [130]. These zones are described as disks of

Cu atoms (Figure **I-14**), with diameters ranging from approximately 4-20 nm, lying on (100) planes of the (FCC) Al lattice [130]. The formation of GP zones in aluminum alloys is associated with the annihilation of excess vacancies after quenching, which promotes the diffusion of Cu atoms and leads to the formation of GP zones at room temperature (natural aging) [131].

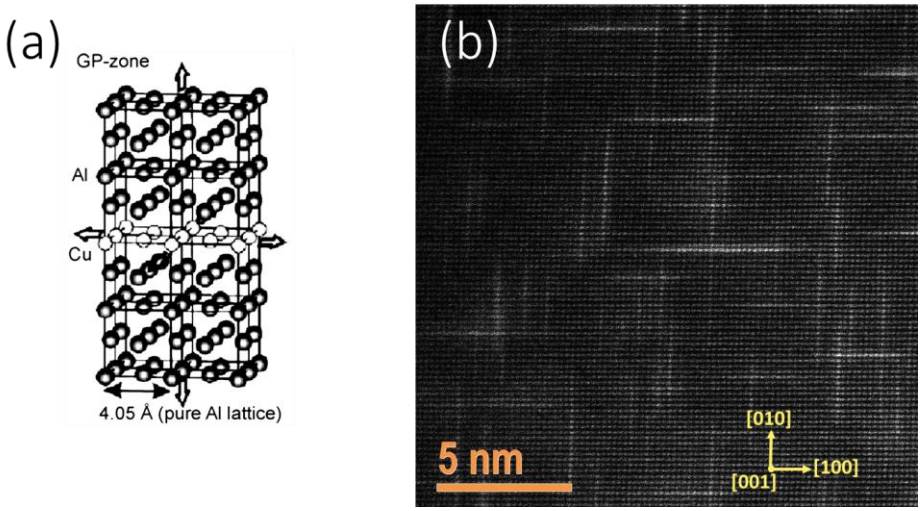


*Figure **I-14**: (a) Schematic representation of the crystal structure of GP-zones [132], and (b) STEM HAADF image showing GP-zones in Al-5.3wt.%Cu alloy (this PhD work).*

GP II zones or θ" consist of several layers of copper atoms (Figure **I-15**) [133]. With increasing aging time, θ" precipitates may exhibits two-layer and/or multilayer configurations [133]. The θ" (Al_3Cu) phase is coherent with the face-centered cubic (FCC) aluminum matrix and plays a critical role in the nucleation of the strengthening phase θ' (Al_2Cu) through a template-directed nucleation mechanism facilitated by vacancies [19].

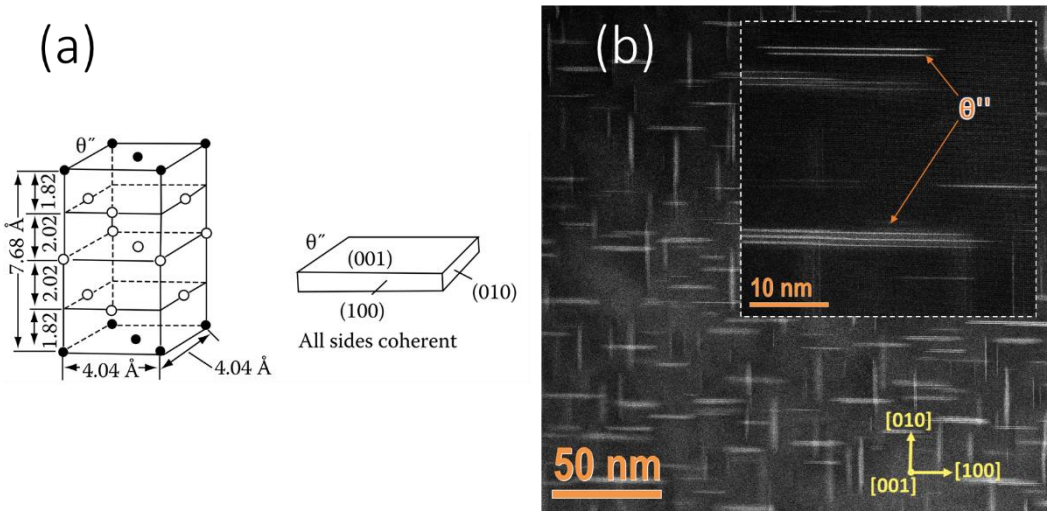


*Figure **I-15** : (a) Schematic representation of the crystal structure of θ" phase [17], and (b) STEM HAADF image showing a θ" precipitate in the Al-5.3wt.%Cu alloy (this PhD work).*

The θ' phase in aluminum-copper alloys, referred to as θ' (Al_2Cu), is characterized by its formation on the $(100)_{\theta'}$ planes within the aluminum matrix. It has a body-centered tetragonal structure (Figure **I-16**) with lattice constants $a_{\theta'} = 4.04$ Å and $c_{\theta'} = 5.80$ Å, and exhibits a specific orientation relationship with the aluminum matrix, allowing full coherence across its $(001)_{\theta'}$ plane.

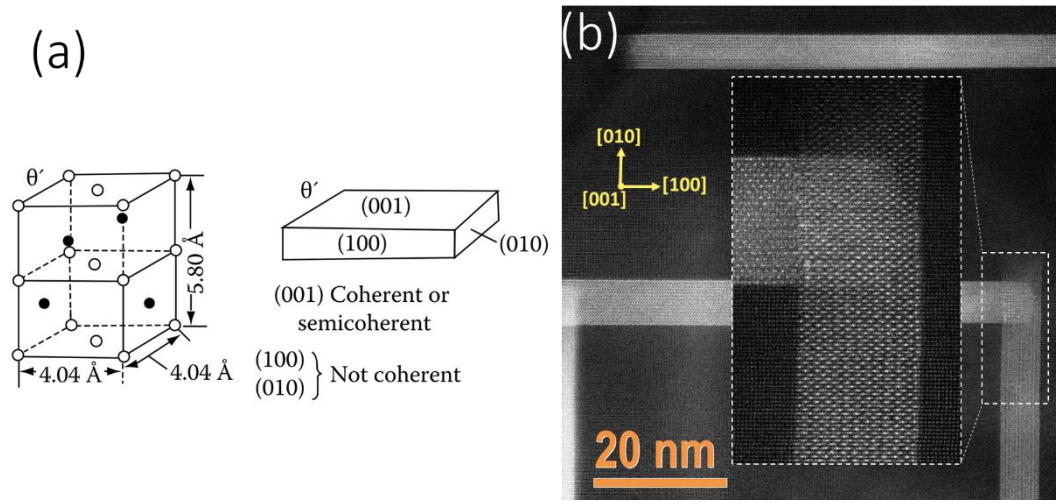


*Figure **I-16** : (a) Schematic representation of the crystal structure of θ' phase [17], and (b) STEM HAADF image showing a real example of θ' phase precipitate in Al-5.3wt.%Cu alloy (this PhD work).*

The θ phase (the equilibrium phase) appears at the final stage of the aging sequence. It has a crystal structure characterized by specific lattice parameters (a = 6.05 Å, c = 4.87 Å [132]) and

can exhibit various orientations and morphologies within the aluminum matrix (Figure **I-17**). The systematic study by Vaughan and Silcock has identified 159 known orientations relationships for θ particles relative to the α-Al matrix, highlighting the complexity and diversity of its manifestation within the microstructure [134,135].

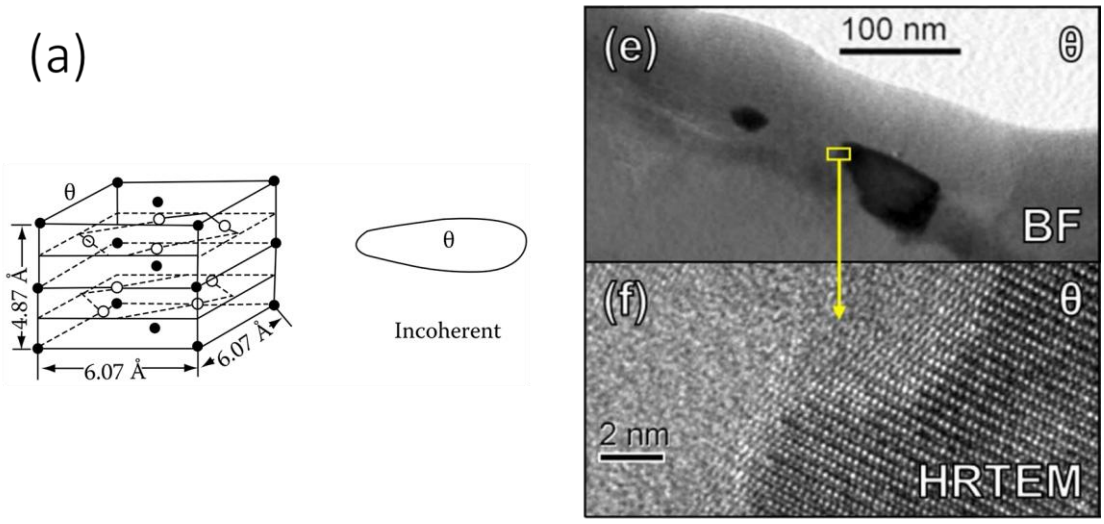


*Figure **I-17**: (a) Schematic representation of the crystal structure of θ phase [17], (e, f) θ precipitates at a grain boundary and HRTEM images of the biggest one [136].*

2.4.Precipitation in the Al-Zr System

In aluminum alloys, zirconium is generally added to inhibit recrystallization or reduce grain growth through the formation of Zr-rich particles at grain boundaries [137]. In the binary Al-Zr system, the supersaturated solid solution decomposes through homogeneous nucleation, forming nanoscaled precipitates that strengthen the aluminum matrix [73]. It should be noted that the equilibrium solubility of Zr in Al matrix is extremely low (< 0.1 at.% at the eutectic temperature) as evidenced by Al-Zr phase diagram (Figure **I-18**). As a result, the amount of Zr that can be dissolved during solution treatment and thus the maximum precipitate volume fraction that can be achieved after aging is intrinsically limited.

The precipitation sequence typically involves the formation of metastable phases before equilibrium structures develop (Figure **I-18**). These metastable phases have an $L1_2$ structure with an Al_3Zr stoichiometry and exhibit a small lattice misfit (δ = 0.75% at 25°C) with the Al matrix [138].

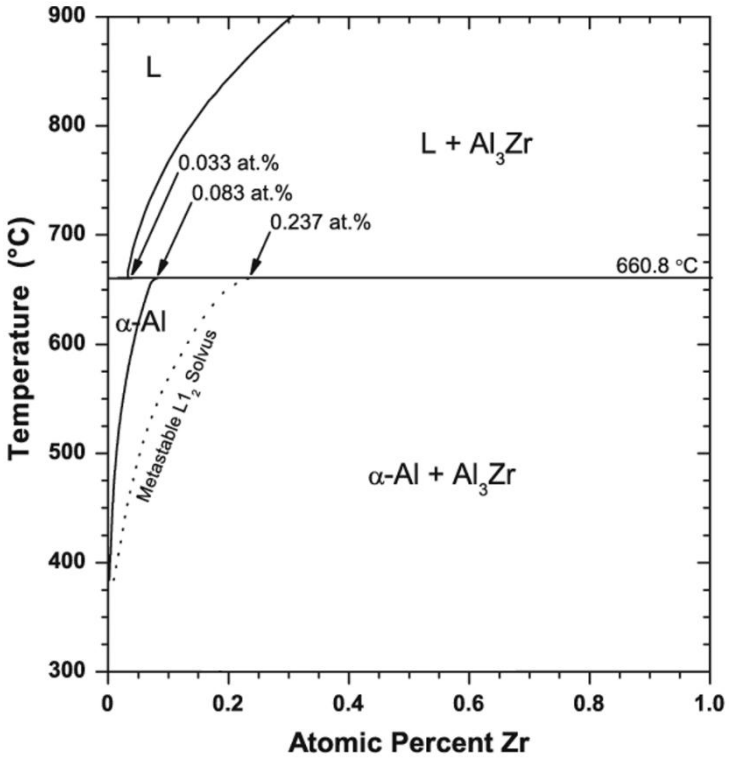


*Figure **I-18**: Equilibrium phase diagram of the Al–Zr system [139]showing the metastable Al_3Zr solvus as calculated by Liu et al. [140].*

Figure **I-19** shows the cubic $L1_2$ and tetragonal DO_{23} structure of the Al_3Zr precipitates. The transition from the metastable $L1_2$ to the stable DO_{23} structure occurs at higher aging temperature and/or longer aging times *(e.g.*, 500°C for 100 hours) [141], and is mainly limited to heterogeneously nucleated precipitates on dislocations and grain boundaries which coarsen by dissolution of surrounding $L1_2$ precipitates [142]. During transformation, $L1_2$ precipitates show preferential growth along the (100) directions (resulting in elongated spheroids), indicating a transition to a stable $D0_{23}$ structure [112,138].

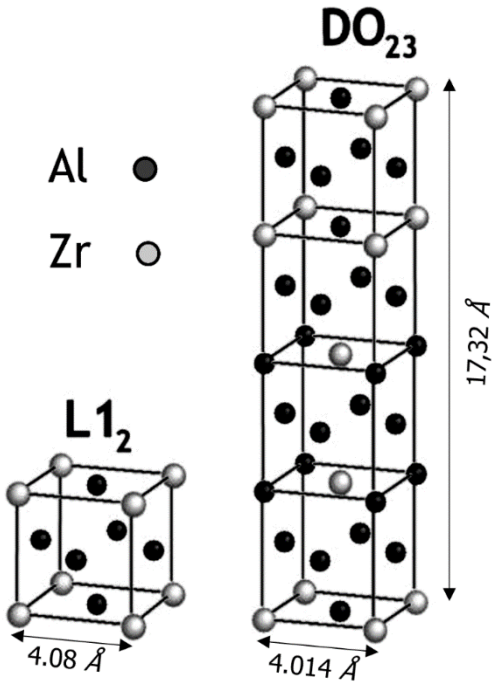


*Figure **I-19** :Description of the atomic arrangement of structures $L1_2$ and DO_{23} [138].*

TEM observations revealed the initial stages of the transition from $L1_2$ to DO_{23} at the atomic scale (Figure **I-20**) [112]. The transition begins at the center of $L1_2$ precipitates rather than at matrix-precipitate interface, contradicting some thermodynamic and kinetic expectations. Indeed, Thermodynamic and kinetic expectations generally assume that the transition starts at the interface, where stresses are higher. But in this case, the center appears to be energetically more favorable. This central initiation leads to the progressive formation of an APB (Anti-Phase Boundary), and as further APBs form, the precipitate elongates and adopts an oval shape. The final structure of DO_{23} is characterized by its elongated, non-spherical morphology (Figure **I-20**), which is influenced by anisotropic elastic stress fields [112].

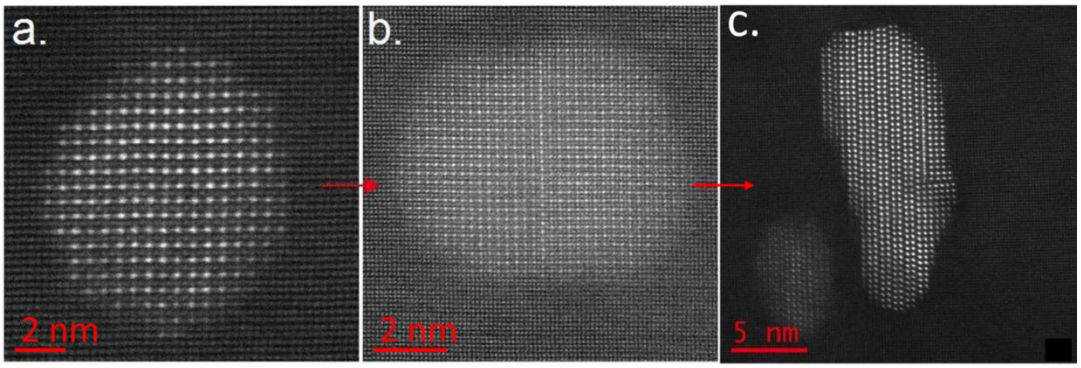


*Figure **I-20** :TEM images of the evolution stages of Al_3Zr precipitates from their metastable $L1_2$ structure to their stable DO_{23} structure [112].*

The thermal stability of Al_3Zr precipitates is high, and their coarsening rate is low (see Eq I-11). This stability is attributed to the low solubility of Zr in aluminum, high coherence of precipitate with the matrix and the slow diffusion of Zr in aluminum [81,139,142–145].

Figure **I-21** demonstrates a comparison of the diffusion coefficient of Zr in Al with that of other common alloying elements (Cu, Si, Mg, Ni, and Fe), clearly illustrating that Zr exhibits the lowest mobility among all other elements across the entire temperature range of 100-600°C.

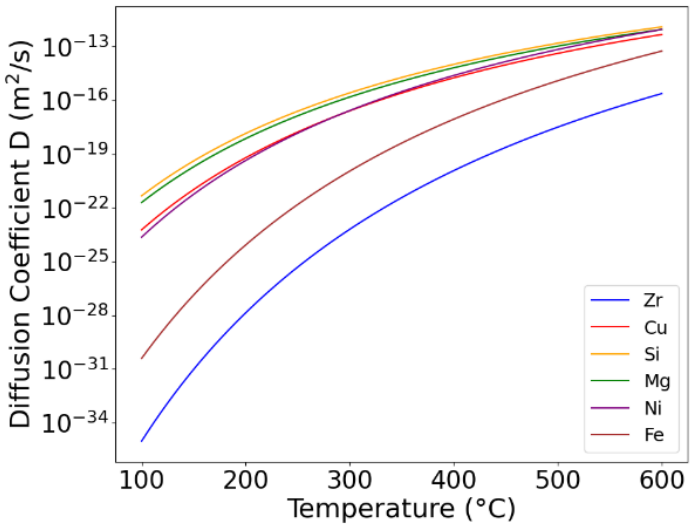


*Figure **I-21** : Impurity Diffusion Coefficients of Different Elements in FCC Al. The assessed Arrhenius parameters are extracted from references [112,146].*

2.5.Precipitation Strengthening Mechanisms

The presence of precipitates contributes to enhancing the yield stress of metallic alloys [147,148]. The mechanism relies on the interaction between moving dislocation and precipitates that act as obstacles to dislocation motion [149]. Its effectiveness depends on several key factors including precipitate volume fraction, size, shape, spatial distribution as well as the nature of the precipitate–matrix interface [150].

Ardell, in his 1985 review [149], discusses various contributions to hardening that must be considered during precipitation. Two primary mechanisms are involved: shearing of coherent precipitates and Orowan looping around non-shearable precipitates (larger or incoherent) forming a dislocation loop [151], as illustrated in Figure **I-22**.

The variation in ductility is mainly controlled by the strain hardening and the mode of dislocation–precipitate interaction. Shearable precipitates provide limited strain hardening as dislocations can cut them, resulting in strain localization and reduced ductility. In contrast, the

transition to non-shearable precipitates promote significant strain hardening by generating dislocation loops that increases dislocation density [149,152].

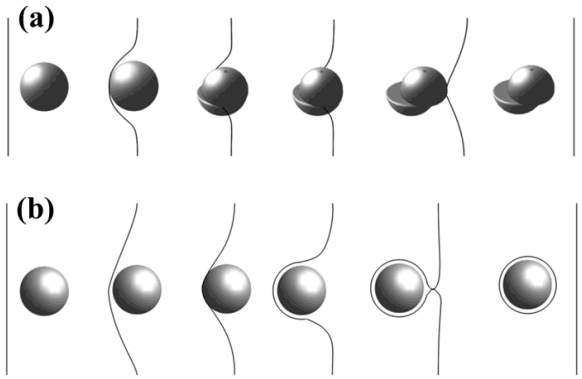


*Figure **I-22** :Scheme of shearing (a) and bypassing (b) of a precipitate by a dislocation [112].*

The balancing of forces resisting the movement of dislocations is shown by the following equation [153,154]:

$$F = 2T \sin \theta \qquad \text{I-12}$$

Where F is the resistance force of the precipitate, T is the line tension of the dislocation, and θ is the angle of the dislocation line curve (Figure **I-23**). As F increases, the dislocation curves more significantly, which indicates greater resistance to movement.

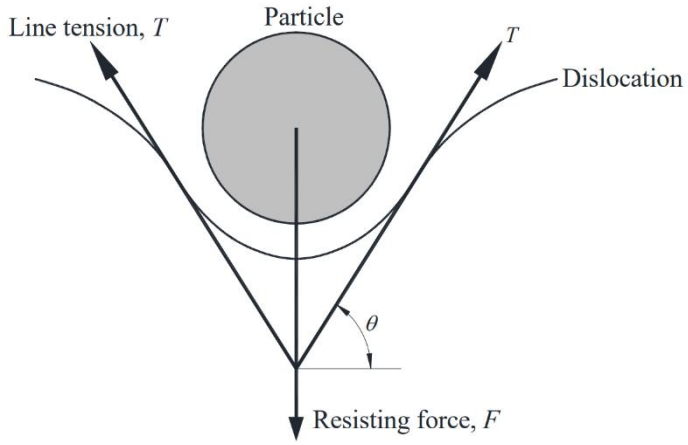


*Figure **I-23** : Balance of forces acting to resist dislocation motion [153].*

When particles are hard and the resistance force F is greater than 2T, dislocations can bypass the particle either by Orowan looping or cross-slip, leaving the particle essentially unchanged. This mechanism allows the dislocation to move around the particle by forming a dislocation loop, contributing to the strain hardening [153]. If the maximum resistance force is reached

before $\sin(\theta) = 1$, then particles are sheared, and the dislocation passes through the resistance zone.

The outcome of the interaction whether through bypassing or shearing depends on the specific conditions of the material, such as the size, spacing, and strength of the precipitates, as well as the applied stress. Factors like particle coherency with the matrix and the material's overall microstructural state play significant roles [153,155].

For homogeneously distributed particles (diameter *d*), the strength increment due to dislocation bypassing (non-shearable precipitates) writes as [156–159]:

$$\Delta\sigma_{\text{Orowan}} = \frac{\mu b}{2\pi\lambda\sqrt{1-v}}\, ln\frac{d}{r_0} \qquad \text{I-13}$$

Where, μ is the shear modulus of the matrix, b is the Burgers vector, r_o is the dislocation core radius (~b), λ is the inter-particle spacing.

The inter-particle spacing λ can be expressed for two types of precipitates, spherical and plate-like, with uniform diameter d and thickness t, as follows [158,159]:

$$\lambda_{Spherical} = \left(\frac{0.779}{\sqrt{f_v}} - 0.785\right) d \qquad \text{I-14}$$

$$\lambda_{Plates} = 0.825\sqrt{\frac{d \times t}{f_v}} - 0.393d - 0.866t \qquad \text{I-15}$$

Where f_v is the volume fraction of precipitates [149].

For shearable precipitates, four main contributions are involved; coherency strengthening, interface strengthening, modulus strengthening and order strengthening. Coherency strengthening arises from the elastic stress field produced by lattice misfit between the precipitate and matrix phases. The coherent strengthening increment is given by [160]:

$$\Delta\sigma_{coherent} = 4.1M\ \mu\ \varepsilon^{\frac{2}{3}}\left(\frac{f_v\ d}{2\ b}\right)^{1/2} \qquad \text{I-16}$$

Where M is the Taylor factor, ε is the lattice misfit parameter.

For semi-coherent or incoherent precipitates, strengthening occurs through the creation of new interfaces during dislocation cutting. The interfacial strengthening is expressed as [160]:

$$\Delta\sigma_{interface} = \frac{M\ 1.21\ d\ \gamma_i^{\frac{3}{2}}}{t^2}\sqrt{\frac{b\ f_v}{\Gamma}} \qquad \text{I-17}$$

Where γ_i is the interfacial energy, Γ dislocation line tension ($= \mu b^2/2$). When precipitates have different elastic moduli compared to the matrix, additional strengthening occurs due to the elastic interaction. The modulus mismatch strengthening can be approximated as [161]:

$$\Delta\sigma_{modulus} = \frac{0.9\ \Gamma}{b}\left(\frac{\Delta\mu}{\mu}\right)^{3/2}\ln\left(\frac{2\pi}{\lambda}\right)^{-3/2}(rf_v)^{1/2} \qquad \text{I-18}$$

Where $\Delta\mu = |\mu_p - \mu|$ is the difference in shear moduli of precipitate and matrix.

In the case of order strengthening, ordered precipitates embedded within a matrix give rise to the formation of an antiphase boundary (APB) when they are sheared by a dislocation. The generation of this APB, which disrupts atomic order within the precipitate, requires additional energy and therefore contributes to an increase of critical stress. The corresponding strengthening increment is given by [162,163]:

$$\Delta\sigma_{Order} = \frac{0.81M\gamma_{APB}}{2b}\left(\frac{3\pi f_v}{8}\right)^{\frac{1}{2}} \qquad \text{I-19}$$

where γ_{APB} is the anti-phase boundary energy of precipitates.

The nature of dislocation-precipitate interactions is fundamentally determined by the relative strength of the precipitate compared to the applied stress and the precipitate size [164–166]. Figure **I-24**, schematically illustrates the relationship between precipitate size and strengthening, for spherical precipitates at constant volume fraction (Figure **I-24**a) [162], as well as for spherical carbide precipitates with varying volume fraction and uniform hardening (Figure **I-24**b) [167]. Order strengthening remains constant with increasing precipitate diameter, as indicated by the horizontal line. When the precipitate size is small ($D < D_{c1}$), order strengthening is the dominant mechanism.

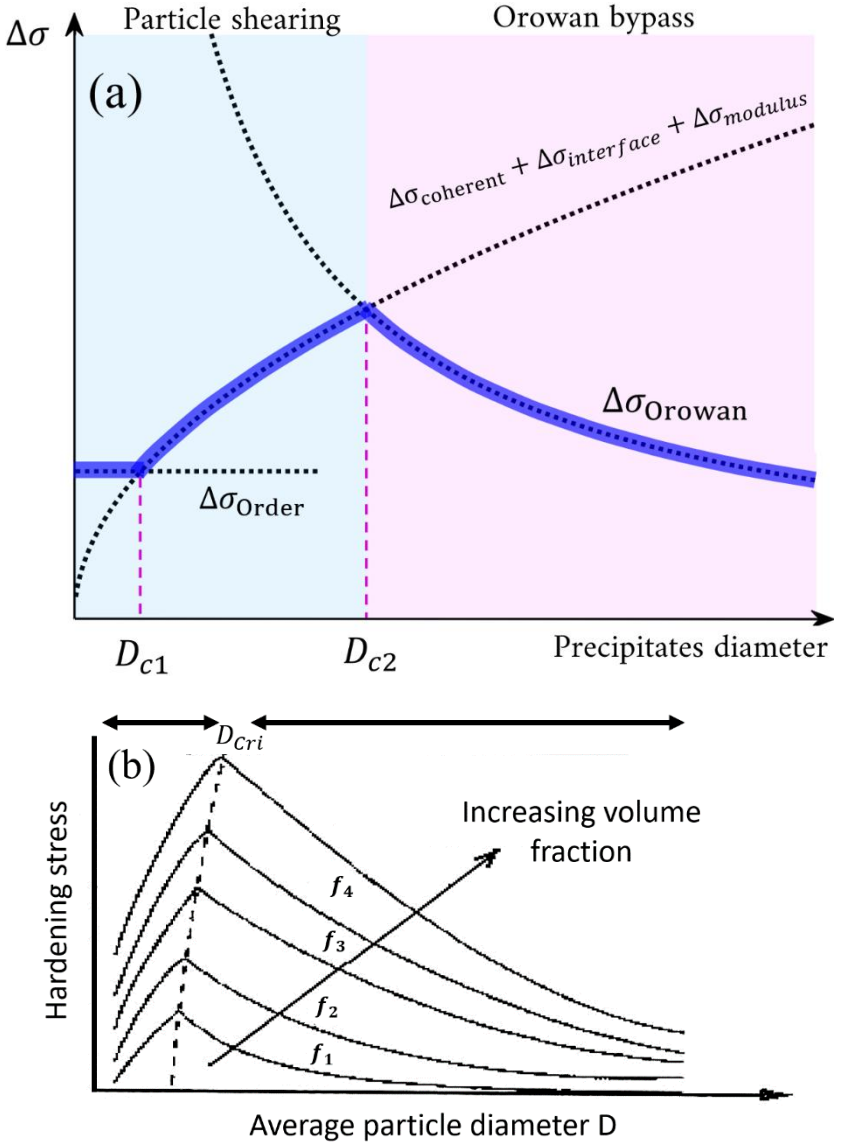


*Figure **I-24** (a) Variation of the different strengthening contributions with precipitate diameter with f_v constant [162]. (b) Dependence of strengthening on both precipitate diameter and volume fraction [167].*

2.6.Age-hardening Behavior of Al-Cu and Al-Zr systems

2.6.1. Al-Cu system

The microstructure and mechanical properties of Al-Cu alloys are fundamentally controlled by thermo-mechanical treatments, which govern the precipitation sequence and resulting strengthening mechanisms [168,169]. J. Silcock and H. Hardy [170] have studied the hardness of Al-Cu alloy as a function of time during artificial aging at 130°C and 190°C (Figure **I-25**), focusing on the associated microstructural changes.

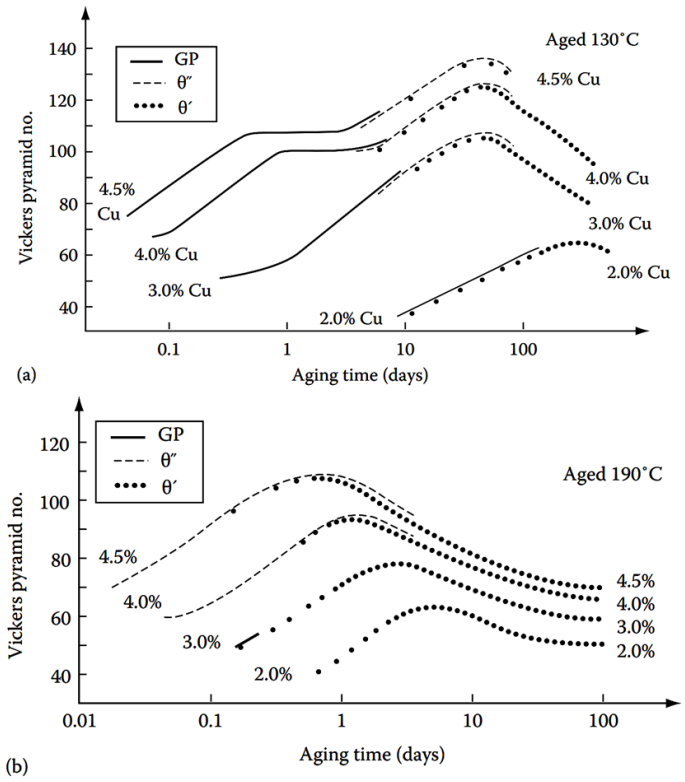


*Figure **I-25**: Hardness versus time for various Al-Cu alloys at (a) 130 ˚C and (b) 190 ˚C [170].*

During aging at 130°C the hardness increases gradually over time. The increase in hardness can be attributed to the formation and growth of GP zones and the subsequent formation of coherent θ" precipitates. After reaching the peak, hardness decreases as the structure over-ages, with precipitates coarsening and losing coherence with the matrix, which leads to a reduction in strengthening. Aging at 190 °C accelerates the kinetics of the precipitation processes. The hardness increases more quickly than at 130 °C, reaching a peak in a shorter amount of time due to faster diffusion rates. However, the peak hardness achieved is lower than at 130°C. This is because the higher temperature promotes the fastest formation of θ' and θ phases, which are less effective at hindering dislocation movement than the finely dispersed GP zones and θ" precipitates. Besides, the volume fraction of precipitates also changes with temperature, further influencing the peak hardness.

Recent research has provided more detailed understanding of temperature effects [123]: At 160°C, the microstructure at peak-age consists mainly of θ″ precipitates, providing maximum strengthening. At 200°C, the θ′ phase becomes dominant, resulting in lower peak hardness but faster aging kinetics.

2.6.2. Al-Zr system

Studies by Knipling *et al*. [139,142] on Al-Zr alloys containing 0.3 wt% and 0.6 wt% Zr aged at 375°C, 400°C, and 425°C demonstrated the combined effects of composition and temperature on precipitation behavior and hardness evolution.

Alloys with 0.6 wt.% Zr reached peak hardness after 25–30 hours of aging, while it appears after 100h for 0.3%wt Zr. The higher Zr concentration provides a higher driving force for precipitation thereby accelerating the kinetics of hardening. Aging at 375°C results in a finer precipitate dispersion and higher hardness (Figure **I-26**). In contrast, higher aging temperatures of 400–425 °C, lead to coarser precipitates and resulted in reduced peak hardness. At 500 °C [138], significant precipitate coarsening occurred, leading to a drop in hardness. The significantly lower hardness levels in Al-Zr alloys compared to Al-Cu systems is due to the lower solubility of Zr in the Al matrix and thus the lower volume fraction of precipitates.

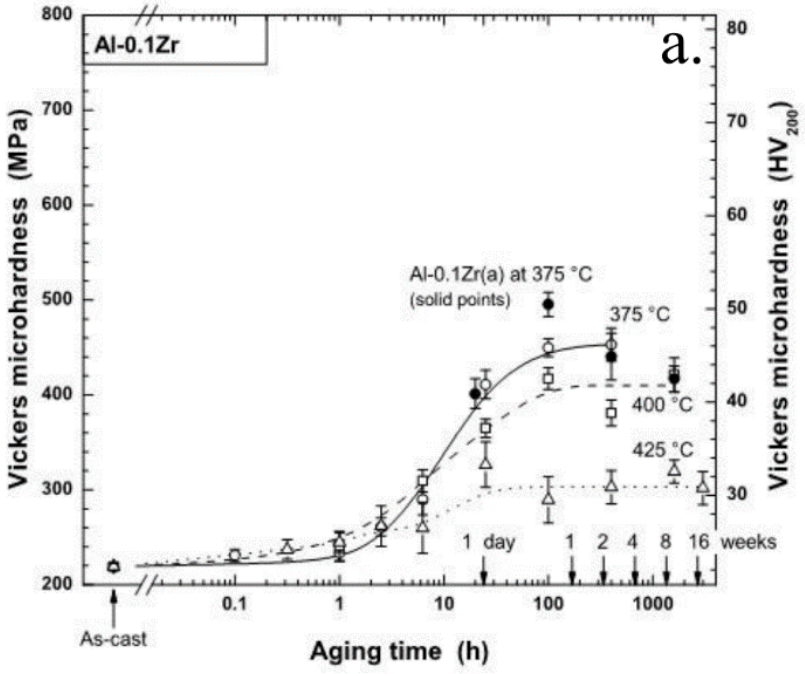


*Figure **I-26** :Vickers hardness measurement on Al-0.3%wt Zr alloy aged at 375-400-425°C [112].*

3. Hydrogen in Aluminum and Its Alloys

3.1. Hydrogen Solubility

Once adsorbed, hydrogen atoms can penetrate the aluminum crystal lattice. This penetration is governed by thermodynamic solubility and is influenced by factors such as temperature and pressure, as well as the presence of alloying elements or structural defects in the aluminum. The

maximum amount of hydrogen that can dissolve in aluminum at a specific temperature and pressure is called the solubility of hydrogen.

Sieverts' law help in determining solubility under varying pressures, establishing a relationship where solubility is proportional to the square root of the gas pressure over the metal, provided the system is at a constant temperature [171,172].

$$C_H = k \,.\sqrt{P_H} \qquad \text{I-20}$$

Where: C_H is the solubility of hydrogen in aluminum, k is the Sieverts' constant for hydrogen in metal, which depends on the metal type and temperature. P_H is the partial pressure of hydrogen gas, also known as the fugacity.

Additionally, the temperature dependence of hydrogen solubility in aluminum can be expressed by incorporating an Arrhenius-type equation for the Sieverts' constant [171,172]:

$$k(T) = C_0 \,.\, e^{-\frac{\Delta H}{RT}} \qquad \text{I-21}$$

Combining these two equations provides a model for hydrogen solubility in aluminum across different temperatures and pressures:

$$C_H = C_0 \,.\sqrt{P_H} \,.\, e^{-\frac{\Delta H}{RT}} \qquad \text{I-22}$$

Where C_0 is the pre-exponential factor, ΔH is the enthalpy change of solution, representing the heat absorbed or released when hydrogen dissolves in aluminum, typically expressed (*J/mol*). R is the universal gas constant, T is the absolute temperature in Kelvin.

The purity of the metal and its microstructure significantly impact hydrogen solubility. High-purity aluminum exhibits lower hydrogen solubility due to fewer defects like interfaces, which can act as trapping sites for hydrogen. Table **I.1** provides values for the apparent hydrogen solubility in pure Al and Al-lithium alloys. These values show how the addition of lithium to Al increases the hydrogen solubility and how this solubility is affected by the interface of coherent precipitates within the alloys.

Figure **I-27** illustrates the temperature dependence of hydrogen solubility for various Al alloys, demonstrating the pronounced effect of alloying elements on hydrogen absorption behavior. Pure aluminum exhibits the lowest hydrogen solubility across the entire temperature range, with values ranging from approximately 10^{-10} atomic fraction at 300 K to 10^{-7} atomic fraction at

higher temperatures. In contrast, Al-Li alloys demonstrate significantly higher hydrogen solubilities, with values reaching 10^{-5} to 10^{-2} atomic fraction at elevated temperatures. Other commercial alloys, including Al-Mg, Al-Cu, and 2324 Alloy, exhibit intermediate solubility values between pure Al and the Al-Li alloys.

*Table **I.1**: Apparent hydrogen solubility for pure aluminum and aluminum-lithium binary alloys [28].*

Alloy	Temperature range (K)	C_o (atom frac.* $atm^{-½}$)	ΔH_S (kJ/mol)	C_H (atom frac.)**
Al (99.99%)	623–933	5.51×10^{-5}	49.3	3.31×10^{-8}
Al–1 wt.% Li (one phase)	698–873	8.91×10^{-6}	11.6	1.57×10^{-6}
Al–1 wt.% Li (two phases)	473–648	8.05×10^{-6}	6.85	2.04×10^{-6}
Al–2 wt.% Li (one phase)	748–873	1.21×10^{-5}	12.9	1.74×10^{-6}
Al–2 wt.% Li (two phases)	473–723	8.20×10^{-6}	5.22	2.88×10^{-6}
Al–3 wt.% Li (one phase)	798–873	2.94×10^{-5}	15.9	2.71×10^{-6}
Al–3 wt.% Li (two phases)	523–723	3.76×10^{-5}	11.8	3.56×10^{-6}

* atom frac. = atomic fraction, atoms H/atom metal.
** C_H evaluated at: T = 800 K in the case of one phase; T = 600 K, P_{H_2} = 1 atm (0.1 mPa) for 2 phases.

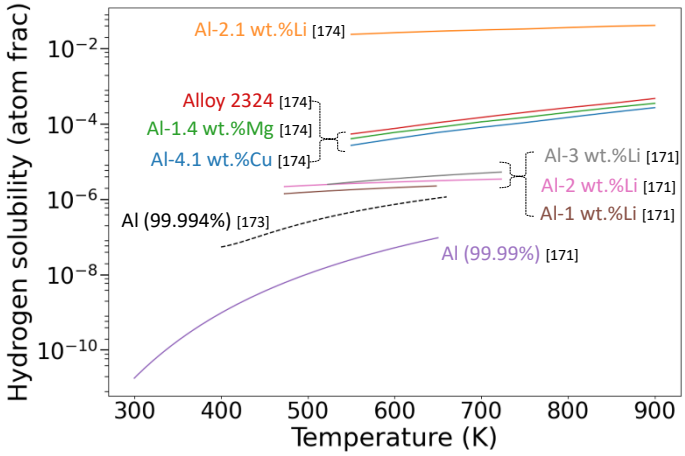


*Figure **I-27**: Hydrogen solubility for pure aluminum and its alloys, with P=1atm [171,173,174].*

Generally, for most aluminum alloys, increasing the solute content leads to an increase in hydrogen solubility [174], as shown in Figure **I-28**. The apparent hydrogen solubility in Al-Cu alloys was investigated by Anyalebechi *et al* [174], and compared with various aluminum alloys (Figure **I-28**). Al-Li alloys exhibit significantly higher hydrogen solubility compared to Al-Cu alloys. For example, in Al-5 wt.% Cu the solubility is about 10^{-6} wt.%, while in Al-3 wt.%Li it reaches about 10^{-4} wt.%. This difference is primarily attributed to lithium's ability to enhance both intrinsic solubility and hydrogen trapping efficiency of Al_3Li coherent precipitates with a small misfit [28].

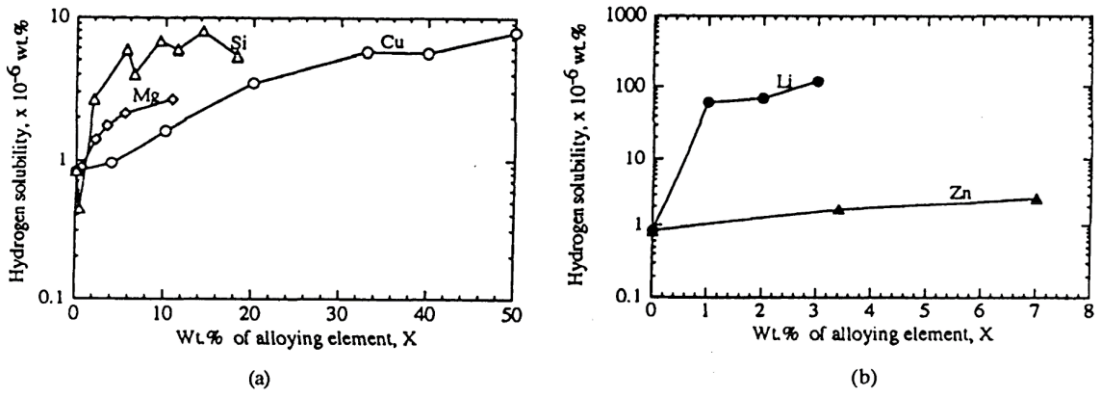


*Figure **I-28**: Effects of adding alloying elements on hydrogen solubility in solid aluminum at 500°C and 1 atm Partial Pressure of Hydrogen [174].*

3.2.Hydrogen Transport and Diffusion

Hydrogen diffuses mainly by occupying interstitial sites in the lattice of metals [28]. The small size of a hydrogen atom and the high density of interstitial sites in metal lattices largely explain its high mobility, particularly in cubic structures. It is the element for which diffusion rates are directly measurable at room temperature.

The interstitial diffusion of hydrogen in a cubic structure depends on the energy barrier that an atom must overcome to jump from one interstitial site to another. However, this barrier varies from one crystal lattice to another. For example, in BCC iron, hydrogen is reported to preferentially occupy tetrahedral sites [175–177]. By contrast in FCC aluminum, the preferred interstitial site for hydrogen remains debated, with both octahedral and tetrahedral sites proposed in various experimental and theoretical studies [171,178]. Wolverton *et al*.[178] calculated the migration energy for hydrogen moving between tetrahedral and octahedral sites to be 0.18 eV in the FCC Al, enabling rapid interstitial mobility at modest temperatures. DFT studies have reported almost the same activation energy (~0.167 eV) [179]. De Vita and Gillan [180] note that the energy difference between octahedral and tetrahedral sites is extremely small, falling within the uncertainty of calculations, so that different studies could reasonably reach different conclusions.

The diffusion of hydrogen in aluminum is typically described by an Arrhenius type equation [181] and has been studied using various methods and experimental setups. These investigations have revealed differences in diffusion coefficients, as shown in Figure **I-29** and Table **I.2**, primarily due to the small solubility of hydrogen in solid aluminum, which

complicates the accurate measurement of outgassing rates [182] and the strong influence of microstructural defects [183].

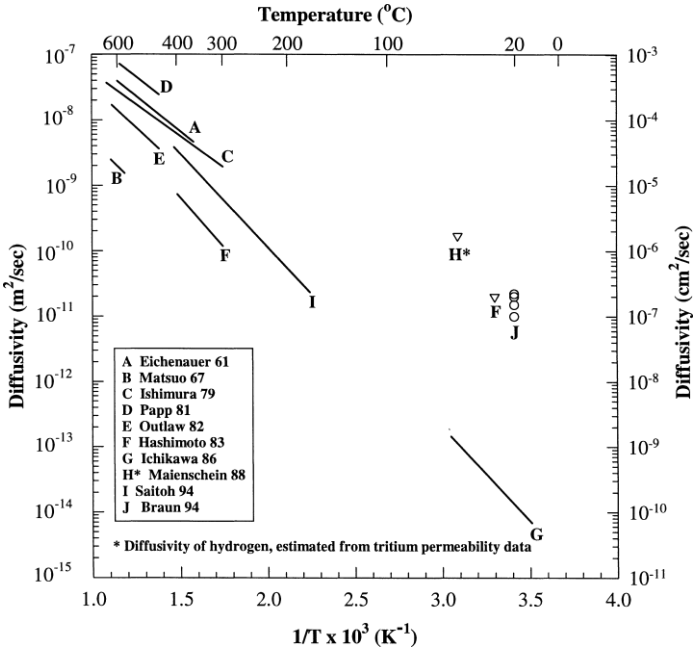


*Figure **I-29**: Summary plot of hydrogen diffusion data for hydrogen in solid aluminum as a function of temperature [183].*

*Table **I.2**: Apparent diffusion data for hydrogen in solid aluminum. D_0 is the pre-exponential factor, Q is the activation energy for diffusion.*

Material	Temperature range (°C)	Experimental technique	D_0 (m^2/s)	*Q (kJ/mol)*	Diffusivity at 20°C (m^2/s)	Reference
99.995% Al	12–55	Electrolytic pulse	9.2×10^{-5}	55.25	1.3×10^{-14}	[184]
99.999% Al	173–408	Permeation	6.1×10^{-5}	54.8	1.0×10^{-14}	[182]
99.999% Al	30–600	Desorption	1.75×10^{-8}	16.2	2.3×10^{-11}	[183]

3.3.Hydrogen Trapping

Hydrogen can be trapped in various microstructural features [185], such as, dislocations, vacancies and grain boundaries, coherent, semi-coherent or incoherent precipitate interfaces can also trap hydrogen. These traps can significantly change the apparent solubility of hydrogen and also influence hydrogen transport through two primary mechanisms, (i) serving as fast diffusion pathways that facilitate hydrogen mobility, or (ii) acting as trapping sites that temporarily or permanently immobilize hydrogen atoms (Figure **I-30**). The trapping behavior depends on the binding energy between hydrogen and the specific defect type level [175,186–

188]. Reversible traps (low binding energy, typically < 0.3 eV [189]) allow hydrogen to escape at room temperatures, while irreversible traps (high binding energy, > 0.3 eV [189]) retain hydrogen more permanently.

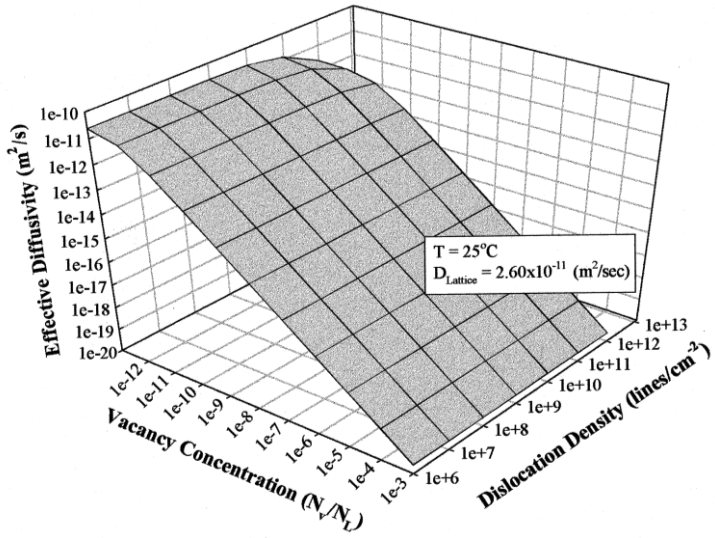


*Figure **I-30**: The influence of dislocation and vacancy traps on the diffusivity of hydrogen in polycrystalline 99.999 wt% aluminum. Plot illustrates the influence of vacancy concentration and dislocation density on the diffusivity at 25°C, using isothermal and constant heating rate desorption techniques [183].*

Dislocation cores, vacancies and incoherent precipitate interfaces are the main sites of irreversible trapping [183,190]. In contrast, the main microstructural defects acting as reversible traps are the hydrostatic field around edge dislocations [183], and coherent and/or semi-coherent precipitates [191,192]. Figure **I-31**, compares the hydrogen trapping energies of various particles, precipitates, and defects in Al alloys, showing the effectiveness of each in trapping hydrogen. These energies were calculated using *ab initio* calculations [193].

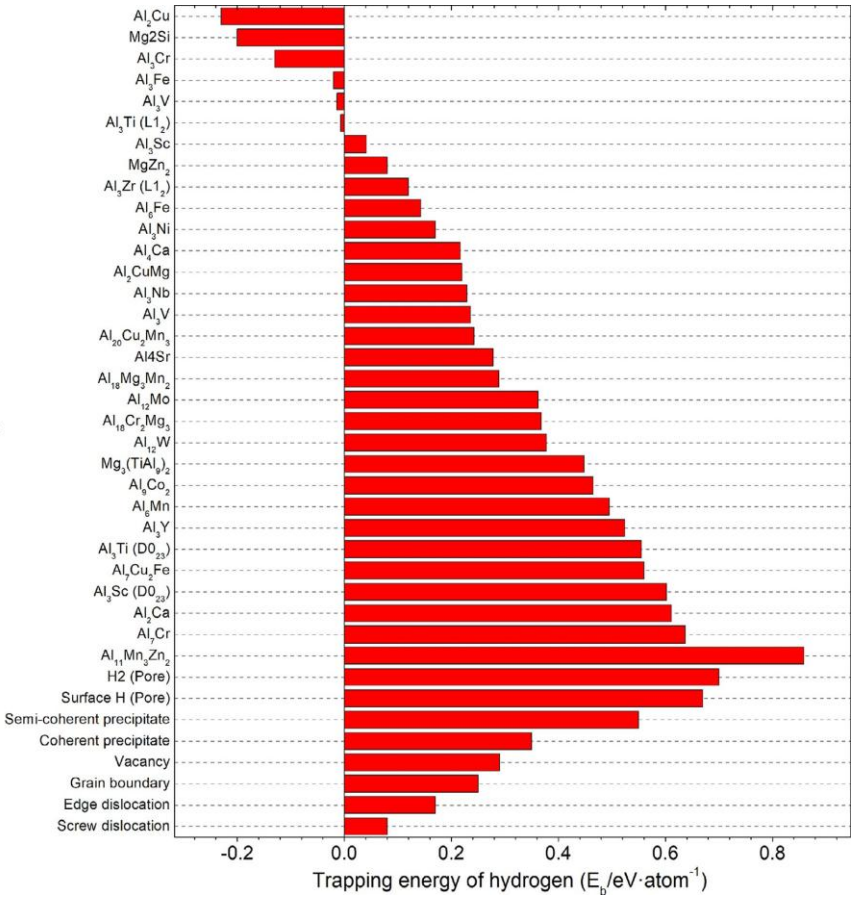


*Figure **I-31** : The trapping energies of various particles and defects to hydrogen in Al alloys were calculated by first-principles density functional theory (DFT) [193].*

In aluminum alloys, certain precipitate–matrix interfaces, such as Al_2Cu, Al_3Zr, can trap hydrogen [89,194–197]. These traps are generally weaker than dislocations or vacancies but can still influence the overall hydrogen trapping behavior. Leger and Piercy used internal friction experiments to quantify hydrogen–solute binding energy in Al–Cu and Al–Mg alloys, finding that Cu and Mg act as relatively weak traps with binding energies of 0.050 eV and 0.060 eV, respectively [198]. Safyari *et al* [196], studied hydrogen trapping in an Al-Cu alloy. A trap site originating from coarse Al_2Cu particles of average size 1.5 μm act as strong traps with a desorption energy of 0.58 eV.

Using tritium autoradiography, Saitoh *et al* [89]. investigated the interactions between hydrogen and lattice defects, as well as precipitates, in pure aluminum, Al-4 wt% Cu, and Al-1 wt% Mg_2Si alloys. It was found that dislocations in pure aluminum and the Al-1 wt% Mg_2Si alloy act as trapping sites for hydrogen and serve as short-circuit diffusion paths for hydrogen. GP zones in the Al-4 wt% Cu alloy act as trapping sites for hydrogen, whereas in the Al-1 wt% Mg_2Si alloy, they repel hydrogen. This difference is attributed to the variation in the stress field

around the GP zones in both alloys. Additionally, the interfaces of θ precipitate in the Al-4 wt% Cu alloy also acts as a trapping site for hydrogen [89,197].

In a recent study [199], it was found that the addition of Zr to 7xxx series Al alloy results in the formation of coherent Al_3Zr dispersoids, which trap hydrogen more effectively (Table **I.3**) and eventually lead to superior hydrogen embrittlement resistance of the alloy.

*Table **I.3**: Hydrogen trapping data determined from thermal desorption spectroscopy (TDS) at a heating rate of 5 ◦C/min, for Al-8.2 Zn-0.15 Zr wt% [199].*

Peak	Approx. peak position [°C]	Trap site	Average concentration of H (mass ppm)	Desorption energy, E_d [kJ mol^{-1}]	Binding energy, E_b [kJ mol^{-1}]
1	185.4	Lattice	0.057	16.8	–
2	312.0	Dislocations	0.240	33.45	17.18
3	412.5	Al_3Zr dispersoids	0.469	47.04	30.77
4	507.5	GBs/ vacancies	0.343	64.87	48.60

Certain particles or precipitates in Al alloys play a critical role in trapping hydrogen, offering a potential solution for reducing hydrogen embrittlement (HE). In aluminum alloys, especially those containing lithium, precipitates such as Al_2CuLi have a high hydrogen trapping ability with a significant trapping energy of 0.736 eV/H atom [25].

3.4.Hydrogen Charging Techniques

Hydrogen can be introduced into metals and alloys in certain environments, and there are numerous ways for hydrogen to penetrate metals. These include exposure to hydrogen gas and electrolytic deposition of hydrogen on metal electrodes. High-pressure hydrogen gas, electrochemical hydrogen charging, and corrosion reactions are the typical sources of hydrogen in metals. Below, we discuss the different charging methods.

3.4.1. High-pressure Hydrogen Charging

For high-pressure hydrogen gas, the uptake of hydrogen can be described as a series of three steps [14,200], as shown in Figure **I-32**.

Physical absorption is a weak electrostatic interaction with a solid surface, is reversible and known as Van der Waals, with a low absorption energy of ~ 0.04 eV. The second step, known as chemical absorption, typically occurs at elevated temperatures and is irreversible. In this process, a covalent bond is formed between the dissociated hydrogen gas molecules and the

metal surface. Chemisorption (strong interaction) involves a short-range, that takes place within a single atomic layer. After chemical absorption, hydrogen atoms diffuse into the metal following a concentration gradient which we call hydrogen dissolution.

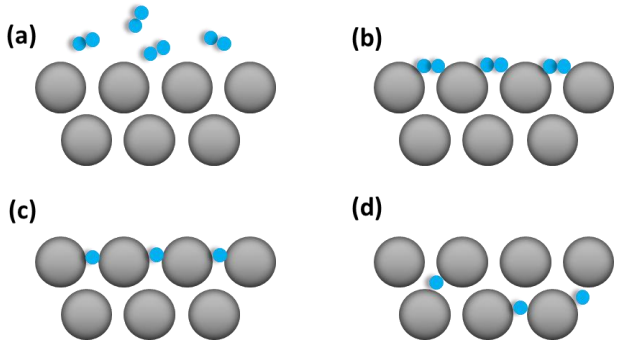


*Figure **I-32**: Schematic of hydrogen entry from the gas phase: (a) H2 molecules nearing the material surface, (b) physisorption, (c) chemisorption, (d) absorption. Blue balls represent hydrogen atoms or molecules, gray balls metal atoms.*

The dissociation of hydrogen (H_2) into atomic hydrogen (H) is a rate limiting step for the penetration of hydrogen into metals, requiring a dissociation energy of around 4.48 eV [169]. This energy can be reduced by the interaction between H_2 and the surface which facilitates chemisorption of H atoms, as shown in Figure **I-33**.

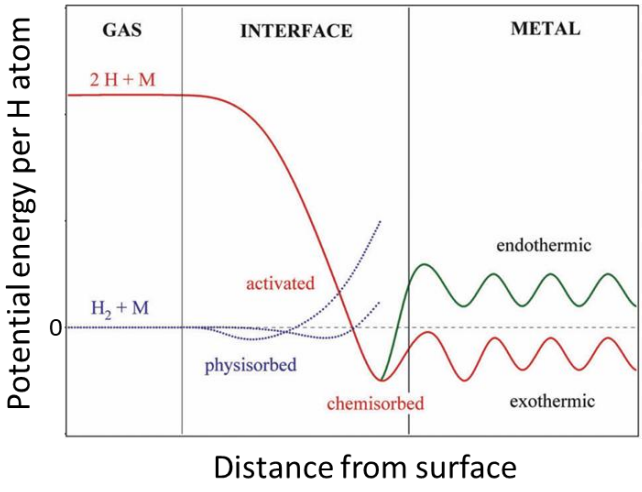


*Figure **I-33**: A schematic illustrating the potential energy landscape for a H_2 molecule and corresponding atomic H (2H) as they approach a metal surface. Initially, the molecular H_2 is in a physisorbed state. To transition to chemisorbed H atoms, it must overcome an activation energy barrier for dissociation. and finally, the absorbed H atoms diffuse through the metal lattice [201].*

In Aluminum at room temperature, molecular hydrogen (H_2) cannot dissociate on the passive Al_2O_3 layer [202], and the rate of hydrogen adsorption in dry gaseous hydrogen is negligible. Al_2O_3 does not facilitate the dissociation of hydrogen molecules. Consequently, chemisorption on the aluminum surface requires a direct supply of monoatomic hydrogen. This makes Al_2O_3 a protective layer, rendering it non-reactive to molecular hydrogen under standard conditions, though interactions increase at elevated temperatures or pressure [203,204].

However, at temperatures above 500 K, thermal energy helps overcome the energy barrier, thereby increasing the adsorption rate. High hydrogen pressure further increases the chemical potential (fugacity) of hydrogen, thus enhancing interaction with the surface. In the presence of water vapor, the oxide layer can also facilitate the generation of atomic hydrogen *via* electrochemical reactions [202,205].

3.4.2. Electrochemical (cathodic) Charging

Electrochemical hydrogen charging by cathodic polarization is currently used to study hydrogen embrittlement, in this process, a voltage is applied to a metal, resulting in a high concentration of hydrogen at the surface [206]. Based on the electrolyte condition, the hydrogen evolution reaction can be identified in two different cases:

$$\text{Volmer Reaction: } H_3O^+ + M + e^- \rightarrow MH_{ads} + H_2O$$

$$\text{Heyrovsky Reaction: } MH_{ads} + H_3O^+ + e^- \rightarrow M + H_2 + H_2O$$

$$\text{Tafel Reaction: } 2\,MH_{ads} \rightarrow 2M + H_2$$

In Neutral or Alkaline Solutions:

$$\text{Volmer Reaction: } H_2O + M + e^- \rightarrow MH_{ads} + OH^-$$

$$\text{Heyrovsky Reaction: } MH_{ads} + H_2O + e^- \rightarrow M + H_2 + OH^-$$

The difference between electrochemical and chemical hydrogen charging lies in the mechanism by which the hydrogen enters the material. In the case of chemical loading, hydrogen is generated at the material surface by a spontaneous chemical reaction, such as the dissociation of water molecules in an alkaline solution (NaOH). The hydrogen atoms produced absorb on to the metal's (chemisorption) and diffuse into its structure, it can also be indirect *via* molecular precursors [207]. Generally, this process results in lower hydrogen concentrations and lower hydrogen fugacity (effective pressure/activity of hydrogen that drives absorption) compared to electrochemical methods, in which an electric current is applied to drive electrochemical

reactions at the surface, generating hydrogen atoms by cathodic reduction. The current density provides precise control over the rate of hydrogen generation and hydrogen fugacity.

For electrochemical hydrogen charging, there are no universal or unique conditions for charging pure aluminum and its alloys. Various conditions and solutions are used, as described in Table **I.4**, with varying amounts of hydrogen that can be charged.

*Table **I.4**: summary of different hydrogen charging methods for aliminium and its alloys.*

Charging Technique	Material	Conditions	Hydrogen Quantity (appm)	Reference
Electrochemical charging	Al 99.999%	1 N H_2SO_4 + $NaAsO_2$, pH 2, 35°C, 1.7 mA/cm²	1090	[172]
	Al 99.999%	1 N HCl + $NaAsO_2$, pH 1.5, 35°C, 1.7 mA/cm²	675	[172]
	Al 99.999%	1 N H_2SO_4 + $NaAsO_2$, pH 1, 35°C, 50 mA/cm²	2000	[172]
	5754	3N HCl 25-300 mA/cm² , 2h	2000-10000	[208]
	7B05-T5	0.1 N HCl + 150 mg/L $SC(NH_2)_2$, 2 mA/cm²	624	[209]
	7050	1 N H_2SO_4+ As_2O_3, 20 mA/cm², 6-24h	-	[210]
	2024	10 mN H_2SO_4, -0.8 mA/cm², 40h	494	[211]
Ultrasonic bath	Al 99.999%	D_2O, 6 hours	2500	[172]
	Al 99.999%	H_2O, 10 hours	1300	[172]
Chemical Charging	Al 99.999%	1 N NaOH, pH 12	600-1300	[172]

Most studies on hydrogen have been conducted using electrochemical charging. One reason for this is that gaseous hydrogen charging installations are limited and must comply with strict safety protocols [212].

3.4.3. Plasma Charging Methods

As previously mentioned, hydrogen must be dissociated in atomic form to enter the structure. To promote this, a plasma-assisted activation step can be applied. This method can achieve hydrogen concentrations up to fourfold higher compared to those achieved using gaseous hydrogen under equivalent pressure conditions [213].

However, direct plasma exposure may lead to sample temperature changes, surface modifications, causing oxide layer removal or blister formation [214]. Recent developments in plasma configurations confine the plasma-generation region near the source so that only reactive species reach the specimen, thus reducing heating and surface damage during charging [215].

CHAPTER II: Materials and Methods

1. Selected Al Alloys and Thermal Treatment 51

2. Cold Rolling 52

3. Hydrogen Charging Methods 53

4. Characterization Techniques 55

4.1. Vickers Microhardness Testing 55

4.2. Transmission Electron Microscopy (TEM) 56

4.2.1. Fundamentals of TEM 56

4.2.2. TEM Imaging 59

4.2.3. STEM mode 60

4.2.4. Energy Filtered Transmission Electron Microscopy 62

4.2.5. TEM Sample Preparation 62

4.2.6. Determination of Precipitate Size and Number Density 63

4.3. Atom Probe Tomography (APT) 66

4.4. Thermal Desorption Spectroscopy (TDS) 70

1. Selected Al Alloys and Thermal Treatment

Two aluminum alloys were investigated in this study, an Al-5Cu alloy and an industrial Al-0.2Zr alloy. The Al-5Cu alloy was supplied by Goodfellow® (Lille, France). Its nominal composition is reported in Table **II.1**.

*Table **II.1**: Nominal composition of the Al-5Cu alloy.*

Element	Cu	Fe	Si	Zn	Bi	Pb	Other	Al
(wt. %)	5.3	0.7	0.4	0.3	0.4	0.3	0.15	balanced
(at. %)	2.35	0.35	0.4	0.13	0.05	0.04	0.08	balanced

The second material is an industrial Al-2Zr-based alloy, produced by Lorena®, its nominal composition is detailed in Table **II.2**. This alloy contains zirconium as the main alloying element.

*Table **II.2**: Nominal composition of the industrial Al-0.2Zr alloy.*

Element	Zr	Fe	Si	La	V	Ti	Ni	Mg	Al
(wt. %)	0.24	0.09	0.07	0.014	0.012	0.001	0.001	0.0034	balanced
(at. %)	0.07	0.04	0.06	0.003	0.006	0.0006	0.0006	0.004	balanced

The Al-5Cu and Al-0.2Zr alloys were received in the form of rods, which were cut into disks of 1 mm thickness, with diameters of 6 mm for the Al-5Cu alloy and 6–10 mm for the Al-0.2Zr alloy. Prior to any aging treatments or hydrogen charging experiments, all samples were subjected to a solution heat treatment (Figure **II-1**). The Al-5Cu alloy was solutionized at 540 °C for 1 hour [64], followed by quenching in water. The Al-0.2Zr alloy required a significantly longer solution treatment due to the low mobility of Zr atoms [65], with a solutionizing step conducted at 620 °C for 288 hours [112], also followed by water quenching.

For the Al-5Cu alloy, after quenching, samples were kept at room temperature for 5 h (time required for chemical charging). Subsequent aging was performed either (I) by natural aging at room temperature, or (II) by artificial aging at 140 °C for various aging times. Aging was carried out in air and also under hydrogen atmosphere (more details on hydrogen introduction methods

are in the next section (II.3). In Al-5Cu alloys precipitation treatments are typically carried at temperatures higher than 140°C [216–219], however, this temperature was chosen in order to slow the loren, thus making it easier to track the precipitation sequence.

For the Al-0.2Zr alloy, after quenching, no precipitation of Al_3Zr occurs at room temperature. Thus, only artificial aging was performed at 375 °C (the optimum temperature known to achieve a fine distribution of nanoscaled precipitates in the Al-Zr system [112,139,142,143]), either with pre-chemical charging or aging under hydrogen/air atmosphere.

For solution treatments and aging at 375 °C, a high-temperature furnace (Nabertherm) was utilized, while for aging at 140 °C, a Memmert^{TM} UF30 oven was used.

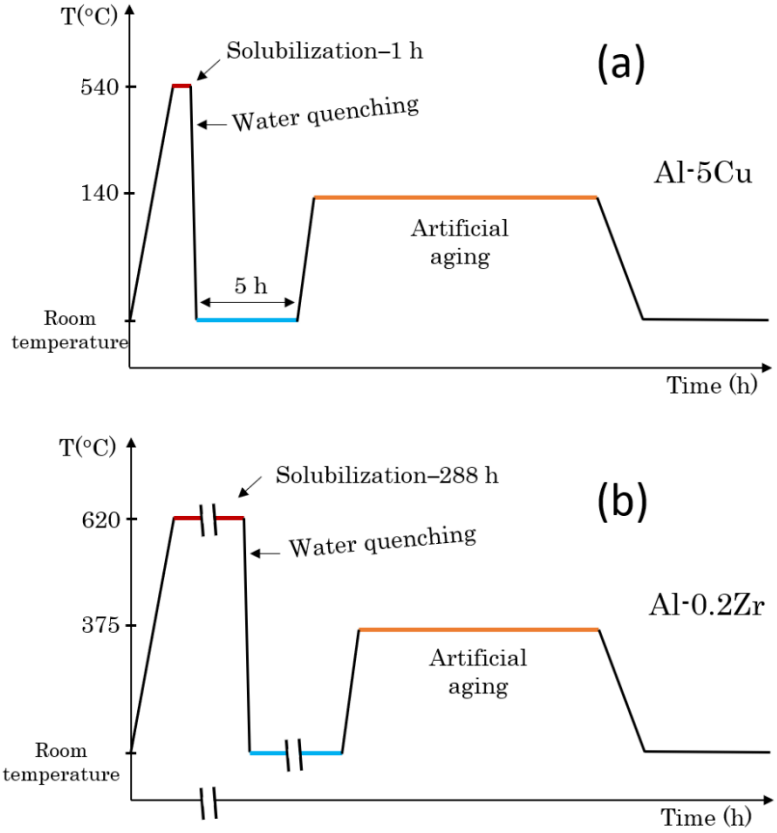


Figure II-1:Schematic of the heat-treatment protocols applied to Al–5Cu (a) and Al–0.2Zr (b).

2. Cold Rolling

Cold rolling was applied as a mechanical deformation step prior to hydrogen charging in Al-5Cu samples. The goal was to introduce dislocations and investigate their influence on precipitation and on hydrogen uptake and subsequent microstructural change. The rolling process was carried out at room temperature using a laboratory rolling mill (TUI W130 Single

at GPM Laboratory, and YoshidaKinen at Kaveh Lab, Japan), operated at a controlled speed of 5 rpm.

Prior to cold rolling, samples were solutionized and quenched. Each sample had an initial thickness of 2 mm. Thickness reduction, denoted *Rx* (where *x* is the reduction rate), was controlled by adjusting the rolling gap and measuring the sample thickness before and after deformation. The reduction rate was calculated as:

$$Rx(\%) = \frac{t_i - t_f}{t_i} \times 100 \qquad \text{II-1}$$

where t_i and t_f are the initial and final thicknesses, respectively.

Reduction rates of 10%, 20%, 50%, etc., were applied to generate various dislocation densities and structures. Immediately after rolling, samples were polished and subjected to hydrogen charging.

3. Hydrogen Charging Methods

To introduce hydrogen into our alloys, two experimental approaches were employed in this study: (I) chemical charging before aging using a 0.1 M NaOH aqueous solution, and (II) annealing treatments performed under hydrogen atmosphere (10 MPa).

Chemical hydrogen charging was carried out by immersing the samples in a 0.1 M NaOH solution (400 ml) for 5 hours at room temperature, following the method introduced in [64,172]. It allows for the insertion of hydrogen levels typically in the range of tens of (appm) [28,172]. Charging was performed either immediately after quenching or after a prior cold deformation step.

The second approach relied on aging the samples under a hydrogen pressure of 10 MPa using a Sieverts-type apparatus (Suzuki Shokan Co. Ltd., Japan), at 140 °C for Al-5Cu and 375 °C for Al-0.2Zr. These experiments were conducted at I^{2}CNER institute in Kaveh Edalati laboratory (Fukuoka, Japan).

Considering the diffusion coefficient of hydrogen in aluminum at 375 °C [28], the diffusion length ($L = \sqrt{6D_H\, t}$, with *t* is the time) is larger than a few mm for one hour. Thus, the hydrogen concentration in aged samples may quickly reach equilibrium (fig). In contrast, at 140 °C, hydrogen diffusion is much slower, and the equilibrium hydrogen solubility is reached only

after about 30 h, For this reason, in the Al–5Cu alloy the hydrogen was introduced chemically (NaOH) prior to the aging.

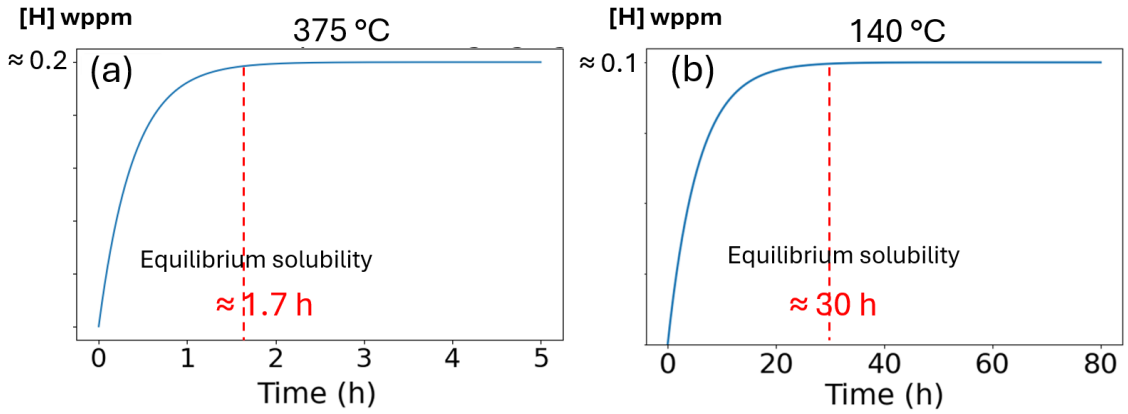


Figure II-2: Time evolution of hydrogen concentration in aluminum toward equilibrium at (a) 375 °C and (b) 140 °C.

This method promotes the insertion of hydrogen into the material under controlled temperature and pressure conditions (Figure **II-3**), and is widely used in the literature for Al alloys [220,221].

Prior to both hydrogen charging or treatment, a polishing procedure using SiC abrasive papers ranging from 1200 to 4000 grit was applied to remove the native oxide layer and produce a flat, uniform surface taking about 10 minutes. The choice of polishing papers is critical to ensure surface flatness, which facilitates effective hydrogen insertion during hydrogen charging. Indeed, as reported by Kim *et al* [222], surface finish plays a significant role in controlling hydrogen uptake, with flat polished surfaces showing higher hydrogen absorption compared to rougher surfaces due to reduced atomic hydrogen recombination at the surface. All samples were identically grinded to have a similar surface and the same hydrogen uptake.

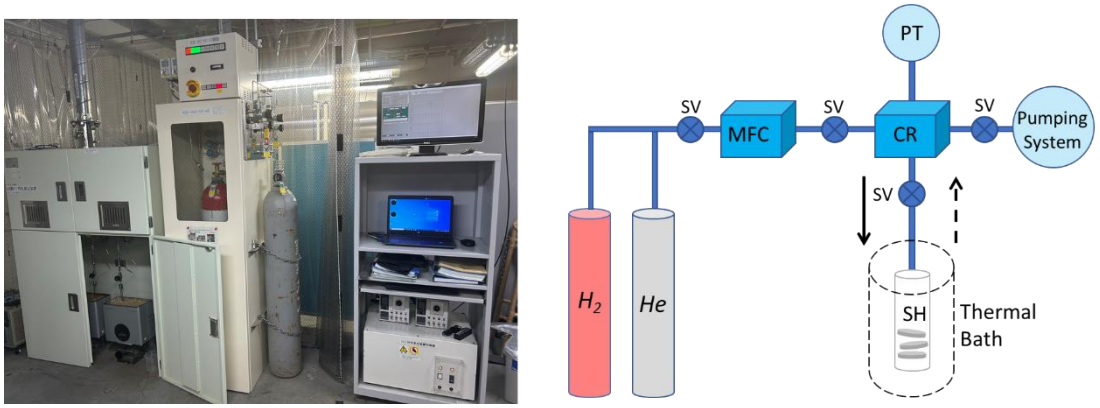


Figure II-3: Sieverts-type apparatus (left) and its schematic diagram (right) based on [223]. MFC: mass flow controller; CR: calibrated reservoir; SH: sample holder; PT: pressure transducer; SV: solenoid valve.

4. Characterization Techniques

4.1. Vickers Microhardness Testing

Vickers microhardness measurements were performed using an automated DUROMETRE PRESI® hardness tester at GPM Laboratory and MITUTOYO at Kaveh's laboratory in Japan**.** The indenter is a diamond pyramid with an inverted square base and a face angle of 136°. A force of 2.9 N (corresponding to a mass of 300 g) was applied to the indenter, which slightly penetrated the sample surface. The force was held for a dwell time of 10 seconds. The average length *d* of the two diagonals of the indentation was measured using an integrated optical system. The Vickers hardness values (HV) were then calculated using the following standard formula:

$$HV_{300} = \frac{2F \times \sin\left(\frac{136^{\circ}}{2}\right)}{g\, d^2} \qquad \text{II-2}$$

where *F* is the applied force, *g* is the acceleration due to gravity (9.81 m. s^{-2})

For 6 mm diameter discs, hardness measurements were performed along the diameter with a step size of 1± 0.2 mm, giving a total of nine measurements per disc (Figure **II-4**). This measurement strategy provides a reliable estimation of the average hardness over the entire disc, while ensuring that individual indentations are sufficiently spaced to avoid interaction effects such as strain hardening. The uncertainty associated with the mean hardness value for each disc was estimated as the standard deviation.

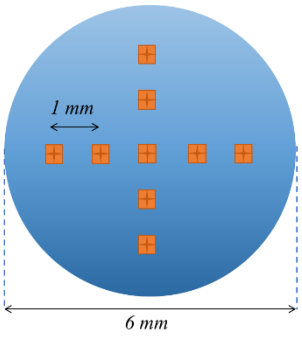


*Figure **II-4**: Schematic illustration of the distribution of Vickers indentations on a 6 mm diameter disc.*

4.2. Transmission Electron Microscopy (TEM)

4.2.1. Fundamentals of TEM

Transmission Electron Microscopy (TEM) was the primary characterization technique used throughout this PhD work, enabling characterization of the microstructure and morphology of precipitates of the studied materials at the atomic scales [19,224]. The aim of this section is to provide a brief description of the operating principles of TEM.

Two main types of electron sources are commonly used in electron microscopy: thermionic emission guns and field emission guns (FEG). Thermionic guns were used in earlier generations of electron microscopes, whereas modern instruments typically employ field emission guns (FEG).

The FEG involves subjecting a fine tip to a strong electric field (Figure **II-5**), high enough to allow electron emission through quantum tunnelling. In this case, the gun is referred to as a field emission gun (FEG). There are two main types of FEG: Cold Field Emission (CEF) and heat-assisted guns (Schottky). Cold emitters are typically made of tungsten, while Schottky emitters use tungsten coated with ZrO. A key advantage of FEGs over thermionic sources is their significantly lower energy spread ($\Delta E \approx 0.7$ eV for Schottky and 0.3–0.5 eV for cold FEGs) compared to thermionic emission guns ($\Delta E \approx 2.0$ eV) leads to a significant reduction in chromatic aberration, which improves spatial resolution in high-resolution TEM and STEM imaging [225].

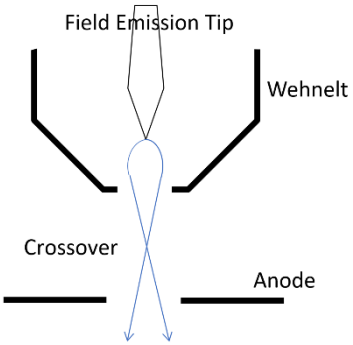


*Figure **II-5**: Schematic of an electron gun (adapted from [226]).*

The emitting tip is subjected to an electric field generated by Wehnelt cylinder, which is held at a potential higher than that of the tip. The Wehnelt acts as an initial electrostatic lens, focusing the electron beam to a point called the cross-over, typically with a radius of ~20 nm for Schottky emitters (Figure **II-5**). One or more anodes, held at a potential higher than that of the Wehnelt, are then used to accelerate the electrons to reach the required energy (*e.g.*, 200 keV). The beam is subsequently guided to the sample by condenser lenses. These are magnetic lenses that generate a variable magnetic field, allowing control over the intensity and spatial distribution of the electron beam on the sample.

Electromagnetic lenses are subjected to several aberrations that limit resolution, and influence image quality in TEM. The most significant ones are [227,228]:

Spherical aberration (Figure **II-6**) occurs when electrons out of the optical axis are focused at different points. The result is electrons converging on different focal points, blurring the image.

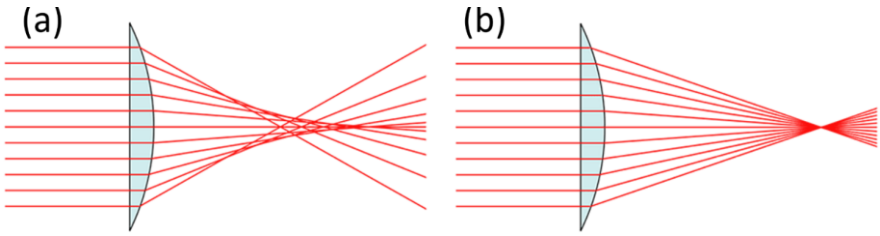


*Figure **II-6**: (a) a lens with spherical aberration, (b) without spherical aberration [229].*

Chromatic aberration is due to electron energy spread in the beam. Electrons with different energies are focused at different positions along the optical axis, leading to a blurred image. This aberration is generally negligible for field emission guns, due to their quasi-monochromatic emission.

Astigmatism, caused by non-uniform magnetic fields, is another common challenge in electron microscopy. It occurs when the lens field is not perfectly symmetric, causing the electron beam to focus at different points along orthogonal directions. This results in elliptical, distorted spots rather than circular spots. Astigmatism can originate from inhomogeneities in the lens iron core, misalignment, and is corrected using stigmators that generate compensatory magnetic fields.

In TEM, the objective lens plays a central role in image formation. Located immediately below the specimen (Figure **II-7**), it collects both the transmitted and scattered electrons that emerge from the sample, forming the first magnified image. The objective lens largely defines the system's resolution and contrast, with a short focal length typically a few millimetres, allowing for the high spatial resolution that characterizes TEM. The best objective lenses in TEMs operated at 200 kV acceleration voltage, exhibit spherical aberration coefficients C_s of 0.5 mm enabling a resolution of 0.19 nm, as in the case of the ARM 200F [112].

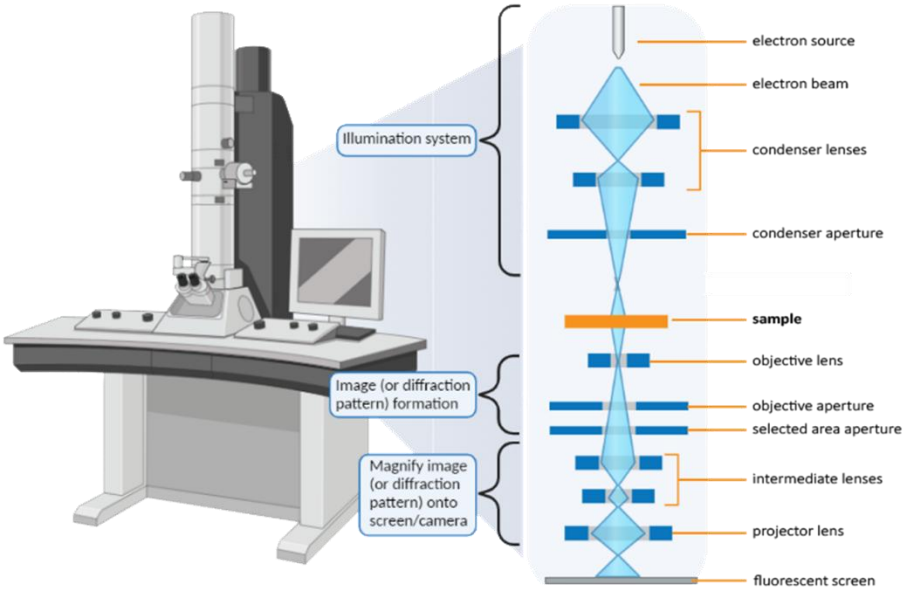


*Figure **II-7**: Simplified schematic of a TEM, showing the main components along the column [230].*

Below the objective lens are the projector lenses (typically two to four), which serve to project either the real space image of the specimen or its diffraction pattern onto the fluorescent screen or camera [225]. Figure **II-8** illustrates the electron trajectories in both cases.

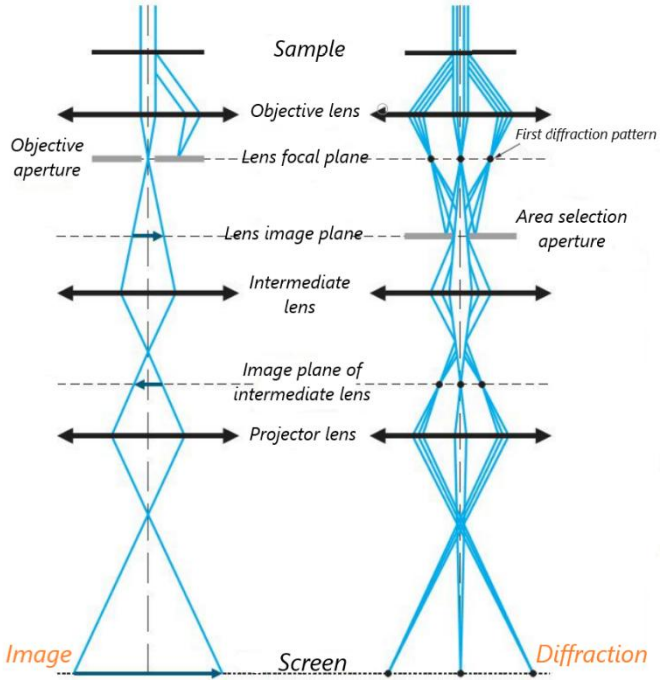


*Figure **II-8**: Electron path from sample to screen in diffraction and TEM imaging modes [231].*

After interacting with the specimen, the electron beam is detected by a high-resolution digital camera placed at the bottom of the column. The image is thus formed by detecting the primary electrons that have transmitted through and interacted with the sample, which is observed through transparency. To obtain an interpretable contrast, the sample must be sufficiently thin (typically less than 100 nm) to avoid excessive absorption of beam electrons by the sample.

Detection of directly transmitted electrons, elastically or inelastically scattered electrons, or electrons diffracted by the crystalline structure of the specimen leads to different microscopy modes, each providing distinct types of information about the sample.

4.2.2. TEM Imaging

To control electron beam propagation and image contrast, apertures are inserted at different positions in the column. Among the various apertures, the objective aperture plays the most critical role in controlling electron beam propagation and enhancing image contrast, which is placed in the back focal plane of the objective lens [225]. In bright-field (BF) imaging, the objective aperture is centered on the transmitted beam, selectively allowing electrons scattered at small angles to pass, thereby improving image contrast. In dark-field (DF) imaging, the electron beam is tilted so that a selected diffracted beam is aligned with the optical axis and passes through the objective aperture, making it particularly useful for enhancing contrast for specific crystallographic orientations, defects or specific grains.

4.2.3. STEM mode

Scanning Transmission Electron Microscopy (STEM) is achieved by focusing the electron beam into a fine probe (< 0.1 nm). A system of magnetic scan coils is used to scan the probe over the sample surface (with a convergence angle of 24–27 mrad depending on the aperture diameter for condenser lens). Various detectors are positioned at different scattering angles relative to the incident beam (Figure **II-9**) to collect electrons and provide different imaging contrasts.

High-Angle Annular Dark Field (HAADF) STEM imaging (Figure **II-9**) is particularly well adapted for the characterization of precipitates in Al-Cu and Al-Zr alloys, as it provides both structural and chemical information at the atomic scale [19,224]. In this imaging mode, the electrons scattered at high angles (resulting from interactions with atomic nuclei) are collected. Their intensity is highly dependent on the atomic number (Z) of the elements, enabling the acquisition of Z-contrast images.

For ordered precipitates, HAADF imaging enables clear visualization of their atomic structure and the precise positions of individual atoms. In systems such as Al-Cu and Al-Zr, the significant difference in atomic number between the constituent elements ($Z_{Al} = 13$, $Z_{Cu} = 29$, $Z_{Zr} = 40$) facilitates chemical discrimination at the atomic scale.

In STEM dark-field (DF) imaging, elastically scattered electrons are collected by the annular dark-field (ADF) detector, typically positioned to collect electrons scattered at intermediate angles (Figure **II-9**). This mode reveals diffraction contrast in the image. Then, electrons transmitted at low angles are collected by the bright-field (BF) detector, producing bright-field images.

Energy Dispersive X-ray Spectroscopy (EDS) detector (Figure **II-9**), are used to collect characteristic X-rays emitted when the electron beam interacts with the sample. Incident electrons can eject an electron from the inner shell, creating an electron hole. An electron from a higher-energy shell then fills this hole, emitting X-ray whose energy equal to the difference between the two shell energies. An energy-dispersive spectrometer measures the energies and intensities of these X-rays to generate spectra, line profiles, and chemical maps. Since the characteristic energies (X-rays) are unique to each element, EDS enables qualitative identification and, with appropriate calibration (*e.g.*, k-factors), can also provide quantitative compositional analysis [232].

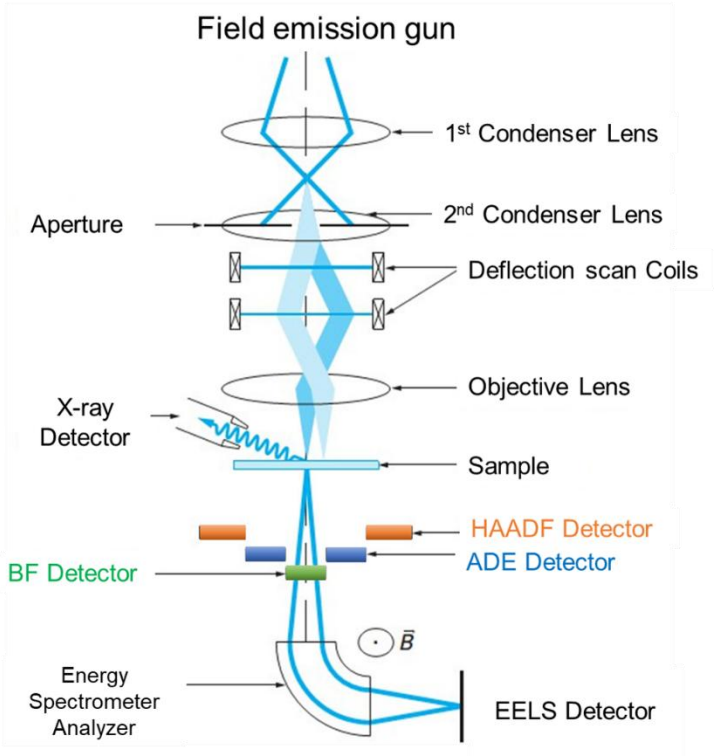


*Figure **II-9**: Schematic diagram of the Scanning Transmission Electron Microscope (STEM), highlighting the electron beam path and the position of each detector [231].*

All TEM analyses presented in this study were conducted using a JEOL ARM-200F microscope operated at 200 kV equipped with a Cs spherical aberration corrector for STEM mode, which is located between the condenser aperture and the specimen holder. This correction system allows for a spatial resolution down to 0.08 nm. More detailed information on aberration correctors can be found in [233]. The experimental STEM acquisition parameters used in this work are listed in Table **II.3**.

*Table **II.3**: Experimental STEM acquisition parameters*

Parameter	**Value**
Convergence angle	25 mrad
BF detector collection angle	0 – 30 mrad
ADF detector collection angle	20 – 80 mrad
HAADF detector collection angle	50 – 180 mrad
Condenser aperture (STEM mode)	30 µm
Probe size	8C
Probe current	~23 pA

EDS analyses were performed in STEM mode with an Oxford Instruments X-max detector (collection angle of 0.7 sr). For spectra, a lifetime of 60 s was used, and chemical maps were acquired with a pixel size of 0.2 nm. During mapping, drift correction was applied to maintain spatial accuracy and minimize image distortion caused by specimen movement. Quantification was carried out with Cliff–Lorimer method with k-factor calibration using Aztec® software.

4.2.4. Energy Filtered Transmission Electron Microscopy

Upon interaction with the electron beam, most electrons are transmitted through the specimen without significant energy loss. However, a proportion of them undergo inelastic scattering events, resulting in a measurable energy loss. The resulting distribution of energy losses is recorded as the Electron Energy Loss Spectrum (EELS), which contains several features corresponding to different inelastic processes. One of the main features of the EELS spectrum is the zero-loss peak (ZLP), located at 0 eV, which represents electrons that have not lost energy and have undergone only elastic scattering.

In order to measure the thickness of the analyzed region in TEM, energy filtered transmission electron microscopy (EFTEM) was used to generate thickness maps. This technique enables the determination of relative sample thickness based on the energy loss characteristics of transmitted electrons.

The relative thickness t of the sample can be estimated from the ratio of the zero-loss intensity I_0 and the total unfiltered intensity (I_{unfilt}), according to the following equation [234]:

$$\frac{t}{\lambda} = \ln\left(\frac{I_{unfilt}}{I_0}\right) \qquad \text{II-3}$$

where λ is the inelastic mean free path, which depends on the accelerating voltage and the material's properties. At 200 keV for aluminum, λ is typically around 120 nm [235]. By acquiring both a zero-loss filtered image and an unfiltered image, thickness maps can be computed. These maps then enable measurement of number density and/or volume fraction of precipitates.

4.2.5. TEM Sample Preparation

Various methods exist for TEM sample preparation, and the choice depends on both the nature of the material and the type of information desired. In this work, double-jet electro-polishing was selected as the most appropriate method due to its efficiency.

Initially, bulk samples were mechanically polished to a thickness of around 300 µm and subsequently punched into 3 mm diameter discs to fit the TEM specimen holder. The discs were then further thinned to a thickness of 100–150 µm by mechanical polishing, followed by cleaning in acetone and ultrasonic agitation for a few minutes to remove surface contaminants.

The twin jet electro-polishing method is illustrated in Figure **II-10**. This technique was performed using a TenuPol-5® system. It involves immersing the sample in an electrolyte solution composed of 2/3 methanol and 1/3 nitric acid (15%) at a temperature of -30 °C. A voltage of 17 V is applied to the sample. When a light beam directed at one side of the specimen becomes visible through the opposite side, it stops electropolishing with the formation of one or more holes near the center of the disc. The surrounding regions near the hole, typically with thicknesses ranging from 50 to 200 nm are suitable for TEM observation, as they are thin enough to allow electron transparency.

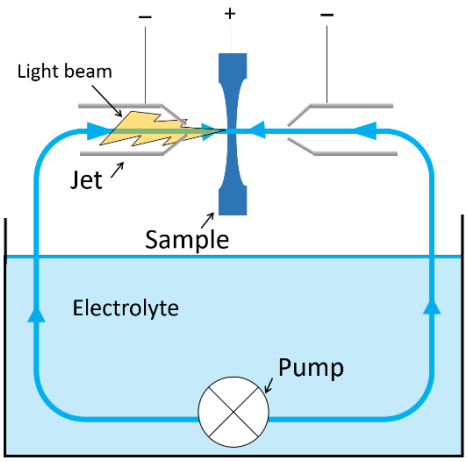


*Figure **II-10**: Schematic of the double jet electro polishing process.*

The final step before inserting the sample holder into the TEM is to clean it with argon plasma for 5 to 15 minutes using a Gatan Solarus 950 apparatus. This process helps remove surface carbon contamination, which can significantly hinder high-resolution imaging. For more details on plasma cleaning, see (Isabell *et al* [236]). To ensure optimum imaging conditions in STEM mode, plasma cleaning was repeated regularly during the experiments, as carbon redeposition over time can lead to severe degradation of image quality, particularly at high magnifications.

4.2.6. Determination of Precipitate Size and Number Density

The size and morphology of the precipitates were analyzed using HAADF-STEM images. For Al_3Zr precipitates, which typically exhibit a quasi-spherical morphology, the equivalent

diameter was estimated using the Feret diameter method [237]. This approach evaluates the particle size based on the average of the maximum and minimum diameters throughout the precipitate boundary. Feret's equivalent diameter d is calculated as follows:

$$d = \frac{D_{max} + D_{min}}{2} \qquad \text{II-4}$$

Where D_{max} and D_{min} are the maximum and minimum Feret diameters, respectively, defined as the largest and smallest distances between two parallel tangents on opposite sides of the precipitate boundary (Figure **II-11**).

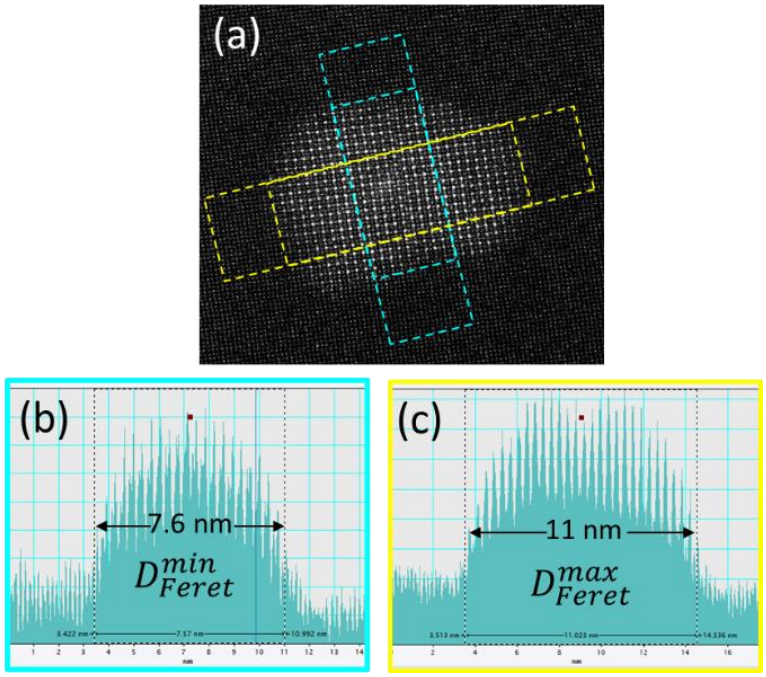


*Figure **II-11**: Determination of Feret diameters from HAADF-STEM images of an Al_3Zr precipitate, (a) HAADF-STEM image showing Al_3Zr precipitate with two rectangular profiling zones (blue and yellow) used for Feret diameter measurements. (b) Intensity profile over the blue rectangular zone. (c) Intensity profile averaged over the yellow rectangular zone.*

Precipitates in Al-Cu alloys, usually exhibit a disk-shaped morphology, lying in (100) planes, thus there are typically three orientation variants.

TEM images were acquired along the $[100]_{Al}$ and $[110]_{Al}$ zone axes. Imaging along the $[100]_{Al}$ zone axis enabled the observation of two of the three precipitate variants, as their habit planes were oriented parallel to the electron beam (Figure **II-12**b). Instead, the $[110]_{Al}$ zone axis enabled visualization of a single variant (Figure **II-12**c). Both the diameter and thickness were directly measured from HAADF-STEM images using ImageJ® software.

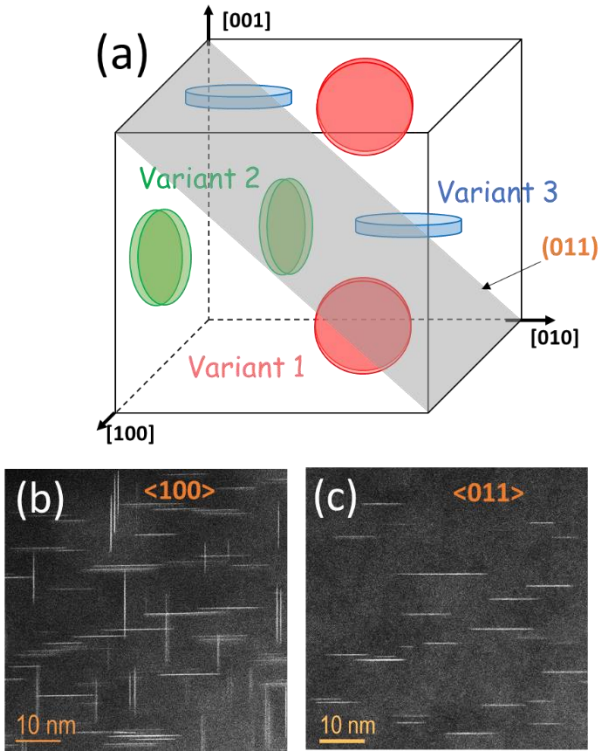


*Figure **II-12**: (a) Schematic illustration of the spatial distribution of precipitate variants in a cubic volume of the aluminium matrix. HAADF-STEM images show GP zones and θ" precipitates observed along the $[100]_{Al}$ zone axis (b), where two variants are visible, and (c) along the $[011]_{Al}$ zone axis, where a single variant is visible.*

The number density of precipitates (N_p, number per unit volume) was estimated by counting the number of precipitates in a known projected area in the HAADF images and combining it with the local sample thickness, which was measured by EFTEM. N_p was then calculated using the following relation [159]:

$$N_p = \frac{N_1 + N_2 + N_3}{A \times (d + t)} \qquad \text{II-5}$$

Where N_1, N_2, N_3 are the number of precipitates of the three variants counted in a projected area A, and t is the local sample thickness measured by EFTEM.

For the images acquired along the $[100]_{Al}$ zone axis where only two variants were observed (N_1 and N_2), the total number ($N_{Total} = N_1 + N_2 + N_3$) was calculated by estimating the third variant (N_3) using the following equation [159]:

$$N_3 = \left(\frac{N_1 + N_2}{2}\right)\left(\frac{d + t}{\sqrt{A}}\right) \qquad \text{II-6}$$

Similarly, for images acquired along the $[110]_{Al}$ zone axis the sum of the other two variants ($x = N_1 + N_2$) was also estimated by the same equation, then added to N_3 ($N_{Total} = N_3 + x$).

4.3.Atom Probe Tomography (APT)

Atom probe tomography (APT) is an analytical technique that enables three dimensional (3D) chemical characterization at atomic resolution [238,239]. In this work, APT was mainly used to measure solute concentrations in the solid solution. A schematic illustration of the operating principle of APT is shown in Figure **II-13**.

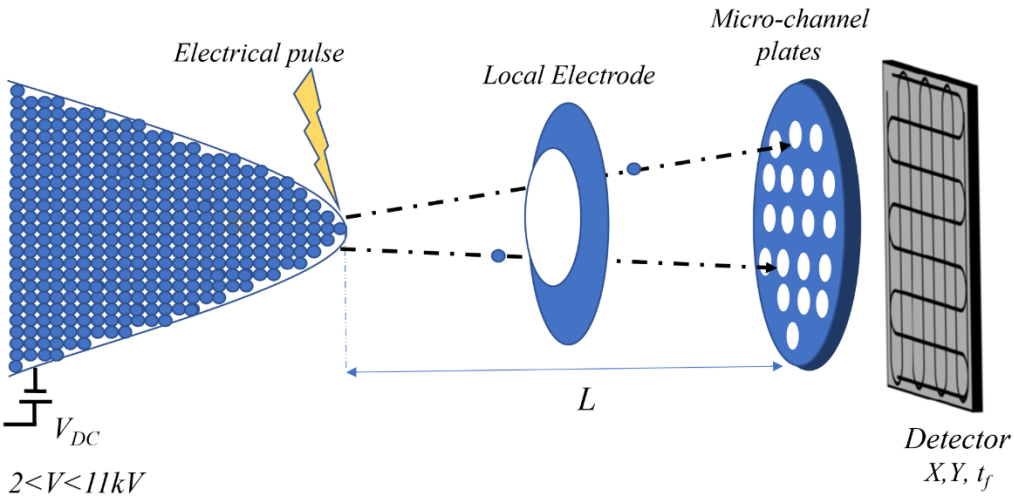


*Figure **II-13**: Schematic illustration of Atom probe tomography.*

The APT technique involves the controlled, atom-by-atom field evaporation of a needle-shaped sample with a tip radius ranging from 20 to 100 nm, APT samples were prepared using a plasma focused ion beam (PFIB, Thermo Fisher) *via* lift-out and annular milling methods applying Xe ions. More detailed information can be found in [239–242].

The tip is subjected to a high electrical potential, typically between 2 and 11 kV, under ultra-high vacuum conditions (10^{-8}–10^{-9} Pa) and at cryogenic temperature to minimize thermal agitation, and thus improve APT resolution [16,243]. Evaporation is triggered by a sequence of ultrafast electrical pulses. These pulses induce the ionization and consequent evaporation of surface atoms, preferentially those located at the top of the tip. The ions are then accelerated toward a position-sensitive detector.

The detector system, based on microchannel plates (MCP), records both the position (X, Y) of each ion impact and the time of flight (TOF), defined as the time interval between the emission

pulse and the arrival of the ion at the detector. As the ion's kinetic energy is derived from the electrical potential, the TOF is directly related to its mass-to-charge ratio.

The electric field (E) at the top of the tip is described by:

$$E = \frac{V}{kR} \qquad \text{II-7}$$

Where V is the applied voltage, R is the radius of curvature, k is a geometric field factor (between 2 and 8).

The kinetic energy of an ion with charge state n is given by:

$$E = n\,eV \qquad \text{II-8}$$

Assuming negligible acceleration period and conservation of energy, the kinetic energy of the ion can be related to its mass *via*:

$$n\,eV = \frac{1}{2}mcv^2 = \frac{1}{2}m\left(\frac{L}{t_v}\right)^2 \qquad \text{II-9}$$

which leads to the expression for the mass/charge ratio:

$$\frac{m}{n} = 2eV\left(\frac{t_f}{L}\right)^2 \qquad \text{II-10}$$

where m is the ion mass, t_f is the time of flight, L is the flight path length, e is the charge element.

Thus, the chemical identification of each ion is determined from its TOF, while its spatial coordinates (X, Y) are provided by the detector. The coordinate (Z) is deduced from the sequence of evaporation events, which corresponds to the depth of the analyzed volume and is calibrated using known crystallographic planes. The experimental conditions for the atom probe analyses are summarized in Table **II.4**.

*Table **II.4**: Operating and processing parameters used for atom probe tomography analyses*

Parameter	Value/Condition
Detection efficiency	80%
Pulse frequency	500 kHz
Detection rate	0.2%
Pulse fraction	20%
Specimen temperature	60 K
3D reconstruction	IVAS® software
Post-processing	GPM_3dSAT (IDDN.FR.001.430017.000. S.P.2020.000.10000)
Instrument	LEAP® 5000 XS

In studies of hydrogen trapping in aluminum alloys, APT is particularly useful for visualizing hydrogen, notably at precipitate-matrix interfaces and grain boundaries. Numerous studies have successfully mapped hydrogen with 3D reconstruction [24,244–246]. The early work of Kesten *et al* [247] provided a distribution of hydrogen and deuterium in metallic multilayers at the sub-nanometer scale using APT. They demonstrated that deuterium, which exhibits slower mobility compared to hydrogen, it was possible to determine the equilibrium deuterium concentration. Subsequently, Gemma *et al* [248–250] successfully visualized 3D distributions of deuterium by APT, demonstrating the technique's capability to map light element distributions in some metallic systems at the atomic scale.

Recently Zhao *et al* [24], conducted an extensive study using cryo-APT and cryo-FIB to analyze the sites and mechanisms of hydrogen trapping in aluminum alloys. Their results revealed that the S-phase (Al2CuMg) acts as an important hydrogen trap, as shown in Figure **II-14**a, with a one-dimensional composition profile across the matrix-S-phase interface. In addition, evidence of hydrogen trapping at grain boundaries was provided by Figure **II-14**c, showing significant concentrations of hydrogen and deuterium at grain boundaries. The role of Al_3Zr dispersoids as effective hydrogen traps was also confirmed (Figure **II-14**e,f), in agreement with the results of previous conventional APT studies [245]. These results highlight the critical contribution of these microstructural features to improve the resistance of aluminum alloys against hydrogen embrittlement.

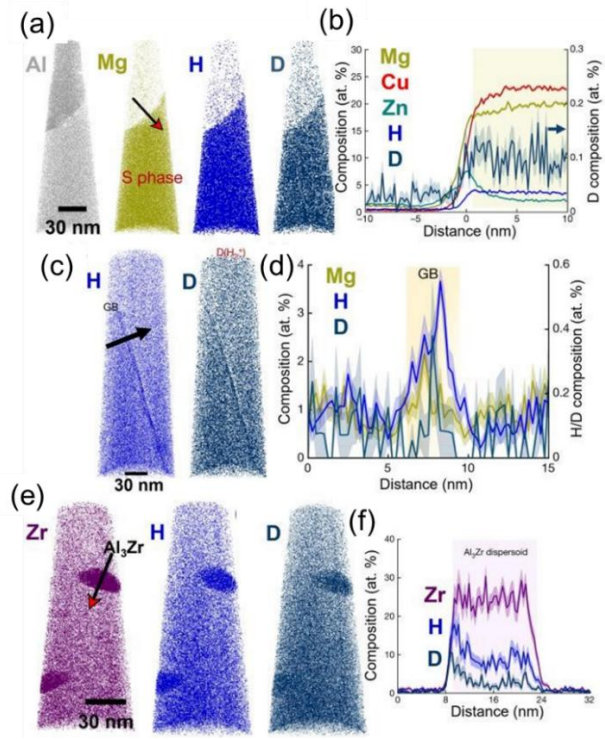


*Figure **II-14**: APT observations of trapped H and deuterium in an aluminum alloy (Al–6.2Zn–2.4Mg–2.1Cu–0.1Zr in wt%). (a) Atom maps of Al (gray), S phase Mg (dark yellow), protium (blue), and deuterium (dark blue). (b) Composition profile along the arrow in (a). D content uses the second Y axis on the right. (c) The H and D maps in a sample with a GB. (d) The GB region profile. (e) Maps of Zr, protium, and deuterium in the region of Al_3Zr dispersoids. (f) The profile corresponds to the arrow in (e). The experiments were conducted using LEAP 5000 XS and LEAP 5000 XR at 25 K, a pulse fraction of 20%, and a pulse frequency of 250 kHz [24].*

Nevertheless, hydrogen analysis by APT is not yet a standard technique due to its complexity and limitation, which requires precise experimental set-ups adapted to specific scientific questions. Several challenges stand in the way of hydrogen quantification and large-scale application. APT has a small field of view that can only cover a volume of around 100 × 100 × 300 nm^3, limiting the overall view of the distribution of H throughout a sample [16,244].

In addition, residual hydrogen from the walls of the vacuum chamber can interfere with signals from the sample, complicating data interpretation. In addition, the high mobility of hydrogen in most materials can lead to losses during sample preparation or even during APT analysis, sample handling can also induce structural damage or introduce additional hydrogen [16]. Charging with deuterium can be an alternative, however, another challenge is that during analysis, hydrogen is detected in different ionic forms (H^+, H^{2+}, H^{3+}), with distributions that

depend strongly on the electrostatic field applied, complicating the interpretation of mass spectra and requiring strict control of analysis conditions [16]. Besides, the very low solubility of hydrogen in aluminum [28], often below the detection limit, makes it even more difficult to measure it reliably. For these reasons, despite its potential, APT was not used in this PhD work for quantifying hydrogen.

4.4. Thermal Desorption Spectroscopy (TDS)

TDS was originally developed as a surface science tool, providing information on adsorption and desorption kinetics, as well as the binding states and thermal evolution of the adsorbate layer [251]. Regarding the hydrogen quantification, the technique has been applied to both bulk and surface measurements. Historically, Mendelsohn and Gruen [252] were the first to study hydrogen desorption kinetics using TDS on various hydride compositions, followed later by Choo *et al* [253], who applied the method to pure iron.

TDS involves heating a sample at a controlled rate to induce progressive desorption of hydrogen gas from the material. Heating can be carried under vacuum with mass spectrometer detector or in an inert gas atmosphere (argon or nitrogen) using a thermal conductivity detector. In mass spectrometer detector, hydrogen flow is ionized and analyzed based on the mass-tocharge ratio. In thermal conductivity detector, hydrogen content is quantified based on the difference in thermal conductivity between the pure inert gas flow and the hydrogen-inert gas mixture. This technique can be applied in two modes: (i) melting, which provides the total hydrogen concentration, and (ii) temperature ramping, which enables the identification of different desorption peaks as a function of temperature. While both techniques are widely utilized for hydrogen desorption studies, mass spectrometer detection offers superior resolution, with a detection limit as low as 0.0059 ppm wt [254], compared to 0.01 ppm wt [255], for a thermal conductivity detector.

By integrating desorption spectra obtained by TDS, hydrogen trapped amount can be quantified. In addition, analysis of the TDS data makes it possible to determine the desorption energy and hydrogen concentration at each individual trapping site [28,256,257]. Below is the Kissinger formula used to calculate the desorption energy for each peak, by acquiring multiple TDS spectra at different heating rates.

$$\frac{d\left(\ln\left(\frac{\Phi}{T_m^2}\right)\right)}{d\left(\frac{1}{T_m}\right)} = -\frac{E_d}{R} \qquad \text{II-11}$$

Where T_m is the temperature of desorption peak, Φ the heating rate, E_d is the desorption energy for each peak corresponding to a specific trapping site, and R is the gas constant.

It should be noted that any role of diffusion after detachment is neglected. This is generally true in the case of steels, where the migration energy (6 kJ/mol) is significantly lower than the binding energy of reversible traps (48 kJ/mol) [256]. However, for aluminum alloys, such as studied by Stephen *et al* [256], the diffusion of hydrogen to the free surface cannot be ignored, and the contribution of the migration energy is relatively higher. For metallic alloys, an inherent issue affecting the interpretation of TDS spectra is the possibility of altering the microstructure of a sample during heating. New trapping sites may form, or existing ones may be eliminated.

Comparing the TDS spectra for pure aluminum with those of an aluminum alloy (Figure **II-15**a, c), it is clear that there are 4 to 5 contributions for an alloy containing phases or precipitates, whereas there are mainly 3 contributions for pure aluminum. In an alloy, the presence of more trapping sites makes their identification more complex. Additionally, there is an effect of the heating rate on the position of the peaks, as the heating rate increases, the peaks shift to higher temperature values, as shown in Figure **II-15**b. The heating rates used for analyzing trapping sites in aluminum alloys range from 90 to 1200°C per hour [204].

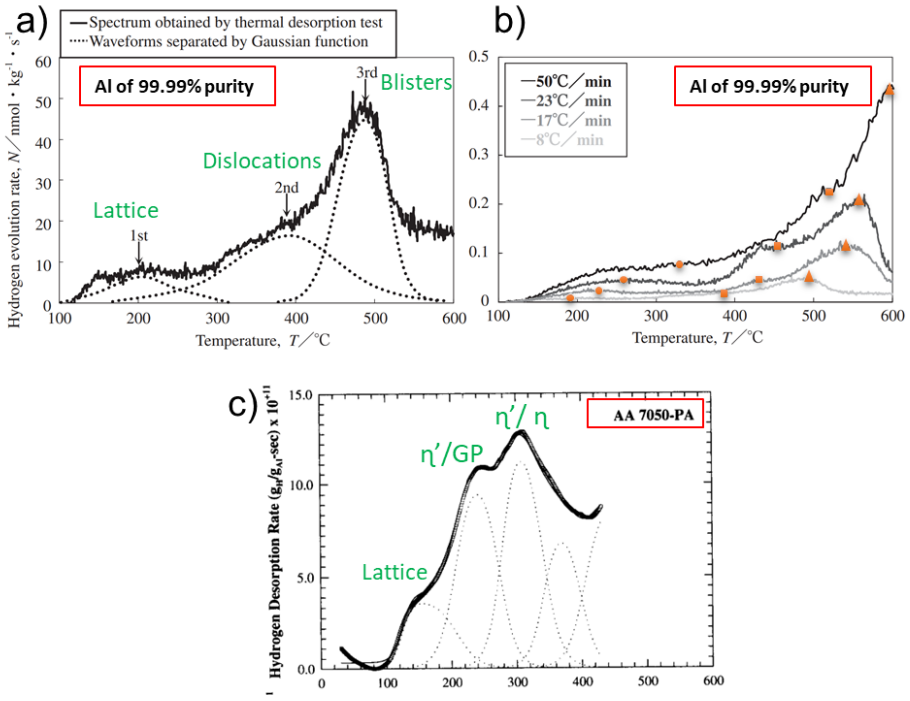


*Figure **II-15**: a) TDS spectra of 99.99% aluminum, taken at a heating rate of 8°C/min. b) TDS spectra of the same material at different heating rates. The locations of the 1st, 2nd, and 3rd peaks are indicated with a circle, square, and triangle, respectively [42]. c) TDS spectra of AA 7050, taken at a heating rate of 10°C/min [171].*

Microhardness measurements and TEM observations have demonstrated structural changes during hydrogen desorption in an AA2090 aluminum alloy [256]. These changes can include phase transformations or dissolutions as well as variations in dislocation density. Any changes can lead to hydrogen redistribution, where hydrogen trapped at weaker sites migrates to higher-energy sites like dislocations or grain boundaries as the microstructure evolves. This is why it is crucial to combine TDS with Differential Scanning Calorimetry (DSC) to detect any phase formation or dissolution occurring during TDS.

In the same work by Stephane *et al* [256], found that, in a different manner, the TDS spectra of the Al- 4Cu wt, binary system did not vary significantly with aging (as indicated by the green and orange curves in Figure **II-16**. Furthermore, this system traps less hydrogen compared to Al-Li. This difference may be attributed to the fact that copper-rich precipitates do not seem to act as significant sites for hydrogen trapping. However, interpreting the TDS spectra and the attribution of each peak to a specific trapping site remains challenging, especially for a complex system containing multiple phases or precipitates with thermal sensitivity. In the present work, this issue is bypassed as the focus is primarily on determining the total amount of hydrogen.

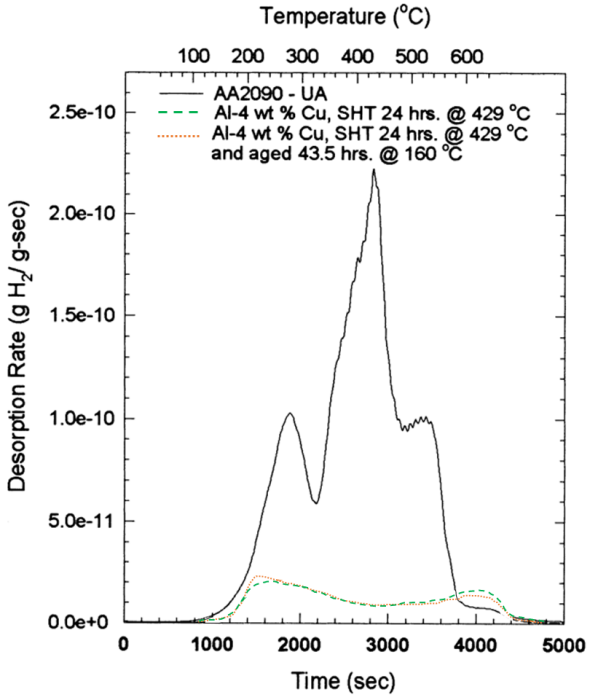


*Figure **II-16**: TDS spectra of AA2090 and Al-4% Cu wt, with 10 °C/min as heating rate. All samples have a thickness of 1.2 mm and are pre-charged with hydrogen by electro-chemical charging [256].*

In this PhD work, preliminary TDS analyses were first performed in Japan with Kaveh Edalati using an ESCO EMD-WA1000S/WK apparatus. But these initial tests did not provide reliable results (see Appendix 1). Therefore, additional TDS measurements were conducted at the LaSIE laboratory (La Rochelle) using a HORIBA EMGA-621W hydrogen analyzer (Figure **II-17**a), operating with catharometric detection (Figure **II-17**b). Argon was used as the carrier gas at a pressure of 4 bar.

Hydrogen is detected by changes in thermal conductivity through a Wheatstone bridge circuit, which records changes in electrical resistance. Accurate quantification requires instrument calibration, two separate calibrations are actually required, one for the total dosing mode and one for the ramp mode (for more details [258]). Temperature in the TDS system is not measured directly but deduced from the applied electrical power, based on an internal conversion table integrated into the acquisition software. This approach introduces a temperature uncertainty of ± 10°C. Two operating modes were used: (i) melting, and (ii) temperature ramping with a heating rate of 130 °C/min.

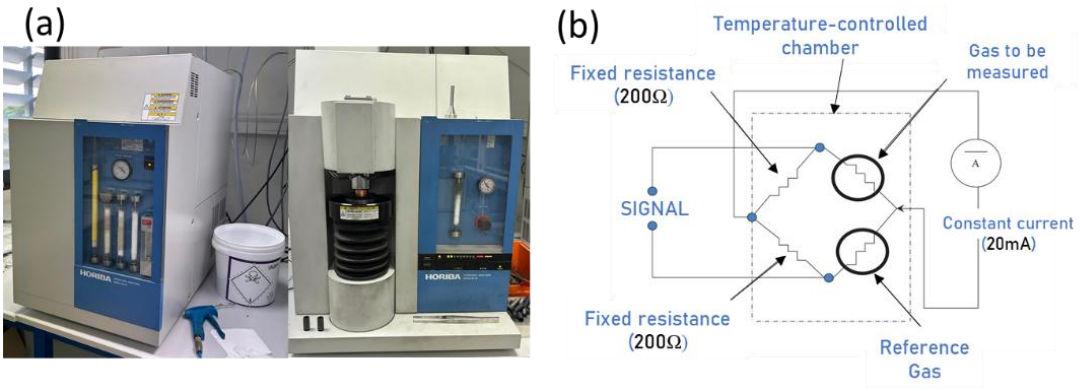


*Figure **II-17**: Thermal Desorption Spectroscopy (TDS) apparatus (a) and its schematic drawing (b).*

CHAPTER III: Influence of hydrogen on the growth kinetics of Al_3Zr precipitates in the Al-0.2Zr alloy

1. Introduction 76

2. Microhardness Evolution During Aging 76

2.1. Aging In Air 76

2.2. Aging Under Hydrogen Atmosphere 78

3. Precipitates in the Al-0.2Zr alloy aged in Air 79

3.1. Precipitate Morphology and Structure (TEM) 79

3.2. Solid Solution and precipitate compositions (APT) 86

4. Effect of Hydrogen on Precipitation 90

4.1. Precipitate Morphology and Structure (TEM) 90

4.2. Solid solution and precipitate compositions (APT) 93

5. Discussion 94

5.1. Growth Rate of Al_3Zr Precipitates 94

5.2. Influence of Hydrogen on Zr Mobility 97

6. Conclusions 99

1. Introduction

As discussed in Chapter I, hydrogen interacts strongly with defects, such as grain boundaries, and dislocations, that are diffusion pathways [30], but also with vacancies [11,28,181,259]. Hydrogen-vacancy complexes are known to affect the dislocation mobility [41,64,260,260–262], while hydrogen-vacancy (H-V) interactions influence both the vacancy mobility and concentration. Thus, hydrogen may influence the diffusion mechanism of solutes in Al alloys [63,64]. For example, H-V interactions has been shown to significantly delay the formation of Guinier-Preston zones in the Al-Cu system [64].

In this chapter, we present a structural and chemical investigation of Al_3Zr precipitates in an Al-0.2Zr alloy. Given the high affinity of hydrogen for zirconium (enthalpy of solution for hydrogen in α-Zr: -0.46 eV [263]) it is suggested that hydrogen may have a significant influence on the nucleation and growth of $L1_2$-Al_3Zr precipitates. To evaluate this, samples aged under hydrogen environment and in air were systematically compared. The structure, size, distribution and volume fraction of precipitates were measured by transmission electron microscopy (TEM) and atom probe tomography (APT).

2. Microhardness Evolution During Aging

2.1. Aging In Air

Microhardness measurements were first conducted to evaluate the influence of aging on the mechanical response of the Al-0.2Zr alloy. The hardness evolution was plotted for aging at 375 °C (Figure **III-1**), showing that the hardness values remain relatively stable during aging. This is consistent with earlier studies, for similar alloys and same aging temperature (375 °C) [73,264], confirming that the aging treatment has no significant effect on hardness, which reflects the limited contribution of Al_3Zr precipitates.

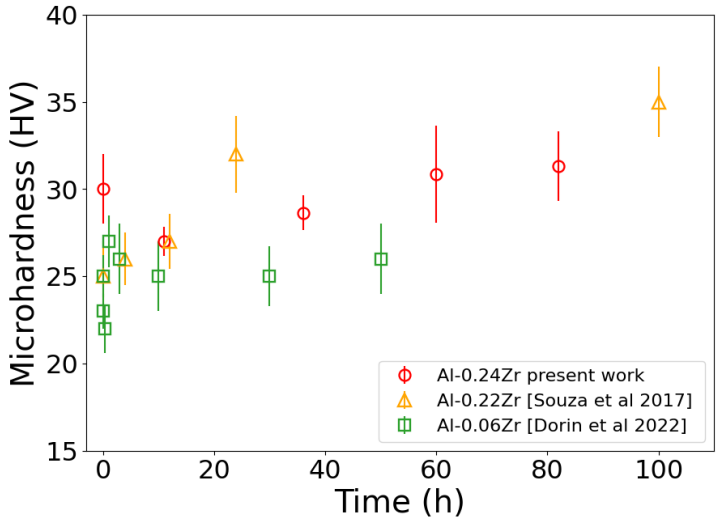


Figure III-1: Evolution of Vickers microhardness (HV) as a function of aging time at 375 °C for Al–Zr alloys: Al–0.24Zr (present work, red), Al–0.22Zr ([73], orange), and Al–0.06Zr ([264], green).

Aging at higher (425 °C) and lower (300 °C) temperatures (Figure **III-2**) was also tested to evaluate the effect of thermal conditions on hardness evolution. The data indicate that the microhardness values are relatively similar for these three temperatures, the hardness remains within 30 ± 2 HV.

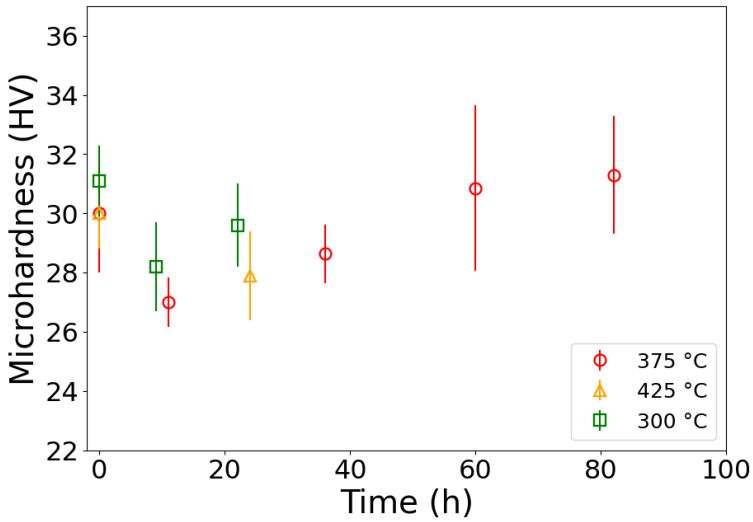


*Figure **III-2**: Evolution of Vickers microhardness (HV) as a function of aging time for the Al–0.2Zr alloy aged at different temperatures: 375 °C (red), 425 °C (orange), and 300 °C (green).*

2.2.Aging Under Hydrogen Atmosphere

Identical aging treatments were carried out under a hydrogen pressure of 10 MPa, to investigate the effect of hydrogen on mechanical behavior. As shown in Figure **III-3**, microhardness values for samples aged under hydrogen remain close to those obtained in air for all aging times studied (up to 96 h).

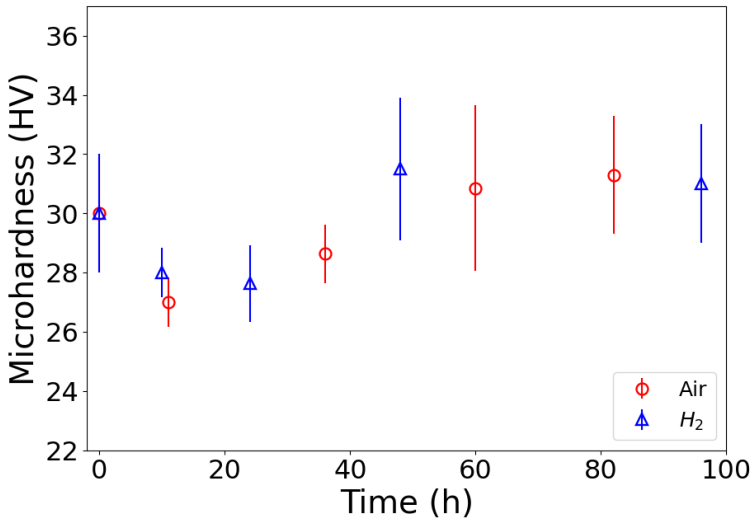


*Figure **III-3**: Evolution of Vickers microhardness (HV) as a function of aging time for the Al–0.2Zr alloy aged at 375 °C in air (red) and under 10 MPa of hydrogen (blue).*

These results suggest that the mechanical hardening associated with Al_3Zr precipitation is minor in the range of heat treatments studied. This may be attributed to the relatively low volume fraction of Al_3Zr precipitates (equilibrium volume fraction of Al_3Zr precipitates in our alloy at 375 °C is about 0.26 % as estimated using Thermo-Calc® with the TTAL6 database). Besides, hydrogen seems to also have no significant effect on the alloy's hardness response.

Hydrogen uptake in the Al–0.2Zr alloy was assessed by TDS after chemical charging. Since it was not possible to directly measure the absorbed hydrogen under a hydrogen atmosphere, the results indicate no significant change in the detected hydrogen concentration. More details are provided in Appendix 2.

3. Precipitates in the Al-0.2Zr alloy aged in Air

3.1. Precipitate Morphology and Structure (TEM)

TEM analyses were performed on the Al-0.2Zr alloy aged at 375 °C for different aging times to characterize the precipitates morphology, structure and their growth over time.

After 48 h of aging, HAADF-STEM images reveal a low density of homogeneously distributed nanoscale precipitates (Figure **III-4**a). High-resolution image of these precipitates is shown in Figure **III-5**. The arrangement of atomic columns corresponds perfectly to the Al_3Zr precipitates with $L1_2$ structure [137]. The Fast Fourier Transform (FFT) of the high-resolution image (Figure **III-5**, insets), taken in two distinct zones within the matrix and precipitate confirms the coherent $L1_2$ crystallographic structure. These observations are consistent with previous studies conducted on this system [72,142,265].

To assess the evolution of precipitate size and distribution over aging, low-magnification STEM images were acquired and compared for samples aged after 48 h, 96 h, 170 h, and 500 h (Figure **III-4**). Across the three first aging conditions (48-170 h), Al_3Zr precipitates are relatively homogeneously distributed in the matrix. After 500 h of aging, a noticeable decrease in the precipitate number density is exhibited (Figure **III-4**d), and they are significantly larger. This suggests that the coarsening stage may have started.

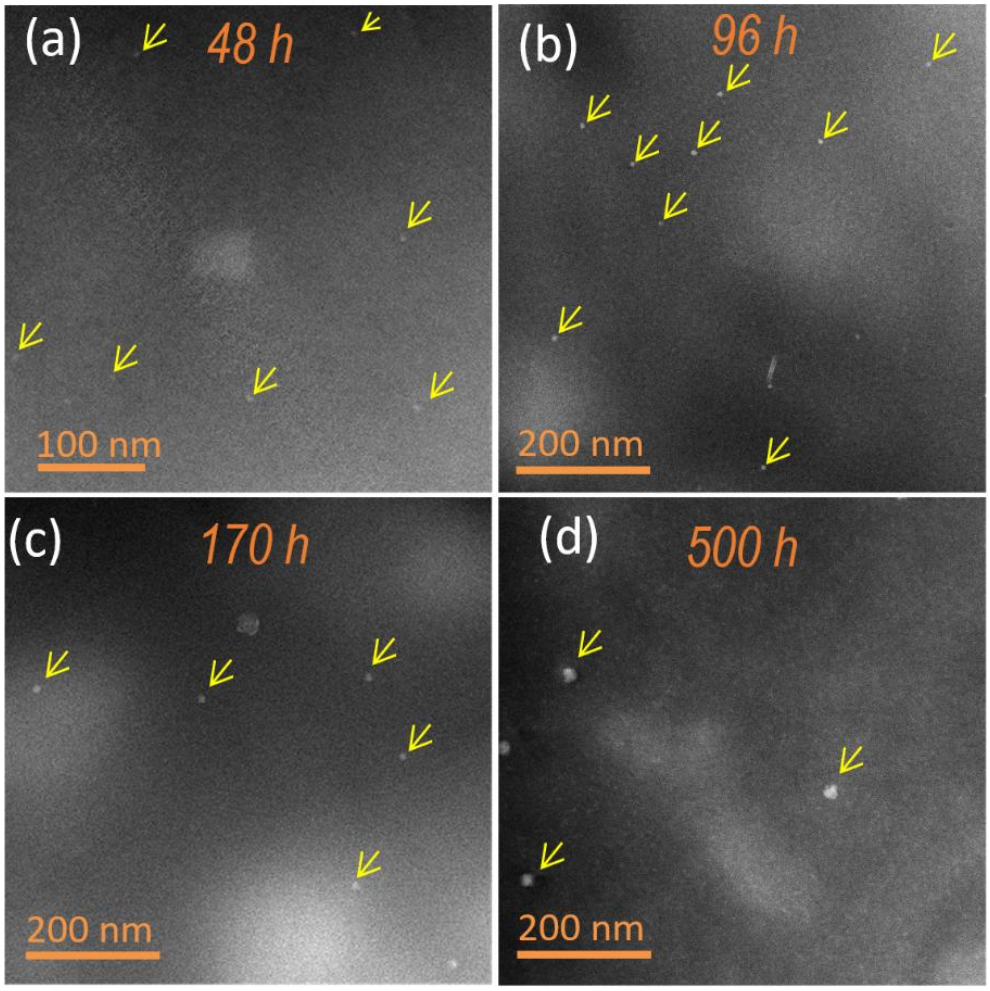


*Figure **III-4**: HAADF-STEM images of the Al-0.2Zr alloy aged at 375 °C during (a) 48 h, (b) 96 h, (c) 170 h, and (d) 500 h. Images (a), (c) and (d) were acquired along the ⟨001⟩ zone axis, while (b) was taken along the ⟨110⟩ zone axis.*

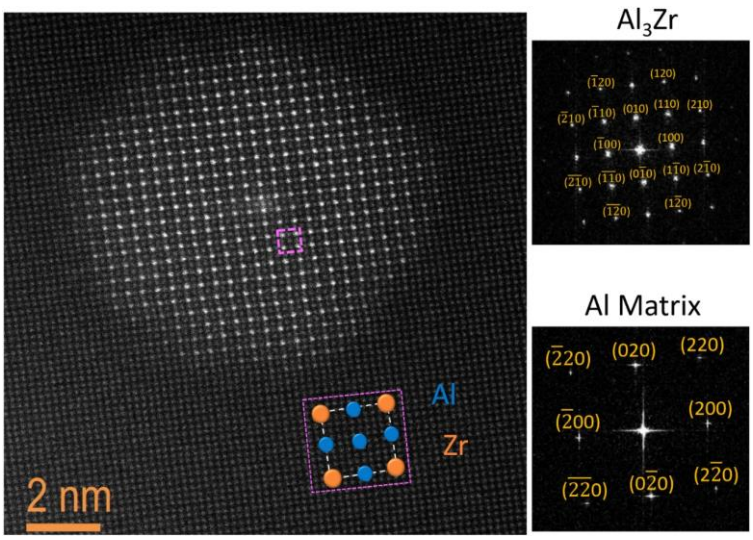


*Figure **III-5**: High-resolution HAADF-STEM image of an Al_3Zr precipitate embedded in the Al matrix, taken along the ⟨001⟩ zone axis. The inset shows the atomic arrangement, with blue spheres are Al atoms and orange spheres are Zr atoms. The corresponding FFT patterns are taken from the Al_3Zr precipitate, indexed with the $L1_2$ structure, and from the Al matrix, indexed with the FCC structure.*

The growth of precipitates over time is illustrated by high-magnification HAADF-STEM images shown in Figure **III-6**. When the aging time is extended to 48h, 96 h, 170 h, and 500 h, the Al_3Zr precipitates significantly grow, reaching an average diameter of 5.6 ± 1.2 nm, 8.0 ± 1.5 nm, 11.7 ± 2.1 nm and 21 ± 2.1, respectively. Despite the increase in size, the precipitates maintain their coherent $L1_2$ structure throughout the aging sequence, as evidenced by the ordered atomic arrangement in the high-resolution images Figure **III-6**d.

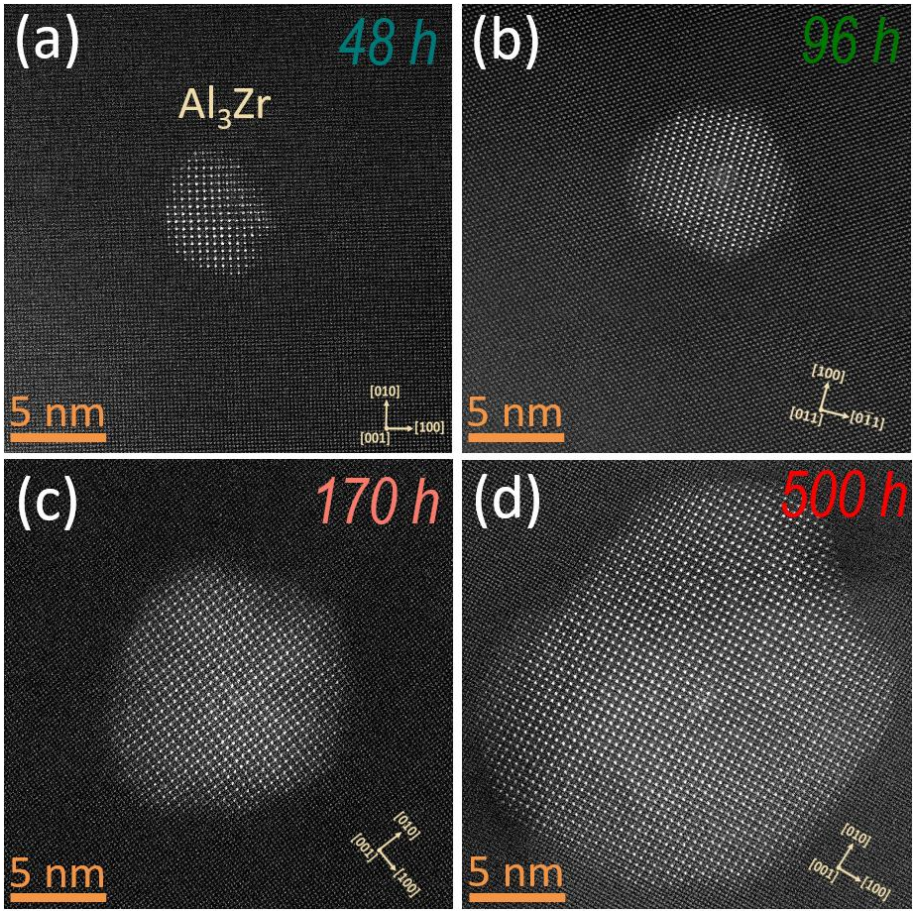


*Figure **III-6**: HAADF-STEM images showing the Al_3Zr precipitates in the Al-0.2Zr alloy aged at 375 °C during 48 h (a), 96 h (b), 170 h (c) and 500 h (d). All images were recorded in ⟨100⟩ zone axis, excepted (b) in ⟨110⟩ zone axis.*

Interestingly, some "merged" precipitates with the $L1_2$ structure were also observed after 500 h (Figure **III-7**). However, the equilibrium $D0_{23}$ phase was never detected in any of the studied conditions even for such a long aging time (500 h), suggesting that the chosen temperature (375 °C) remains within the stability range of the $L1_2$ structure as previously reported [72,142,143], a very long aging time is needed to initiate transformation to the equilibrium phase. Thus, it can also be attributed to the very low mobility of Zr in the Al matrix [138,266].

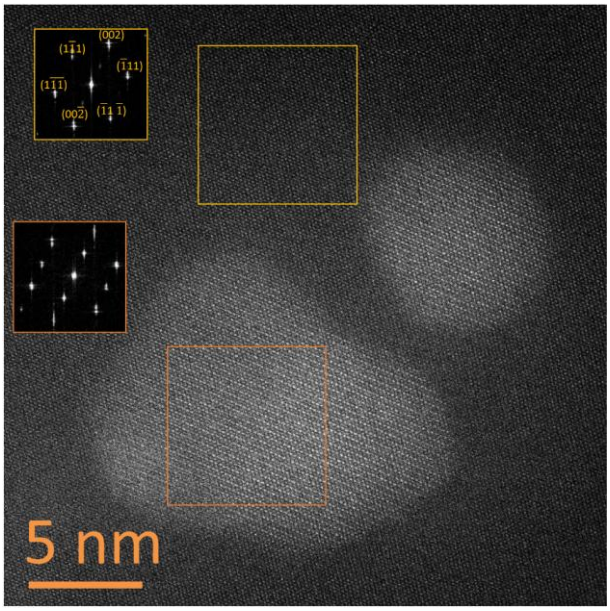


*Figure **III-7**: HAADF-STEM image showing the "merging" of Al_3Zr precipitates. The precipitates retain the $L1_2$ structure, as confirmed by the corresponding FFT patterns (insets), taken along the ⟨110⟩ zone axis.*

The variation in shape of precipitate was also evaluated by calculating the aspect ratios (minor/major diameter) of each precipitate.

The aspect ratios remained close to 0.85 for all aging durations (Table **III.1**), except after 500 h of aging, where the aspect ratio decreased down to about 0.7. Thus, precipitates maintain an almost spherical morphology throughout the aging process, up to 500 h, where a morphological change begins to appear. This may indicate the onset of the transformation to the stable $D0_{23}$ phase, as previously reported [112,142,143].

*Table **III.1**: aspect ratio (shortest/longest diameter) of Al_3Zr precipitates aged at 375 °C for different aging times, measured from HAADF-STEM images.*

Aging time (h)	Aspect ratio (d_{min}/d_{max})
48	0.86 ± 0.02
96	0.85 ± 0.03
170	0.83 ±0.03
500	0.69 ± 0.05

The precipitate size distribution for each aging time is summarized in histograms displayed in Figure **III-8**. The histograms clearly show a progressive shift toward larger diameters with increasing aging time. After 48 hours, the distribution is narrow and centered around 5.6 nm, after 96 h it moves to 8–10 nm with a modest spread. After 170 h and 500 h distribution becomes broader. This growth kinetic at 375 °C for Al_3Zr precipitates is consistent with that reported by Souza *et al* for a similar alloy [73].

A measurement of the precipitate number density directly from TEM images, is not reliable due to the small number of precipitates that were observed. Therefore, another approach based on APT data is presented in the next section.

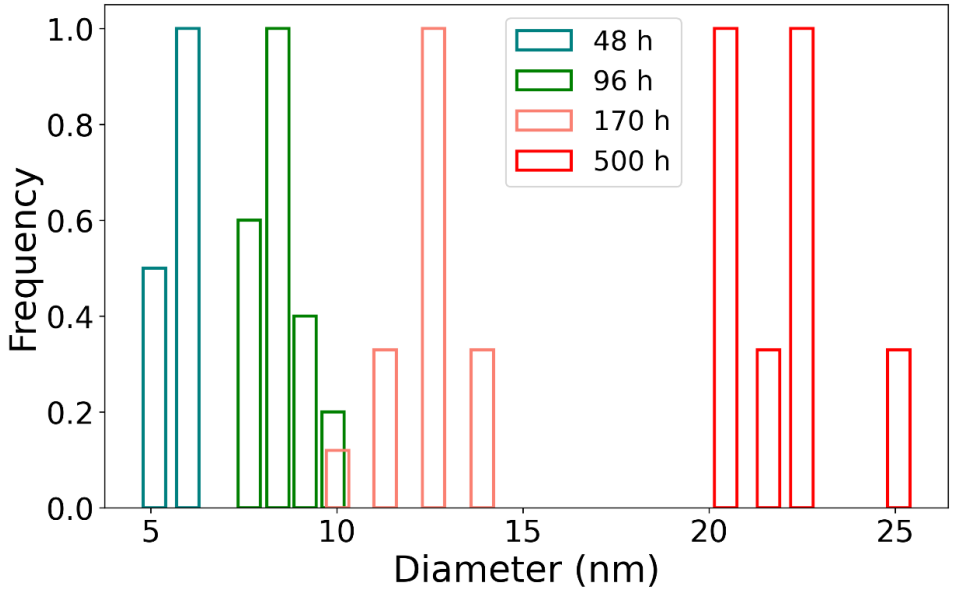


*Figure **III-8**: Size distribution histograms of Al_3Zr precipitates measured from HAADF-STEM images after aging at 375 °C in air over 48 h, 96 h, 170 h, and 500 h.*

In addition to the Al_3Zr precipitates, elongated particles have been occasionally observed. The structure of these particles, revealed by the HAADF image in Figure **III-9**, shows a multi-layered structure, a central region with a complex structure, covered on both sides by an ordered phase. FFT taken from the outer layers display the characteristic reflections of the $L1_2$ ordered structure.

STEM-EDS maps and spectra (Figure **III-10**) indicate that these ordered layers contain Zr, while the core is enriched in Fe and Si with traces of Ni. These features are consistent with the "D-phase" reported by Dorin *et al*.[264], a Fe-rich pseudo-icosahedral core surrounded by a Zr-

enriched $L1_2$ bilayer. In their study, Dorin *et al*. indicate that the presence of Sc is required for the formation of this phase, which is not the case in the present alloy.

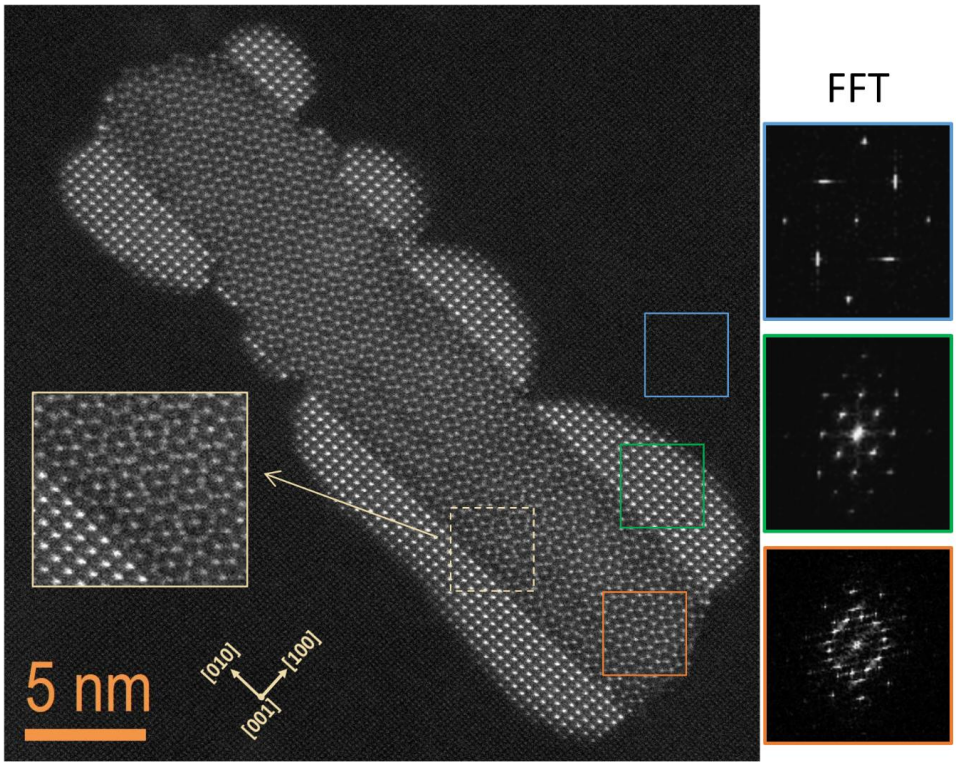


*Figure **III-9**: STEM-HAADF image of an elongated multilayer particle (Al-0.2Zr aged 170 h at 375 °C), showing a core and two $L1_2$ outer layers, insets show the corresponding FFTs from the matrix, outer $L1_2$ bilayer, and the core.*

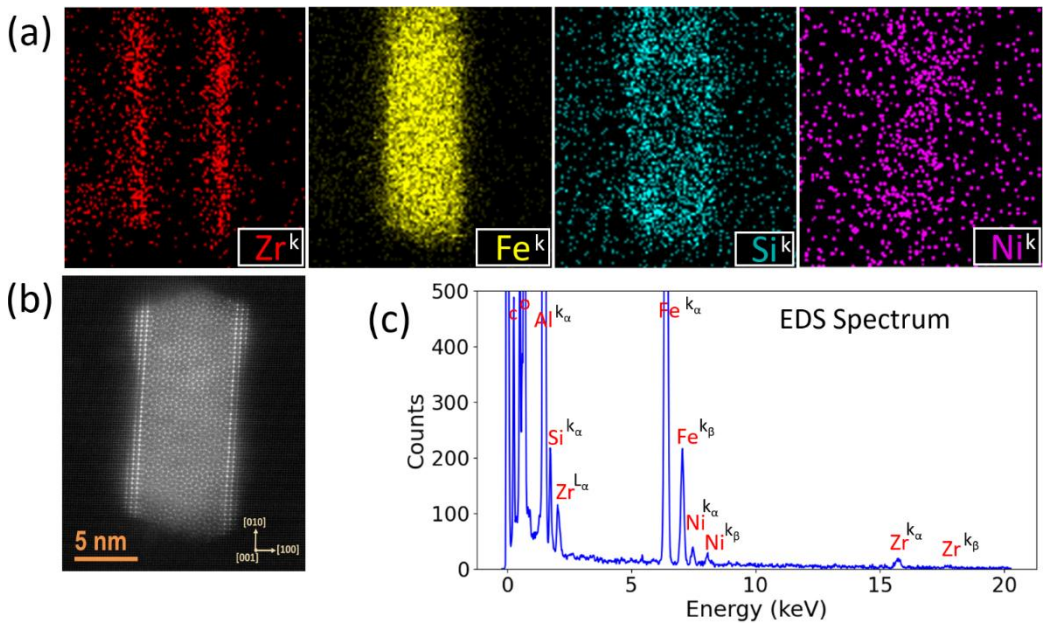


*Figure **III-10**: (a) EDS chemical maps showing the elemental distribution in the elongated precipitate. (b) HAADF-STEM image of the elongated precipitate. (c) EDS spectrum corresponding to the chemical maps (Al-0.2Zr aged 96 h at 375 °C).*

3.2.Solid Solution and precipitate compositions (APT)

Atom probe tomography (APT) was employed to measure the Zr concentration in precipitates and in the matrix after different aging times. The number density of Al_3Zr precipitates was then estimated based on these measurements and on TEM data (size).

Figure **III-11** shows the mass spectrum obtained from a sample aged for 48 h at 375 °C. The spectrum is dominated by aluminum ions, with intense peaks corresponding to Al^+ and Al^{2+}. A series of hydrogen peaks (H^+, H_2^+, H_3^+) is also exhibited, they result from residual gas in the chamber and/or contamination introduced during sample preparation [16].

The inset in Figure **III-11** expands the 42–50 *Da* window which corresponds to the Zr^{2+} isotopic region and the associated hydrides ZrH_x^{2+} [267]. Five Zr^{2+} isotope peaks are expected near 45.0, 45.5, 46.0, 47.0 and 48.0 *Da* (corresponding to ^{90}Zr, ^{91}Zr, ^{92}Zr, ^{94}Zr and ^{96}Zr, respectively), with the peak at ≈ 45.0 *Da* being the most intense (blue), consistent with the natural isotopic abundances. Besides, Zr hydrides are also detected, but their signals overlap with those of Zr isotopes, leading to mixed contributions (orange). Some peaks, however, such as 46.5, 47.5, and 48.5 *Da* (green), can be attributed only to ZrH_x^{2+} molecular ions. The detection of such molecular ions during APT analysis is well-known and commonly reported [268–270].

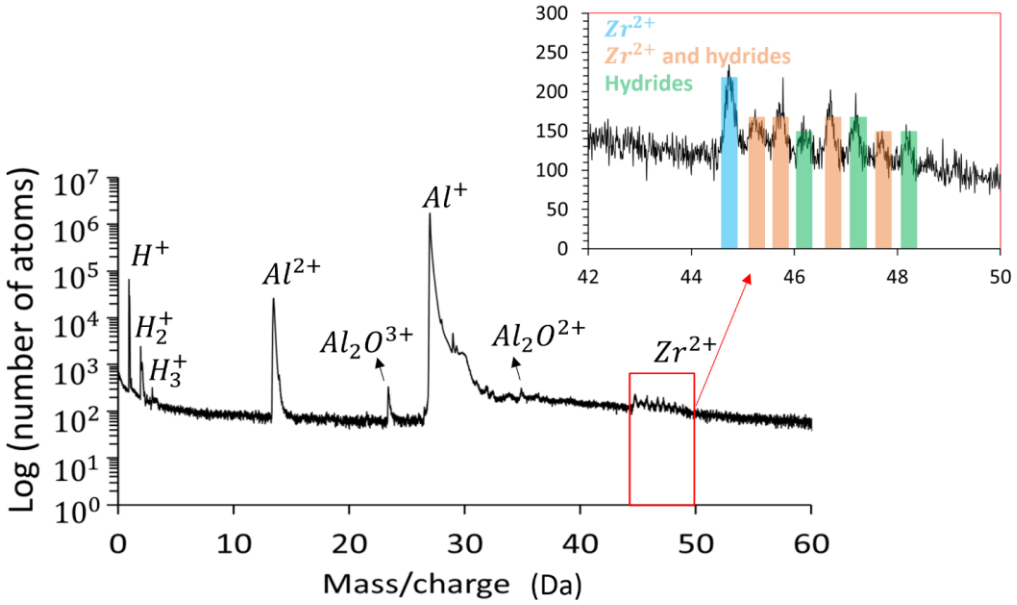


*Figure **III-11**: APT mass spectrum of the Al–0.2Zr alloy aged at 375 °C after 48 h. The inset shows an expanded view of the 42–50 u/e range corresponding to the Zr^{2+} isotopic region, where peaks from Zr^{2+} and possible ZrH^{2+} molecular ions are highlighted.*

Three-dimensional reconstructions of two tips (Figure **III-12**) aged after 48 h and 96 h reveal Zr-rich clusters identified as Al_3Zr precipitates. Concentration profiles across individual precipitates for both aging times show a well-defined plateau at ~25 at.% Zr within the precipitates, confirming the Al_3Zr stoichiometry.

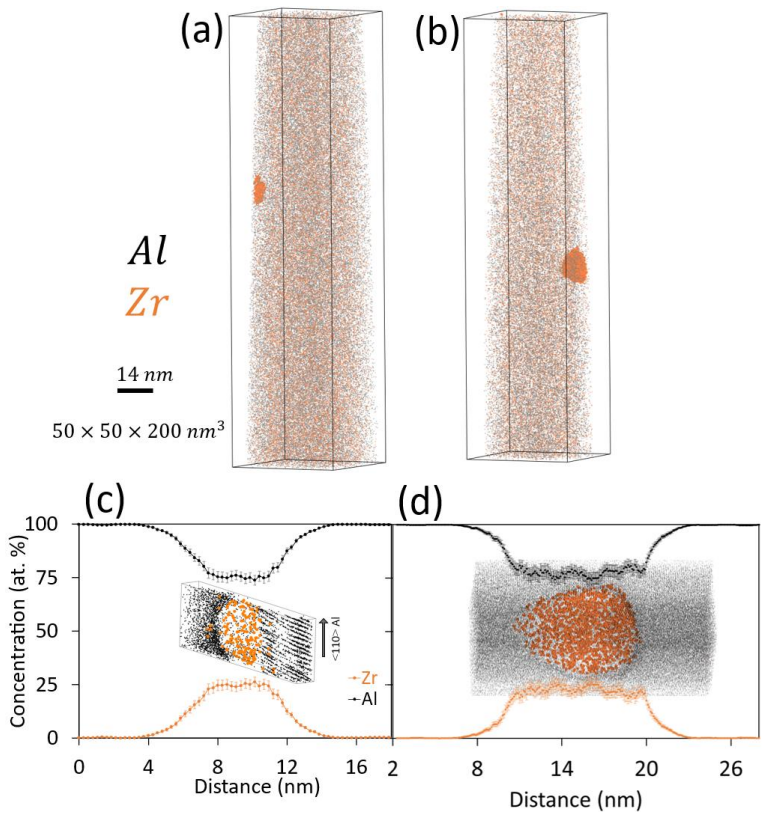


*Figure **III-12**: 3D reconstructions of volumes analyzed by APT (50 × 50 × 200 nm³) in the Al-0.2Zr alloy aged during 48 h (a) and 96 h (b). Al atoms are plotted in gray and Zr atoms in orange. Data were filtered to display only Zr atoms in Zr rich regions (threshold 10 at %) to highlight Al_3Zr precipitates. (c) and (d) show concentration profiles through the Al_3Zr precipitate in (a) and (b), respectively, with a sampling volume thickness of 0.4 nm.*

Zr quantification was performed by integrating counts in the Zr^{2+} windows. Background subtraction was applied using the standard procedure implemented in GPM_3dSAT software.

Considering that Al_3Zr precipitates are spherical, the number density of precipitates per unit volume N_p can be determined using the following equation:

$$N_p = \frac{f_v}{V_p} \qquad \text{III-1}$$

where V_p is the mean volume of Al_3Zr precipitates ($V_p = \frac{4\pi}{3} r^3$) where r is the mean radius measured from TEM data. The volume fraction of Al_3Zr precipitates f_v can then be estimated based on the mass balance [271], assuming that Zr atoms are exclusively shared between the matrix and Al_3Zr precipitates:

$$C_0 = C_m.(1 - f_v) + C_p.f_v \quad \text{III-2}$$

where C_0 is the initial atomic fraction of Zr (0.07 at%), C_p is the mean concentration of Zr in precipitates, and C_m is the Zr concentration in the matrix.

The resulting Zr concentrations, volume fractions, and number densities are summarized in Table **III.*2***. After 48 h at 375 °C, the matrix contains 0.047 ± 0.011 at. % Zr, while the precipitates contain 23.9 ± 3.4 at. % Zr. After 96 h, the Zr concentration in matrix decreases to 0.035 ± 10^{-4} at. %, and the precipitate composition is 25.6 ± 3.1 at. %, consistent with Al_3Zr stoichiometry.

Thermo-Calc® (with TTAL6 database) predicts an equilibrium solubility of 0.004 at. % Zr at 375 °C. The measured Zr concentration in the matrix after 48 h and 96 h of aging are therefore well above equilibrium, showing that the alloy is still far from equilibrium after 96 h of aging.

The precipitate volume fraction increases from 0.11 ± 0.02 % to 0.16 ± 2×10^{-4} % after 48 h and 96 h, respectively, but remains below the equilibrium value (0.26%). The number density is statistically similar between the two ageing times 0.9 ± 0.34 × 10^{22} m^{-3} after 48 h and 0.6 ± 0.33 × 10^{22} m^{-3} after 96 h, indicating that, under these conditions, the system is still in the growth stage, with no evidence of coalescence.

*Table **III.2**: Zr concentration (at%) in precipitates and matrix from APT data (the total number of atoms collected for each state is over 60 million). precipitate volume fraction fv (estimated from Eq* III-2 *using compositions measured by APT), and number density N_p of Al_3Zr precipitates calculated from Eq* III-1.

Aging time	**Precipitates (at% Zr)**	**Matrix (at% Zr)**	f_v **(%)**	N_p **(10^{22} m^{-3})**
48 h	23.9 ± 3.4	0.047 ± 0.011	0.11 ± 0.02	0.9 ± 0.34
96 h	25.6 ± 3.1	0.035 ± 10^{-4}	0.16 ± 2 × 10^{-4}	0.6 ± 0.33
Equilibrium Thermo-Calc®	-	0.004	0.26	-

4. Effect of Hydrogen on Precipitation

4.1. Precipitate Morphology and Structure (TEM)

To investigate the influence of hydrogen on precipitation, TEM observations were performed on samples aged under H_2 atmosphere and compared to those aged in air with identical conditions.

As shown in Figure **III-13**(d–f), nanoscale Al_3Zr precipitates nucleated and grew with a similar spatial distribution, but seem to be larger than those aged in air. Figure **III-13**(j–l) shows that their morphology remains relatively spherical. However, their size is systematically larger for all aging times under hydrogen. The average diameters are 8.4 ± 2.0, 11.5 ± 1.5 and 21.0 ± 2.0 nm after 48 h, 96 h and 170 h respectively, which is significantly greater than those measured for samples aged in air, as previously reported (section III.3.1). Besides, after 170 h in H_2, a change in precipitate morphology is observed, although the $L1_2$ structure is kept with no evidence of transformation to the stable $D0_{23}$ phase (Figure **III-13**l). This is similar to the observations carried out in sample aged at 500 h in air, with comparable diameters: 21.0 ± 2.0 nm after 170 h under hydrogen and 21.0 ± 2.1 nm after 500 h in air.

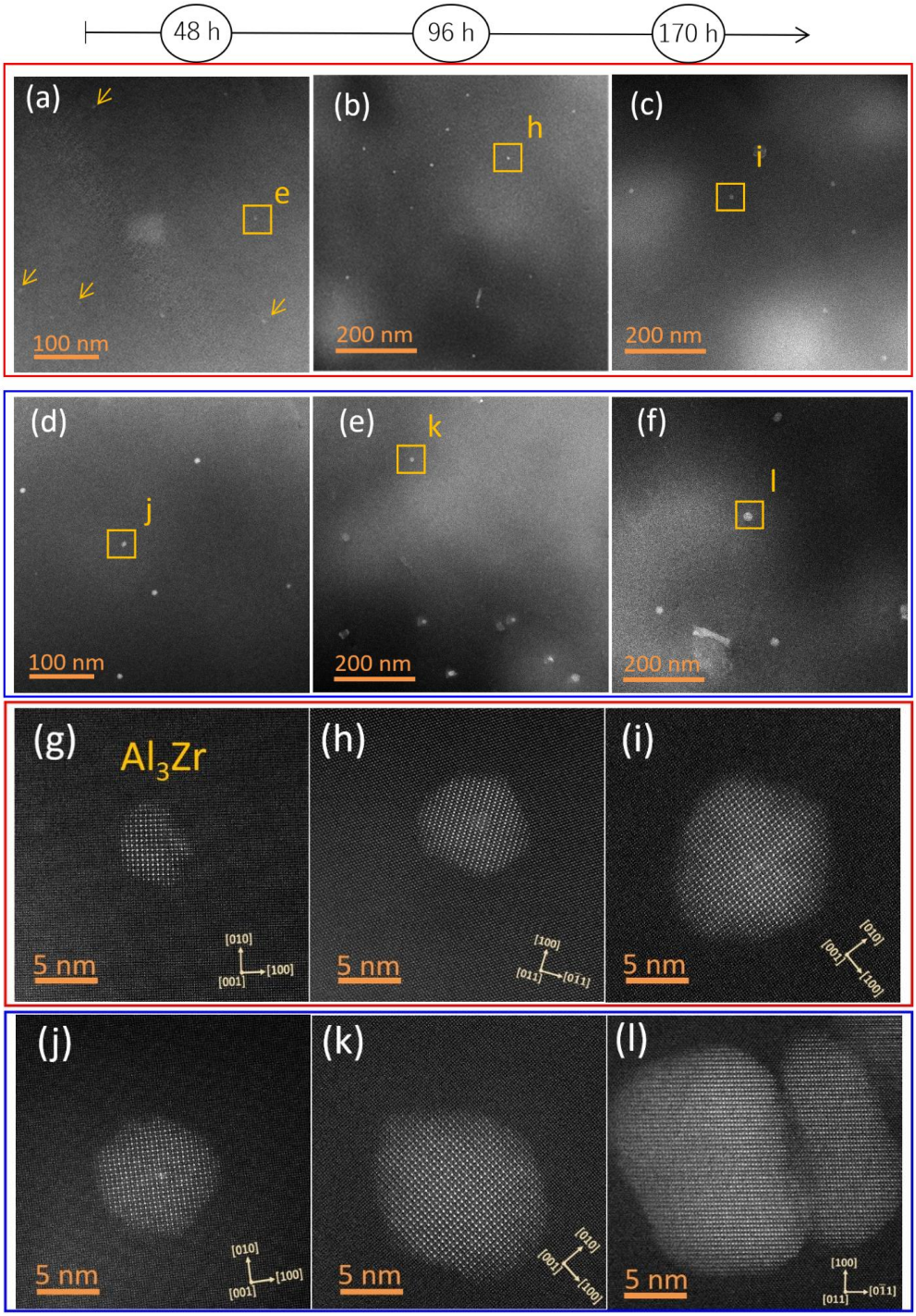


*Figure **III-13**: HAADF-STEM images of the Al-0.2Zr alloy aged at 375 °C in air (a, b, c) and in hydrogen (d, e, f), during 48 h (a, d), 96 h (b, e), 170 h (c, f). All images were recorded in ⟨100⟩ zone axis, except (b) and (f) in ⟨110⟩ zone axis. (g-l) are high-resolution images showing the $L1_2$ ordered structure of Al_3Zr precipitates in each state.*

For more clarity, precipitate size distributions for both aging conditions (H_2 atmosphere and air) are displayed in Figure **III-14**. There is a clear shift of the size distributions toward higher

values under hydrogen after all aging times, indicating a markedly faster growth rate under hydrogen than for samples aged in air.

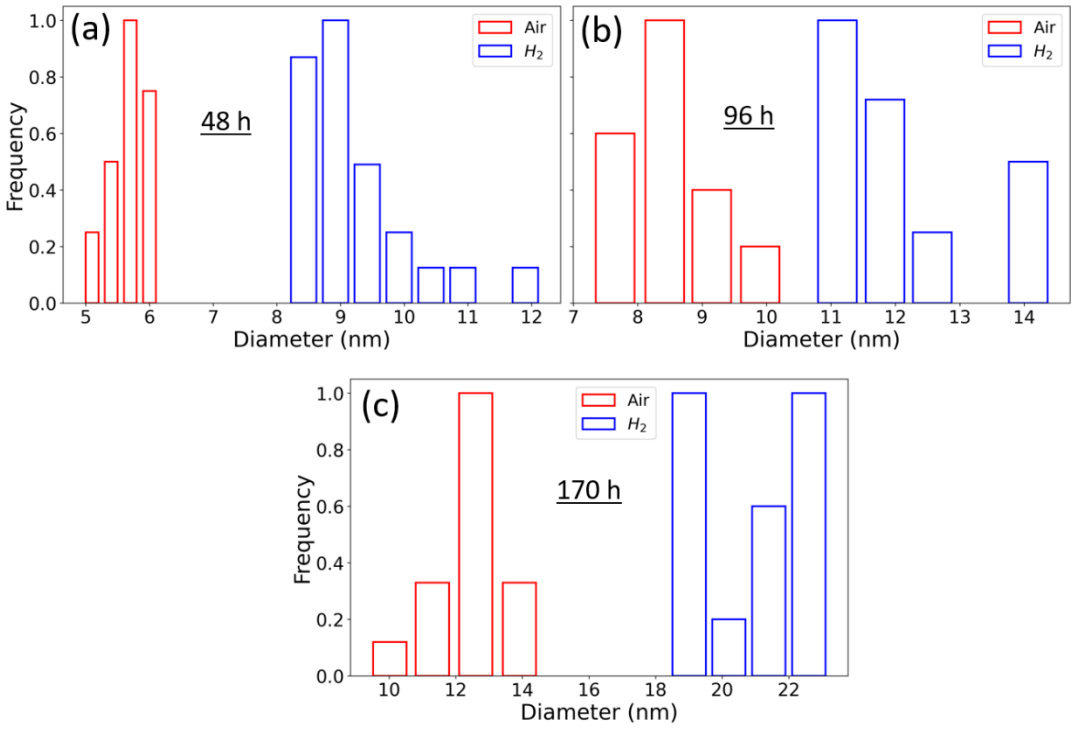


*Figure **III-14**: Al_3Zr precipitates size histogram, measured from HRSTEM images of samples aged under air (red) and hydrogen atmosphere (blue). During 48 h (a), 96 h (b), and 170 h (c).*

The aspect ratios of precipitates in samples aged under hydrogen were also estimated and compared with those aged in air (Table **III.3**). For 48 h and 96 h of aging, aspect ratios are relatively similar between the two conditions. A significant difference appears after 170 h of aging: the sample aged under hydrogen reaches an aspect ratio of 0.7, which is comparable to that of the sample aged in air only after 500 h of aging.

*Table **III.3**: aspect ratio (shortest/longest diameter) of Al_3Zr precipitates aged at 375 °C in air and under hydrogen for different aging times.*

Aging time (h)	Aspect ratio (under H_2)	Aspect ratio (in air)
48	0.85 ± 0.03	0.86 ± 0.02
96	0.83 ±0.03	0.85 ± 0.03
170	0.7 ± 0.05	0.83 ±0.03
500	-	0.69 ± 0.05

The equilibrium $D0_{23}$ phase was not detected at any aging time (up to 170 h) under hydrogen. In contrast, D-phase precipitates were also observed for samples aged under hydrogen. An example of such a precipitate in a sample aged 48 h is shown in Figure **III-15**. However, due to their extremely low number density, the influence of hydrogen on the growth of these precipitates could not be addressed statistically.

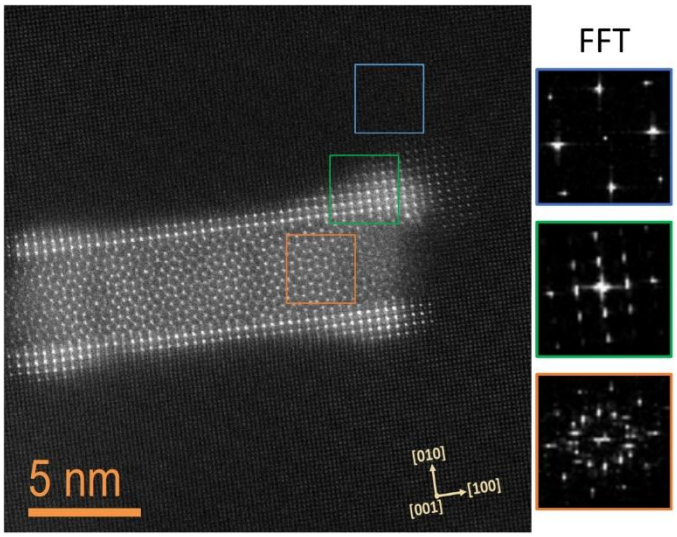


Figure III-15: HAADF-STEM image of Al-0.2Zr alloy aged 48 h under hydrogen, showing the structure of the "D-phase". The insets display the FFT reflections from selected regions in the matrix (blue), outer layer (green), and core (orange). The image was taken along the ⟨001⟩ zone axis.

4.2.Solid solution and precipitate compositions (APT)

Similarly to the samples aged in air, Zr concentrations in the precipitates and matrix were measured by APT for samples aged under hydrogen and compared with those aged in air (Table **III.*4***). The corresponding 3D reconstructions and mass spectra are provided in Appendix 3.

After 48 h aging under hydrogen, Zr concentration in the matrix is 0.028 ± 0.013, still above the equilibrium solubility limit (0.004). However, Zr concentrations in the matrix are systematically lower in samples aged under hydrogen than in air (0.047 ± 0.011 after 48 h), suggesting that hydrogen may promote the decomposition of the Zr supersaturated solid solution. Besides, this lower concentration of Zr in the matrix is consistent with TEM observations, in which Al_3Zr precipitates in samples aged under hydrogen appear larger than those in sample aged in air. The volume fraction is higher for sample aged under hydrogen (0.19 ± 0.02 %) than in air (0.11 ± 0.02 %) for the same aging time (48 h).

For all samples, the number density of Al_3Zr precipitates is relatively similar (Table **III.*4***), indicating that the nucleation rate is not significantly affected by hydrogen. Since the nucleation barrier for homogeneous precipitation is mostly dependent on the precipitate-matrix interfacial energy, it seems then that hydrogen does not significantly affect the (Al_3Zr/Al) interfacial energy.

*Table **III.4**: Comparison of Zr concentrations (at.%) in precipitates and matrix, obtained from APT data, for samples aged in air and under hydrogen.*

Aging conditions	**Precipitates (at% Zr)**	**Matrix (at% Zr)**	**f_v (%)**	**N_p (10^{22} m^{-3})**
48 h /Air	23.9 ± 3.4	0.047 ± 0.011	0.11 ± 0.02	0.9 ± 0.34
48 h /H_2	24.4 ± 3.2	0.028 ± 0.013	0.19 ± 0.02	0.6 ± 0.4
96 h /Air	25.6 ± 3.1	0.035 ± 10^{-4}	0.16 ± 2 × 10^{-4}	0.6 ± 0.33

5. Discussion

5.1. Growth Rate of Al_3Zr Precipitates

The mean radius of Al_3Zr precipitates, as measured from HRSTEM images for both aging condition (H_2 atmosphere and air) was plotted as a function of aging time in Figure **III-16**.

From the classical model (Equation I-9) detailed in Chapter 1, it is possible to predict the theoretical growth rate of Al_3Zr precipitates at 375 °C as a function of time. The corresponding curve was plotted (Figure **III-16**), using the parameters listed in Table **III.*5***. Even if this model assumes that the matrix composition remains constant (growth of a single precipitate in an infinite media), it fits relatively well experimental data, confirming that the system remains in the growth regime throughout the aging times considered, consistent with the APT data showing that the matrix Zr concentration is higher than the equilibrium solubility.

In the case of samples aged under hydrogen, experimental data could be fit with a diffusion coefficient twice larger than in air (Figure **III-16**), indicating that hydrogen may increase the mean diffusion coefficient of Zr by a factor of two. Some discrepancy between experimental data and the theoretical fit appears for longer aging time (170 h) which might be due to a change in precipitate morphology when they become relatively larger (Figure **III-13**l).

*Table **III.5**: Parameters of Eq. (*I-10 *&* I-9 *), from* [74,112,266].

Parameter	**Value**
R_0 (nm)	0.8
D_0 (m^2/s)	5.4×10^{-3}
Q (kJ/mol)	222
T (°C)	375 °C

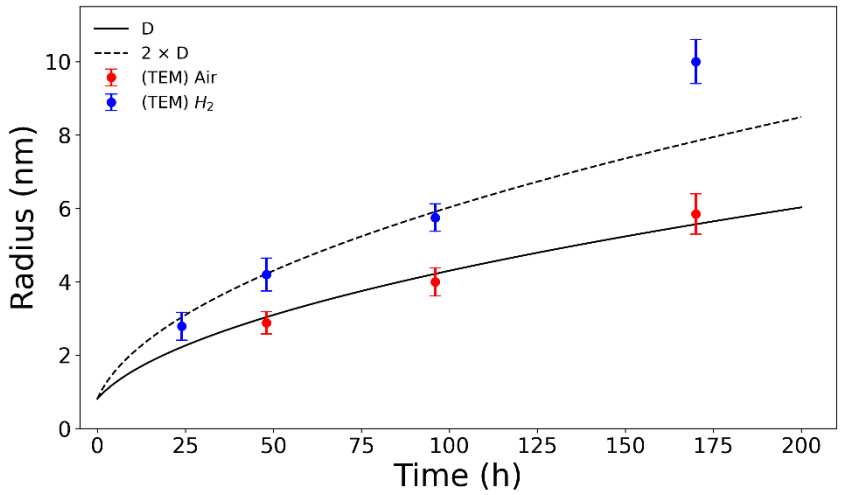


*Figure **III-16**: Growth rate of Al_3Zr precipitate. The red and blue dots are TEM experimental data for the material aged under air and under hydrogen, respectively. The solid black line was plotted from Eq.* I-9 *with D given in Table **III.5**. The dashed black line was plotted from* I-9 *to fit the growth rate under hydrogen with a diffusion coefficient (D) twice larger than under air.*

However, classical coarsening model used in (Figure **III-16**) was established without considering that during the precipitate growth (decomposition of the supersaturated solid solution), the Zr concentration in matrix decreases. Indeed, this assumption does not reflect the experimental observations, as shown in Table **III.*4***. For example, it can be seen that the Zr concentration in the matrix decreases by a factor of ~3 after 48 hours under H_2 atmosphere (C_m = 0.028 at%) compared to the initial stage (C_m = 0.07 at%). To evaluate the influence of this composition change on the growth rate, a numerical integration has been carried out based on the following formalism:

At the time t_i, the Zr concentration in the matrix $C_m(t_i)$ depends on the volume fraction of precipitates f_v (t_i), that can be estimated from the number density d_p (constant under our conditions), and the mean volume of precipitates V_p (t_i) given by:

$$\boldsymbol{V_p(t_i)} = \frac{4\pi}{3}\boldsymbol{r(t_i)}^3 \qquad \text{III-3}$$

The volume fraction at t_i is then determined from Eq. III-1:

$$\boldsymbol{f_v(t_i)} = d_p \times \mathbf{V_p}(\boldsymbol{t_i}) \qquad \text{III-4}$$

Then, $C_m(t_i)$ can be estimated from Eq. III-2:

$$\boldsymbol{C_m(t_i)} = \frac{(C_0 - C_p \times \frac{4\pi}{3} d_p \times \boldsymbol{r(t_i)}^3)}{(1 - \frac{4\pi}{3} d_p \times \boldsymbol{r(t_i)}^3)} \qquad \text{III-5}$$

Finally, the mean radius of precipitate at time t_{i+1} is estimated from Eq. I-9 adapted as follow:

$$\boldsymbol{r(t_{i+1})} = \left(R_0^2 + 2D\frac{\boldsymbol{C_m(t_i)} - C_e}{C_p - C_e}\Delta t\right)^{\frac{1}{2}} \qquad \text{III-6}$$

Where Δt is the integration time step.

The evolution of the mean radius of precipitate estimated from Eq. I-9 and III-6 are compared in Figure **III-17**. It clearly shows that there is no significant difference up to about 100 h of aging, as reported earlier by Souza *et al* [73]**.** Then, the simple model of Eq. I-9 can be considered to quantify the variation in Zr mobility induced by hydrogen.

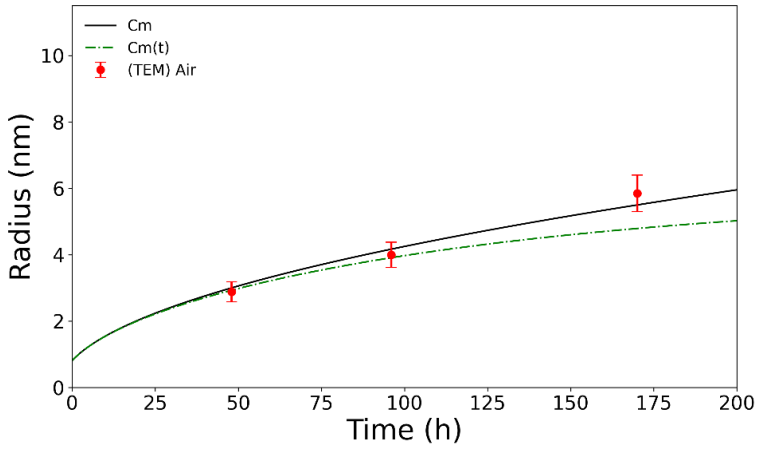


*Figure **III-17**: Growth rate of Al_3Zr precipitate. The red dots are TEM experimental data for the material aged under air. The solid black line is drawn from Eq.* I-9 *assuming that the matrix composition remains constant, the dashed green line is drawn from Eq.* III-6 *where the decrease of the Zr concentration in the matrix is taken into account (integration time step Δt = 10s).*

5.2. Influence of Hydrogen on Zr Mobility

Several hypotheses could be raised to account for this faster decomposition of the supersaturated solid solution under hydrogen. First, hydrogen may influence the atomic mobility of Zr, which is controlled by the vacancy concentration and mobility. Some studies have demonstrated that hydrogen may indeed significantly reduce the vacancy formation enthalpy in metallic alloys [272,273]. Besides, the high pressure (*i.e.* 10 MPa) may also affect both the formation enthalpy and the migration enthalpy of vacancies [274]. Pressure is also known to influence vacancy formation and migration in FCC systems [274]. This effect on vacancies can, in turn, alter the solute diffusion.

Since the two samples were aged under different pressures (10 MPa for hydrogen and 0.1 MPa for air), the influence of pressure should be considered first. Extrapolation of the data of Connétable *et al*. [274] between 0.1 and 10 MPa, indicates that the change in enthalpy is negligible (0.0008 eV for vacancy formation and 0.0002 eV for vacancy migration), leading to a 2% decrease in the diffusion coefficient of Zr under 10 MPa. Thus, the accelerated growth of Al_3Zr precipitates cannot be attributed to the high pressure.

The increase of the diffusion coefficient of Zr could be due to an increase in vacancy concentration, which results from a decrease in vacancy formation energy, or from an enhancement in vacancy mobility [275]. According to the thermodynamic model of vacancy diffusion, the solute diffusivity is related to the vacancy formation and migration energies (E_f, E_m) through the following equation:

$$D_{Zr} = a^2 v \exp\left(\frac{S_f + S_m}{k}\right) \exp\left(-\frac{E_f + E_m}{kT}\right) \qquad \text{III-7}$$

where a is the jump length, v is the vacancy jump frequency, and S_f and S_m refers to the vacancy formation and migration entropy, respectively. An increase in the enthalpies of formation and migration generally leads to a decrease in the diffusion coefficient.

X-ray diffraction studies have shown that hydrogen decreases the vacancy formation energy [276,277]. *Ab initio* calculations have also demonstrated that hydrogen can influence vacancy mobility. In Cu and Pd, hydrogen enhances vacancy mobility [278], while in Ni, it significantly slows it down [279]. In the case of chemical or gaseous hydrogen loading, hydrogen forms a vacancy–hydrogen complex at the surface of the samples and diffuses into the material, which

is suggested by a hydrogen-vacancy ratio close to one, often observed in aluminum [28,172]. Such a complex may have a significant impact on the equilibrium vacancy concentration.

Besides, As mentioned earlier, Zr binds strongly to hydrogen [263], which itself has a high affinity for vacancies [261]. Since Zr exhibits limited interaction with vacancies in Al alloys compared to other solutes [66], then hydrogen-vacancy interactions could modify the Zr mobility that is driven by a vacancy mechanism.

Assuming that hydrogen influences only E_m and E_f, without affecting the exchange probability between Zr and vacancies, as observed in the Al-Cu system [64], the variation in vacancy migration energy and formation energy can be estimated from the change in the diffusion coefficient using III-7, which leads to:

$$\Delta E_f + \Delta E_m = -KT\, ln(\frac{\mathrm{D^H_{Zr}}}{\mathrm{D^A_{Zr}}}) \qquad \text{III-8}$$

where D_{Zr}^{H} and D_{Zr}^{Air} are the diffusion coefficients of Zr during aging under hydrogen and air, respectively. With $\mathrm{D^H_{Zr}} \approx 2 \times \mathrm{D^{Air}_{Zr}}$, it can be estimated that the reduction of the vacancy migration or formation energies is about 0.04 eV.

The equilibrium vacancy concentration is given by [280,281]:

$$\mathrm{C_v} = \exp^{(\frac{\mathrm{S_f}}{\mathrm{k_B}})} . \exp^{\left(-\frac{\mathrm{E_f}}{\mathrm{k_B T}}\right)} \qquad \text{III-9}$$

In aluminum at 375 °C (with E_f = 0.63 eV and S_f = 1.03k_B [261]), the vacancy concentration is estimated to be about 3.5 10^{-5}. Assuming that hydrogen affects only the vacancy formation energy with $E_f^H = E_f + 0.04$. The vacancy concentration could increase up to 7.2 10^{-5}, thus increasing Zr mobility. Figure **III-18** illustrates this mechanism, where hydrogen–vacancy complexes increase the vacancy concentration and promote Zr diffusion toward precipitates.

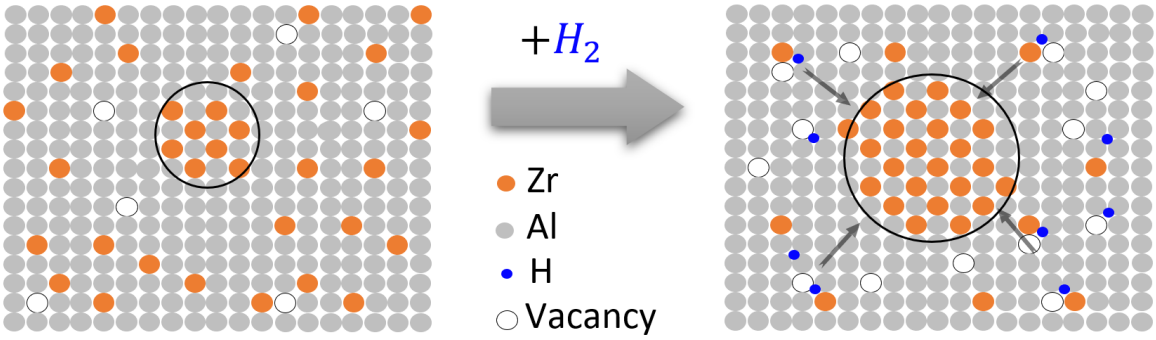


*Figure **III-18**: Schematic illustration of the mechanism suggested. Left, in the absence of hydrogen, the diffusion of Zr atoms is limited by the low vacancy concentration and the weak Zr–vacancy interactions. Right, aging under hydrogen, hydrogen atoms form complexes with vacancies (H–V), increasing the vacancy concentration and mobility which in turn facilitate Zr diffusion towards the growing precipitate, accelerating its growth.*

6. Conclusions

In this chapter, the precipitation and growth kinetics of Al_3Zr in an Al-0.2Zr alloy were systematically investigated under conventional aging conditions in air and in a hydrogen atmosphere. Microstructural analyses by TEM and APT revealed that Al_3Zr precipitates exhibit a coherent $L1_2$ structure and remain stable without transformation to the $D0_{23}$ equilibrium phase even after prolonged aging at 375 °C, owing to the low mobility of Zr in the aluminum matrix.

Hydrogen was found to significantly accelerate the growth of Al_3Zr precipitates, resulting in systematically larger precipitates at all aging times studied compared to samples aged in air. However, the nucleation rate does not seem to be affected, as evidenced by comparable precipitate number densities in both environments, suggesting that hydrogen does not significantly alter the precipitate-matrix interfacial energy.

Kinetic modeling using classical coarsening model showed a good agreement with experimental data, and revealed that hydrogen increases the effective diffusion coefficient of Zr by a factor of about two. APT analyses have also confirmed the enhanced decomposition of the Zr supersaturated solid solution under hydrogen, consistent with the observed growth acceleration.

This enhancement is attributed to hydrogen-vacancy interactions, which reduce vacancy formation or migration energies by approximately 0.04 eV, thus enhancing Zr mobility. From a processing perspective, hydrogen appears interesting as it could reduce the requirements of

aging treatments, by shortening the time or lowering the temperature needed to achieve a given precipitate state. However, hydrogen may also affect the thermal stability of the alloy, which could be detrimental for high-temperature applications under hydrogen environment.

CHAPTER IV: Influence of hydrogen on precipitation in the Al-5Cu Alloy

1. Introduction 102

2. Hardness Evolution During Aging 102

3. Measurement of hydrogen concentration 105

4. Microstructural Characterization 107

4.1. As-quenched state 107

4.2. Precipitation at 140 °C 112

4.3. Influence of hydrogen on precipitation sequence 118

5. Relationship between microstructure and hardness 122

5.1. Precipitate Strengthening Models 122

5.2. Calculated Strengthening Contributions 125

5.3. Theoretical versus experimental hardness comparison 128

6. Hydrogen Trapping and its Effect on GP zones Transformations 130

7. Influence of deformation and hydrogen on precipitation 135

7.1. Microstructure characterization of the deformed Al-5Cu alloy 135

7.2. Influence of Hydrogen on Precipitation (chemical charging) 136

7.3. Influence of Hydrogen on Precipitation (aging under hydrogen environment) 142

7.3.1. Hardness Evolution 142

7.3.2. Microstructure characterization 144

7. Discussion 150

1. Introduction

This chapter investigates the influence of hydrogen on precipitation in the Al-5Cu alloy aged at 140 °C. Using Vickers micro-hardness testing and high-resolution STEM, we outline the classical precipitation sequence (GP zones → θ″ → θ′ → θ) and track its kinetics as a function of aging time. A comprehensive qualitative and quantitative comparison is made between hydrogen-charged and uncharged samples, including a comparison of precipitate structure, size, thickness, distribution, and number density. Two hydrogen introduction methods were employed: pre-chemical charging and aging under a hydrogen atmosphere. TDS was also performed to assess hydrogen uptake for different states. Additionally, a precipitation strengthening model was applied based on experimental results to link microstructural observations to the micro-hardness response. The effect of deformation and hydrogen on precipitation was investigated through microstructural characterization.

2. Hardness Evolution During Aging

The age-hardening behavior of Al-Cu alloys is driven by the precipitation sequence SSSS → GP zones → θ″ → θ′ → θ (precipitation strengthening), during which the precipitate size, distribution, and volume fraction evolve, strongly affecting the mechanical properties of the alloy (see Chapter 1). Age-hardening response at 140 °C of the Al-5Cu alloy is shown in Figure **IV-1**. The microhardness increases rapidly with aging time during the early stages of aging, reaching 127 ± 3 HV after approximately 10 h. This increase is likely associated with the nucleation and growth of coherent metastable precipitate θ″(Al_3Cu), as reported in previous studies [17,217]. Then, the microhardness increases at a slower rate up to 142 ± 3 HV after about 100 h.

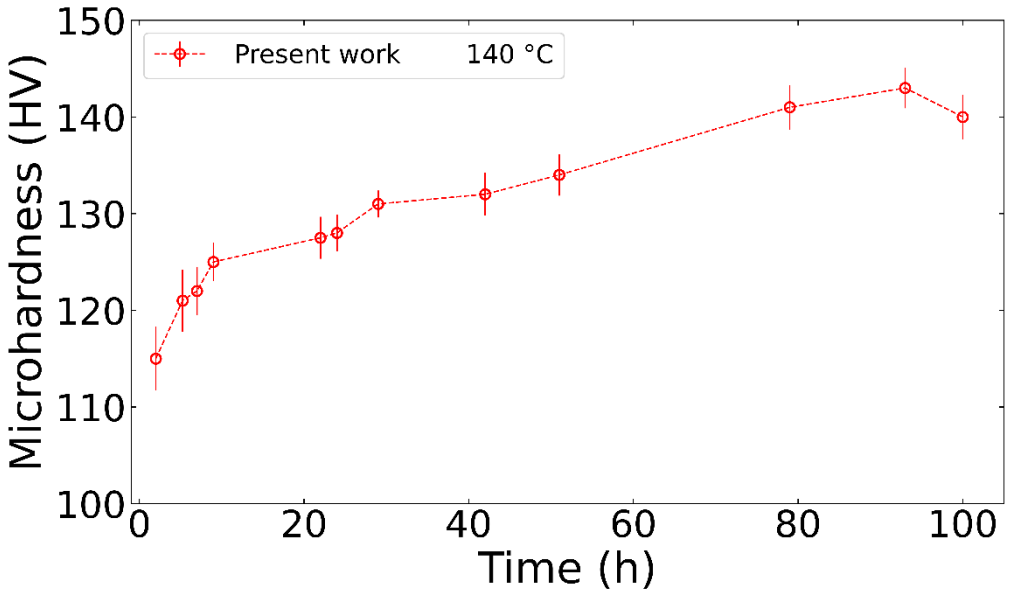


Figure IV-1: Vickers microhardness as a function of aging time at 140°C for Al-5Cu alloy.

For comparison with previous studies, Figure **IV-2** also includes hardness curves from similar alloys aged at different temperatures (130 °C, 155 °C, and 180 °C). No published data were found for a similar alloy aged at 140 °C, but this does not preclude a useful comparison. Aging at 130°C (S.P. Ringer [282]) displays significantly slower hardness kinetics, the Vickers hardness reaches approximately 100 HV after 20 hours and continues to increase to 122 HV after 100 h. Aging at 155 °C (Wu Wei [217]) shows a similar behavior to that observed in the present study during the early stages of aging, with a peak-aged of about 134 HV reached at 32 h. By contrast, samples aged at 180 °C (P.P. Ma [218] and X.Q. Zhao [219]) exhibit a more rapid hardening response, attaining peak hardness in the first 10 h, followed by a pronounced decrease due to the coarsening and transformation of precipitates [218,219].

The maximum hardness achieved at 140 °C in the present study (142 HV) is comparable to that observed at higher temperatures (180 °C), but the time required to reach this peak-aged, is significantly longer. This difference is attributed to the aging temperature which changes the precipitation kinetics in Al-Cu alloys (Cu mobility) as well as the solubility limit of Cu in Al which increases with temperature. Artificial aging is usually performed at higher temperatures (>140 °C) to accelerate the kinetics and shorten the aging time.

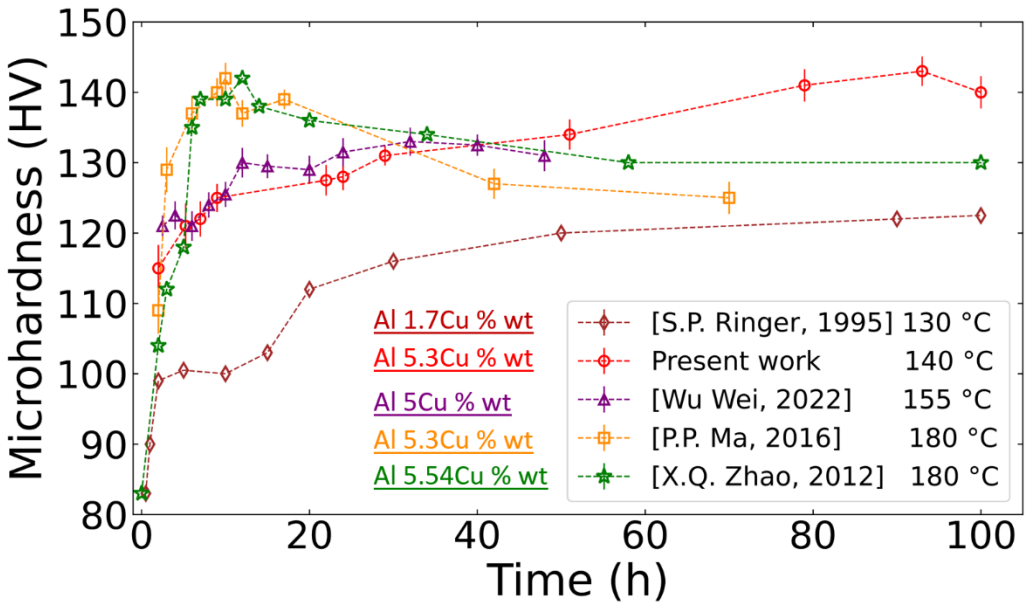


*Figure **IV-2:** Vickers micro-hardness (HV) as a function of isothermal aging time for Al-5Cu alloys of similar composition. Brown diamonds are Al-1.7Cu alloy aged at 130 °C (S.P. Ringer* [282]*). Red circles are the alloy investigated in the present work, aged at 140 °C. Purple triangles are Al-5Cu alloy aged at 155 °C (Wu Wei* [217]*). Orange squares and green stars are Al–5Cu alloy aged at 180 °C from P.P. Ma* [218] *and X.Q. Zhao* [219] *respectively.*

To investigate the influence of hydrogen on the age-hardening response, the samples were kept at room temperature for 5 hours after quenching in water. This interval corresponds to the time taken for hydrogen charging in NaOH (see chapter II for details). Thus, the same conditions (temperature, time) were applied to the uncharged samples to allow direct comparison of the hardening evolution in both conditions.

Figure **IV-3** compares the evolution of Vickers micro-hardness during aging at 140 °C for both hydrogen-charged (5 h in NaOH solution) and uncharged Al-5Cu sample. In the early stages of aging ($t \leq 10$ h), the hydrogen-charged sample exhibits significantly lower hardness. Then after 20 h both hardness curves are relatively similar, but surprisingly, a significant drop appears for the hydrogen-charged sample after 30 h. Then it increases and converges toward hardness values similar to that of the uncharged sample. Thus, the influence of hydrogen seems rather significant during the early to intermediate stages of precipitation (~ 5 h to 30 h), but then becomes negligible for longer aging duration.

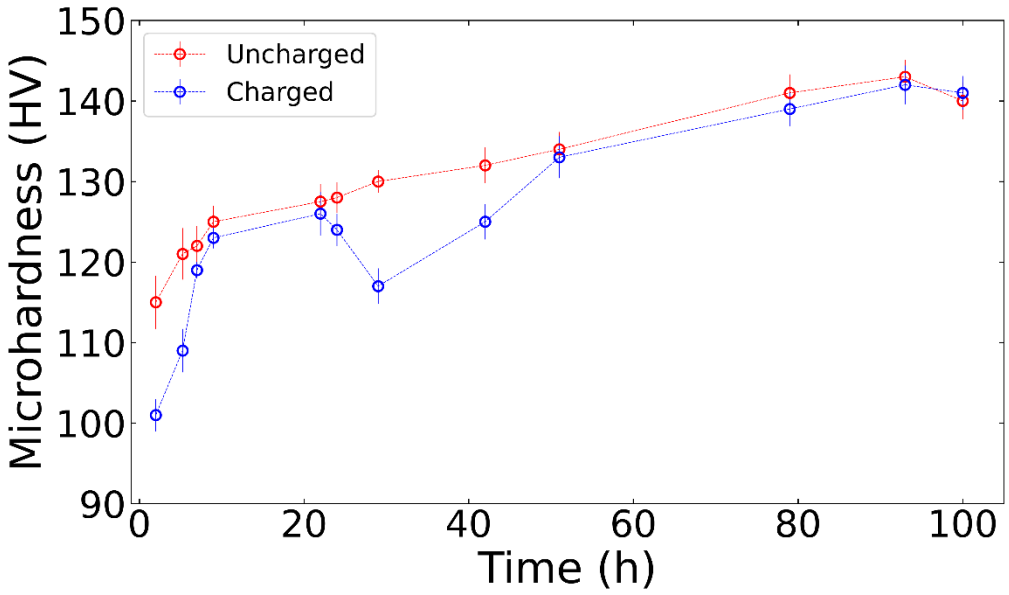


*Figure **IV-3:** Vickers microhardness as a function of aging time at 140°C for Al-5Cu alloy. Uncharged samples are displayed as red circles, while hydrogen-charged samples are blue circles.*

The initial delay in hardness increase observed for the charged sample, is consistent with earlier studies of Hachet *et al.* [64] who have shown that hydrogen affects the growth of GP zones during natural aging (see Chapter 1). The drop after 20 h of aging may indicate that hydrogen may also affect part of the precipitates sequence (GP-to-θ″ and/or θ″-to-θ′ transitions).

TDS analyses were carried out to quantify the amount of hydrogen trapped in the alloy and the influence of precipitates.

3. Measurement of hydrogen concentration

TDS spectra were acquired for two as-quenched samples, an uncharged reference sample and a sample charged in 0.1 M NaOH solution for 5 hours at room temperature (Figure **IV-4**). The uncharged sample was also maintained at room temperature for the same duration to ensure equivalent thermal and time history.

As expected, the hydrogen signal is significantly higher for the charged sample (Figure **IV-4**). The total amount of trapped hydrogen was estimated by integrating the desorption curves for each sample, and an average hydrogen concentration was calculated based on three independent measurements for each condition (charged and uncharged). As summarized in Figure **IV-5**, 7 ± 1.2 wppm of hydrogen was detected for the charged sample, against 1.8 ± 0.8 wppm for the

uncharged sample. The hydrogen concentration of about 5wppm detected after charging is lower than that reported in other studies (see Table **I.4**).

Experimental desorption curves (black lines) were adjusted with four Gaussian contributions, corresponding to different hydrogen trapping sites for both samples. For the uncharged sample (Figure **IV-4**a), the hydrogen signal is low and composed of four desorption peaks centered approximately at 200 °C, 330 °C, 500 °C, and 620 °C, with the most intense peak located at high temperature (peak 4). The signal could also be adjusted with four Gaussian contributions for the charged samples (Figure **IV-4**b), with a small shift of desorption peaks to lower temperature. This shift to lower values in charged samples may be first due to the accuracy of the temperature measurements. Second, it can attributed to the higher initial hydrogen concentration, that can promote faster release from reversible traps and reduce the activation energy for de-trapping [283,284].

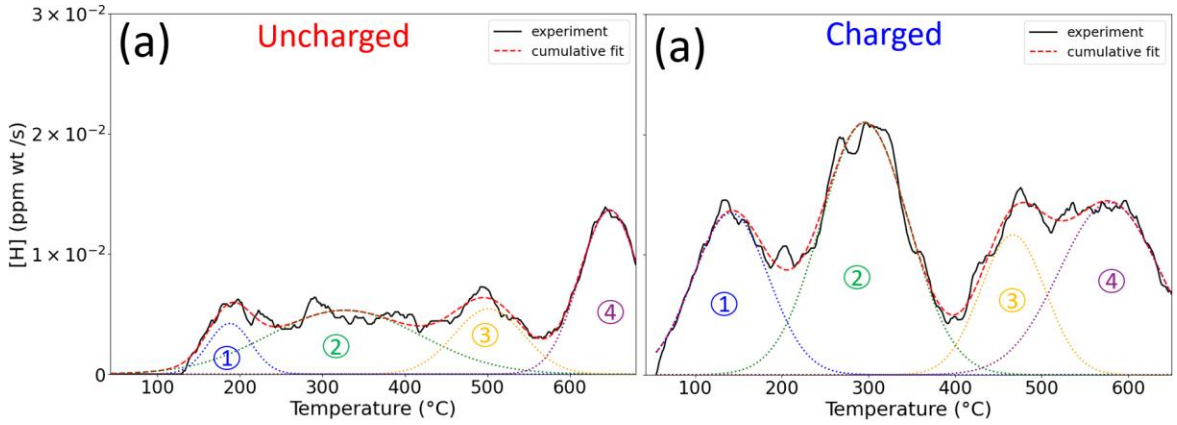


*Figure **IV-4**: TDS spectra showing the hydrogen desorption rate as a function of temperature for (a) uncharged and (b) hydrogen-charged Al-5Cu samples. The black curves represent the experimental data, while the red dashed lines correspond to the cumulative Gaussian fit.*

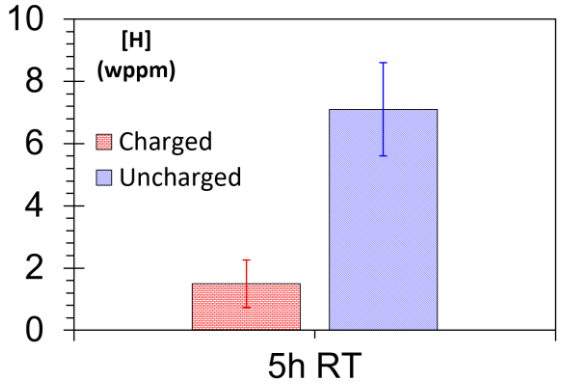


*Figure **IV-5**: Total hydrogen concentration in wtppm for charged (blue) and uncharged (red) sample.*

TDS measurements were carried out for two other samples, to evaluate if hydrogen remains trapped in the microstructure during thermal aging at 140°C. one charged with hydrogen and then aged for 24 h at 140°C, and the other having undergone the same aging treatment without prior hydrogen charging (Figure **IV-6**).

The results clearly show that a higher hydrogen concentration is detected in the charged sample, thus indicating that even after 24 h at 140 °C, some hydrogen remains trapped in the material.

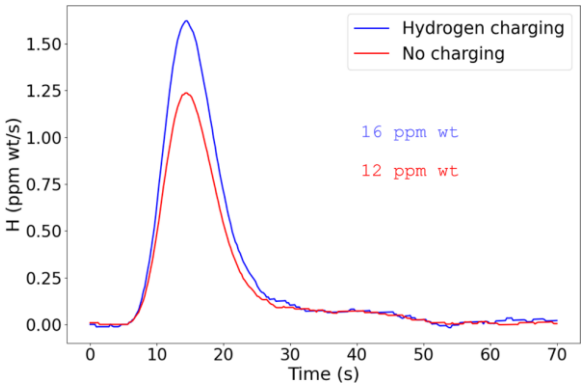


*Figure **IV-6**: TDS spectra as a function of time, for Al-5Cu alloy aged at 140 °C during 24 h. one previously charged with hydrogen (blue curve) and the other uncharged (red curve).*

To clarify the influence of this hydrogen on precipitation hardening, detailed TEM observations were subsequently carried out.

4. Microstructural Characterization

4.1. As-quenched state

The microstructure of the alloy after 5 h of natural aging, which is the initial state for artificial aging, was investigated using TEM. The time between sample preparation and TEM observation was approximately 15 minutes, and any microstructural changes during this period was considered negligible. Besides, two successive TEM observations performed on the same foil on day 1 and day 7, revealed no significant changes (see Appendix 4), indicating that natural aging is stopped in the thin area observed by TEM because of the fast annihilation of vacancies at the surface.

As shown in Figure **IV-7**, low-magnification images reveal few straight and helical dislocations. Dislocations density is typically low after homogenization treatment, but some of them could have been introduced during sample preparation, particularly during mechanical

polishing. Helical dislocations may also result from the annihilation of supersaturated vacancies following quenching as previously reported [285].

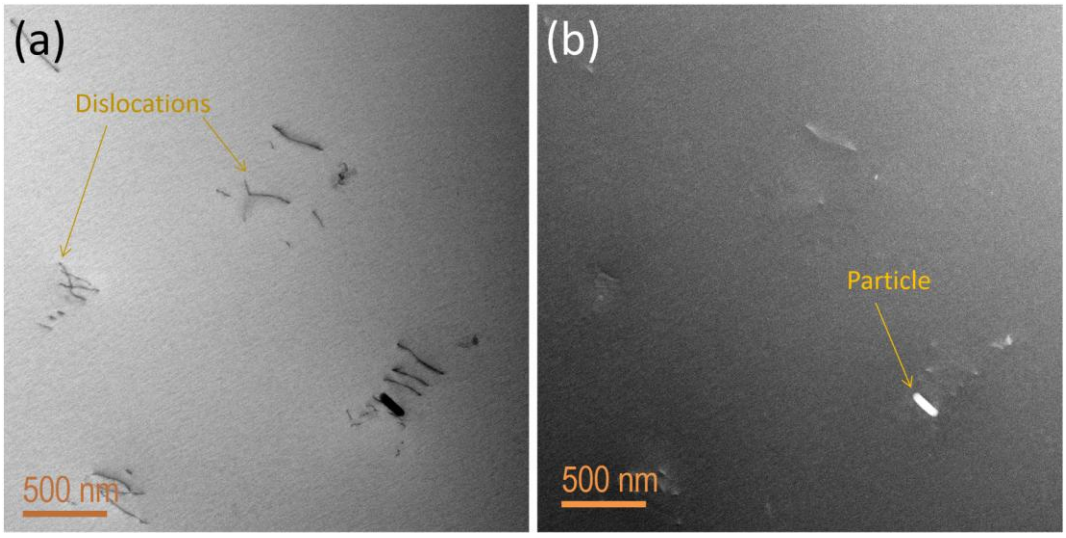


*Figure **IV-7:** (a) Bright-field and (b) HAADF STEM micrographs of the Al-5Cu alloy after solution treatment and 5 h naturel aging. Yellow arrows highlight several isolated dislocations in (a) and a rod-shaped particle in (b).*

Rod-shaped particles (size of about 250 nm) also appear on the HAADF STEM image (Figure **IV-7**b). The EDS spectrum acquired from the particle (Figure **IV-8**b,c) reveals the presence of significant Fe and Cu peaks. Data quantification gives a chemical composition approximately matching the stoichiometry of Al_7FeCu_2 [286,287] (see Table **IV.1**). Instead, the matrix area (Figure **IV-8**c) is aluminium rich with 3 ± 1.5 at. % of Cu and trace of Si.

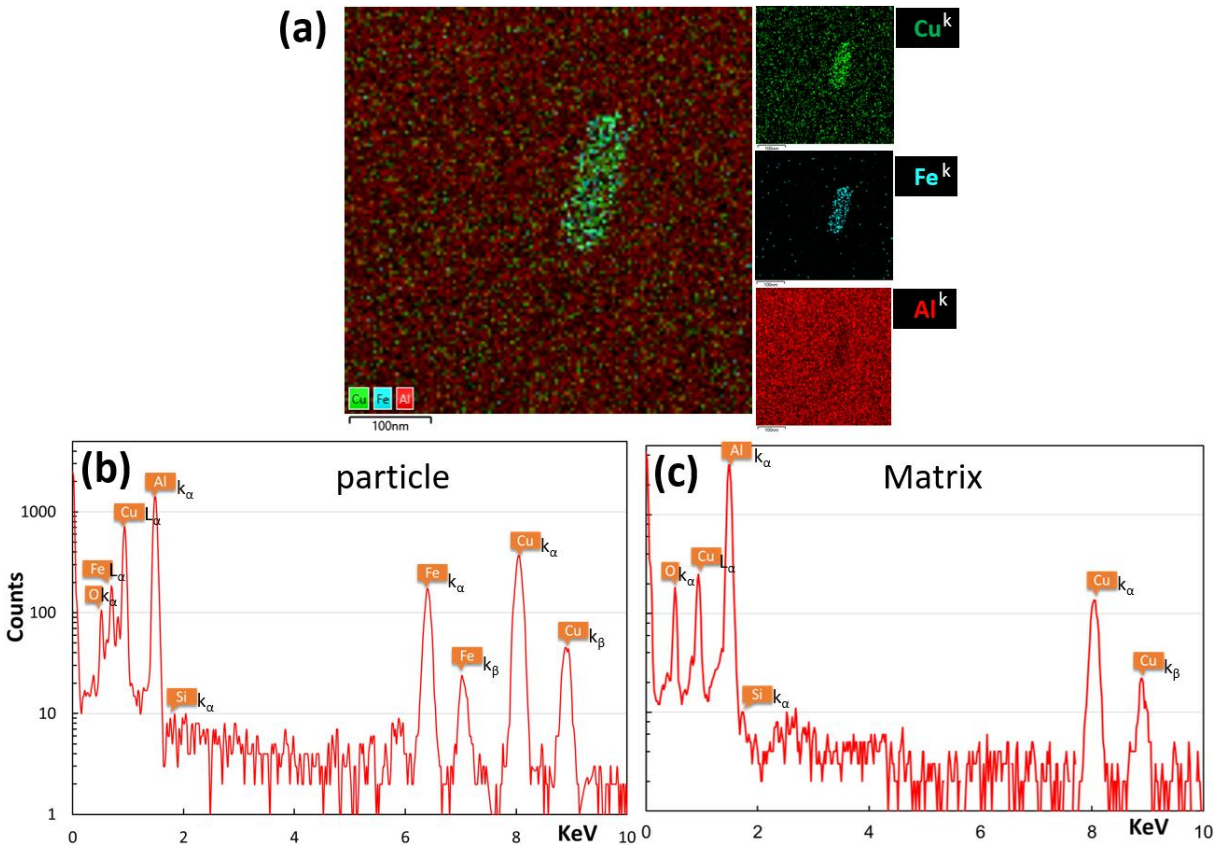


*Figure **IV-8:** EDS analysis of the rod-shaped particle. (a) EDS elemental mapping showing the distribution of Cu (green), Fe (blue), and Al (red). (b) and (c) are EDS spectrum acquired from the rod-shaped particle and Al matrix respectively.*

*Table **IV.1:** Quantitative EDS analysis (in at. %) of the particle of Figure **IV-8**a and of the surrounding Al matrix.*

	Concentration at. %	
Element	**Intermetallic phase**	**Matrix**
Al	68.8 ± 3.5	97 ± 3
Cu	21.9 ± 2.1	3 ± 1.5
Fe	9 ±1.8	–
Si	0.2 ± 0.05	0.12 ± 0.05

Based on thermodynamic simulations using Thermo-Calc with the TTAL6 database (Figure **IV-9**), it appears that during homogenization at 540 °C, not all alloying elements are fully dissolved into solid solution. At this temperature, only about 3.7 wt.% of Cu is in solid solution, compared to the nominal composition of 5.3 wt.%. Similarly, Fe shows a very limited solubility of only 0.02 wt.%, far below its nominal concentration of 0.3 wt.%. In contrast, Si is fully dissolved in the solid solution under these conditions. This is consistent with the persistence of

intermetallic phases rich in Cu and Fe observed after homogenization treatment such as in Figure **IV-8**a.

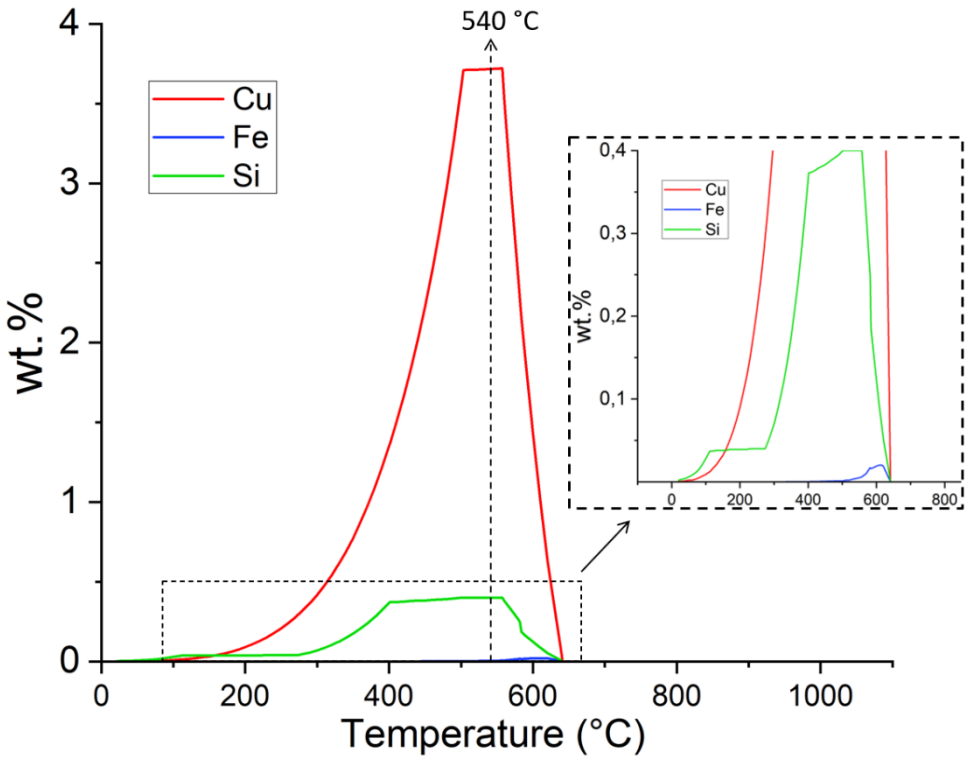


*Figure **IV-9**: Thermodynamic simulation of the equilibrium solubility of Cu, Fe, and Si in the FCC Al matrix as a function of temperature for the studied Al-5Cu alloy, performed using Thermo-Calc with the TTAL6 database.*

High-magnification STEM-HAADF images were also acquired in ⟨001⟩ zone axis. An example is shown in Figure **IV-10**, the microstructure appears homogeneous, with no visible GP zones or contrast variations.

However, Fast Fourier Transform (FFT) of the HAADF image (inset of Figure **IV-10**) shows distinct spots at the (110) positions, which are forbidden reflections in conventional diffraction patterns of (FCC) aluminium. Such reflections have been, however, already reported in FFTs of HRSTEM images [64,288] they were attributed to Cu-rich clusters that act as precursors to GP zone formation [64,118,119,288,289].

A mask was applied to the FFT image, selectively keeping the spots at the (110) positions (Figure **IV-11**a,b). An inverse FFT was then performed to reconstruct an image highlighting the spatial distribution of the corresponding signal (Figure **IV-11**c). Nanoscale clusters are exhibited, they might be copper-rich clusters, formed before the formation of GP zones

[64,118,119,288,289]. Their detection is only possible through this image filtering. As reported in previous studies [64,288], these clusters disappear as the GP zones begin to nucleate and grow.

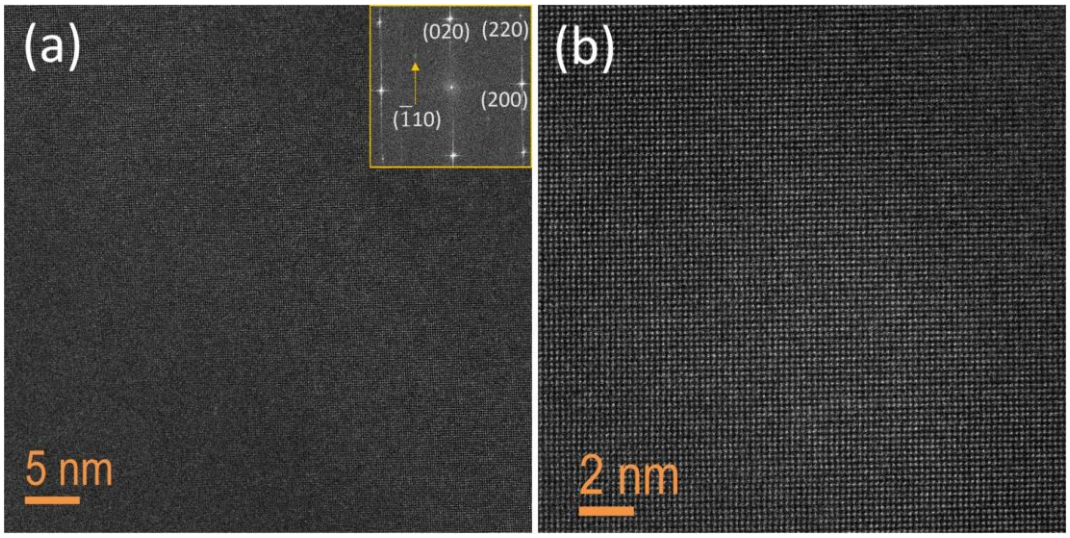


*Figure **IV-10:** (a) High-resolution HAADF image of the Al matrix. (b) High-magnification image showing the atomic arrangement of the structure. The inset shows the corresponding Fast FFT pattern. The sample are oriented in the ⟨001⟩ zone axis.*

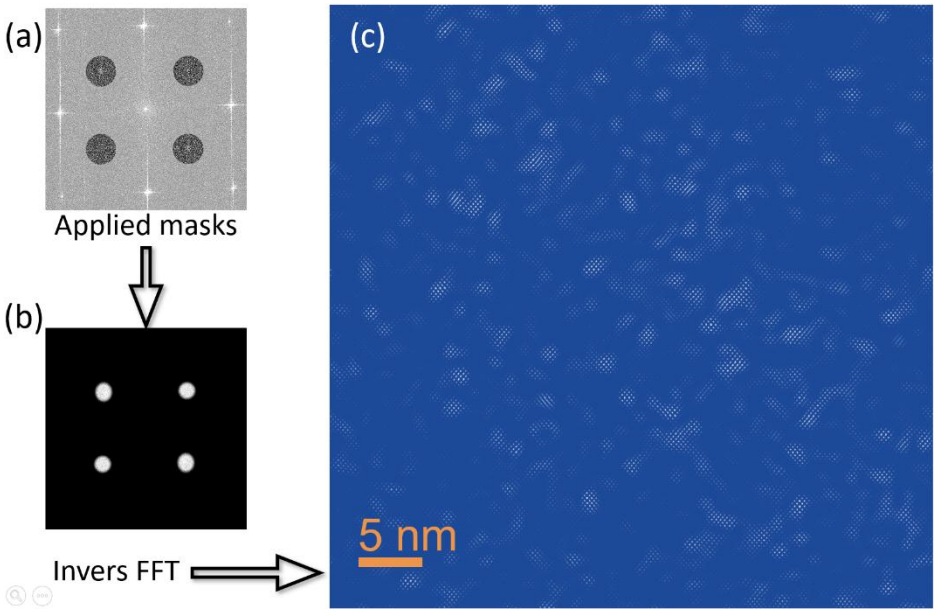


*Figure **IV-11:** (a) FFT image taken from the HAADF micrograph in Fig IV.5, where specific diffraction spots corresponding to the (110) reflections were selected using circular masks (b). (c) Inverse FFT reconstruction based on the masked spots, revealing in green regions with a strong (110) signal on FFT. A blue background is used in (c) to enhance contrast and improve the visibility of the green reflections.*

Lervik *et al* [288]. demonstrated that these clusters correspond to solute orderings on the FCC aluminium lattice and adopt Frank–Kasper σ-type structures. Such arrangements generate additional periodicities and structural modulations, which give rise to intensity at (110) positions. In contrast, Berlin *et al* [290] attributed the (110) reflections to in-plane GP zones. These GP zones introduce Cu atoms on specific (001) planes, breaking the extinction conditions of the FCC structure and allowing otherwise forbidden (110) reflections to appear due to incomplete destructive interference. However, under our conditions (5 h at room temperature), no GP zones are clearly observed.

4.2. Precipitation at 140 °C

The precipitation sequence and microstructural changes in the Al-5Cu alloy during aging at 140 °C was investigated using TEM. HAADF-STEM micrographs acquired along the ⟨110⟩ or ⟨001⟩ zone axis at different aging times are shown in Figure **IV-12**-16.

After 5 h of aging (Figure **IV-12**), homogeneously dispersed thin disks, typically corresponding to a single monolayer of Cu atoms on (001) planes are exhibited. When images are taken along the ⟨110⟩ zone axis, only one variant is visible (as discussed in Chapter II). High-magnification imaging confirms their shape and atomic-scale structure, consistent with previous reports on GP zones [17,64,291]. The average diameter measured was 8 ± 2 nm.

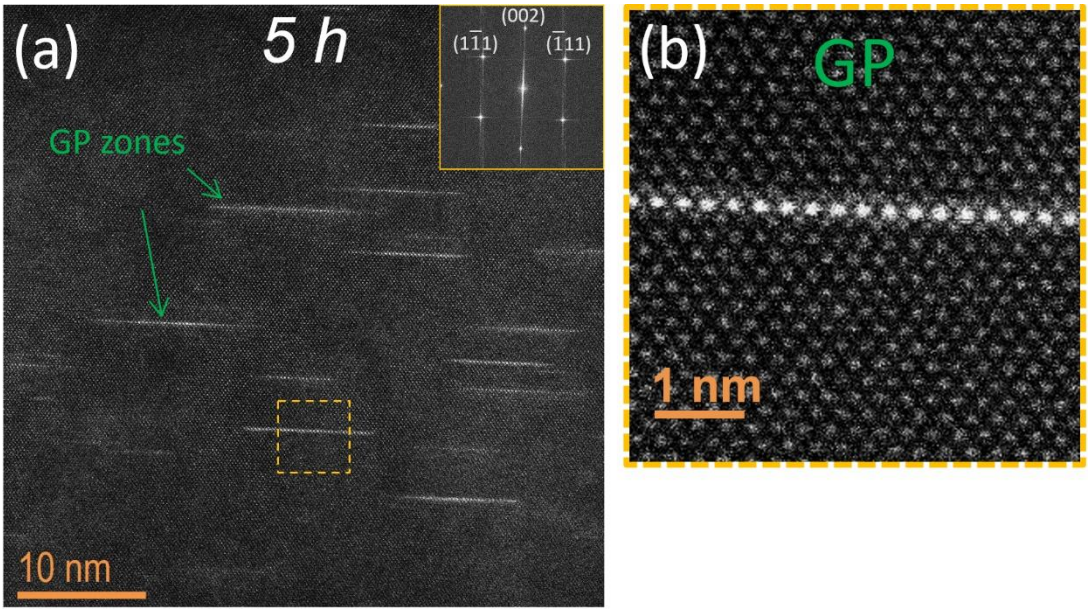


*Figure **IV-12:** (a) HAADF-STEM image taken along the ⟨110⟩ zone axis for Al-5Cu aged for 5 h at 140 °C, showing a uniform distribution of disk-shaped GP zones. The inset displays the corresponding FFT pattern. (b) High-magnification HAADF image of the area marked by the dashed box, revealing a single atomic layer of Cu consistent with monolayer GP zone.*

Extending the aging time up to 15 h (Figure **IV-13**), leads to the nucleation and growth of larger precipitates. These precipitates exhibit a sandwich structure with 2−3 monolayers of Cu atoms, separated by three $(002)_{Al}$ planes, corresponding to the typical θ″ structure [19,289,292,293]. At this stage, some GP zones are still present (average diameter 9 ± 2 nm), and θ″ precipitates are significantly larger (average diameter 12 ± 3 nm).

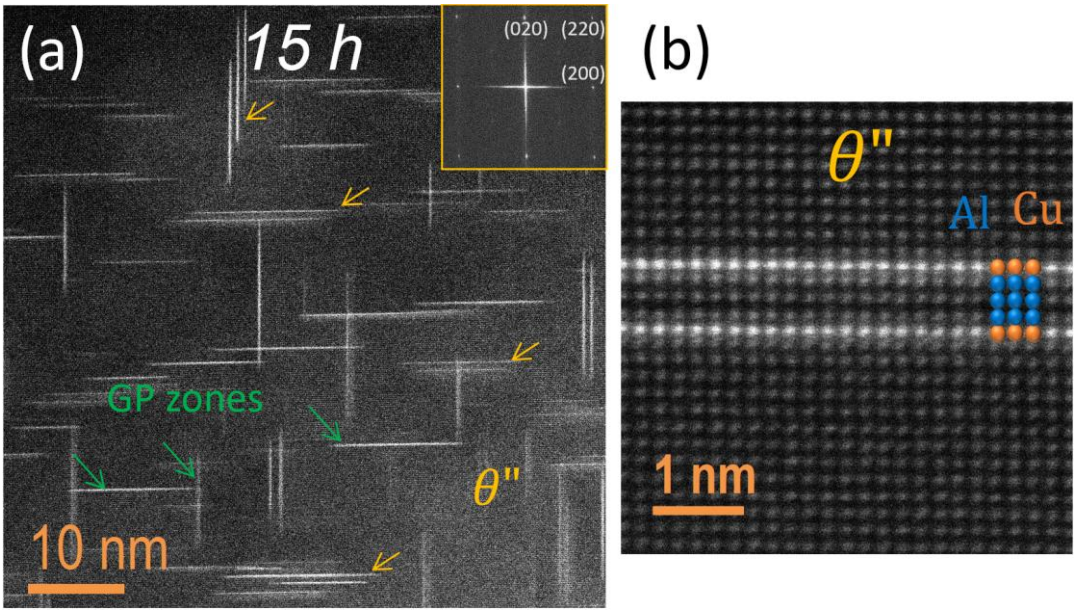


*Figure **IV-13:** (a) HAADF-STEM image taken along the ⟨001⟩ zone axis for the Al-5Cu aged 15 h at 140 °C, showing a coexisting distribution of GP zones and θ″ precipitates. The inset shows the corresponding FFT, confirming the crystallographic orientation. (b) High-magnification HAADF image of a single θ″ precipitate, revealing its typical morphology with stoichiometry Al_3Cu. Image (b) has been corrected for drift (see Appendix 5).*

After 30 h of aging (Figure **IV-14**), only GP zones and θ″ precipitates are also exhibited. Some growth occurred, the mean diameter of θ″ platelets increased to 13 ± 3 nm, and GP zones grew slightly to 9.5 ± 2.5 nm.

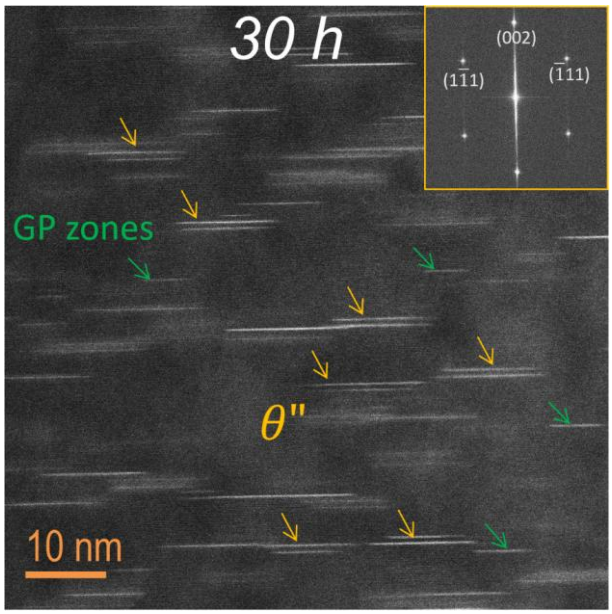


*Figure **IV-14:** HAADF-STEM image taken along the ⟨110⟩ zone axis for the Al-5Cu aged 15 h at 140 °C, showing the coexistence of GP zones (green arrows) and θ" precipitates (yellow arrows).*

After 100 h of aging (Figure **IV-15**), GP zones are no longer observed, indicating their complete transformation and/or dissolution. The microstructure is dominated by θ″ precipitates, some of which exhibit increased thickness with up to four monolayers of Cu, as shown in Figure **IV-15**b. Few θ′ precipitates are also identified (Figure **IV-16**). They exhibit a tetragonal structure with stoichiometry Al_2Cu. Figure **IV-16**b shows a nanoscale image of θ′. They are not homogeneously distributed but it is known that this phase typically nucleates at crystalline defects, in particular dislocations [289,294]. Due to their very low density, θ′ precipitates were not considered in following statistical measurements.

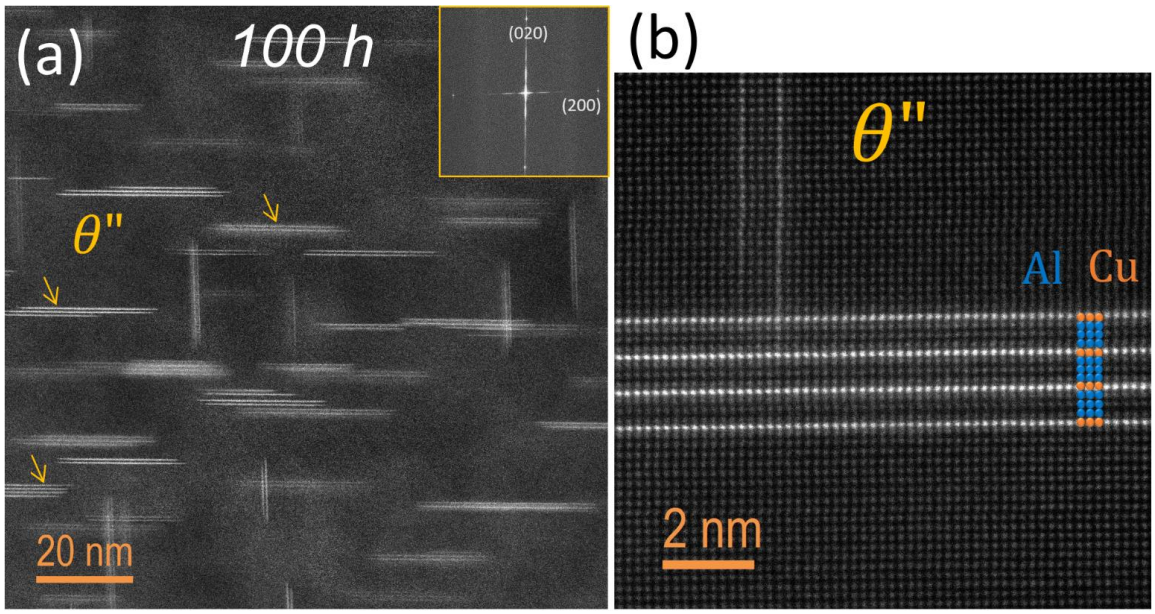


*Figure **IV-15:** (a) HAADF-STEM image along the ⟨001⟩ zone axis revealing a dense distribution of θ" precipitates, with no remaining GP zones after 100 h of aging at 140 °C. (b) High-magnification HAADF image of θ" precipitate showing its multi-layered atomic structure, composed of alternating Cu and Al atomic planes. A schematic overlay illustrates the typical stacking sequence of θ" precipitates.*

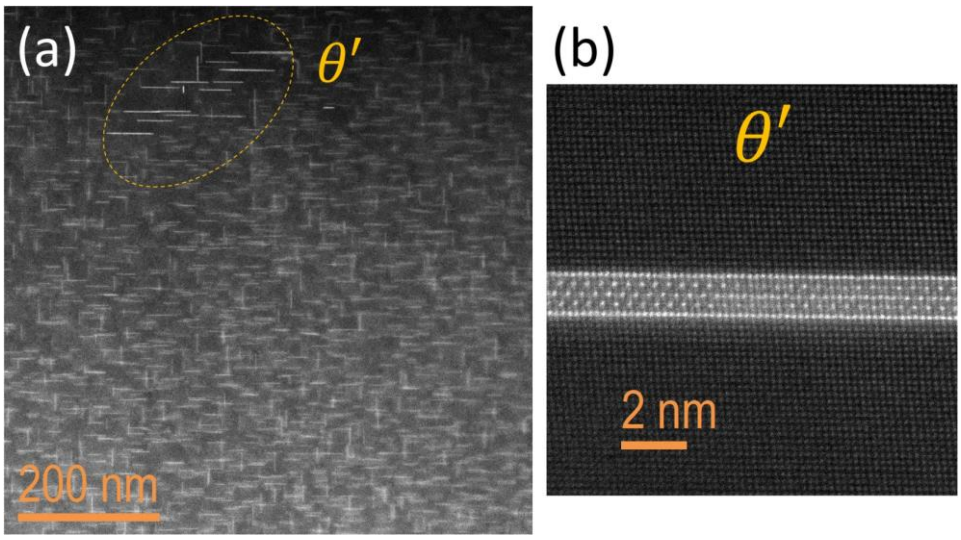


*Figure **IV-16:** (a) Low-magnification HAADF-STEM image (for the same sample presented in Fig IV.15) showing a region enriched in θ' precipitates, which are distinguished by their larger size compared to θ". (b) High-magnification HAADF image of this precipitate exhibiting a thicker morphology, characteristic of the semi-coherent Al_2Cu (θ') phase.*

To quantitatively assess the precipitation kinetics of GP zones and θ″, precipitate size distributions and corresponding number densities were measured and summarized in Figure

IV-17. Number densities were calculated considering the foil thickness that was estimated by EELS (see Chapter 2 for details).

After 5 h of aging, only the GP zones observed exhibited a relatively narrow size distribution, centered around 8 nm (Figure **IV-17**a), with a total number density of about 6.5×10^{-4} nm^{-3} (Table **IV.2**). After 15 h, their density decreases significantly down to 1.7×10^{-4} nm^{-3} (Table **IV.2**). At this stage, θ″ precipitates were also observed displaying a broader distribution toward larger diameters (Figure **IV-17**b), with a total number density of 8.9×10^{-5} nm^{-3} (Table **IV.2**).

Following 30 h of aging, both GP zones and θ″ precipitates coexist, but the number of θ″ increases and shifts toward larger sizes 20–25 nm (Figure **IV-17**c). The total number density of θ″ is about 1.25×10^{-4} nm^{-3}, while GP zones continue to decrease down to 1.1×10^{-4} nm^{-3}. After 100 h, GP zones have disappeared and the distribution is dominated by coarsened θ″ precipitate, with diameters up to ~ 40 nm (Figure **IV-17**d). The number density of θ″ begin to decrease, reaching 4×10^{-5} nm^{-3}, suggesting coarsening or transformation into more stable phase. At this stage the first appearance of θ′ precipitates were observed (Figure **IV-16**), but only occasionally and thus no statistical measurement could be done.

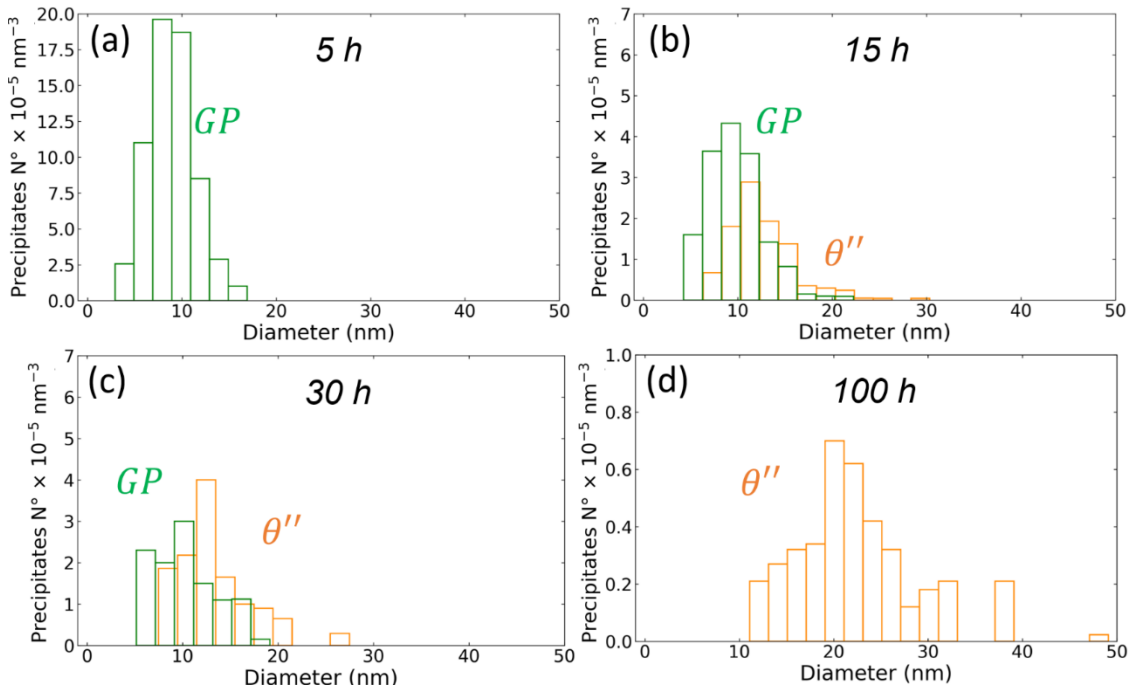


*Figure **IV-17:** Precipitates size histograms for GP zones (green) and θ″ (yellow) precipitates after (a) 5 h, (b) 15 h, (c) 30 h, and (d) 100 h of aging at 140 °C. Vertical axis is quantitative number density per unit volume.*

*Table **IV.2**: Number density measurements (N_p) of GP zones and θ″ precipitates in an Al–5Cu alloy aged at 140 °C for different aging times.*

Aging time (h)	**Precipitate**	***N_p (nm^{-3})*** measured
5	GP	$6.5 \pm 0.08\ 10^{-4}$
15	GP	$1.7 \pm 0.1\ 10^{-4}$
	θ″	$8.9 \pm 0.2\ 10^{-5}$
30	GP	$1.1 \pm 0.09\ 10^{-4}$
	θ″	$1.25 \pm 0.06\ 10^{-4}$
100	θ″	$4 \pm 0.4\ 10^{-5}$

Based on the measured values of precipitate size, thickness, and number density, the volume fraction of each precipitate was estimated by [289]:

$$f_v = \frac{N_p \pi d^2 t}{4} \qquad \text{IV-1}$$

Where N_p is the number density, d is the mean precipitate diameter, and t is the mean precipitate thickness. The variation in the volume fraction for each type of precipitate as a function of aging time is displayed in Figure **IV-18**.

These data show that the volume fraction of GP zones is maximal at early aging times and progressively decreases as θ″ becomes the dominant strengthening phase. The trends observed here are consistent with previously published works on the precipitation kinetics of Al-Cu [289].

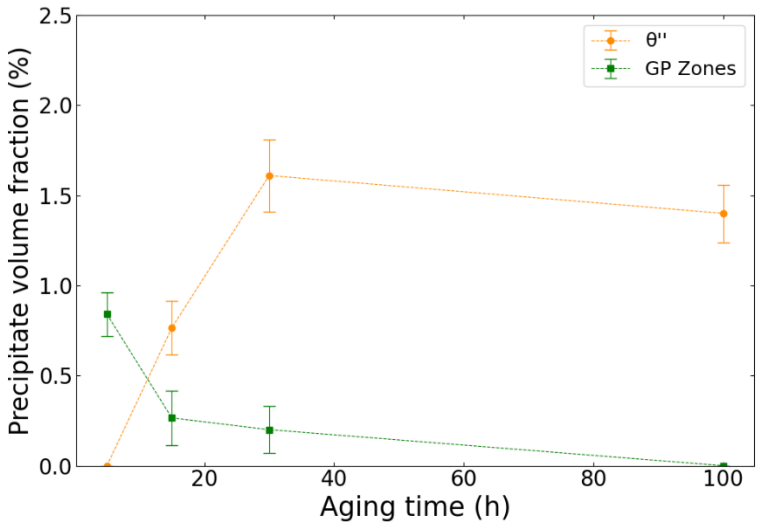


*Figure **IV-18:** The volume fraction of precipitates varies as a function of aging time at 140°C.*

4.3.Influence of hydrogen on precipitation sequence

This section compares the microstructural change, specifically the size and distribution of precipitates in hydrogen-charged and uncharged samples aged at 140 °C for 5, 15, 30 and 100 h. Data were collected by HAADF-STEM with images acquired along ⟨110⟩ and ⟨001⟩ zone axes (Figure **IV-19**a-d).

After 5 h, only GP zones are visible (Figure **IV-19**a) with a size similar to that of the uncharged sample, 7.2 ± 1.5 compared to 8.0 ± 2 for charged and uncharged sample respectively. After 15 h, θ″ precipitates began to grow and are uniformly distributed (Figure **IV-19**b), as observed in the uncharged sample. The mean diameter of both precipitate types (GP zones, θ″) was nearly identical under the two conditions, 8.5 ± 2.4 nm for GP zones and 11.8 ± 2.7 nm for θ″ in the charged sample, compared to 8.8 ± 2.2 nm and 11.7 ± 2.6 nm, respectively, in the uncharged sample.

After 30 h of aging, only GP zones and θ″ precipitates are also exhibited. The GP zones, however, had lengthened significantly, often adopting a “segmented-disc” morphology (Figure **IV-20**), this morphology was not observed in the uncharged sample. A similar segmented shape has previously been reported for θ′ precipitates during their growth [295]. After 100 h at 140 °C, only θ″ precipitates are exhibited (GP zones have completely disappeared). The mean diameter of θ″ is 17.7 ± 5.0 nm, which is similar to that of the uncharged sample (18.7 ± 4.4 nm). The emergence of a small number of θ′ precipitates was also noted for the charged sample as shown in Figure **IV-21**.

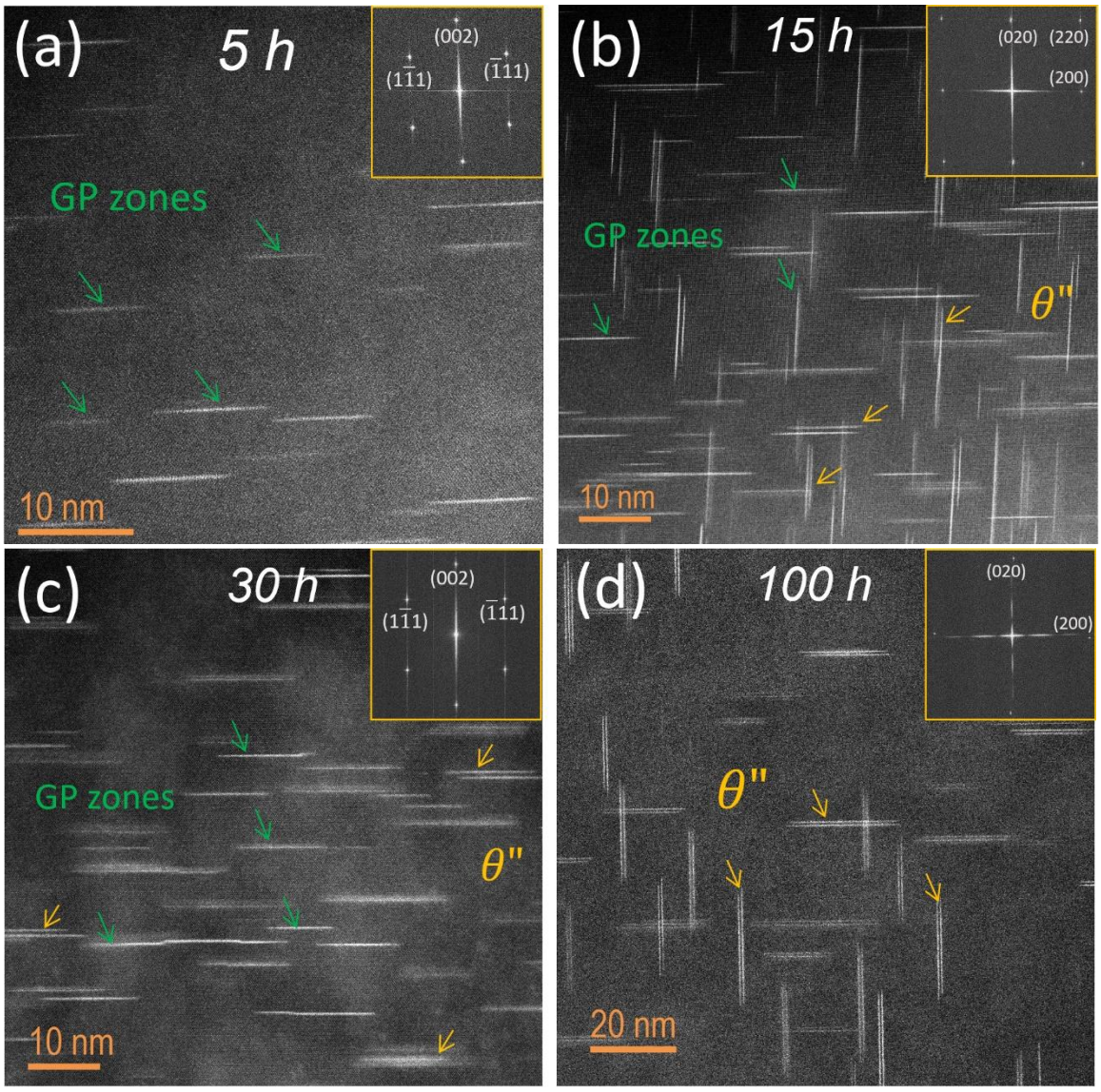


*Figure **IV-19:** HAADF-STEM micrographs of the hydrogen-charged Al-5Cu alloy aged at 140 °C for (a) 5 h, (b) 15 h, (c) 30 h, and (d) 100 h. Images (a) and (c) were acquired along the ⟨110⟩ zone axis, while (b) and (d) were taken along the ⟨100⟩ zone axis.*

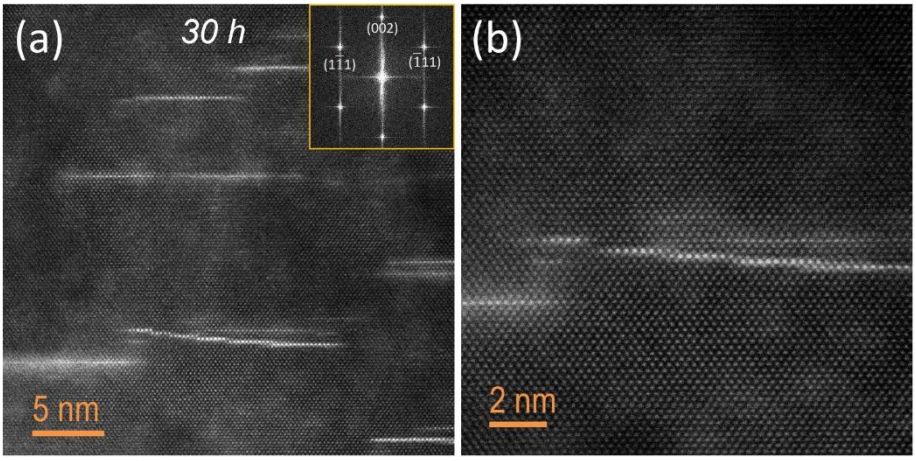


*Figure **IV-20:** (a) HAADF-STEM micrograph of the hydrogen-charged Al–5Cu alloy aged for 30 h (same sample as in Fig IV.14c). (b) High-magnification image highlighting the characteristic "segmented-disc" morphology of the GP zones.*

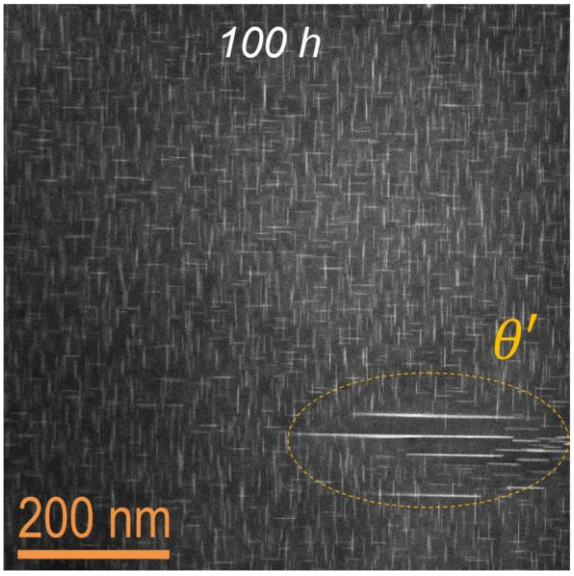


*Figure **IV-21:** Low-magnification HAADF-STEM image (for the same sample presented in Fig IV.19d) showing a region enriched in θ' precipitates.*

To assess the impact of hydrogen on precipitation kinetics and phase transformations, histograms of precipitate diameter distributions and their corresponding number density are compared in Figure **IV-22-25**.

At 5 h (Figure **IV-22**), GP zones size distributions are similar, but the charged sample contains ~30 % less GP zones. This indicates that hydrogen delays GP zones formation at 140 °C, as observed under natural ageing [64]. At 15 h (Figure **IV-23**), the diameter distributions of GP

zones and θ″ precipitates are relatively similar for both conditions, but the GP zones number density is now significantly higher in the charged sample. Thus, it seems that hydrogen may hinder the GP → θ″ transformation. After 30 h (Figure **IV-24**), the GP zone distribution in the charged sample becomes broader and skewed toward larger diameters (up to ~25 nm) and lower number density (5.2 10^{-5} compare to 1.1 10^{-4} nm^{-3} for charged and uncharged sample respectively). The diameter distributions of θ″ precipitates are similar for both conditions, but their number density is ~15 % lower for charged sample. The combination of oversized but fewer GP zones and a reduced θ″ density seems connected to the hardness drop measured after 30 h at 140 °C for the charged sample. After 100 h **(**Figure **IV-25),** the distributions of θ″ precipitates are similar, with mean diameters reaching 18–22 nm and comparable number densities.

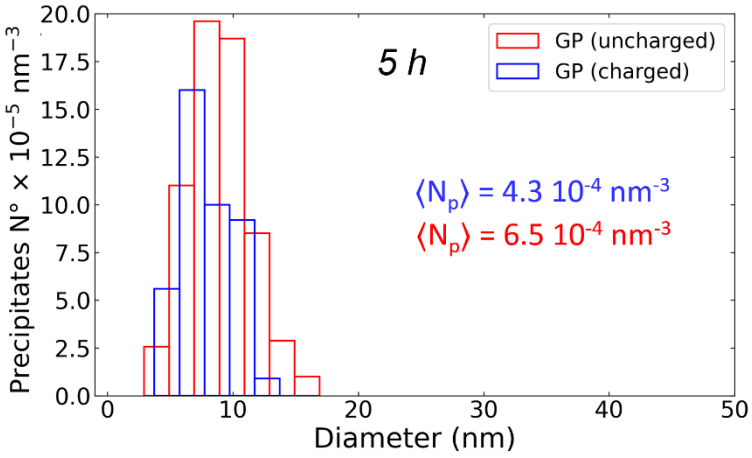


*Figure **IV-22:** Comparison of GP zone size distributions for the uncharged samples (red) and hydrogen-charged sample (blue), after 5 h aging at 140 °C.*

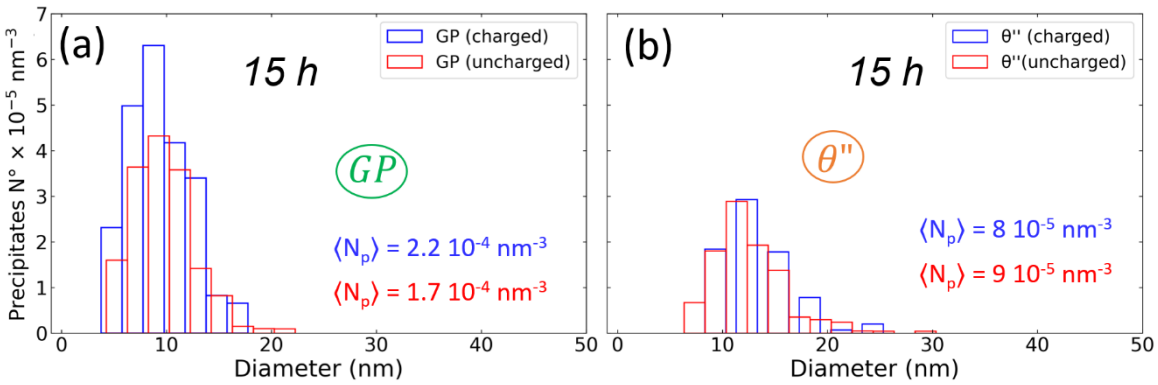


*Figure **IV-23:** Comparison of GP zone (a) and θ"(b) size distributions for the uncharged samples (red) and hydrogen-charged sample (blue), after 15 h aging at 140 °C.*

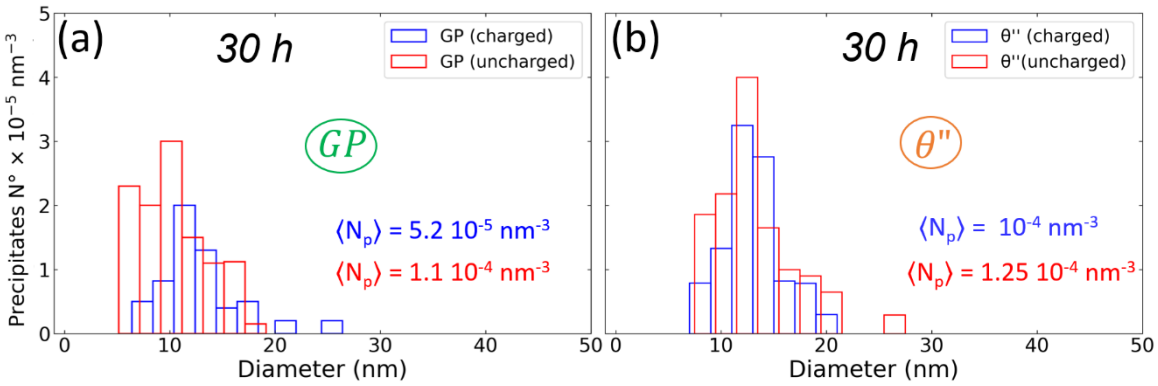


*Figure **IV-24:** Comparison of GP zone (a) and θ"(b) size distributions for the uncharged samples (red) and hydrogen-charged sample (blue), after 30 h aging at 140 °C.*

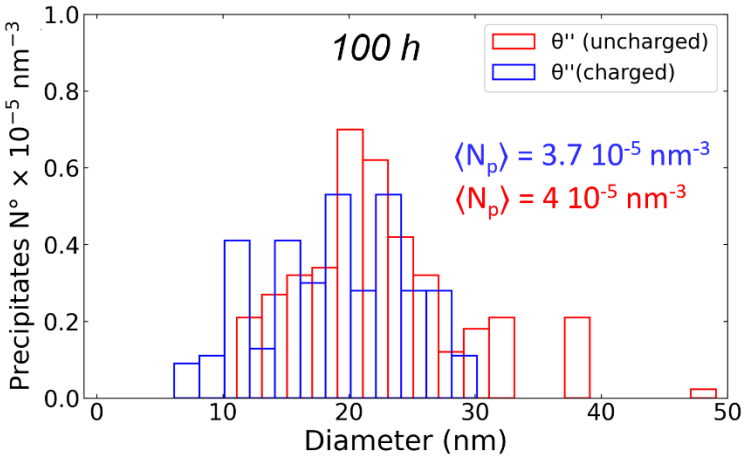


*Figure **IV-25:** Comparison of θ" size distributions for the uncharged samples (red) and hydrogen-charged sample (blue), after 100 h aging at 140 °C.*

5. Relationship between microstructure and hardness

5.1. Precipitate Strengthening Models

To correlate the microhardness to microstructural observations, theoretical models were employed to estimate the contribution of precipitation strengthening, based on the size, morphology and distribution of the precipitates formed at various aging times (5, 15, 30, and 100 h at 140 °C).

The strengthening effect results from several interconnected factors, the most important of which is the way dislocations interact with precipitates whether they cut through them (shearing mechanism) or bypass them (looping mechanism). When shearing dominates, dislocation must

overcome several barriers, the interfacial energy associated with creating new matrix–precipitate interface, the antiphase-boundary (APB) energy generated when the particle exhibits chemical order, coherency strains produced by lattice parameter mismatch and the elastic-modulus mismatch between the two phases. These contributions are classically described by Ardell *et al* [149]. and summarized by Nie & Muddle [296] (see more details in Chapter I). Beyond these mechanisms, the shape, size, distribution and orientation of the precipitates must also be taken into account. The situation becomes even more intricate when multiple types of obstacles coexists.

GP zones are coherent, extremely thin (one atomic layer) and have no ordered structure, the interaction between GP zones and moving dislocations is far more complex than can be described by classical models such as the Orowan looping or shearing approaches. As highlighted in atomistic simulations by Singh and Warner [297], the interaction mechanisms are highly variable and depend on size, orientation and proximity to the dislocation glide plane ranging from full looping, to shearing, or even mixed mechanisms involving partial looping.

Given this complexity, a phenomenological model is often employed to estimate the critical resolved shear stress associated with GP zones (τ_{GP}). This model assumes spherical precipitates, which does not strictly apply to GP zones, nevertheless, previous studies show that this simplification gives τ_{GP} values in good agreement with experimental measurements for GP zones [64,289,298].

This model distinguishes two strengthening regimes based on a critical precipitate radius of r_c = 5 nm [64,298]:

$$\tau_{GP} = \frac{1}{b}\sqrt{\frac{3\,f_v}{2\pi}}(0.72\mu b^2)\left(\frac{1}{r_c}\right)^{1.5}\left(\frac{d}{2}\right)^{0.5} \quad \text{if} \quad \frac{d}{2} < r_c = 5\ \text{nm} \qquad \text{IV-2}$$

$$\tau_{GP} = \frac{2}{d\,b}\sqrt{\frac{3\,f_v}{2\pi}}(0.72\mu b^2) \quad \text{if} \quad \frac{d}{2} > r_c = 5\ \text{nm} \qquad \text{IV-3}$$

Where b is Burgers-vector, μ is the shear modulus (equal to 0.286 nm and 25 GPa respectively [296]), f_v is the precipitate volume fraction and d is the mean diameter.

To estimate the potential strengthening provided by discs-shaped precipitates (*e.g.*, θ″ and θ′), the mechanism of dislocation–precipitate interaction (looping or shearing) must first be

identified. Most experimental studies agree that θ′ precipitates are non-shearable [159,282,289,299–301], whereas θ″ plates remain shearable until their diameter reaches around 40 nm (Santos-Güemes *et al* [302]) or 30 nm (Bellón *et al* [164]). Atomistic simulations by Krasnikov *et al* [303],further indicate a strong thickness effect, θ" precipitates should become non-shearable as their thickness exceeds three Cu atomic layers.

In our case, θ″ precipitates are therefore considered shearable, and are assumed to be bypassed only in the final stage of their growth (100 h of aging) when their transformation into θ′ begins. Because θ′ has just begun to form in our conditions and no sufficient statistical data are available, only GP zones and θ″ precipitates are considered in the evaluation of the strengthening.

For looping mechanism, the increase in critical resolved shear stress (τ_p) depends only on two geometric factors (diameter, thickness) and the space between the precipitates, which becomes the channels for dislocations to glide. Using the Orowan approach, Nie and Muddle [158,159] established the following model for the strengthening contribution of discs-shaped precipitates:

$$\tau_p = \frac{\mu b}{2\pi\sqrt{1-\nu}}\left(\frac{1}{0.931\sqrt{\frac{0.306\,\pi\,d\,t}{f_v}}-\frac{\pi d}{8}-0.061t}\right)\ln\left(\frac{1.225t}{b}\right) \qquad \text{IV-4}$$

where, ν is Poisson's ratio (ν =0.33, [296]), *t* is the precipitates thickness. This model has since been validated experimentally in several independent studies [289,301,304], showing excellent agreement with measured strength.

The strengthening contribution of shearable precipitates becomes more complex, since additional energy terms (interfacial energy, APB energy, elastic modulus mismatch and coherency strains) must be taken into account beyond geometry and inter-precipitate spacing. In the specific case of θ″ precipitates, long-range chemical order is absent. Selected-area diffraction and FFTs of HRTEM images (Figure **IV-14** and Figure **IV-19**c) display only fundamental FCC reflections with satellites from elastic strain induced by θ″ precipitates without additional spots, proving the absence of an ordered sub-lattice, no ordering energy needs to be overcame during shearing, Thus, APB energy can be neglected. The elastic-modulus mismatch between the θ″ precipitates and the Al matrix is small ($\Delta\mu/\mu \approx 0.05$ [304]), modulus strengthening is therefore minor.

By considering only geometric and interfacial contributions, Nie and Muddle (1998) [296] showed that the model quantitatively predicts the evolution of strength with precipitate density for shearable precipitates, and it was later used by Rodríguez-Veiga *et al* for Al-Cu alloy containing θ″ [289].

The predicted increment in critical resolved shear stress is:

$$\tau_{\theta''} = \frac{0.908d}{t^2}\left(\frac{2\pi b f_v}{\mu b^2 \ln\sqrt{\frac{d^2}{2b^2 f_v}}}\right)^{0.5} \gamma^{1.5} \qquad \text{IV-5}$$

Where γ is the interfacial energy, reflects the cost associated with creating a new interface as a dislocation shears through the precipitate. The value of γ was taken as 0.154 J/m² [289].

During the precipitation, the copper concentration in the aluminum matrix changes, which contributes to the alloy's mechanical response through solid solution strengthening. This contribution is commonly expressed as [64,289]:

$$\tau_{ss} = H X_{Cu}^{n} \qquad \text{IV-6}$$

where X_{Cu} is the mass fraction of Cu remaining in solid solution, the constants H and n are taken as 7.2 MPa and 1, respectively [164,305]. The value of X_{Cu} can be estimated for each aging condition by mass balance using the volume fraction of each precipitate (GP zones and θ″) and their corresponding atomic copper contents, assumed to be 100% for GP zones and 33% for θ″ (Al_3Cu) [289].

5.2. Calculated Strengthening Contributions

Table **IV.*3*** summarizes the values of precipitate dimensions (diameter, thickness) measured from HAADF micrographs, together with the corresponding number density d_p and volume fraction f_v at different ageing times. This dataset was used to estimate the individual strengthening contributions of the observed precipitates using the different models previously described.

*Table **IV.3:** Quantitative measurements of GP zones and θ" precipitates in an Al–Cu alloy aged at 140 °C for different aging times. d is the mean precipitate diameter, e is the mean precipitate thickness, X_{cu} is the copper content in solid solution (wt %), f_v and N_p are the precipitate volume fraction and number density respectively. Values are reported for both uncharged and hydrogen-charged specimens.*

Condition	Aging time (h)	Precipitate	*d* (nm) measured	*t* (nm) measured	f_v (%) calculated	N_p (nm^{-3}) measured	X_{cu} (wt. %)
Uncharged sample	5	GP	8±1.9	0.256	0.84 ±0.12	$6.5\pm0.08\ 10^{-4}$	1.08
	15	GP	8.8±2.2	0.256	0.265±0.15	$1.7\pm0.1\ 10^{-4}$	2.3
		θ″	11.7±2.6	0.8 ±0.07	0.765 ±0.16	$8.9\pm0.2\ 10^{-5}$	
	30	GP	9.5±2.5	0.256	0.2 ±0.13	$1.1\pm0.09\ 10^{-4}$	1.86
		θ″	12.8±2.7	1 ±0.15	1.61 ±0.2	$1.25\pm0.06\ 10^{-4}$	
	100	θ″	18.7±4.4	1.2 ±0.2	1.4 ±0.17	$4\pm0.4\ 10^{-5}$	2.6
Charged sample	5	GP	7.2±1.6	0.256	0.44 ±0.13	$4.3\pm0.07\ 10^{-4}$	2.37
	15	GP	8.5±2.4	0.256	0.32 ±0.1	$2.26\pm0.07\ 10^{-4}$	2.2
		θ″	11.8±2.7	0.8 ±0,08	0,7 ±15	$7.8\pm0.3\ 10^{-5}$	
	30	GP	11.8±2.8	0.256	0.15 ± 0.1	$5.2\pm0.15\ 10^{-5}$	2.32
		θ″	12.2±2.2	1 ±0.15	1,23 ±0.15	$1.04\pm0.08\ 10^{-4}$	
	100	θ″	17.7±5	1.22 ±0.3	1.17 ±0.2	$3.65\pm0.4\ 10^{-5}$	2.85

The total strengthening contribution from n different types of precipitates can be calculated as [306]:

$$\tau_p = \left\{ \sum_{i=1}^{n} [\tau_i^2] \right\}^{\frac{1}{2}} \qquad \text{IV-7}$$

The increment due to precipitation strengthening was then added to the solid-solution increment, yielding the total calculated strengthening ($\tau_p + \tau_{ss}$), which is plotted against aging time in Figure **IV-26**. The aim is to verify whether the hardness profiles observed for hydrogen-charged and non-charged samples follow a similar trend when the theoretical strengthening models are applied, and try to understand the reason for the hardness decrease at 30 h observed for the hydrogen-charged sample.

As shown in Figure **IV-26**, at 5 hours of aging, the applicable strengthening model for GP zones predicts a lower yield stress for the hydrogen-charged sample. This trend is consistent with the hardness measurements (Figure **IV-3**), confirming that the hardness reduction is primarily due

to a lower density of GP zones. At 15 hours, both charged and uncharged samples exhibit nearly identical strengthening values, which align well with the measured hardness at this stage (both conditions have similar hardness).

However, at 30 hours of aging, a significant decrease in the strengthening contribution ($\tau_p + \tau_{ss}$) is again observed for the hydrogen-charged sample. This observation is interesting, as it reflects the corresponding drop in measured hardness. This decrease can be attributed to the growth of GP zones, whose diameter appears larger in the charged condition, and to a lower number density of θ″ precipitates for charged sample compared to the uncharged sample. These features suggest a stabilizing effect of hydrogen on GP zones, delaying the transformation to θ″. Overall, these results support the validity of the selected models, which reproduce the trends observed experimentally.

After 100 h of ageing, two strengthening models were considered, the first based on a shearing mechanism (interfacial strengthening), and the second on an Orowan looping mechanism. When the interfacial shear model is applied, the predicted strengthening contribution of τ_p and τ_{ss} decreases, which is not consistent with the hardness measurements. This discrepancy suggests that a shearing mechanism may no longer be effective at this stage. In contrast, the looping model yields a continuous increase in strengthening, in good agreement with the hardness data. This strongly suggests that just before the transformation of θ″ to θ′, the precipitates are predominantly bypassed by dislocations. Milligan *et al* [307] also demonstrated that, as the precipitates are transformed from θ″ to θ′, the dominant interaction mechanism between dislocations and precipitates changes from shearing to Orowan looping. Besides, for both charged and uncharged samples, the values of predicted strengthening are similar, as in the case of measured hardness.

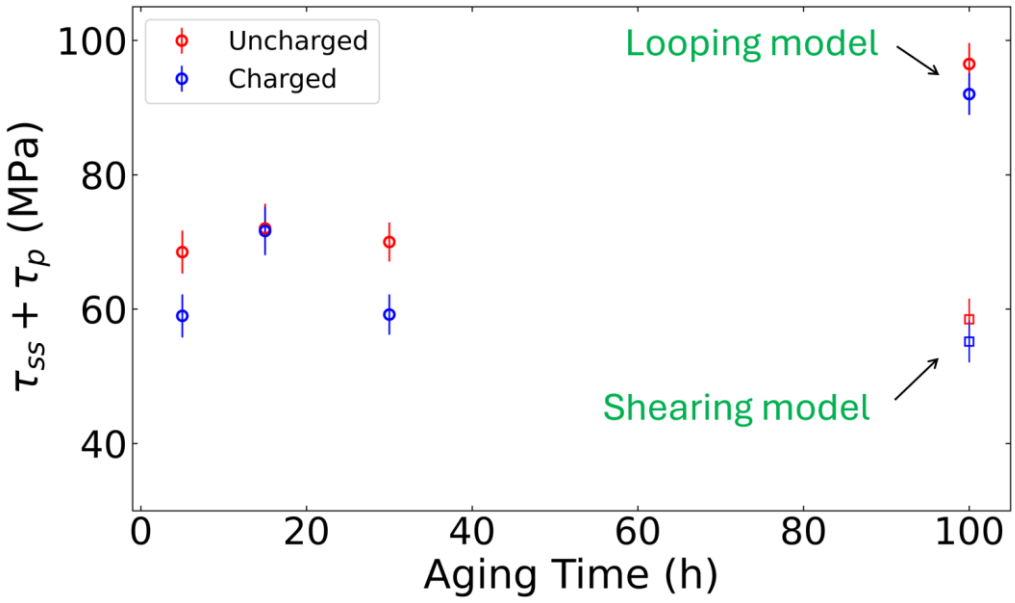


*Figure **IV-26:** Calculated sum of the solid-solution and precipitation contributions to the critical resolved shear stress ($\tau_p + \tau_{ss}$), as a function of ageing time for uncharged (red circles) and hydrogen-charged (blue circles) samples. At 100 h two limiting predictions are highlighted: the upper arrow corresponds to an Orowan looping model, whereas the lower arrow (blue and red squares) corresponds to an interfacial shearing model. Error bars are standard deviation propagated from the measurements of precipitate size, and volume fraction.*

5.3. Theoretical versus experimental hardness comparison

Microhardness is assumed to be related to the yield stress σ_y through the Tabor factor (T = 2.8) [308]. The yield stress is then linked to the stress required to initiate and move dislocations, i.e.: the critical resolved shear stress (CRSS) through a Taylor factor (M = 3.1) [289,309]:

$$CRSS = \frac{T}{M} HV = 0.915\ HV \qquad \text{IV-8}$$

The CRSS can be predicted from microstructural features by considering additive strengthening contributions, it is written as [289,310]:

$$CRSS = \tau_0 + \tau_d + \tau_{GB} + \tau_{ss} + \tau_p \qquad \text{IV-9}$$

where τ_0 is the lattice resistance, τ_d is the strain hardening (associated with the plastic strain developed under the indenter), and τ_{GB} is the contribution of the grain boundaries.

To determine the theoretical hardness, the terms τ_0, τ_d and τ_{GB} must be determined. These contributions are assumed to be constant over the aging conditions and are estimated using the initial supersaturated (quenched) reference state, for which precipitation hardening is negligible. Under this assumption:

$$\tau_0 + \tau_d + \tau_{GB} \approx CRSS_{init} - \tau_{ss} \qquad \text{IV-10}$$

where $CRSS_{init}$ is obtained from the hardness measured immediately after quenching using Eq IV-8.

Figure **IV-27** compares the time evolution of the experimental microhardness with the corresponding theoretical values for both uncharged and hydrogen-charged conditions. The results indicate that the model successfully captures the hardening kinetics, as well as the systematic softening observed after 30 h of aging in the presence of hydrogen. A discrepancy is observed at long aging times (100 h). This deviation may arise from limitations of the strengthening model under these conditions and from the simplifying assumptions adopted in the present approach.

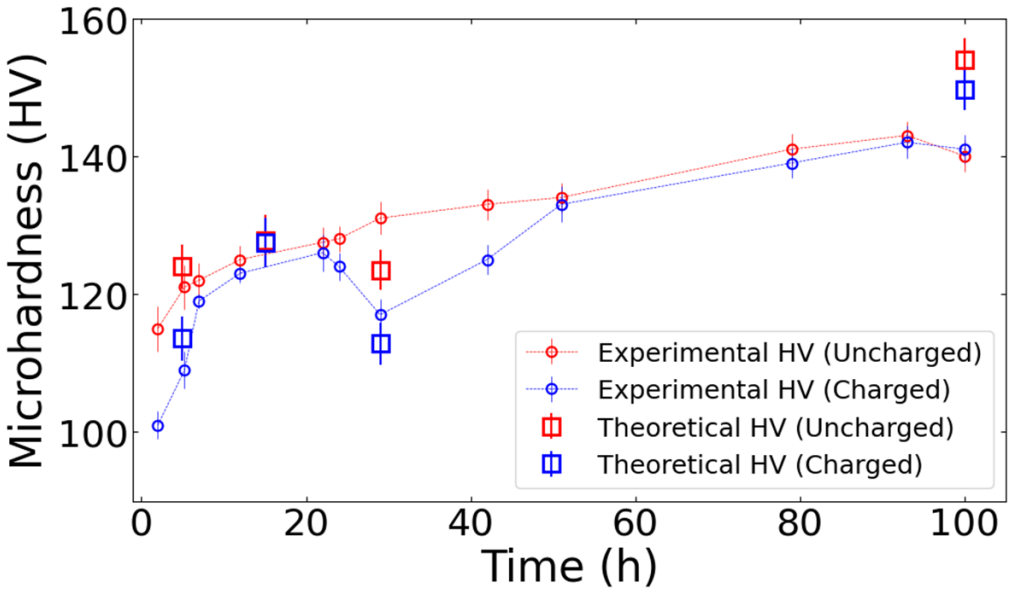


Figure IV-27: Evolution of Vickers microhardness with aging time for uncharged and charged samples. Open circles correspond to experimental measurements, while open square markers denote theoretical values.

6. Hydrogen Trapping and its Effect on GP zones Transformations

The hydrogen trapping ability of different microstructural features was investigated by TDS, in order to better understand the mechanisms behind the role of hydrogen in microstructural evolution. Two additional states were prepared; Natural aging for 168 h at room temperature (20 °C) to form predominantly GP zones. And Artificial aging for 24 h at 140 °C so that θ″ precipitates nucleate while some GP zones remain.

For each state, hydrogen charging was performed after aging, and the samples were compared with uncharged reference. The total hydrogen content was determined through the melt extraction method (Figure **IV-28**), and the distribution among trapping sites was obtained from the temperature ramping (Figure **IV-29**).

Under all aging conditions, the total amount of hydrogen differs significantly between charged and uncharged samples, as expected. The uncharged condition exhibits a lower signal than the charged one for each microstructure. The gap (uncharged − charged) is on the order of ~7.5 wppm for 168 h_20 °C sample and ~8 wppm for 24 h_140 °C sample**.**

Interestingly, for uncharged states, the structure contains GP zones (168 h_20 °C) exhibiting a high detected hydrogen signal. Similarly, for the sample aged 24 h, where θ″ precipitates are formed, an increase in detected hydrogen is also exhibited. This trend indicates that part of the signal depends on the microstructure rather than being solely due to the hydrogen introduced by charging. A possible explanation is that the enthalpy of transformations during heating (*e.g.*, dissolution/evolution of GP zones and θ″) may interfere with the measurements (see Chapter II).

Figure **IV-29** compares the different conditions with respect to the various contributions of trapping sites (the corresponding TDS spectra are presented in Appendix 6). For peaks 1 and 4, the trapped hydrogen in charged samples is almost similar across the three conditions (5 h_20 °C, 168 h_20 °C, 24 h_140 °C). However, for peak 2, there is more hydrogen in the state containing both GP zones and θ″ precipitates (24 h_140 °C), and for peak 3, the hydrogen amount is significantly higher in the state containing only GP zones (168 h_20 °C).

Peak 1 commonly corresponds to hydrogen located in interstitial sites (diffusible hydrogen) [183,311,312]. The second peak (lower-energy reversible traps) corresponds to traps associated with coherent precipitates and their elastic fields, as well as dislocations at the precipitate/matrix

interfaces [183,256,311]. The third peak (reversible traps) has been attributed to elastic fields and to low-angle grain boundaries (LAGBs), as reported by Mondou *et al* [311].

Considering the microstructure of our alloy particularly in the 168 h_20 °C sample where only GP zones are present as precipitates, it is assumed that Peak 3 is characteristic of hydrogen trapped at GP zones and their associated elastic fields. Peak 4 (irreversible traps) attributed to deep traps such as vacancies and dislocation cores [28,256]. Its magnitude is comparable across conditions for charged samples, suggesting that these deep defects are not strongly modified by the aging treatments.

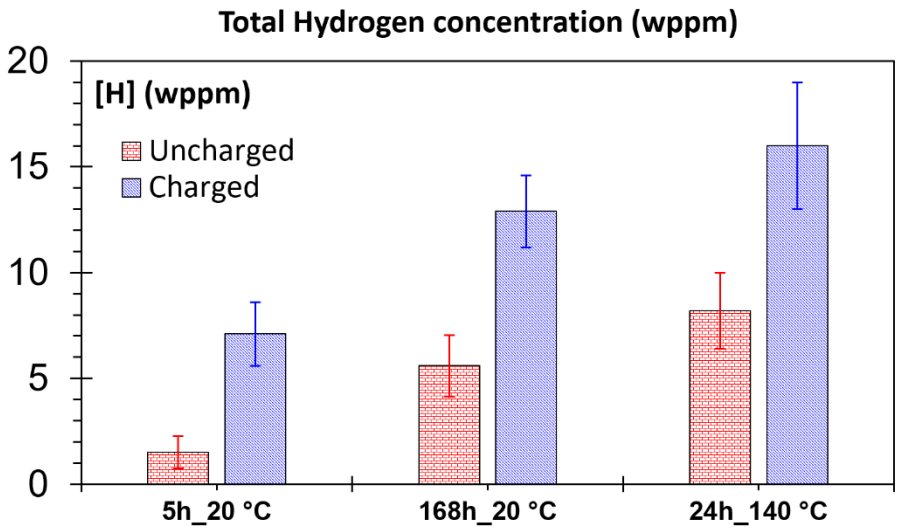


Figure IV-28: Total hydrogen concentration (wppm), measured by TDS. for samples aged 5 h at RT, 168 h at RT (GP zones), and 24 h at 140 °C (GP + θ"), comparing charged (blue) and uncharged (red) conditions.

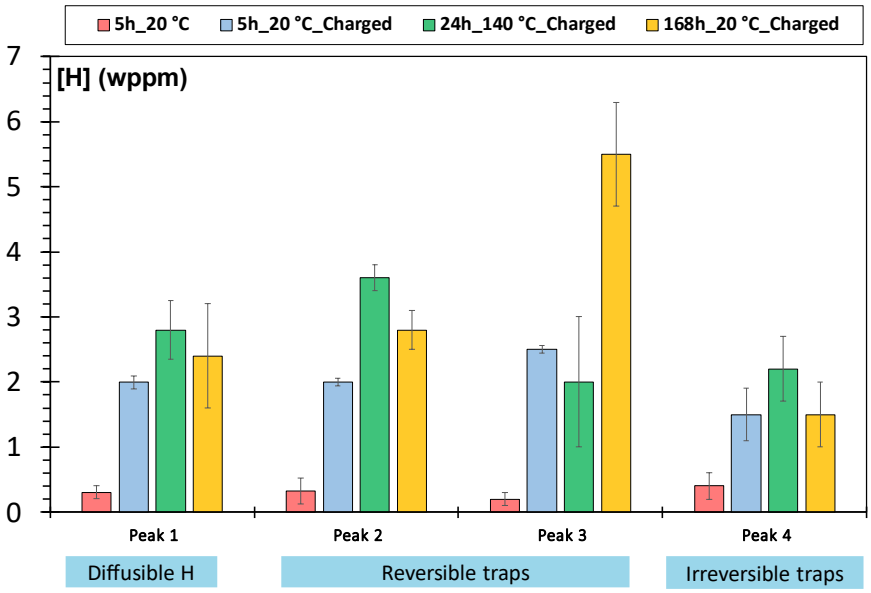


Figure IV-29: Distribution of hydrogen concentration between diffusible (peak 1), reversible (peak 2 & 3) and irreversible (peak 4) trapping sites, as determined from TDS spectra. Different colored bars represent: uncharged samples (red), charged samples (light blue), 24h TT+ charging (green), and 168h RT+ charging (yellow). (Corresponding TDS spectra in appendix 6).

Taken together, these results show that GP zones are highly efficient hydrogen traps (dominant Peak 3). When θ″ precipitates form**,** Peak 3 decreases while Peak 2 increases, indicating a redistribution of reversible traps from only GP zones to both θ″ and the remaining GP zones. Besides, the very high density of GP zones before their transformation to θ″ also plays a role in the trapping capacity.

The number of hydrogen atoms trapped per GP zone can be estimated (see Appendix 7). Peak 3 of the 168h_20 °C_charged sample indicates that about 4 wppm of hydrogen can be trapped in GP zones, corresponding to about one hydrogen atom per GP zone. The distortion of the matrix around GP zones (misfit) has been reported to be about 11.8 % [89] or 10 % as estimated by Zheng *et al* [313]. Saitoh *et al*.[89] demonstrated that, in Al-Cu alloy, this misfit generates a tensile stress field that acts as an effective hydrogen trap.

This behavior is consistent with TEM observations that link hydrogen to the GP → θ″ transformation pathway. The high ability of GP zones to trap hydrogen could explain the observed effect. Figure **IV-30** schematically illustrates the suggested mechanism. The interaction between hydrogen and vacancies decreases Cu mobility, as reported in Hachet's work [64]. This explains the delay in GP zone formation, which in turn results in a delay in the

hardness kinetics at the beginning of aging (Figure **IV-3**). After GP zones formation they trap a significant amount of hydrogen, as confirmed by TDS data. Consequently, hydrogen–GP zone interactions dominate over hydrogen–vacancy interactions, allowing Cu mobility to return to normal, and the hardness evolution overlaps for both charged and uncharged conditions.

After 30 h, a drop in hardness is observed for the charged sample, where the microstructure exhibits GP zones with large diameters and a lower number of θ″. This effect is attributed to hydrogen, which stabilizes the GP zones (stage II and III). The stabilizing effect may arise from different reasons. One possibility is a decrease in the free energy of the state containing GP zones, thus reducing the thermodynamic driving force for the subsequent GP → θ″ transformation. Another hypothesis is that hydrogen increases the energy barrier for θ″ nucleation.

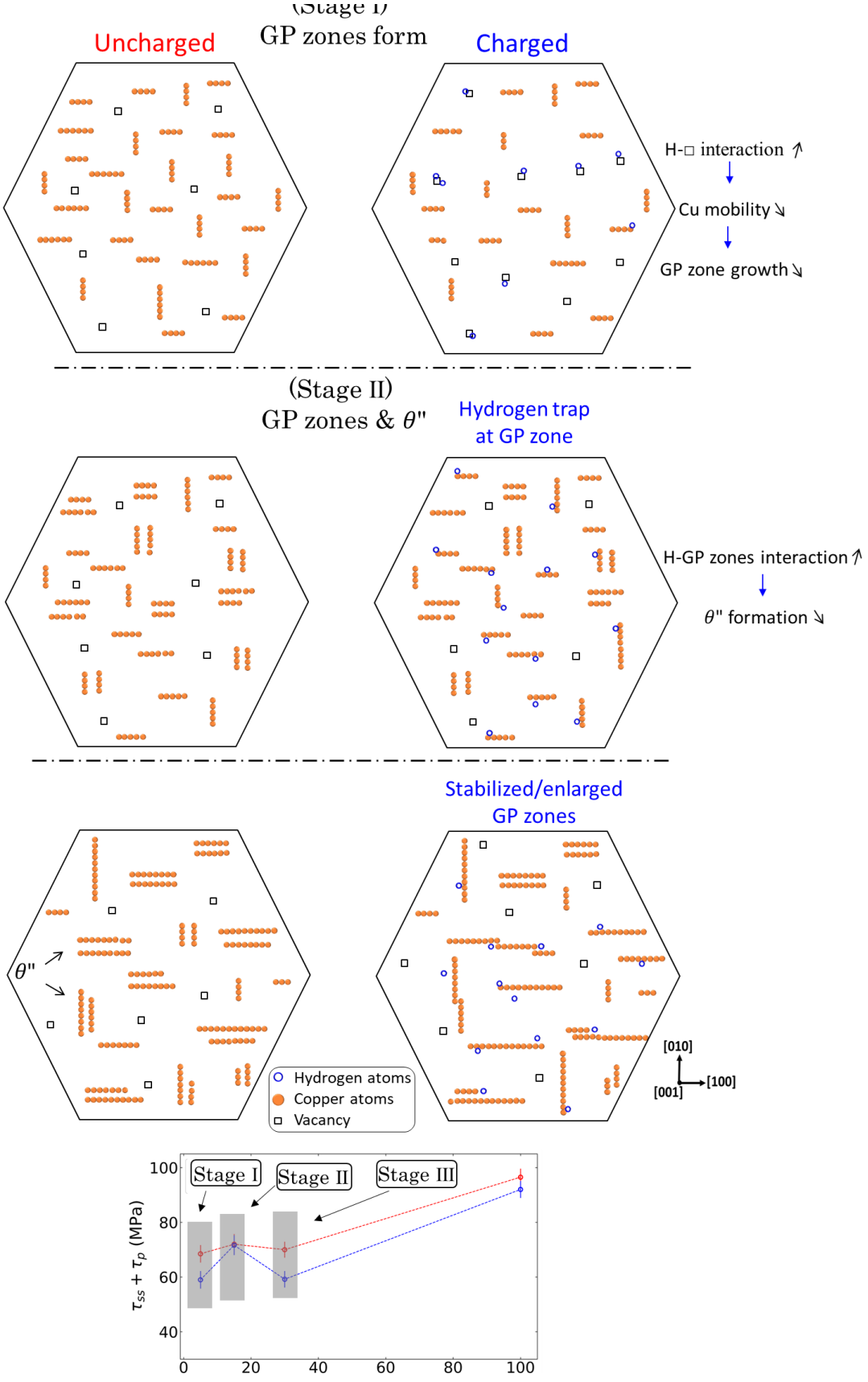


Figure IV-30: Schematic illustration of hydrogen trapping and its effect on the mechanism of GP zone evolution in the Al–5Cu alloy.

7. Influence of deformation and hydrogen on precipitation

Since plastic deformation induces the formation of numerous defects, most notably dislocations, which can act as effective hydrogen traps, it is expected that hydrogen–defect interactions may subsequently influence the precipitation behavior. In this section, we investigate the effect of deformation on precipitation and compare it with hydrogen-charged samples to assess the influence of hydrogen. Two hydrogen introduction methods are considered, pre-chemical charging and aging under a hydrogen atmosphere (10 MPa).

7.1. Microstructure characterization of the deformed Al-5Cu alloy

Figure **IV-31** displays the microstructure after 24 h of aging at 140 °C for a sample rolled to 5% thickness reduction. Some large precipitates (about 50 nm) are exhibited. The morphology and structure of these precipitates, highlighted in Figure **IV-31**d, correspond to the θ′ phase with the Al_2Cu stoichiometry. Besides, the LAADF-STEM image (Figure **IV-31**b) indicates that a large number of dislocations remain in the structure. As reported [19,294,307,314,315], they have promoted the nucleation of θ′ phase. Besides, homogeneously distributed θ″ and GP zones are also exhibited at this aging stage (Figure **IV-31**c). Then, since the structural evolution in pre-deformed samples is dominated mainly by θ′ nucleation and growth, we will mainly focus on these specific precipitates.

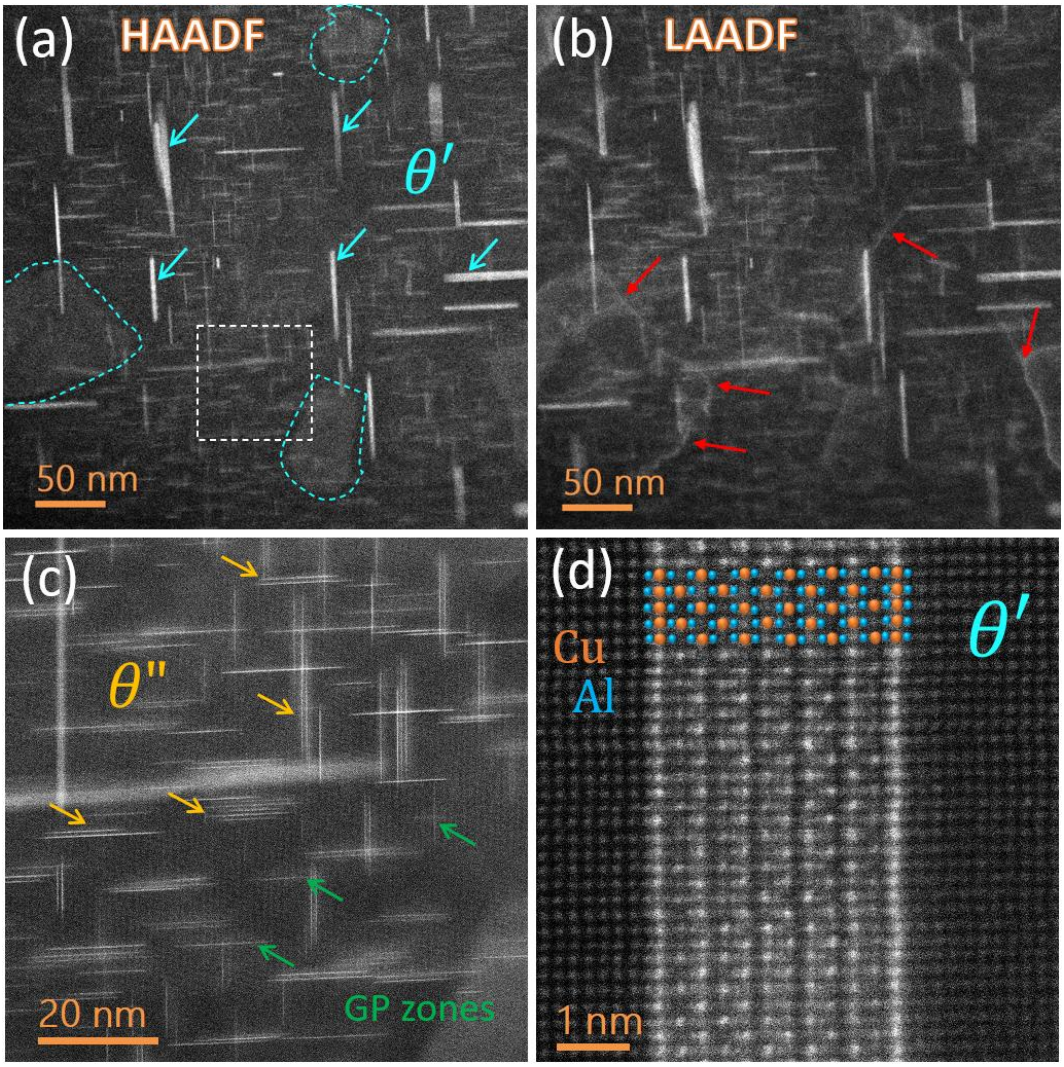


*Figure **IV-31**: (a) HAADF-STEM image of the pre-deformed Al-5Cu alloy (5 %) aged 24 h at 140 °C, showing θ' precipitates (indicated by blue arrows). The blue dashed lines highlight the third variant of θ'. (b) Corresponding LAADF-STEM image revealing the distribution of dislocations (marked by red arrows). (c) HAADF-STEM image of the area marked by the white dashed box in (a), showing the θ" precipitates (yellow arrows) and GP zones (green arrows). (d) High-magnification HAADF image of a single θ' precipitate, revealing its typical morphology with stoichiometry Al_2Cu. All images were acquired along the ⟨001⟩ zone axis.*

7.2.Influence of Hydrogen on Precipitation (chemical charging)

The samples were deformed by cold rolling to different thickness reduction levels after quenching, then either exposed to a 0.1 M NaOH solution for 5 hours for hydrogen charging, or left in air for the same duration. All samples were then subjected to an aging treatment at 140 °C for 24 hours. A comparison between hydrogen-charged and uncharged samples is shown in Figure **IV-32**, both subjected to 5% cold rolling, then aged at 140°C for 24 hours.

In both conditions, the microstructure contains the same types of precipitates (GP zones, θ″, and θ′). No significant change in their morphology or spatial distribution of these precipitates can be discerned. The corresponding selected-area electron diffraction (SAED) patterns (right-hand panels) support this observation, exhibiting identical superlattice reflections from θ′ and θ″ and diffuse streaking attributed to GP zones.

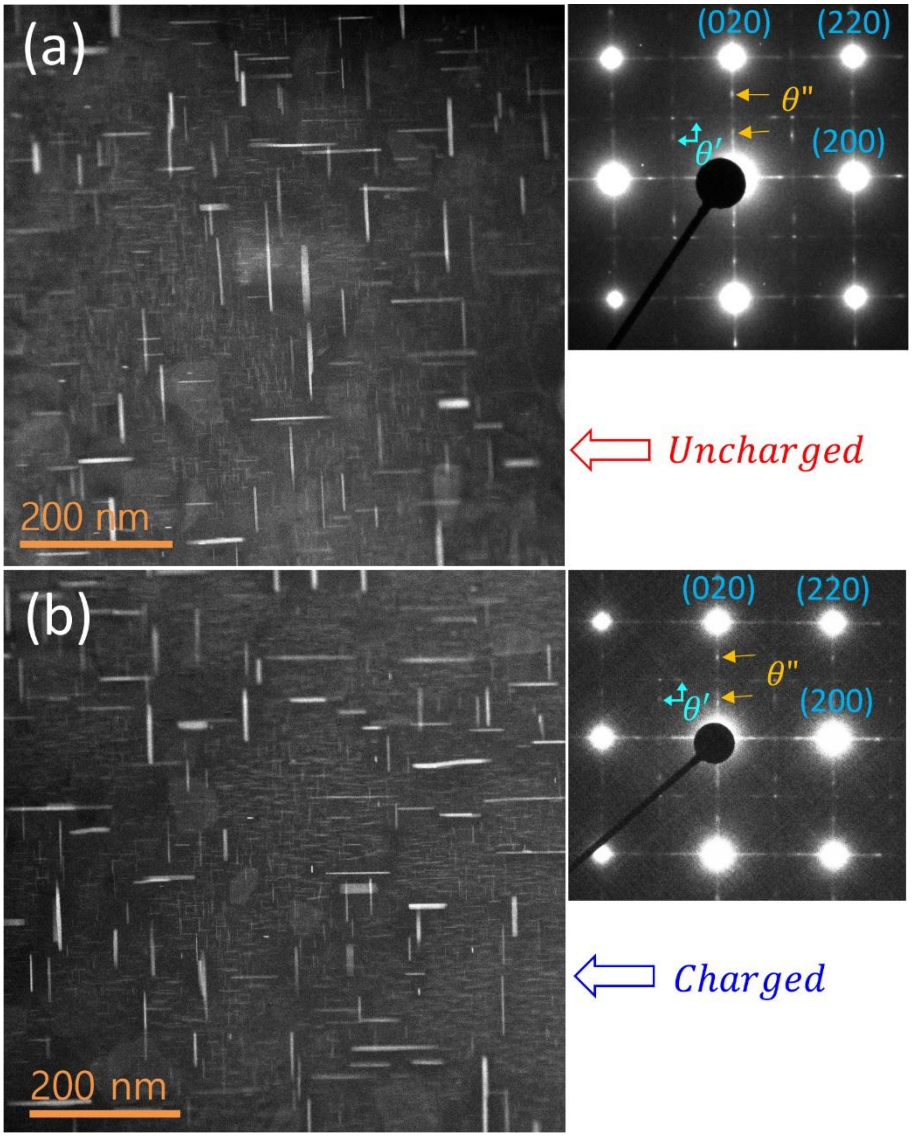


*Figure **IV-32**: HAADF-STEM image of the pre-deformed Al-5Cu alloy (5 %) aged 24 h at 140 °C, (a) is the uncharged sample and (b) is the hydrogen-charged sample. Insets show the corresponding SAED patterns acquired along the [001] zone axis, revealing superlattice reflections associated with θ" and θ' precipitates, as well as diffuse streaking attributed to GP zones.*

Size distributions and number densities were evaluated to compare θ′ diameter and thickness distribution (Figure **IV-33**) of the charged and uncharged samples, overlap almost perfectly.

The mean number density ($4.0 \pm 1 \times 10^{-6}$ nm^{-3}) in the charged sample is similar to that of the uncharged sample ($3.8 \pm 1 \times 10^{-6}$ nm^{-3}). Likewise, the mean equivalent diameter is 72 ± 20 nm compared with 60 ± 17 nm and the mean thickness is 4.2 ± 2.3 nm compared with 3.8 ± 2.0 nm, for the charged and uncharged sample, respectively. This indicates that neither the size nor the number density of θ′ precipitates is affected by hydrogen charging, thus implying that precipitation sequence and kinetics remain unchanged.

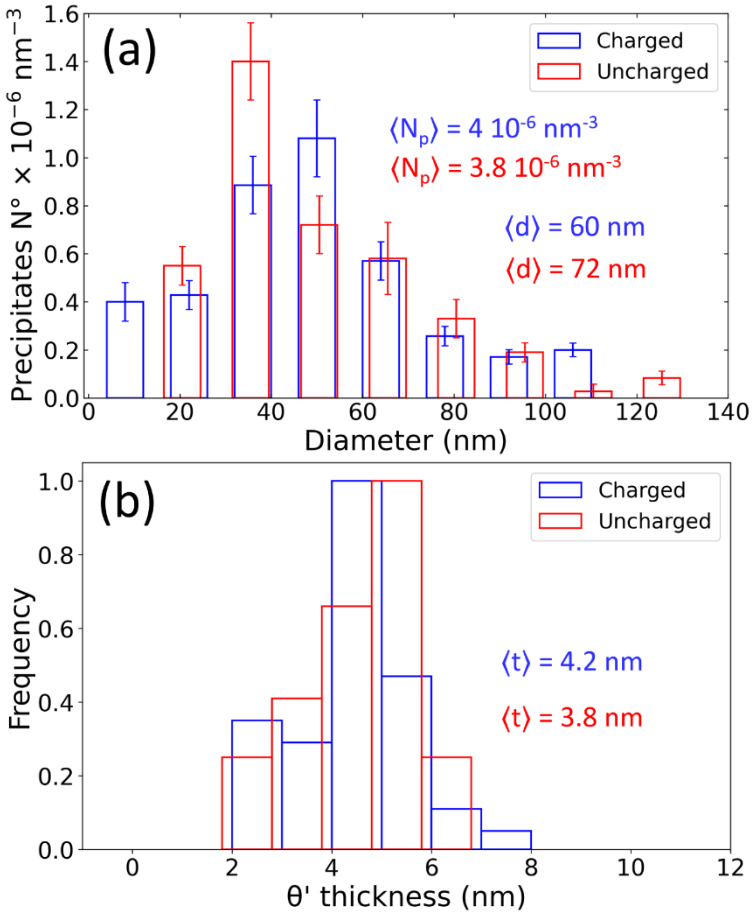


*Figure **IV-33**: Comparison of θ' precipitate diameter (a) and thickness (b) distributions for the uncharged samples (red) and hydrogen-charged sample (blue), for the pre-deformed Al-5Cu alloy (5 %) aged 24 h at 140 °C.*

Taken together, the imaging and diffraction results demonstrate that prior deformation (5% cold rolling) significantly promotes the formation of θ′ precipitates, while hydrogen charging does not appear to have a significant effect on the precipitation mechanism.

To investigate the influence of the dislocation density, some samples were deformed to a higher rolling reduction, up to 20%. The HAADF images in Figure **IV-34** reveal a microstructure similar to that observed at 5% reduction, with θ′ precipitates and remaining of θ″ precipitates

and GP zones. The corresponding SAED patterns further show no significant differences in superlattice reflections between charged and uncharged conditions.

Quantitative measurements support these observations. The distribution of θ′ precipitate diameters (Figure **IV-35**a) shows a strong overlap between the charged and uncharged samples, with comparable mean values of 55 ± 20 nm and 60 ± 20 nm, respectively. Similarly, the thickness distributions are almost identical (Figure **IV-35**b), with mean values of 5.0 ± 1.5 nm for the charged sample and 5.3 ± 2.0 nm for the uncharged one. The number density of θ′ precipitates is almost unchanged, $3.8 \pm 1 \times 10^{-6}$ nm^{-3} (charged) and $4.0 \pm 1 \times 10^{-6}$ nm^{-3} (uncharged).

Comparing the two deformation levels (5 % and 20 %) shows no significant influence on precipitate diameter or number density, only a slight increase in θ′ thickness at 20 % reduction (≈ 5.3 nm) compared to the 5% (≈ 3.8 nm).

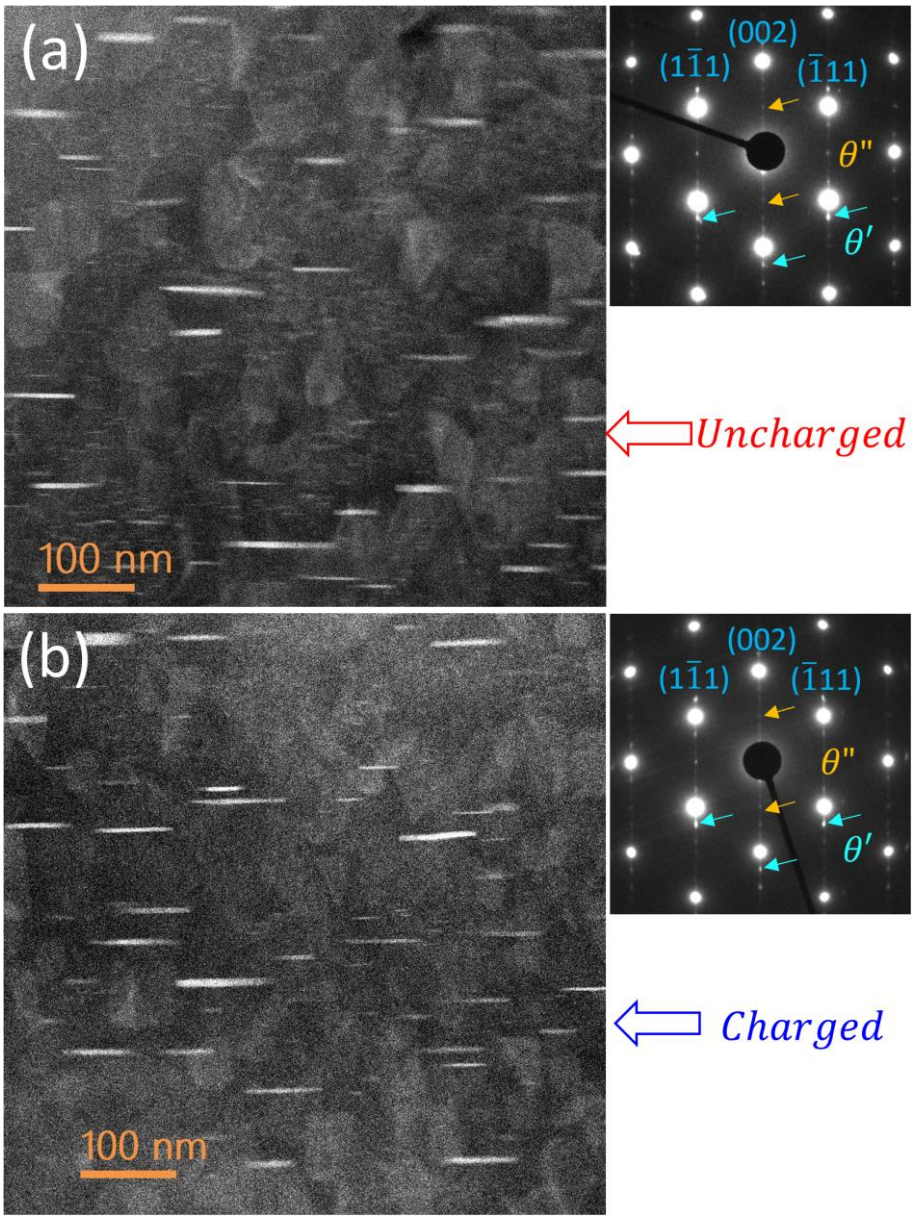


*Figure **IV-34**: HAADF-STEM image of pre-deformed Al-5Cu alloy (20 %) aged 24 h at 140 °C, (a) is the uncharged sample and (b) is the hydrogen-charged sample. Insets show corresponding SAED patterns acquired along the [011] zone axis, revealing superlattice reflections associated with θ" and θ' precipitates, as well as diffuse streaking attributed to GP zones.*

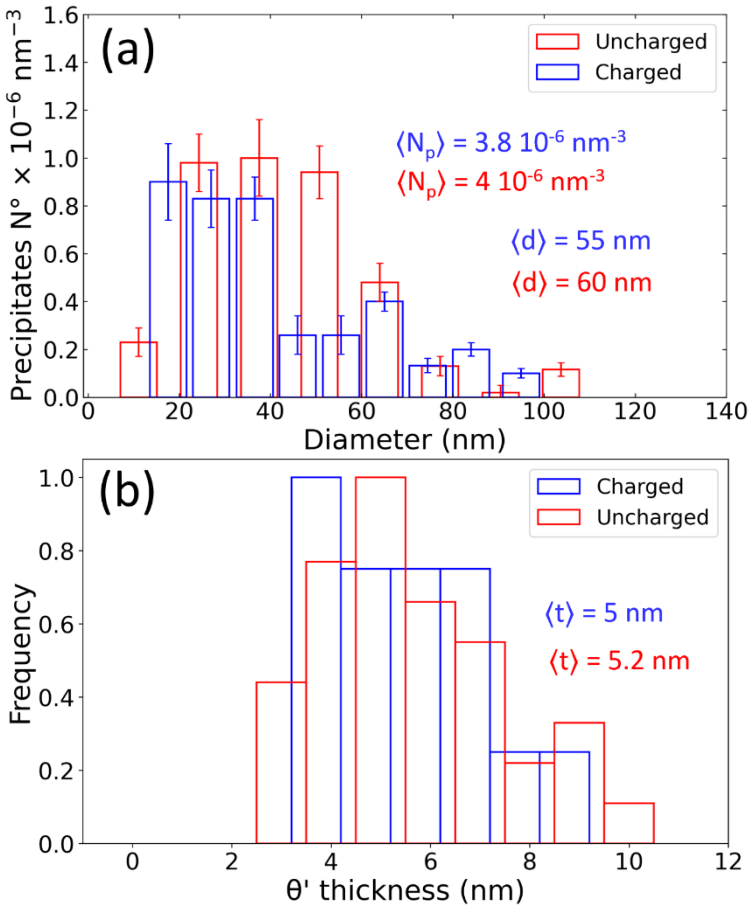


*Figure **IV-35**: Comparison of θ' precipitate diameter (a) and thickness (b) distributions for the uncharged samples (red) and hydrogen-charged sample (blue), for pre-deformed Al-5Cu alloy (20 %) aged 24 h at 140 °C.*

The negligible influence of hydrogen charging on θ′ precipitation observed for pre-deformed samples could be attributed to several factors.

First, it is possible that the hydrogen amount introduced *via* chemical charging at room temperature may have been insufficient to induce detectable changes in the precipitation kinetics of θ′. Although dislocations introduced by cold rolling can serve as hydrogen traps, the concentration of hydrogen retained during aging at 140 °C might not have been high enough to affect the nucleation and/or growth of θ′ precipitates and this hydrogen rapidly diffuse out.

Second, the precipitation behavior in pre-deformed samples is most likely driven by dislocation which could possibly hide any subtle hydrogen effects. The preferential formation of θ′ precipitates at or near dislocations, as seen in the LAADF-STEM images, suggests that dislocations play a primary role in controlling precipitation under these conditions. Besides,

aging at 140 °C may facilitate hydrogen desorption over time, thus reducing its potential influence on precipitation.

Another approach to overcome these limitations will be aging under hydrogen atmosphere (10 MPa), as was previously used for the Al–Zr system.

7.3. Influence of Hydrogen on Precipitation (aging under hydrogen environment)

7.3.1. Hardness Evolution

Figure **IV-36** displays Vickers micro-hardness evolutions at 140 °C for Al5Cu alloy subjected to three pre-deformation states 0 %, 10 % and 50 % thickness reduction, aged under hydrogen atmosphere (10 MPa) and in air (0.1 MPa).

For the non-deformed sample (Figure **IV-36**a), both conditions (in hydrogen and air) exhibit a classical age-hardening response, with hardness increasing rapidly within the first 10 hours with similar value. After 24 h the microhardness is higher for the sample aged in air than under hydrogen (135 ± 3 HV compared to 126 ± 2 HV), the same trend is observed after 48 h, hardness remains consistently ~7 HV lower for sample aged under hydrogen.

For the sample subjected to 10% thickness reduction (Figure **IV-36**b), deformation increases the initial hardness to ~105 HV due to strain hardening. Subsequent aging results in significant hardening, reaching 131 ± 3 HV after 5 hours for the sample aged in air and 119 ± 2 HV for the sample aged under hydrogen. After 24 h, the hardness continues to increase, reaching 145 ± 3 HV and 135 ± 3 HV for the samples aged in air and hydrogen, respectively. The ~10 HV shift persists throughout aging and begins to decrease slightly after 48 h.

A 50% thickness reduction results in a significant increase in initial hardness due to strain hardening (~150 HV), but aging leads to a progressive softening, as observed for sample aged in air (Figure **IV-36**c). Surprisingly, the sample aged in hydrogen exhibits a slower softening during aging and maintains a higher hardness than sample aged in air (*e.g.*, 135 ± 3 HV comped to 120 ± 2 HV after 24 h).

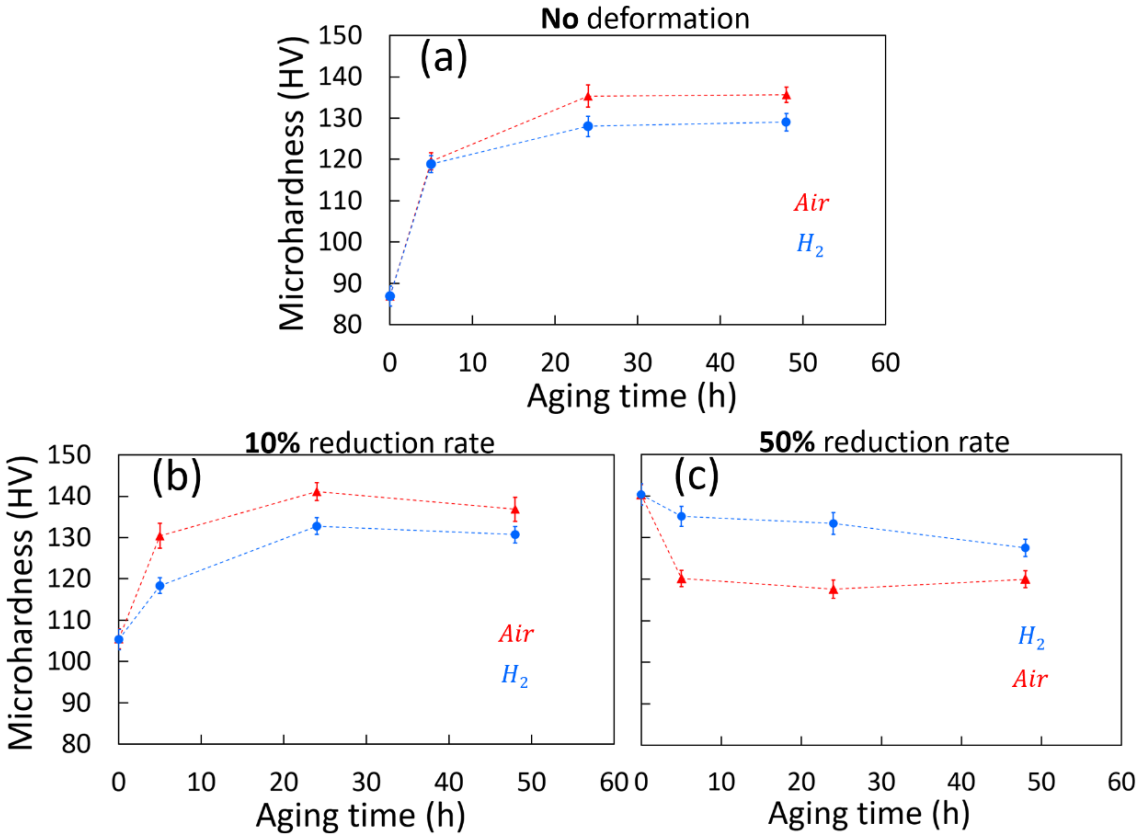


*Figure **IV-36**: Vickers micro-hardness with aging time for sample aged in air (red) and hydrogen (blue). (a) no prior deformation, (b) cold-rolled to 10 % thickness reduction, (c) cold-rolled to 50 % thickness reduction. Error bars denote standard deviation (n ≥ 6 indents).*

In the undeformed sample, no significant difference in hardness is observed between the two aging environments after 5 hours. However, after 24-48 hours the sample aged under hydrogen exhibits a significantly lower hardness. This suggests that hydrogen may not have fully diffused into the structure after 5 h. Considering the reported diffusivity of hydrogen in aluminium at 140 °C (D ≈ 8 × 10^{-13} m^2 s^{-1} [28]) the diffusion length of hydrogen can be estimated using the classical diffusion equation $L = \sqrt{6Dt}$, where D is the diffusion coefficient and t is the time. After 5 hours, the calculated diffusion length is about 0.3 mm, which is significantly smaller than the specimen dimensions (6 mm in diameter and 1 mm in thickness), indicating that hydrogen did not have sufficient time to diffuse uniformly throughout the sample volume during the initial 5 h. Besides, after 24 h and 48 h of aging, the estimated diffusion lengths increase to about 0.6 mm and 0.9 mm, respectively. These values exceed half the thickness of the sample (0.5 mm), suggesting that hydrogen may then diffuse more uniformly through the sample.

In contrast, the 10% cold-rolled sample shows a significant difference in hardness as early as 5 h of aging. This may indicate that hydrogen diffusion and trapping occur much more rapidly in the presence of defects, notably dislocations. These dislocations act as fast diffusion pathways and trapping sites [316], allowing hydrogen to interact with the microstructure earlier during aging and reduce the precipitation strengthening effect. The initial hardness is also significantly higher than in the undeformed condition, as expected due to strain hardening and the increased dislocation density. The delay in hardening under hydrogen is consistent with previous observations for chemically charged samples. As discussed previously, this delay could result from lower Cu mobility or a stabilizing effect on the GP zones that delays their transformation into subsequent metastable phases.

At 50 % reduction, the behavior is markedly different. While the sample aged in air shows continuous softening over time, likely due to recovery at 140 °C and possible coarsening of precipitates. The sample aged under hydrogen maintains a relatively stable and higher hardness throughout aging. This suggests that hydrogen may inhibit recovery processes or dislocation annihilation, thus stabilizing the defect structure. The microstructure at the initial state, before aging and immediately after deformation (50% reduction), was characterized and is presented in Appendix 8.

The interaction between hydrogen and dislocations becomes more pronounced at high strain levels (more than 10% reduction), where the dislocation density is significantly higher. In consequence, the mechanical response may become governed less by precipitation hardening and more by dislocations, and hydrogen–dislocation interactions dominate the overall hardening behavior.

To gain a better understanding of these unexpected hardness observations during aging under hydrogen atmosphere, a complete microstructural characterization by TEM has been carried out and is presented in the following section.

7.3.2. Microstructure characterization

Figure **IV-37** shows HAADF and LAADF STEM micrographs for the pre-deformed sample (50% thickness reduction) after 24 h of aging under hydrogen and in air. In both environments, the microstructure is exclusively composed of θ′ precipitates, as confirmed by the identical superlattice reflections observed in the SAED inserts. LAADF contrast reveals a dense network of dislocations in each specimen (Figure **IV-37**b,d). However, this network seems

systematically more dense in the hydrogen-aged sample. Some dislocation cell structures also appear in the sample aged in air.

Histograms in Figure **IV-38** indicate a mean precipitate diameter of 75 ± 21 nm and a mean thickness of 4.3 ± 1.2 nm for the sample aged under hydrogen. In comparison, the sample aged in air exhibits a larger average diameter of 95 ± 20 nm and a thickness of 7.1 ± 2.2 nm. While the diameter distributions largely overlap, the thickness distribution is clearly shifted toward larger values for sample aged in air.

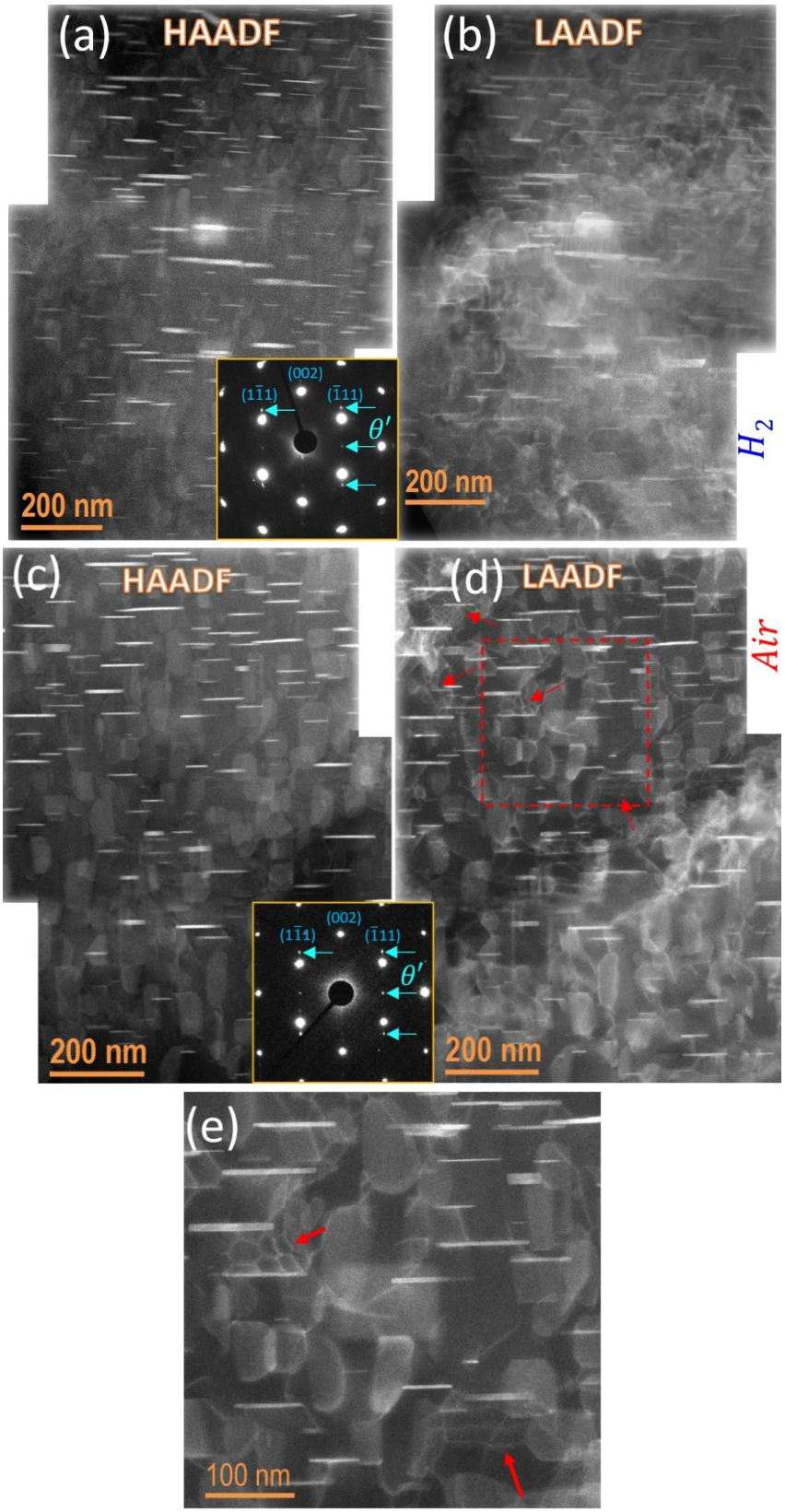


*Figure **IV-37**: HAADF (a, c) and LAADF (b, d, e) STEM micrographs for the pre-deformed sample (50% thickness reduction) after 24 h of aging under hydrogen (a, b) and in air (c, d). (e) is the area marked by the red dashed box in (d). The insets show the corresponding SAED patterns. Red arrows in the LAADF images highlight the dislocation cells.*

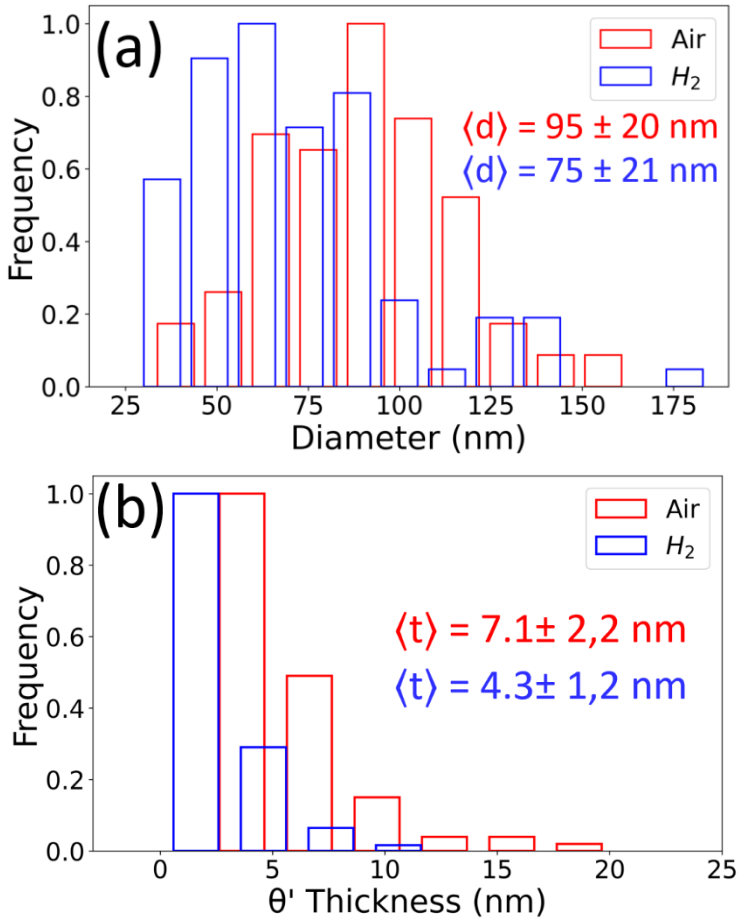


*Figure **IV-38**: Comparison of θ' precipitate diameter (a) and thickness (b) distributions for the samples aged in air (red) and in hydrogen (blue). For the pre-deformed sample (50% thickness reduction) after 24 h of aging.*

θ′ precipitates grow faster in air than under hydrogen, leading to a higher volume fraction. These observations suggest that hydrogen affects the θ″ → θ′ transformation, notably in the case of pre-deformed samples where the dislocation density is high. Besides, after 24 hours of aging at 140°C, it seems that dislocation networks remain highly visible in samples aged under hydrogen atmosphere, as seen by the higher bright contrasts in Figure **IV-37**, suggesting that dislocation recovery may be affected by hydrogen. Recovery appears more advanced in the air-aged sample, as shown by the formation of clearly defined dislocation cells (Figure **IV-37**d). Previous studies have shown that for similar alloys, at 175 °C, the dislocation density decreases by 50 % after 5 h and then stabilizes [317]. Thus, under our conditions (140 °C), regions with dislocation cells are expected.

The bright contrasts observed in sample aged under hydrogen may, however, also arise from local lattice disorientation. Nevertheless, no dislocation cells were observed under these

conditions. If hydrogen affect dislocation recovery, a possible mechanism is the formation of vacancy–hydrogen complexes which act as a lock [41], hindering dislocation motion and delaying annihilation and cell formation.

Figure **IV-39** shows the microstructure of sample aged under hydrogen and in air atmospheres after 48 h, which are mainly composed of θ′ precipitates without any evidence of other precipitate phases. The diameter distributions of θ′ precipitates are relatively similar between air-aged and hydrogen-aged samples (Figure **IV-40**), with mean diameters of 80 ± 21 nm and 70 ± 20 nm, respectively. However, the mean thickness of θ′ precipitates is slightly larger in the air-aged condition (7 ± 1.8 nm) compared to the hydrogen-aged condition (5.5 ± 1.4 nm). The thickness distribution is somewhat different, showing a shift toward higher values for the air-aged samples, although the difference is less pronounced than that observed after 24 h of aging.

These observations after 48 h indicate that, over time, the microstructure tends to become similar for both conditions (hydrogen and air). This is consistent with the hardness measurements, which show that the difference between the hydrogen-aged and air-aged samples narrows after 48 h.

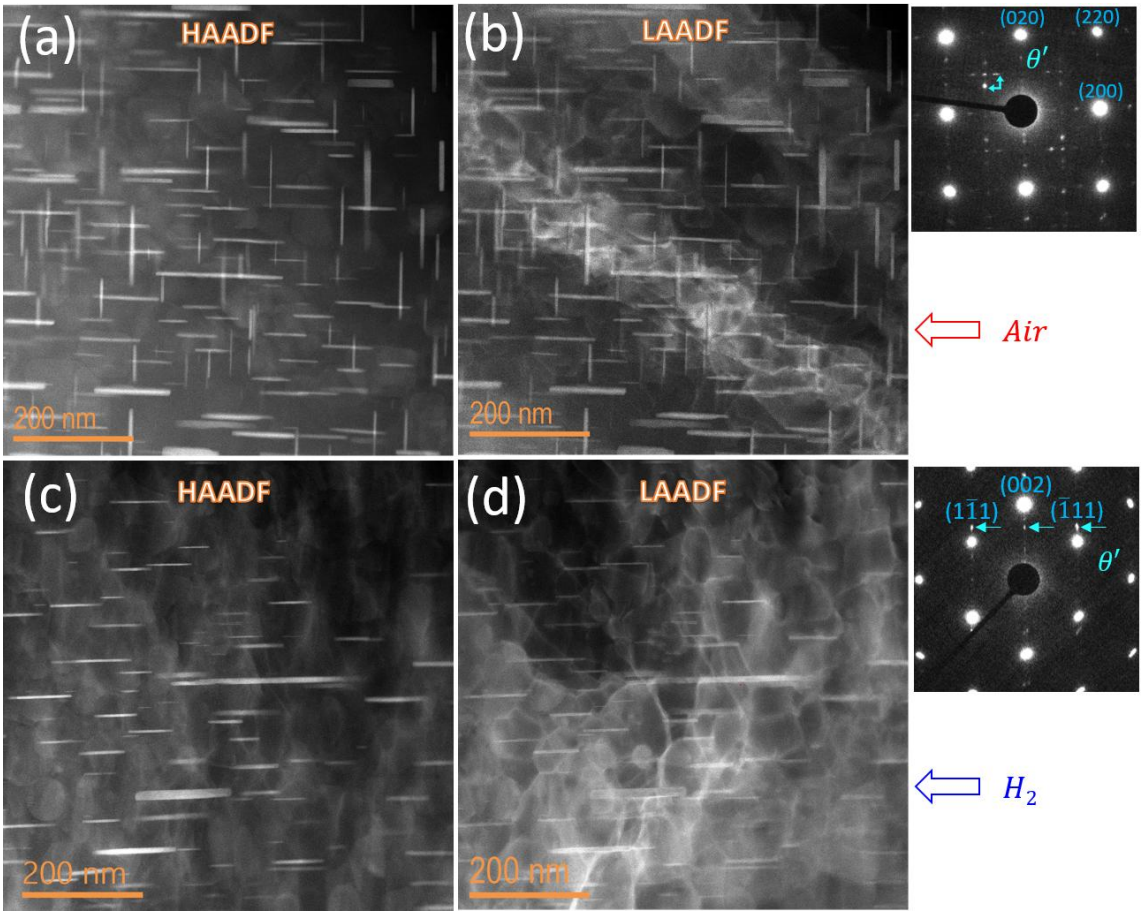


Figure IV-39: HAADF (a, c) and LAADF (b, d) STEM micrographs for the pre-deformed sample (50% thickness reduction) after 48 h of aging in air (a, b) and under hydrogen (c, d). The insets show the corresponding SAED patterns.

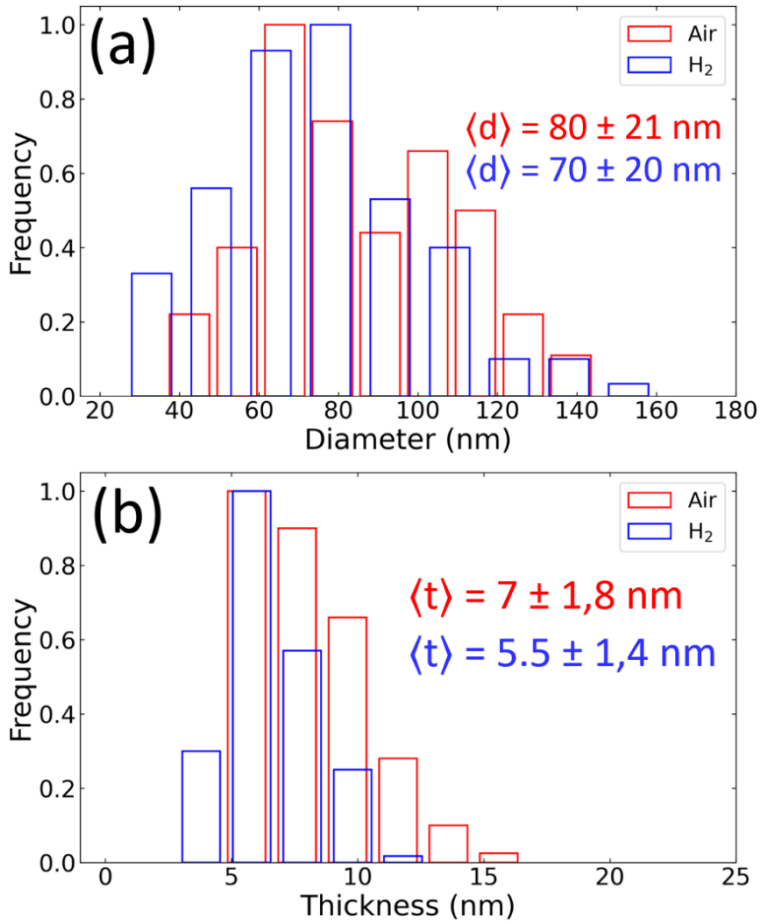


Figure IV-40: Comparison of θ' precipitate diameter (a) and thickness (b) distributions for the samples aged in air (red) and in hydrogen (blue). For the pre-deformed sample (50% thickness reduction) after 48 h of aging.

7. Discussion

Figure **IV-41** schematically illustrates the proposed mechanism for the pre-deformed sample aged under hydrogen atmosphere. Vacancy-hydrogen complexes are formed, these complexes hinder dislocation mobility, thus affecting dislocation recovery processes. Besides, hydrogen atoms become trapped at θ′ precipitate-matrix interfaces, influencing precipitate growth kinetics, significantly with respect to precipitate thickness, which was found to be smaller under hydrogen.

Under air atmosphere and during aging, dislocation recovery is more pronounced, leading to the formation of dislocation cell structures. Concurrently, θ′ precipitates exhibit accelerated growth compared to sample aged under hydrogen. Therefore, hydrogen demonstrates a kinetic effect on precipitation growth, particularly regarding precipitate thickness, as well as on

dislocation recovery processes. This proposed mechanism, involving hydrogen effects on both dislocation behavior and θ′ precipitate evolution, could explains the observed hardness values, which were found to be higher in samples aged under hydrogen atmosphere.

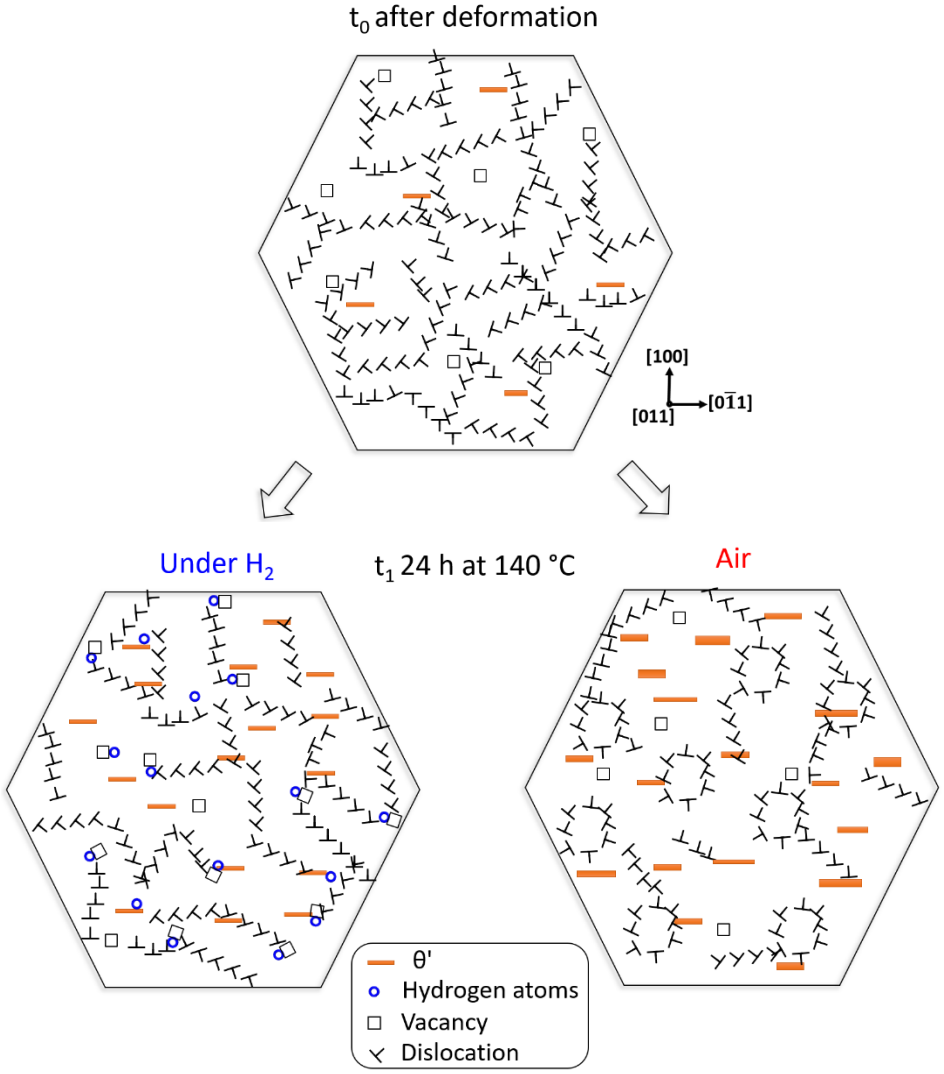


Figure IV-41: Schematic diagram showing microstructural evolution during aging at 140°C. Initial state (t_0) after deformation (top) and after aging time (t_1) under H_2 and air atmospheres for the Al-5Cu alloy.

However, with chemical charging this hydrogen effect was not observed for the pre-deformed sample. Figure **IV-42** schematically illustrates the hydrogen concentration change during aging. In the case of chemical charging, the initial hydrogen concentration is relatively high, which influences the nucleation and growth of GP zones and their transformation into θ″ precipitates. As aging continues, the hydrogen concentration decreases, and therefore it does not significantly affect the subsequent θ′ phase formation. In contrast, during aging under hydrogen (10 MPa), the initial hydrogen concentration is lower but increases with aging time. This

increase is more pronounced in deformed samples due to the higher dislocation density, which provides additional trapping sites for hydrogen and acts as fast diffusion pathways. Consequently, contrary to chemical charging, hydrogen affects the deformed samples, particularly influencing the growth of the θ′ phase in the sample with a 50 % reduction rate.

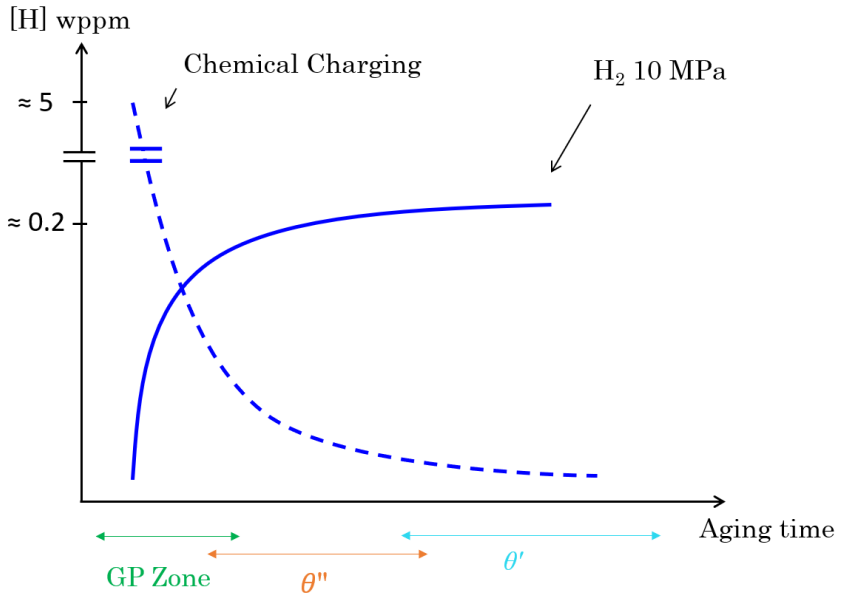


Figure IV-42: Schematic illustration of the variation of hydrogen concentration during aging. The dashed blue curve corresponds to chemical charging. The solid blue curve corresponds to aging under high-pressure hydrogen (10 MPa). The evolution of hydrogen content is correlated with the precipitation sequence GP zones → θ" → θ′.

CONCLUSIONS AND PERSPECTIVES

1. Summary and key results

In this PhD work, we have conducted a microstructural investigation of the influence of hydrogen on precipitation in the Al-Cu and Al-Zr systems.

In chapter III, the growth kinetic of Al_3Zr in an Al-0.2Zr alloy was systematically investigated under conventional aging conditions in air and in a hydrogen atmosphere. Microstructural analyses revealed that Al_3Zr precipitates with coherent $L1_2$ structure remain stable without transformation to the $D0_{23}$ equilibrium phase even after prolonged aging (500 h at 375 °C). Hydrogen was found to significantly accelerate the growth of Al_3Zr precipitates, resulting in systematically larger precipitates at all aging times studied compared to samples aged in air. However, the nucleation rate does not seem to be affected, as evidenced by comparable precipitate number densities in both environments. It suggests that hydrogen does not significantly alter the precipitate-matrix interfacial energy. APT analyses have also confirmed the enhanced decomposition of the Zr supersaturated solid solution under hydrogen, consistent with the fastest growth observed by TEM.

Modeling using a classical coarsening model showed good agreement with experimental data, and revealed that hydrogen increases the effective diffusion coefficient of Zr by a factor of about two. This enhancement is attributed to hydrogen-vacancy interactions, which reduce vacancy formation or migration energies by approximately 0.04 eV, thus enhancing Zr mobility.

In chapter IV, the hardness evolution and microstructural changes in the Al-5Cu alloy during aging at 140 °C was presented, with a focus on the influence of hydrogen on the precipitation sequence and on the resulting hardness.

By chemical charging, hydrogen significantly affects the early stages of aging (0-10 h), leading to a delay in the hardness increase. TDS analyses revealed that the hydrogen concentration detected is higher in hydrogen-charged samples compared to uncharged ones, with an increase of about 5 wppm, confirming the efficiency of the charging method. Besides, 4 wppm of hydrogen was detected in the sample aged 24 h at 140°C, suggesting that hydrogen remains trapped in the structure even after heat treatment.

TEM observations revealed that the delay in hardness for hydrogen-charged samples is due to a delay in GP zone formation. This is likely due to hydrogen-vacancy interaction, which reduces the Cu atom mobility, thus reducing the nucleation and growth rate of GP zones, as reported earlier during natural aging.

After 30 hours of aging, a marked drop in hardness was also observed for the hydrogen-charged sample. At this stage, TEM observations show larger GP zones and a lower number of θ″ precipitates in the hydrogen-charged sample. This is attributed to the stabilizing effect of hydrogen on the GP zones and a delay in their transformation into θ″ precipitates. This hypothesis is supported by TDS results, which confirm a high hydrogen trapping ability for GP zones. Indeed, hydrogen trapped at the GP zone interfaces can decrease the free energy of the state containing GP zones, thus reducing the thermodynamic driving force for the subsequent GP → θ″ transformation or increasing the energy barrier for θ″ nucleation.

During aging up to 100 hours, the effect of hydrogen becomes negligible, as the GP zones completely disappear and the formation of θ′ begins. At this stage, the hardness becomes similar for hydrogen-charged and uncharged conditions. Additionally, the microstructure contains a comparable number and diameter of θ″ precipitates in both conditions. This suggests that after the total transformation of GP zones, hydrogen is detrapped and exits the structure.

Theoretical models for precipitation strengthening, which account for the size, morphology, and distribution of precipitates, provide relatively good fits of experimental hardness profiles. The transition from shearing to Orowan looping mechanisms in θ″ precipitates further explains the observed trends in hardness evolution. This behavior emphasizes hydrogen's impact on the precipitation sequence and its influence on the overall mechanical properties of the alloy.

Pre-deformation enhances the formation of θ′ precipitates as expected, but by chemical charging, hydrogen does not appear to significantly affect the size or number density of these precipitates. In contrast, aging under a hydrogen atmosphere showed a significant difference in hardness evolution; samples aged under hydrogen exhibited lower hardness. However, this delay in hardness appears after 24 and 48 hours of aging, likely due to the time required for hydrogen absorption during aging. When pre-deformation is carried out before aging under hydrogen, the hardness reduction is observed after 5 h, which is due to the increased dislocation density enhancing hydrogen absorption, thus affecting precipitate formation.

Surprisingly, after high deformation (50% thickness reduction), hardness values were found to be higher for samples aged under hydrogen. TEM observations revealed that, at this stage, only θ′ precipitates are evident, but their thickness and diameter are significantly larger for the samples aged in air. This indicates that hydrogen may also affect the θ″ → θ′ transformation or Cu mobility during θ′ growth. Besides, diffraction contrast from STEM images appears more pronounced in samples aged under hydrogen. It suggests that hydrogen may inhibit dislocation recovery and reduce their mobility, thereby affecting the overall hardness response. The interaction between hydrogen and dislocations may play a dominant role in determining the hardening behavior, particularly at high deformation levels.

2. Perspectives

While the influence of hydrogen on phase transformation of Al alloys was clarified in this work, different directions and open scientific question remains.

Hydrogen interacting strongly with vacancies can influence vacancy formation and migration energies. Therefore, direct measurement of vacancy concentrations using techniques such as positron annihilation spectroscopy (PAS) would provide valuable insights and further quantify how hydrogen impacts these energies.

Ab initio calculations are highly recommended to complement experimental findings and provide a deeper understanding of hydrogen-vacancy-Zr interactions at the atomic scale. Such studies could quantify the binding energies and elucidate the mechanisms underlying the enhanced Zr mobility observed experimentally.

Given that lithium exhibits a high affinity for hydrogen, similar to zirconium, investigating Al-Li alloys containing δ′-Al_3Li precipitates would provide valuable comparative data. It would also help clarify if the observed hydrogen-enhanced precipitation kinetics in the Al-Zr system represent a general phenomenon applicable to other systems with similar hydrogen-solute interactions. Additionally, since hydrogen promotes the growth of Al_3Zr precipitates, it will be crucial to assess their influence on the mechanical properties of the alloy.

In the Al-5Cu alloy, the GP zones were identified as effective hydrogen traps. To investigate this further, deuterium charging followed by APT analyses could enable direct visualization and quantification of hydrogen distribution within GP zones or in other precipitates (θ″, θ’). Additionally, differential scanning calorimetry (DSC) studies could elucidate whether

hydrogen affects the dissolution kinetics of GP zones or influences the nucleation of θ″ precipitates during the GP zones → θ″ transformation. DSC analyses would also enable estimation of enthalpy changes associated with hydrogen effects on the formation and/or dissolution of each phase.

For the deformed Al-5Cu sample (50 % reduction rate), hardness remains high during aging under hydrogen atmosphere, and TEM observations revealed high diffraction contrast for this sample. This suggests that hydrogen affects not only precipitation but also the dislocation recovery processes. Indeed, previous studies have demonstrated that hydrogen-vacancy complexes can hinder dislocation mobility. Therefore, quantitative dislocation density measurements at various aging times are crucial.

APPENDIX

Appendix 1:

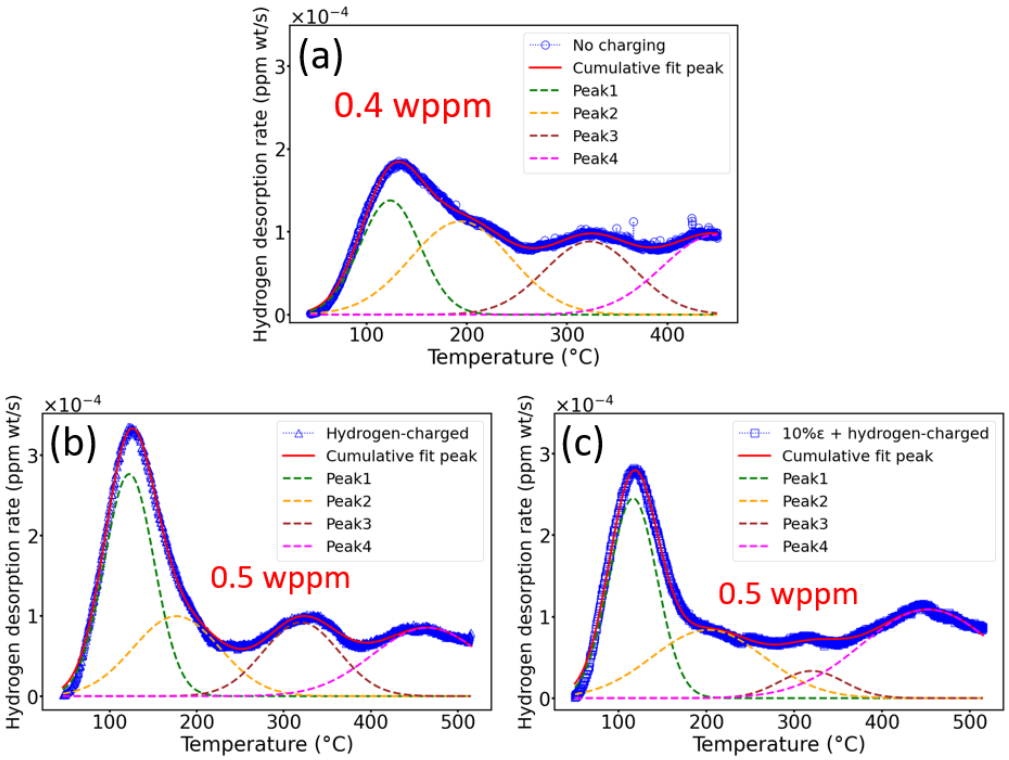


Figure A1-1: TDS spectra for the Al–5Cu alloy: (a) uncharged sample, (b) hydrogen-charged sample (NaOH), and (c) pre-deformed sample with 10 % reduction followed by hydrogen charging. The TDS measurements were performed in Japan using an ESCO EMD-WA1000S/WK apparatus.

Appendix 2:

Hydrogen uptake was assessed by TDS on Al-0.2Zr samples when it is chemically charged (5 h in NaOH). Three conditions were compared: as-quenched uncharged, as-quenched charged, and 24 h aged at 375 °C then charged ("TT + Charged"). As shown in **Error! Reference source not found.**, the hydrogen contents detected are 6.0 ± 0.6 wppm (Uncharged), 5.5 ± 0.5 wppm (Charged), and 7.2 ± 0.8 wppm (TT + Charged). Within the experimental uncertainty, there is no significant difference between these states.

It is noted that hydrogen content of ~6 wppm detected in the as-quenched uncharged sample is relatively high. Several hypotheses may explain this observation. First, it could originate from residual hydrogen which has a high affinity for Zr atoms. Second, some hydrogen may be

trapped by vacancies during the solution treatment at 620 °C. At this temperature, the equilibrium vacancy concentration is estimated to be about 10^{-3} at.% [261], and can provide potential trapping sites for hydrogen. This hypothesis is consistent with previous *ab initio* calculations, which have shown that a single vacancy in FCC Al can accommodate up to 13 hydrogen atoms [318].

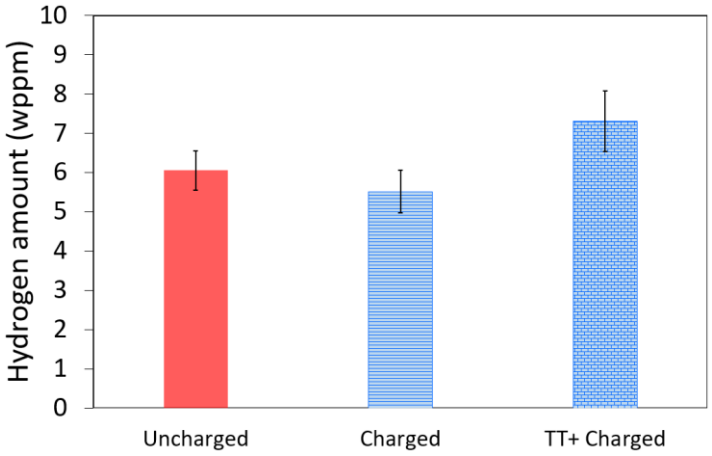


Figure A2-1: Hydrogen content (in wppm) measured by TDS with melt dosage for three conditions: uncharged, charged sample "Charged", and charged sample after 24 h of aging at 375 °C "TT + Charged".

Appendix 3:

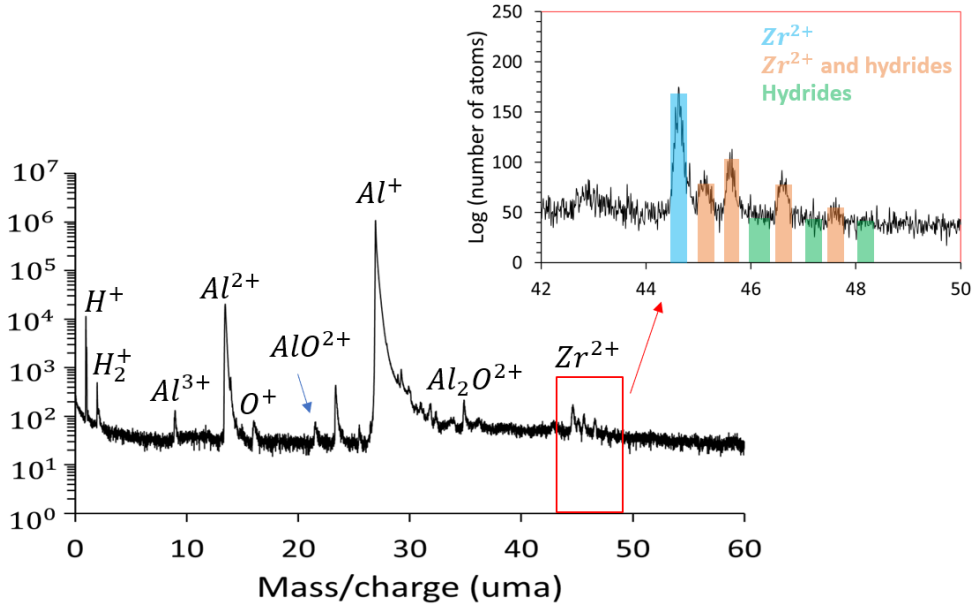


Figure A3-1: APT mass spectrum of the Al–2Zr alloy aged under hydrogen at 375 °C after 48 h. The inset shows an expanded view of the 42–50 u/e range corresponding to the Zr^{2+} isotopic region, where peaks from Zr^{2+} and possible hydrides are highlighted.

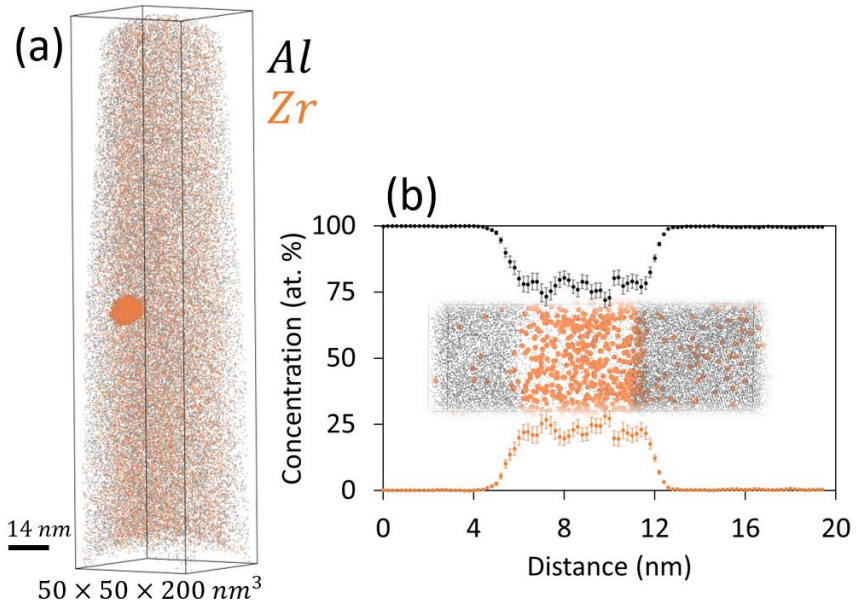


Figure A3-2: 3D reconstructions of volumes analyzed by APT (50 × 50 × 200 nm3) in the Al-2Zr alloy aged during 48 h under hydrogen at 375 °C. Al atoms are plotted in gray and Zr atoms in orange. Data were filtered to display only Zr atoms in Zr rich regions (threshold 10 at %) to highlight Al_3Zr precipitates. (b) show concentration profile through the Al_3Zr precipitate in (a), with a sampling volume thickness of 0.4 nm.

Appendix 4:

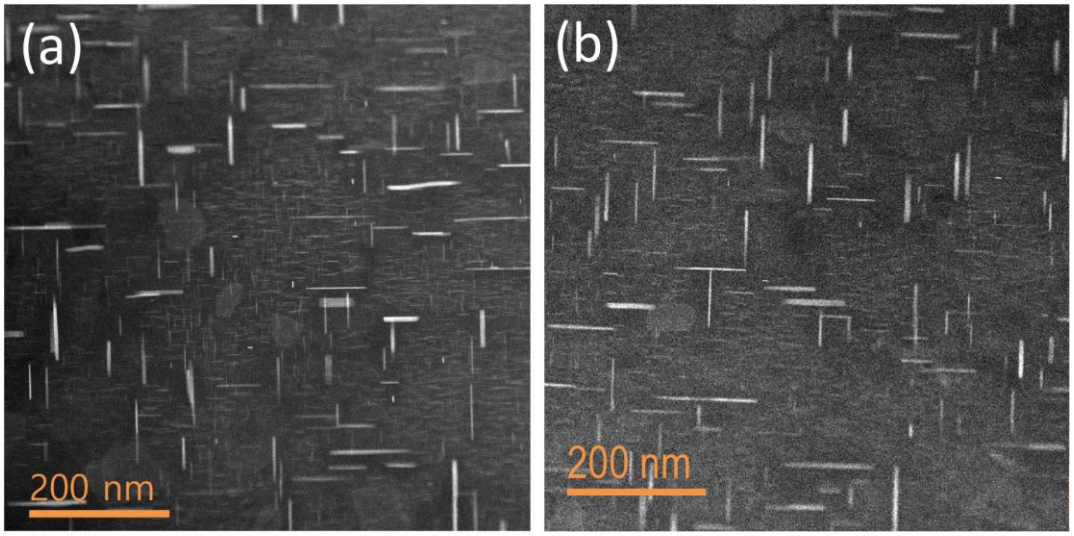


Figure A4-1: HAADF-STEM images of the Al–5Cu alloy pre-deformed to 5 % charged by NaOH and aged for 24 h at 140 °C. (a) Image acquired immediately after preparation. (b) The same TEM foil re-observed after 7 days. No significant microstructural changes are observed, indicating that the microstructure remains stable over time.

Appendix 5:

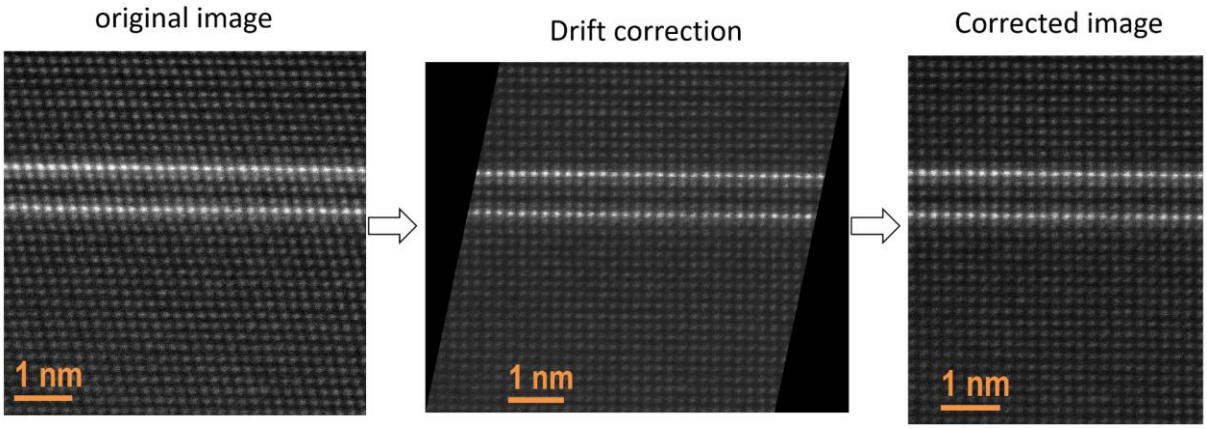


Figure A5-1: Illustration of the image drift correction process applied to HAADF-STEM micrograph.

Appendix 6:

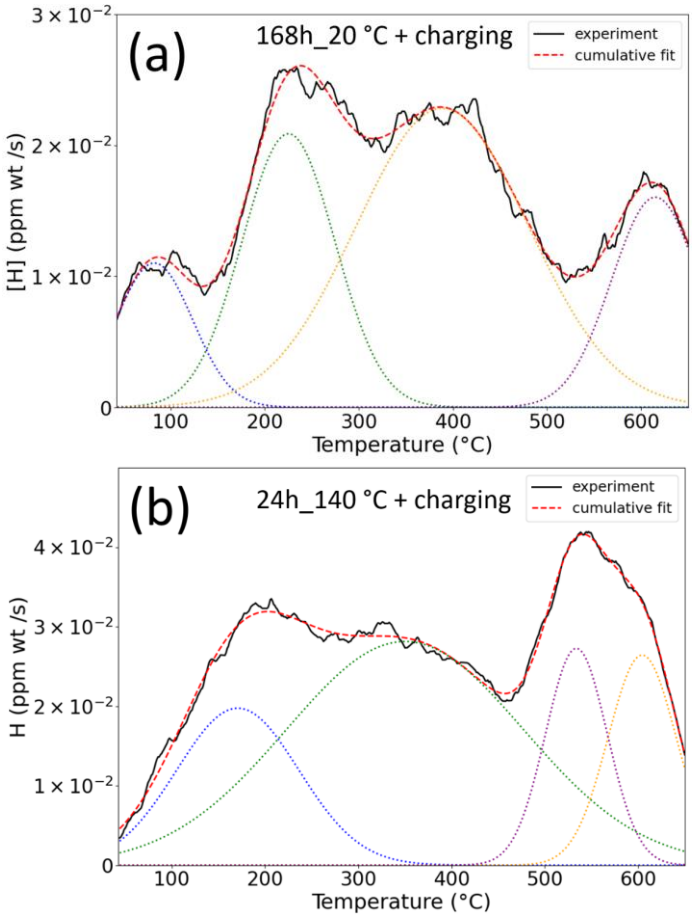


Figure A6-1: TDS spectra showing the hydrogen desorption rate as a function of temperature for (a) Al-5Cu aged for 168 h at room temperature and then charged, and (b) Al-5Cu aged for 24 h at 140°C and charged. The black curves represent the experimental data, while the red dashed lines correspond to the cumulative Gaussian fit.

Appendix 7:

Estimating the number of hydrogen atoms per GP zone

GP zones in Al–5Cu are considered as monolayer discs with radius *r* (figure x). The GP zone area is given by $A_{GP} = \pi r^2$.

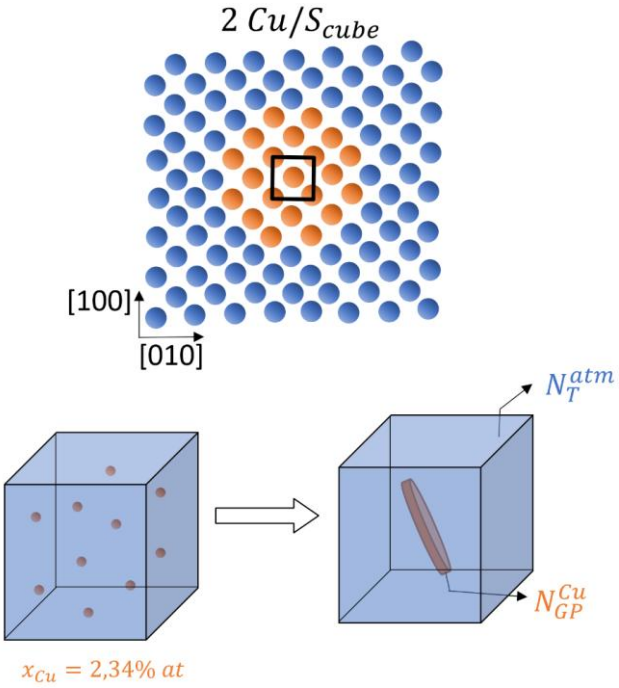


Figure A7-1: Schematic representation of the atomic structure and geometry for GP zone in the Al–5Cu alloy

The number of Cu atoms per GP zone can be expressed as:

$$N_{GP}^{Cu} = 2 \times \frac{\pi \times r^2}{a^2} = 12.5\,\pi\,r^2$$

Were *a* is the lattice parameter ($a = 0.405$ nm). The total number of atoms corresponding to one GP zone is then given by:

$$N_T^{atm} = \frac{N_{GP}^{Cu}}{x_{Cu}} = \frac{12.5\,\pi\,r^2}{x_{Cu}}$$

Where X_{cu} is the Cu atomic fraction.

Consequently, the number of hydrogen atoms per GP zone can be estimated as:

$$N_H^{atm}/GP = \frac{C_H \times \pi \times r^2}{x_{Cu}} \times 1{,}25.10^{-5}$$

Where C_H is the hydrogen concentration in appm.

Appendix 8:

TEM images showing the microstructure of the Al–5Cu alloy pre-deformed to 50 % reduction without subsequent aging at 140 °C (immediately after deformation). At this stage, the microstructure contains some θ′ precipitates and GP zones. In addition, the LAADF images exhibit strong diffraction contrast.

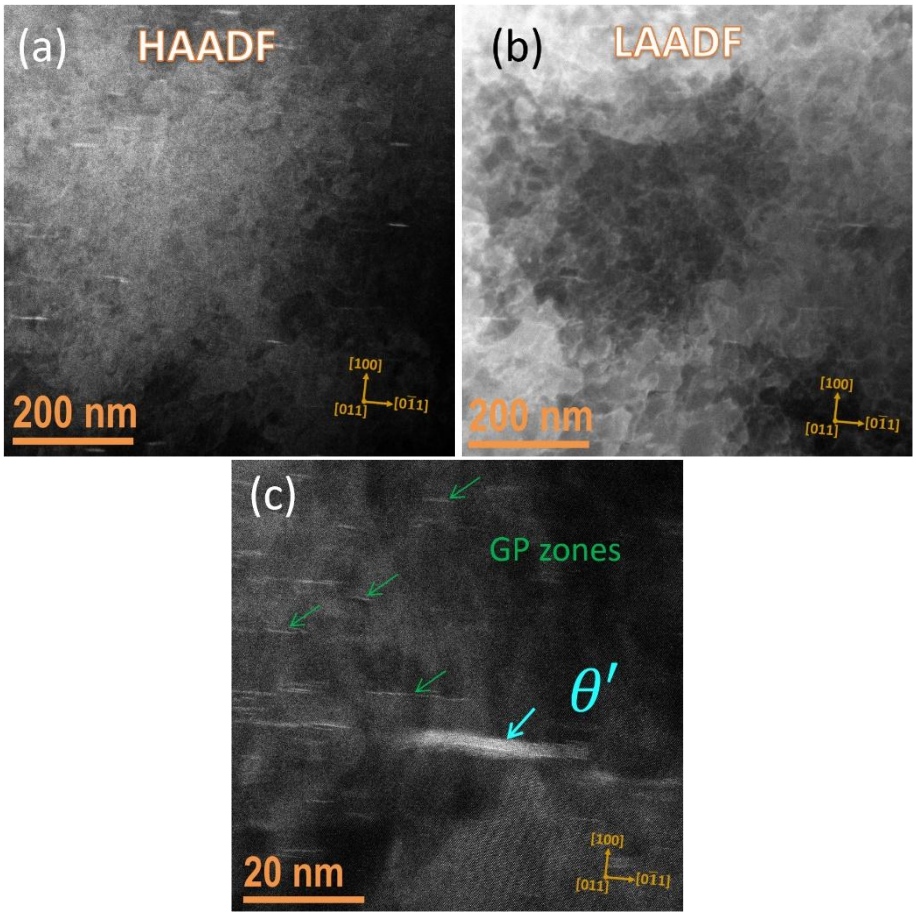


Figure A8-1: HAADF (a) and LAADF (b) STEM micrographs for the pre-deformed sample (50% thickness reduction) of the Al-5Cu alloy. (c) is a high-magnification HAADF image showing the GP zones and θ' precipitates. All images were taken along the [110] zone axis.

REFERENCES:

[1] J.O. Abe, A.P.I. Popoola, E. Ajenifuja, O.M. Popoola, Hydrogen energy, economy and storage: Review and recommendation, Int. J. Hydrog. Energy 44 (2019) 15072–15086. https://doi.org/10.1016/j.ijhydene.2019.04.068.

[2] F. Dawood, M. Anda, G.M. Shafiullah, Hydrogen production for energy: An overview, Int. J. Hydrog. Energy 45 (2020) 3847–3869. https://doi.org/10.1016/j.ijhydene.2019.12.059.

[3] V. Vogl, M. Åhman, L.J. Nilsson, Assessment of hydrogen direct reduction for fossil-free steelmaking, J. Clean. Prod. 203 (2018) 736–745. https://doi.org/10.1016/j.jclepro.2018.08.279.

[4] A. Bhaskar, M. Assadi, H. Nikpey Somehsaraei, Decarbonization of the Iron and Steel Industry with Direct Reduction of Iron Ore with Green Hydrogen, Energies 13 (2020) 758. https://doi.org/10.3390/en13030758.

[5] B. Yao, T. Xiao, O.A. Makgae, X. Jie, S. Gonzalez-Cortes, S. Guan, A.I. Kirkland, J.R. Dilworth, H.A. Al-Megren, S.M. Alshihri, P.J. Dobson, G.P. Owen, J.M. Thomas, P.P. Edwards, Transforming carbon dioxide into jet fuel using an organic combustion-synthesized Fe-Mn-K catalyst, Nat. Commun. 11 (2020) 6395. https://doi.org/10.1038/s41467-020-20214-z.

[6] C. Acar, I. Dincer, The potential role of hydrogen as a sustainable transportation fuel to combat global warming, Int. J. Hydrog. Energy 45 (2020) 3396–3406. https://doi.org/10.1016/j.ijhydene.2018.10.149.

[7] J. Hirsch, Recent development in aluminium for automotive applications, Trans. Nonferrous Met. Soc. China 24 (2014) 1995–2002. https://doi.org/10.1016/S1003-6326(14)63305-7.

[8] W.S. Miller, L. Zhuang, J. Bottema, A.J. Wittebrood, P. De Smet, A. Haszler, A. Vieregge, Recent development in aluminium alloys for the automotive industry, Mater. Sci. Eng. A 280 (2000) 37–49. https://doi.org/10.1016/S0921-5093(99)00653-X.

[9] H.K. Birnbaum, P. Sofronis, Hydrogen-enhanced localized plasticity—a mechanism for hydrogen-related fracture, Mater. Sci. Eng. A 176 (1994) 191–202. https://doi.org/10.1016/0921-5093(94)90975-X.

[10] I.M. Robertson, P. Sofronis, A. Nagao, M.L. Martin, S. Wang, D.W. Gross, K.E. Nygren, Hydrogen Embrittlement Understood, Metall. Mater. Trans. A 46 (2015) 2323–2341. https://doi.org/10.1007/s11661-015-2836-1.

[11] S. Lynch, Hydrogen embrittlement phenomena and mechanisms, Corros. Rev. 30 (2012). https://doi.org/10.1515/corrrev-2012-0502.

[12] V.G. Gavriljuk, V.M. Shyvaniuk, S.M. Teus, Hydrogen in metallic alloys – embrittlement and enhanced plasticity: a review, Corros. Rev. 42 (2024) 267–301. https://doi.org/10.1515/corrrev-2022-0060.

[13] M.S. Hasan, M.F. Kapci, B. Bal, M. Koyama, H. Bayat, W. Xu, An atomistic study on the HELP mechanism of hydrogen embrittlement in pure metal Fe, Int. J. Hydrog. Energy 57 (2024) 60–68. https://doi.org/10.1016/j.ijhydene.2023.12.274.

[14] X. Li, X. Ma, J. Zhang, E. Akiyama, Y. Wang, X. Song, Review of Hydrogen Embrittlement in Metals: Hydrogen Diffusion, Hydrogen Characterization, Hydrogen Embrittlement Mechanism and

Prevention, Acta Metall. Sin. Engl. Lett. 33 (2020) 759–773. https://doi.org/10.1007/s40195-020-01039-7.

[15] S.K. Dwivedi, M. Vishwakarma, Hydrogen embrittlement in different materials: A review, Int. J. Hydrog. Energy 43 (2018) 21603–21616. https://doi.org/10.1016/j.ijhydene.2018.09.201.

[16] B. Gault, A. Saksena, X. Sauvage, P. Bagot, L.S. Aota, J. Arlt, L.T. Belkacemi, T. Boll, Y.-S. Chen, L. Daly, M.B. Djukic, J.O. Douglas, M.J. Duarte, P.J. Felfer, R.G. Forbes, J. Fu, H.M. Gardner, R. Gemma, S.S.A. Gerstl, Y. Gong, G. Hachet, S. Jakob, B.M. Jenkins, M.E. Jones, H. Khanchandani, P. Kontis, M. Krämer, M. Kühbach, R.K.W. Marceau, D. Mayweg, K.L. Moore, V. Nallathambi, B.C. Ott, J.D. Poplawsky, T. Prosa, A. Pundt, M. Saha, T.M. Schwarz, Y. Shang, X. Shen, M. Vrellou, Y. Yu, Y. Zhao, H. Zhao, B. Zou, Towards Establishing Best Practice in the Analysis of Hydrogen and Deuterium by Atom Probe Tomography, Microsc. Microanal. 30 (2025) 1205–1220. https://doi.org/10.1093/mam/ozae081.

[17] D.A. Porter, K.E. Easterling, K.E. Easterling, Phase Transformations in Metals and Alloys (Revised Reprint), 0 ed., CRC Press, 2009. https://doi.org/10.1201/9781439883570.

[18] J.D. Robson, Modelling the overlap of nucleation, growth and coarsening during precipitation, Acta Mater. 52 (2004) 4669–4676. https://doi.org/10.1016/j.actamat.2004.06.024.

[19] L. Bourgeois, Y. Zhang, Z. Zhang, Y. Chen, N.V. Medhekar, Transforming solid-state precipitates via excess vacancies, Nat. Commun. 11 (2020) 1248. https://doi.org/10.1038/s41467-020-15087-1.

[20] A.G. Khachaturyan, Theory of Structural Transformations in Solids, Courier Corporation, 2008.

[21] M. Nagumo, Effects of Microstructural Factors on Hydrogen Embrittlement, in: Fundam. Hydrog. Embrittlement, Springer Singapore, Singapore, 2016: pp. 167–196. https://doi.org/10.1007/978-981-10-0161-1_8.

[22] H. Su, H. Toda, K. Shimizu, K. Uesugi, A. Takeuchi, Y. Watanabe, Assessment of hydrogen embrittlement via image-based techniques in Al–Zn–Mg–Cu aluminum alloys, Acta Mater. 176 (2019) 96–108. https://doi.org/10.1016/j.actamat.2019.06.056.

[23] S.P. Lynch, Hydrogen embrittlement (HE) phenomena and mechanisms, in: Stress Corros. Crack., Elsevier, 2011: pp. 90–130. https://doi.org/10.1533/9780857093769.1.90.

[24] H. Zhao, P. Chakraborty, D. Ponge, T. Hickel, B. Sun, C.-H. Wu, B. Gault, D. Raabe, Hydrogen trapping and embrittlement in high-strength Al alloys, Nature 602 (2022) 437–441. https://doi.org/10.1038/s41586-021-04343-z.

[25] H. Li, S. Luo, H. Xiang, Z. Liu, Y. Yao, J. Li, H. Tao, R. Zhang, D. Liu, The role of lithium in hydrogen trapping and embrittlement of Al-Cu-Li alloys: Experimental study and DFT calculations, J. Alloys Compd. 988 (2024) 174289. https://doi.org/10.1016/j.jallcom.2024.174289.

[26] N.J.H. Holroyd, G.M. Scamans, Crack Propagation During Sustained-Load Cracking of Al-Zn-Mg-Cu Aluminum Alloys Exposed to Moist Air or Distilled Water, Metall. Mater. Trans. A 42 (2011) 3979–3998. https://doi.org/10.1007/s11661-011-0793-x.

[27] M. Abe, K. Ouchi, K. Asano, A. Fujiwara, Environmental embrittlement of an Al-Zn-Mg alloy, (1981). https://pascal-

francis.inist.fr/vibad/index.php?action=getRecordDetail&idt=PASCAL8300224047 (accessed August 9, 2025).

[28] J.R. Scully, G.A. Young, S.W. Smith, Hydrogen embrittlement of aluminum and aluminum-based alloys, in: Gaseous Hydrog. Embrittlement Mater. Energy Technol., Elsevier, 2012: pp. 707–768. https://doi.org/10.1533/9780857093899.3.707.

[29] Wu, Newman, Zhao, Swain, Ding, Phillips, SMALL CRACK GROWTH AND FATIGUE LIFE PREDICTIONS FOR HIGH-STRENGTH ALUMINIUM ALLOYS: PART I—EXPERIMENTAL AND FRACTURE MECHANICS ANALYSIS, Fatigue Fract. Eng. Mater. Struct. 21 (1998) 1289–1306. https://doi.org/10.1046/j.1460-2695.1998.00080.x.

[30] H. Yu, A. Díaz, X. Lu, B. Sun, Y. Ding, M. Koyama, J. He, X. Zhou, A. Oudriss, X. Feaugas, Z. Zhang, Hydrogen Embrittlement as a Conspicuous Material Challenge–Comprehensive Review and Future Directions, Chem. Rev. 124 (2024) 6271–6392. https://doi.org/10.1021/acs.chemrev.3c00624.

[31] F.F. Dear, G.C.G. Skinner, Mechanisms of hydrogen embrittlement in steels: discussion, Philos. Trans. R. Soc. Math. Phys. Eng. Sci. 375 (2017) 20170032. https://doi.org/10.1098/rsta.2017.0032.

[32] H.K.D.H. Bhadeshia, Prevention of Hydrogen Embrittlement in Steels, ISIJ Int. 56 (2016) 24–36. https://doi.org/10.2355/isijinternational.ISIJINT-2015-430.

[33] Z.-X. Tong, S. Lin, C.-M. Hsiao, The influence of hydrogen on atomic binding energy, critical slip shear stress, and fatigue crack propagation rate of aluminum single crystals, Metall. Trans. A 20 (1989) 921–924. https://doi.org/10.1007/BF02651658.

[34] M.L. Martin, M. Dadfarnia, A. Nagao, S. Wang, P. Sofronis, Enumeration of the hydrogen-enhanced localized plasticity mechanism for hydrogen embrittlement in structural materials, Acta Mater. 165 (2019) 734–750. https://doi.org/10.1016/j.actamat.2018.12.014.

[35] M. Nagumo, K. Takai, The predominant role of strain-induced vacancies in hydrogen embrittlement of steels: Overview, Acta Mater. 165 (2019) 722–733. https://doi.org/10.1016/j.actamat.2018.12.013.

[36] S.P. Lynch, Environmentally assisted cracking: Overview of evidence for an adsorption-induced localised-slip process, Acta Metall. 36 (1988) 2639–2661. https://doi.org/10.1016/0001-6160(88)90113-7.

[37] P.J. Ferreira, I.M. Robertson, H.K. Birnbaum, Hydrogen effects on the interaction between dislocations, Acta Mater. 46 (1998) 1749–1757. https://doi.org/10.1016/S1359-6454(97)00349-2.

[38] I.M. Robertson, The effect of hydrogen on dislocation dynamics, Eng. Fract. Mech. 68 (2001) 671–692. https://doi.org/10.1016/S0013-7944(01)00011-X.

[39] L. Huang, D. Chen, D. Xie, S. Li, Y. Zhang, T. Zhu, D. Raabe, E. Ma, J. Li, Z. Shan, Quantitative tests revealing hydrogen-enhanced dislocation motion in α-iron, Nat. Mater. 22 (2023) 710–716. https://doi.org/10.1038/s41563-023-01537-w.

[40] A.H. Cottrell, B.A. Bilby, Dislocation Theory of Yielding and Strain Ageing of Iron, Proc. Phys. Soc. Sect. A 62 (1949) 49–62. https://doi.org/10.1088/0370-1298/62/1/308.

[41] D. Xie, S. Li, M. Li, Z. Wang, P. Gumbsch, J. Sun, E. Ma, J. Li, Z. Shan, Hydrogenated vacancies lock dislocations in aluminium, Nat. Commun. 7 (2016) 13341. https://doi.org/10.1038/ncomms13341.

[42] Y. Zhu, Z. Li, M. Huang, H. Fan, Study on interactions of an edge dislocation with vacancy-H complex by atomistic modelling, Int. J. Plast. 92 (2017) 31–44. https://doi.org/10.1016/j.ijplas.2017.03.003.

[43] S. Lynch, Understanding Mechanisms and Kinetics of Environmentally Assisted Cracking, BHM Berg- Hüttenmänn. Monatshefte 161 (2016) 3–18. https://doi.org/10.1007/s00501-016-0448-8.

[44] B. Sun, H. Zhao, X. Dong, C. Teng, A. Zhang, S. Kong, J. Zhou, X.-C. Zhang, S.-T. Tu, Current challenges in the utilization of hydrogen energy-a focused review on the issue of hydrogen-induced damage and embrittlement, Adv. Appl. Energy 14 (2024) 100168. https://doi.org/10.1016/j.adapen.2024.100168.

[45] Y. Zong, B. Shao, X. Wang, B. Guo, D. Shan, Effect of Hydrogen on Phase Transformation, Thermal Deformation Behavior, and Forming Limit of TC2 Alloy, Adv. Eng. Mater. 20 (2018) 1800690. https://doi.org/10.1002/adem.201800690.

[46] J. Wen, E. Fleury, F. Cao, N. Allain, Hydrogen concentration dependence of phase transformation and microstructure modification in metastable titanium alloy β-21S, J. Mater. Sci. 56 (2021) 5161–5172. https://doi.org/10.1007/s10853-020-05568-5.

[47] M. Taherijam, S. Marashi, A. Tondro, H. Abdolvand, On the effects of transformation strain induced by hydride precipitation, Acta Mater. 261 (2023) 119356. https://doi.org/10.1016/j.actamat.2023.119356.

[48] N. Pushilina, A. Panin, M. Syrtanov, E. Kashkarov, V. Kudiiarov, O. Perevalova, R. Laptev, A. Lider, A. Koptyug, Hydrogen-Induced Phase Transformation and Microstructure Evolution for Ti-6Al-4V Parts Produced by Electron Beam Melting, Metals 8 (2018) 301. https://doi.org/10.3390/met8050301.

[49] Y. Zong, S. Huang, B. Guo, D. Shan, In situ study of phase transformations in Ti–6Al–4V–xH alloys, Trans. Nonferrous Met. Soc. China 25 (2015) 2901–2911. https://doi.org/10.1016/S1003-6326(15)63916-4.

[50] D. Wen, Y. Zong, W. Xu, D. Shan, B. Guo, The effect of hydrogen on phase transformation and mechanical properties of a β containing γ–TiAl based alloy, Int. J. Hydrog. Energy 39 (2014) 17404–17415. https://doi.org/10.1016/j.ijhydene.2014.08.051.

[51] B. Zhang, Y. Wang, H. Chang, I.V. Alexandrov, Z. Sun, Y. Dong, R.Z. Valiev, Y. Wang, L. Zhou, Effect of hydrogen on microstructure evolution and deformation behaviors of Ti-2Fe-0.1B alloy, J. Alloys Compd. 900 (2022) 163473. https://doi.org/10.1016/j.jallcom.2021.163473.

[52] G.S. Mogilny, S.M. Teus, V.N. Shyvanyuk, V.G. Gavriljuk, Plastic deformation and phase transformations in austenitic steels in the course of hydrogen charging and subsequent mechanical tests, Mater. Sci. Eng. A 648 (2015) 260–264. https://doi.org/10.1016/j.msea.2015.09.015.

[53] K.R. Hebert, O.O. C¸apraz, P. Shrotriya, G. Zhang, Electrochemical and Metal-Phase Processes Accompanying Hydrogen Absorption in Aluminum During Aqueous Corrosion, ECS Meet. Abstr. MA2012-02 (2012) 2167–2167. https://doi.org/10.1149/MA2012-02/21/2167.

[54] S.K. Konovalov, B.M. Bulychev, The P,T-State Diagram and Solid Phase Synthesis of Aluminum Hydride, Inorg. Chem. 34 (1995) 172–175. https://doi.org/10.1021/ic00105a029.

[55] H. Saitoh, A. Machida, Y. Katayama, K. Aoki, Formation and decomposition of AlH3 in the aluminum-hydrogen system, Appl. Phys. Lett. 93 (2008) 151918. https://doi.org/10.1063/1.3002374.

[56] X.P. Niu, L. Froyen, L. Delaey, C. Peytour, Hydride formation in mechanically alloyed Al□Zr and Al□Fe□Zr, Scr. Metall. Mater. 30 (1994) 13–18. https://doi.org/10.1016/0956-716X(94)90350-6.

[57] K. Batalović, J. Radaković, B. Paskaš Mamula, B. Kuzmanović, M. Medić Ilić, Predicting the Heat of Hydride Formation by Graph Neural Network - Exploring the Structure–Property Relation for Metal Hydrides, Adv. Theory Simul. 5 (2022) 2200293. https://doi.org/10.1002/adts.202200293.

[58] H. Saitoh, High-Pressure and High-Temperature Syntheses of Aluminum-Transition Metal Alloy Hydrides with the Aid of *in situ* Synchrotron Radiation X-ray Diffraction Technique, Nihon Kessho Gakkaishi 64 (2022) 165–169. https://doi.org/10.5940/jcrsj.64.165.

[59] H. Saitoh, S. Takagi, N. Endo, A. Machida, K. Aoki, S. Orimo, Y. Katayama, Synthesis and formation process of Al2CuH *x* : A new class of interstitial aluminum-based alloy hydride, APL Mater. 1 (2013) 032113. https://doi.org/10.1063/1.4821632.

[60] M. Dornheim, Thermodynamics of Metal Hydrides: Tailoring Reaction Enthalpies of Hydrogen Storage Materials, in: J.C. Moreno Pirajn (Ed.), Thermodyn. - Interact. Stud. - Solids Liq. Gases, InTech, 2011. https://doi.org/10.5772/21662.

[61] Y. Fukai, Superabundant Vacancies Formed in MetalHydrogen Alloys, Phys. Scr. T103 (2003) 11. https://doi.org/10.1238/Physica.Topical.103a00011.

[62] S. Linderoth, H. Rajainmäki, R.M. Nieminen, Defect recovery in aluminum irradiated with protons at 20 K, Phys. Rev. B 35 (1987) 5524–5528. https://doi.org/10.1103/PhysRevB.35.5524.

[63] G. Hachet, X. Sauvage, Influence of hydrogen vacancy interactions on natural and artificial ageing of an AlMgSi alloy, J. Alloys Compd. 905 (2022) 164251. https://doi.org/10.1016/j.jallcom.2022.164251.

[64] G. Hachet, X. Sauvage, Hydrogen delaying the formation of Guinier-Preston zones in aluminium alloys, Acta Mater. 241 (2022) 118373. https://doi.org/10.1016/j.actamat.2022.118373.

[65] T. Marumo, S. Fujikawa, K. Hirano, Diffusion of zirconium in aluminum, J. Jpn. Inst. Light Met. 23 (1973) 17–25. https://doi.org/10.2464/jilm.23.17.

[66] C. Wolverton, Solute–vacancy binding in aluminum, Acta Mater. 55 (2007) 5867–5872. https://doi.org/10.1016/j.actamat.2007.06.039.

[67] T. Philippe, D. Blavette, A mean field approach of nucleation, Scr. Mater. 67 (2012) 77–80. https://doi.org/10.1016/j.scriptamat.2012.03.025.

[68] M. Perez, M. Dumont, D. Acevedo-Reyes, Implementation of classical nucleation and growth theories for precipitation, Acta Mater. 56 (2008) 2119–2132. https://doi.org/10.1016/j.actamat.2007.12.050.

[69] H. Men, A molecular dynamics study on the boundary between homogeneous and heterogeneous nucleation, J. Chem. Phys. 160 (2024) 094702. https://doi.org/10.1063/5.0192069.

[70] I. Polmear, Light alloys: from traditional alloys to nanocrystals, Elsevier, 2005. https://books.google.fr/books?hl=en&lr=&id=td0jD4it63cC&oi=fnd&pg=PP1&dq=Polmear,+I.J.,+%22Light+Alloys:+From+Traditional+Alloys+to+Nanocrystals,%22+Fourth+edition+2006.&ots=pdq9ug0zoi&sig=480TutugOR-GfxSnIAHoztTOKNI (accessed August 8, 2025).

[71] Y. Yang, T.R. Li, T. Jia, Z.D. Wang, R.D.K. Misra, Modeling of Precipitation Behavior of Complex Precipitates in Ferrite and Validation with Experiment, Steel Res. Int. 89 (2018) 1700466. https://doi.org/10.1002/srin.201700466.

[72] J.D. Robson, P.B. Prangnell, Dispersoid precipitation and process modelling in zirconium containing commercial aluminium alloys, Acta Mater. 49 (2001) 599–613. https://doi.org/10.1016/S1359-6454(00)00351-7.

[73] P.H.L. Souza, J.M.D.V. Quaresma, C.A.S.D. Oliveira, Precipitation Evolution and Modeling of Growth Kinetics of L12-structured Al3Zr Particles in Al-0.22Zr and Al-0.32Zr (wt.%) Alloys Isothermally Aged, Mater. Res. 20 (2017) 1600–1613. https://doi.org/10.1590/1980-5373-mr-2017-0481.

[74] J.D. Robson, A new model for prediction of dispersoid precipitation in aluminium alloys containing zirconium and scandium, Acta Mater. 52 (2004) 1409–1421. https://doi.org/10.1016/j.actamat.2003.11.023.

[75] A.D. Le Claire, Diffusion, in: N.B. Hannay (Ed.), Treatise Solid State Chem., Springer US, Boston, MA, 1976: pp. 1–59. https://doi.org/10.1007/978-1-4684-8082-5_1.

[76] A. Lin, Robert W. Balluffi, Samuel M. Allen, W. Craig Carter Kinetics of Materials Wiley Interscience (2005), (n.d.). https://www.academia.edu/23984647/Robert_W_Balluffi_Samuel_M_Allen_W_Craig_Carter_Kinetics_of_Materials_Wiley_Interscience_2005_ (accessed August 17, 2025).

[77] M. Bishop, K.E. Fletcher, Diffusion in Aluminium, Int. Metall. Rev. 17 (1972) 203–225. https://doi.org/10.1179/imtlr.1972.17.1.203.

[78] M. Conti, Curvature effects in rapid alloy solidification, Phys. Rev. E 63 (2001) 041507. https://doi.org/10.1103/PhysRevE.63.041507.

[79] A. Roy, M.P. Gururajan, Growth kinetics and morphological stability of precipitates in 3-D: a phase field study, (2014). https://doi.org/10.48550/ARXIV.1412.6922.

[80] M. Zhang, M. Chen, C. Yang, Z. Wang, THE GROWTH OF PRECIPITATES IN A SOLUTION WITH CROSS DIFFUSION BETWEEN SOLUTES, Surf. Rev. Lett. 29 (2022) 2250148. https://doi.org/10.1142/S0218625X22501487.

[81] J.D. Robson, P.B. Prangnell, Modelling Al3Zr dispersoid precipitation in multicomponent aluminium alloys, Mater. Sci. Eng. A 352 (2003) 240–250. https://doi.org/10.1016/S0921-5093(02)00894-8.

[82] D.L. Beke, Z. Erdélyi, Growth Kinetics on Nanoscale: Finite Diffusion Permeability of Interfaces, Defect Diffus. Forum 266 (2007) 1–12. https://doi.org/10.4028/www.scientific.net/DDF.266.1.

[83] E.A. Jägle, E.J. Mittemeijer, Kinetics of interface-controlled phase transformations: atomistic and mesoscopic simulations, Int. J. Mater. Res. 102 (2011) 837–845. https://doi.org/10.3139/146.110538.

[84] E.L. Hall, M.G. Benz, L.E. Rumaner, K.D. Jones, Interface Structure, Grain Morphology, and Kinetics of Growth of the Superconducting Intermetallic Compound Nb_3 Sn Doped with ZrO_2 and Copper, MRS Proc. 205 (1990) 263. https://doi.org/10.1557/PROC-205-263.

[85] M. Enomoto, G. Spanos, R.A. Masumura, The Growth Kinetics and Shape Evolution of Precipitates Growing by the Ledge Mechanism, MRS Proc. 237 (1991) 119. https://doi.org/10.1557/PROC-237-119.

[86] S.M. Northover, The Use of Size Distributions in Determining Growth Mechanisms: The Growth of Grain Boundary Precipitates in Cobalt-20 Iron, Metall. Mater. Trans. A 46 (2015) 164–177. https://doi.org/10.1007/s11661-014-2565-x.

[87] Yu.S. Kaganovskii, L.N. Paritskaya, V.V. Bogdanov, Kinetics and Mechanisms of Intermetallic Growth by Surface Interdiffusion, MRS Proc. 527 (1998) 303. https://doi.org/10.1557/PROC-527-303.

[88] Y. Yang, T. Li, T. Jia, Z. Wang, Precipitation kinetics of complex precipitate in multicomponent systems, J. Iron Steel Res. Int. 25 (2018) 1086–1093. https://doi.org/10.1007/s42243-018-0147-7.

[89] H. Saitoh, Y. Iijima, K. Hirano, Behaviour of hydrogen in pure aluminium, Al-4 mass% Cu and Al-1 mass% Mg2Si alloys studied by tritium electron microautoradiography, J. Mater. Sci. 29 (1994) 5739–5744. https://doi.org/10.1007/BF00349974.

[90] A. Sarikov, Kinetic Model of Precipitate Growth during Phase Separation in Metastable Binary Solid Solutions, Solid State Phenom. 242 (2015) 196–202. https://doi.org/10.4028/www.scientific.net/SSP.242.196.

[91] I.M. Lifshitz, V.V. Slyozov, The kinetics of precipitation from supersaturated solid solutions, J. Phys. Chem. Solids 19 (1961) 35–50. https://doi.org/10.1016/0022-3697(61)90054-3.

[92] C. Wagner, Theorie der Alterung von Niederschlägen durch Umlösen (Ostwald-Reifung), Z. Für Elektrochem. Berichte Bunsenges. Für Phys. Chem. 65 (1961) 581–591. https://doi.org/10.1002/bbpc.19610650704.

[93] J. Zuo, L. Hou, J. Shi, H. Cui, L. Zhuang, J. Zhang, Effect of deformation induced precipitation on grain refinement and improvement of mechanical properties AA 7055 aluminum alloy, Mater. Charact. 130 (2017) 123–134. https://doi.org/10.1016/j.matchar.2017.05.038.

[94] S. Ha, S.H. Kayani, K. Lee, S. Park, H. Choi, J.B. Seol, J.G. Kim, H. Sung, Microscopic-plastic deformation behavior of grain boundary precipitates in an Al–Zn–Mg alloy, J. Mater. Res. Technol. 30 (2024) 3420–3429. https://doi.org/10.1016/j.jmrt.2024.04.044.

[95] A. Deschamps, Y. Brechet, Influence of predeformation and agEing of an Al–Zn–Mg alloy—II. Modeling of precipitation kinetics and yield stress, Acta Mater. 47 (1998) 293–305. https://doi.org/10.1016/S1359-6454(98)00296-1.

[96] A. Deschamps, F. Livet, Y. Bréchet, Influence of predeformation on ageing in an Al–Zn–Mg alloy—I. Microstructure evolution and mechanical properties, Acta Mater. 47 (1998) 281–292. https://doi.org/10.1016/S1359-6454(98)00293-6.

[97] A. Duchaussoy, X. Sauvage, A. Deschamps, F. De Geuser, G. Renou, Z. Horita, Complex interactions between precipitation, grain growth and recrystallization in a severely deformed Al-Zn-Mg-Cu alloy and consequences on the mechanical behavior, Materialia 15 (2021) 101028. https://doi.org/10.1016/j.mtla.2021.101028.

[98] T. Takeyama, S. Koda, Preferred Precipitation on Dislocation Lines in an Aluminium Alloy, Nature 179 (1957) 777–778. https://doi.org/10.1038/179777b0.

[99] G. Thomas, M.J. Whelan, Observations of precipitation in thin foils of aluminium +4% copper alloy, Philos. Mag. 6 (1961) 1103–1114. https://doi.org/10.1080/14786436108239672.

[100] A. Suzuki, H. Kimura, Nucleation of θ' precipitates in an Al□4% Cu alloy, Mater. Sci. Eng. 6 (1970) 384–390. https://doi.org/10.1016/0025-5416(70)90006-6.

[101] Lorimer: The mechanism of phase transformations in... - Google Scholar, (n.d.). https://scholar.google.com/scholar_lookup?title=The%20Mechanisms%20of%20Phase%20Transformations%20in%20Crystalline%20Solids&publication_year=1969&author=G.W.%20Lorimer&author=R.B.%20Nicholson (accessed August 8, 2025).

[102] G. Thomas, J. Nutting, Precipitation on dislocations in aluminium-4% copper alloys, Acta Metall. 7 (1959) 515–516. https://doi.org/10.1016/0001-6160(59)90032-X.

[103] L. Jiang, T. Langan, T. Wood, P. Sanders, T. Dorin, Isotropy of precipitate distribution in pre-stretched Al-Cu-(Sc)-(Zr) alloys, Scr. Mater. 210 (2022) 114452. https://doi.org/10.1016/j.scriptamat.2021.114452.

[104] P.N.T. Unwin, G.W. Lorimer, R.B. Nicholson, The origin of the grain boundary precipitate free zone, Acta Metall. 17 (1969) 1363–1377. https://doi.org/10.1016/0001-6160(69)90154-0.

[105] H.S. Rosenbaum, D. Turnbull, Metallographic investigation of precipitation of silicon from aluminum, Acta Metall. 7 (1959) 664–674. https://doi.org/10.1016/0001-6160(59)90143-9.

[106] J.D. Embury, R.B. Nicholson, The nucleation of precipitates: The system Al-Zn-Mg, Acta Metall. 13 (1965) 403–417. https://doi.org/10.1016/0001-6160(65)90067-2.

[107] P.A. Rometsch, Y. Zhang, S. Knight, Heat treatment of 7xxx series aluminium alloys—Some recent developments, Trans. Nonferrous Met. Soc. China 24 (2014) 2003–2017. https://doi.org/10.1016/S1003-6326(14)63306-9.

[108] A.K. Vasudévan, R.D. Doherty, Grain boundary ductile fracture in precipitation hardened aluminum alloys, Acta Metall. 35 (1987) 1193–1219. https://doi.org/10.1016/0001-6160(87)90001-0.

[109] M. Li, Y. Yang, Z. Feng, B. Huang, X. Luo, J. Lou, J. Ru, Precipitation sequence of η phase along low-angle grain boundaries in Al-Zn-Mg-Cu alloy during artificial aging, Trans. Nonferrous Met. Soc. China 24 (2014) 2061–2066. https://doi.org/10.1016/S1003-6326(14)63312-4.

[110] R. Ranganatha, V.A. Kumar, V.S. Nandi, R.R. Bhat, B.K. Muralidhara, Multi-stage heat treatment of aluminum alloy AA7049, Trans. Nonferrous Met. Soc. China 23 (2013) 1570–1575. https://doi.org/10.1016/S1003-6326(13)62632-1.

[111] H. Zhao, F. De Geuser, A. Kwiatkowski Da Silva, A. Szczepaniak, B. Gault, D. Ponge, D. Raabe, Segregation assisted grain boundary precipitation in a model Al-Zn-Mg-Cu alloy, Acta Mater. 156 (2018) 318–329. https://doi.org/10.1016/j.actamat.2018.07.003.

[112] N. Masquelier, CARACTERISATION ET MODELISATION DE TRANSFORMATIONS MICROSTRUCTURALES POUR LA MISE AU POINT D'UNE NOUVELLE GENERATION D'ALLIAGES, Thèses et écrits académiques, University of Rouen Normandy, 2012.

[113] Z. Ma, M. Bignon, F. Gao, S. Michalik, J.D. Robson, In-situ investigation of dynamic precipitation in pre-aged Al-Zn-Mg-Cu alloy AA7075, J. Alloys Compd. 968 (2023) 172098. https://doi.org/10.1016/j.jallcom.2023.172098.

[114] A. Falahati, P. Lang, E. Kozeschnik, Precipitation in Al-Alloy 6016 – The Role of Excess Vacancies, Mater. Sci. Forum 706–709 (2012) 317–322. https://doi.org/10.4028/www.scientific.net/MSF.706-709.317.

[115] B. Klobes, T.E.M. Staab, M. Haaks, K. Maier, I. Wieler, The role of quenched-in vacancies for the decomposition of aluminium alloys, Phys. Status Solidi RRL – Rapid Res. Lett. 2 (2008) 224–226. https://doi.org/10.1002/pssr.200802123.

[116] O.R. Myhr, C.D. Marioara, O. Engler, Modeling the Effect of Excess Vacancies on Precipitation and Mechanical Properties of Al–Mg–Si Alloys, Metall. Mater. Trans. A 55 (2024) 291–302. https://doi.org/10.1007/s11661-023-07249-9.

[117] C. Sigli, F. De Geuser, A. Deschamps, J. Lépinoux, M. Perez, Recent advances in the metallurgy of aluminum alloys. Part II: Age hardening, Comptes Rendus Phys. 19 (2018) 688–709. https://doi.org/10.1016/j.crhy.2018.10.012.

[118] M.J. Starink, Analysis of aluminium based alloys by calorimetry: quantitative analysis of reactions and reaction kinetics, Int. Mater. Rev. 49 (2004) 191–226. https://doi.org/10.1179/095066004225010532.

[119] S.K. Son, M. Takeda, M. Mitome, Y. Bando, T. Endo, Precipitation behavior of an Al–Cu alloy during isothermal aging at low temperatures, Mater. Lett. 59 (2005) 629–632. https://doi.org/10.1016/j.matlet.2004.10.058.

[120] V. Vaithyanathan, C. Wolverton, L.Q. Chen, Multiscale modeling of θ′ precipitation in Al–Cu binary alloys, Acta Mater. 52 (2004) 2973–2987. https://doi.org/10.1016/j.actamat.2004.03.001.

[121] J. Konno, Direct imaging of Guinier-Preston zones by high-angle annular detector dark-field scanning transmission electron microscopy, J. Electron Microsc. (Tokyo) 50 (2001) 105–111. https://doi.org/10.1093/jmicro/50.2.105.

[122] D.R. Haeffner, J.B. Cohen, X-ray diffuse scattering study of G.P. zones in Al-4 at.% Zn, Acta Metall. 37 (1989) 2185–2195. https://doi.org/10.1016/0001-6160(89)90144-2.

[123] X. Tao, H. He, K. Li, Q. Ding, T. Wang, Y. Mo, Q. Jin, Z. Gong, Influence of temperature on the precipitation phase transformation behavior of RR350 aluminum alloy during artificial aging and related mechanisms, J. Alloys Compd. 970 (2024) 172550. https://doi.org/10.1016/j.jallcom.2023.172550.

[124] J.P. Lokker, A.J. Bottger, G.C.A.M. Janssen, S. Radelaar, *In-Situ* Characterisation of Precipitation in AI-Cu thin films, MRS Proc. 562 (1999) 269. https://doi.org/10.1557/PROC-562-269.

[125] J. Wang, C. Wolverton, S. Müller, Z.-K. Liu, L.-Q. Chen, First-principles growth kinetics and morphological evolution of Cu nanoscale particles in Al, Acta Mater. 53 (2005) 2759–2764. https://doi.org/10.1016/j.actamat.2005.02.035.

[126] G.D. Preston, The diffraction of X-rays by age-hardening aluminium copper alloys., Proc. R. Soc. Lond. Ser. Math. Phys. Sci. 167 (1938) 526–538. https://doi.org/10.1098/rspa.1938.0152.

[127] G.D. Preston, LXXIV. *The diffraction of X-rays by an age-hardening alloy of aluminium and copper. The structure of an intermediate phase*, Lond. Edinb. Dublin Philos. Mag. J. Sci. 26 (1938) 855–871. https://doi.org/10.1080/14786443808562177.

[128] Livre:Comptes rendus hebdomadaires des séances de l'Académie des sciences, tome 206, 1938.djvu - Wikisource, (n.d.). https://fr.wikisource.org/wiki/Livre:Comptes_rendus_hebdomadaires_des_s%C3%A9ances_de_l%E2%80%99Acad%C3%A9mie_des_sciences,_tome_206,_1938.djvu (accessed August 8, 2025).

[129] A. Guinier, Structure of Age-Hardened Aluminium-Copper Alloys, Nature 142 (1938) 569–570. https://doi.org/10.1038/142569b0.

[130] T.J. Bastow, S. Celotto, Structure evolution in dilute Al(Cu) alloys observed by 63Cu NMR, Acta Mater. 51 (2003) 4621–4630. https://doi.org/10.1016/S1359-6454(03)00299-4.

[131] M. Wintenberger, Croissance cristalline des zones de Guinier-Preston dans les alliages d'aluminium, (1969). https://doi.org/10.3406/bulmi.1969.6289.

[132] A. Hayoune, D. Hamana, Structural evolution during non-isothermal ageing of a dilute Al–Cu alloy by dilatometric analysis, J. Alloys Compd. 474 (2009) 118–123. https://doi.org/10.1016/j.jallcom.2008.06.070.

[133] H. Yoshida, D.J.H. Cockayne, M.J. Whelan, A study of Guinier-Preston zones in aluminium-copper alloys using the weak-beam technique of electron microscopy, Philos. Mag. 34 (1976) 89–100. https://doi.org/10.1080/14786437608228176.

[134] D. Vaughan, J.M. Silcock, The Orientation and Shape of θ Precipitates Formed in an Al□Cu Alloy, Phys. Status Solidi B 20 (1967) 725–736. https://doi.org/10.1002/pssb.19670200235.

[135] S.P. Ringer, K. Hono, Microstructural Evolution and Age Hardening in Aluminium Alloys, Mater. Charact. 44 (2000) 101–131. https://doi.org/10.1016/S1044-5803(99)00051-0.

[136] L.J.C. Bergers, J.Th.M. De Hosson, M.G.D. Geers, J.P.M. Hoefnagels, Anomalous precipitation hardening in Al-(1 wt%)Cu thin films, Mater. Sci. Eng. A 722 (2018) 37–46. https://doi.org/10.1016/j.msea.2018.02.083.

[137] N. Masquelier, H. Zapolsky, W. Lefebvre, S.G. Fries, R. Patte, P. Pareige, Precipitation Kinetics Study of Al – Zr – X(Sc or Ti) Alloys by Phase Field Simulations and Atom Probe Tomography, Solid State Phenom. 172–174 (2011) 869–874. https://doi.org/10.4028/www.scientific.net/SSP.172-174.869.

[138] K.E. Knipling, D.C. Dunand, D.N. Seidman, Criteria for developing castable, creep-resistant aluminum-based alloys – A review, Z. Für Met. 97 (2006) 246–265. https://doi.org/10.3139/146.101249.

[139] K.E. Knipling, D.C. Dunand, D.N. Seidman, Nucleation and Precipitation Strengthening in Dilute Al-Ti and Al-Zr Alloys, Metall. Mater. Trans. A 38 (2007) 2552–2563. https://doi.org/10.1007/s11661-007-9283-6.

[140] J.Z. Liu, G. Ghosh, A. Van De Walle, M. Asta, Transferable force-constant modeling of vibrational thermodynamic properties in fcc-based Al − T M (T M = Ti , Zr, Hf) alloys, Phys. Rev. B 75 (2007) 104117. https://doi.org/10.1103/PhysRevB.75.104117.

[141] C.G. Jiao, M. Aindow, G.F. Yu, M.G. Yan, Al3Zr Precipitation Behaviour in a Melt-Spun Al-0.2Cu-1.2Mg-0.5Zr Alloy, in: Electron Microsc. Anal. 1997, 1st ed., CRC Press, Boca Raton, 2022: pp. 553–556. https://doi.org/10.1201/9781003063056-143.

[142] K. Knipling, Precipitation evolution in Al–Zr and Al–Zr–Ti alloys during aging at 450–600°C, Acta Mater. 56 (2008) 1182–1195. https://doi.org/10.1016/j.actamat.2007.11.011.

[143] K.E. Knipling, R.A. Karnesky, C.P. Lee, D.C. Dunand, D.N. Seidman, Precipitation evolution in Al–0.1Sc, Al–0.1Zr and Al–0.1Sc–0.1Zr (at.%) alloys during isochronal aging, Acta Mater. 58 (2010) 5184–5195. https://doi.org/10.1016/j.actamat.2010.05.054.

[144] E. Clouet, M. Nastar, C. Sigli, Nucleation of Al 3 Zr and Al 3 Sc in aluminum alloys: From kinetic Monte Carlo simulations to classical theory, Phys. Rev. B 69 (2004) 064109. https://doi.org/10.1103/PhysRevB.69.064109.

[145] E. Clouet, A. Barbu, L. Lae, G. Martin, Precipitation kinetics of AlZr and AlSc in aluminum alloys modeled with cluster dynamics, Acta Mater. 53 (2005) 2313–2325. https://doi.org/10.1016/j.actamat.2005.01.038.

[146] Y. Du, Y.A. Chang, B. Huang, W. Gong, Z. Jin, H. Xu, Z. Yuan, Y. Liu, Y. He, F.-Y. Xie, Diffusion coefficients of some solutes in fcc and liquid Al: critical evaluation and correlation, Mater. Sci. Eng. A 363 (2003) 140–151. https://doi.org/10.1016/S0921-5093(03)00624-5.

[147] T. Perrin, A. Després, P. Heugue, A. Deschamps, F. De Geuser, Precipitate evolution and related strengthening during long term ageing of 2618A aluminium alloy, Acta Mater. 296 (2025) 121264. https://doi.org/10.1016/j.actamat.2025.121264.

[148] A. Deschamps, M. Militzer, W.J. Poole, Precipitation Kinetics and Strengthening of a Fe-0.8wt%Cu Alloy., ISIJ Int. 41 (2001) 196–205. https://doi.org/10.2355/isijinternational.41.196.

[149] A.J. Ardell, Precipitation hardening, Metall. Trans. A 16 (1985) 2131–2165. https://doi.org/10.1007/BF02670416.

[150] R.E.A. Williams, Characterization of Mn Containing Precipitates Observed in 7Series Al Alloys Using Aberration Corrected STEM, Microsc. Microanal. 28 (2022) 806–807. https://doi.org/10.1017/S1431927622003622.

[151] Orowan: Zur kristallplastizität. III: Über den... - Google Scholar, (n.d.). https://scholar.google.com/scholar_lookup?&title=&journal=Z.%20Phys&volume=89&publication_year=1934&author=Orowan%2CE (accessed August 8, 2025).

[152] J.M. Fragomeni, The Plastic Deformation Mechanisms, Strength, and Fracture Behavior of a Precipitation Hardened Aluminum-Lithium-Zirconium Alloy, Mater. Sci. Forum 331–337 (2000) 1567–1582. https://doi.org/10.4028/www.scientific.net/MSF.331-337.1567.

[153] R.R. Ambriz, D. Jaramillo, Mechanical Behavior of Precipitation Hardened Aluminum Alloys Welds, in: W.A. Monteiro (Ed.), Light Met. Alloys Appl., InTech, 2014. https://doi.org/10.5772/58418.

[154] M.R. Ahmadi, E. Povoden-Karadeniz, K.I. Öksüz, A. Falahati, E. Kozeschnik, A model for precipitation strengthening in multi-particle systems, Comput. Mater. Sci. 91 (2014) 173–186. https://doi.org/10.1016/j.commatsci.2014.04.025.

[155] Physical metallurgy principles, 4th ed, SI, Cengage Learning, Stamford, 2010.

[156] R. Santos-Güemes, J. Segurado, J. LLorca, A generalized line tension model for precipitate strengthening in metallic alloys, Eur. J. Mech. - ASolids 93 (2022) 104540. https://doi.org/10.1016/j.euromechsol.2022.104540.

[157] D.J. Bacon, U.F. Kocks, R.O. Scattergood, The effect of dislocation self-interaction on the orowan stress, Philos. Mag. 28 (1973) 1241–1263. https://doi.org/10.1080/14786437308227997.

[158] J.F. Nie, Effects of precipitate shape and orientation on dispersion strengthening in magnesium alloys, Scr. Mater. 48 (2003) 1009–1015. https://doi.org/10.1016/S1359-6462(02)00497-9.

[159] J.F. Nie, B.C. Muddle, Strengthening of an Al–Cu–Sn alloy by deformation-resistant precipitate plates, Acta Mater. 56 (2008) 3490–3501. https://doi.org/10.1016/j.actamat.2008.03.028.

[160] Q. Liu, X. Li, W. Xiao, Z. Li, K. Zhu, K. Wen, L. Yan, Y. Li, H. Yan, Y. Zhang, B. Xiong, Insights into precipitation characteristics and strengthening mechanisms in a low Cu/Mg ratio Al-Cu-Mg-Ag alloy, Mater. Des. 240 (2024) 112836. https://doi.org/10.1016/j.matdes.2024.112836.

[161] Z. Guo, W. Sha, Quantification of Precipitation Hardening and Evolution of Precipitates, Mater. Trans. 43 (2002) 1273–1282. https://doi.org/10.2320/matertrans.43.1273.

[162] A. Cui, X. Wang, Y. Cui, Multiscale modelling of precipitation hardening: a review, J. Mater. Sci. Mater. Theory 8 (2024) 13. https://doi.org/10.1186/s41313-024-00066-6.

[163] Q. Wang, Z. Li, S. Pang, X. Li, C. Dong, P.K. Liaw, Coherent Precipitation and Strengthening in Compositionally Complex Alloys: A Review, Entropy 20 (2018) 878. https://doi.org/10.3390/e20110878.

[164] B. Bellón, S. Haouala, J. LLorca, An analysis of the influence of the precipitate type on the mechanical behavior of Al - Cu alloys by means of micropillar compression tests, Acta Mater. 194 (2020) 207–223. https://doi.org/10.1016/j.actamat.2020.05.040.

[165] R. Alizadeh, J. LLorca, Interactions between basal dislocations and $β_1'$ precipitates in Mg-4Zn alloy: mechanisms and strengthening, (2020). https://doi.org/10.48550/ARXIV.2001.04380.

[166] A. Keyhani, Multi-scale Modeling of Plasticity Nearby Precipitates in Nanostructured Materials, (2017). https://doi.org/10.48550/ARXIV.1710.02075.

[167] G. Béranger, G. Henry, G. Sanz, Le livre de l'acier, Tec et doc, Paris Londres New York, 1994.

[168] R. Ferragut, A. Dupasquier, C. Macchi, A. Somoza, R. Lumley, I. Polmear, Vacancy–solute interactions during multiple-step ageing of an Al–Cu–Mg–Ag alloy, Scr. Mater. 60 (2009) 137–140. https://doi.org/10.1016/j.scriptamat.2008.09.011.

[169] D.H. Xiao, J.N. Wang, D.Y. Ding, H.L. Yang, Effect of rare earth Ce addition on the microstructure and mechanical properties of an Al–Cu–Mg–Ag alloy, J. Alloys Compd. 352 (2003) 84–88. https://doi.org/10.1016/S0925-8388(02)01162-3.

[170] Silcock, J.M., Heal, T.J. and Hardy, H.K., Structural Ageing Characteristics of Aluminum-Copper Alloys, J. Inst. Met. (1953) 82, 239-248.

[171] J.R. Scully, G.A. Young Jr., S.W. Smith, Hydrogen Solubility, Diffusion and Trapping in High Purity Aluminum and Selected Al-Base Alloys, Mater. Sci. Forum 331–337 (2000) 1583–1600. https://doi.org/10.4028/www.scientific.net/MSF.331-337.1583.

[172] H.K. Birnbaum, C. Buckley, F. Zeides, E. Sirois, P. Rozenak, S. Spooner, J.S. Lin, Hydrogen in aluminum, J. Alloys Compd. 253–254 (1997) 260–264. https://doi.org/10.1016/S0925-8388(96)02968-4.

[173] A. San-Martin, F.D. Manchester, The al-h (aluminum-hydrogen) system, J. Phase Equilibria 13 (1992) 17–21. https://doi.org/10.1007/BF02645371.

[174] P. Anyalebechi, Analysis and Thermodynamic Prediction of Hydrogen Solution in Solid and Liquid Multicomponent Aluminum Alloys, 1998.

[175] S. Frappart, X. Feaugas, J. Creus, F. Thebault, L. Delattre, H. Marchebois, Study of the hydrogen diffusion and segregation into Fe–C–Mo martensitic HSLA steel using electrochemical permeation test, J. Phys. Chem. Solids 71 (2010) 1467–1479. https://doi.org/10.1016/j.jpcs.2010.07.017.

[176] H. Addach, P. Berçot, M. Rezrazi, M. Wery, Hydrogen permeation in iron at different temperatures, Mater. Lett. 59 (2005) 1347–1351. https://doi.org/10.1016/j.matlet.2004.12.037.

[177] G.A. Esteban, A. Peña, F. Legarda, R. Lindau, Hydrogen transport and trapping in ODS-EUROFER, Fusion Eng. Des. 82 (2007) 2634–2640. https://doi.org/10.1016/j.fusengdes.2007.02.002.

[178] C. Wolverton, V. Ozoliņš, M. Asta, Hydrogen in aluminum: First-principles calculations of structure and thermodynamics, Phys. Rev. B 69 (2004) 144109. https://doi.org/10.1103/PhysRevB.69.144109.

[179] G. Lu, D. Orlikowski, I. Park, O. Politano, E. Kaxiras, Energetics of hydrogen impurities in aluminum and their effect on mechanical properties, Phys. Rev. B 65 (2002) 064102. https://doi.org/10.1103/PhysRevB.65.064102.

[180] A.D. Vita, M.J. Gillan, The energetics of hydrogen in aluminium calculated from first principles, J. Phys. Condens. Matter 4 (1992) 599–611. https://doi.org/10.1088/0953-8984/4/2/028.

[181] R. Kirchheim, A. Pundt, Hydrogen in Metals, in: Phys. Metall., Elsevier, 2014: pp. 2597–2705. https://doi.org/10.1016/B978-0-444-53770-6.00025-3.

[182] H. Saitoh, Y. Iijima, H. Tanaka, Hydrogen diffusivity in aluminium measured by a glow discharge permeation method, Acta Metall. Mater. 42 (1994) 2493–2498. https://doi.org/10.1016/0956-7151(94)90329-8.

[183] G.A. Young, J.R. Scully, The diffusion and trapping of hydrogen in high purity aluminum, Acta Mater. 46 (1998) 6337–6349. https://doi.org/10.1016/S1359-6454(98)00333-4.

[184] T. Ishikawa, R.B. McLellan, The diffusivity of hydrogen in aluminum, Acta Metall. 34 (1986) 1091–1095. https://doi.org/10.1016/0001-6160(86)90219-1.

[185] A. Pundt, R. Kirchheim, HYDROGEN IN METALS: Microstructural Aspects, Annu. Rev. Mater. Res. 36 (2006) 555–608. https://doi.org/10.1146/annurev.matsci.36.090804.094451.

[186] S. Frappart, X. Feaugas, J. Creus, F. Thebault, L. Delattre, H. Marchebois, Hydrogen solubility, diffusivity and trapping in a tempered Fe–C–Cr martensitic steel under various mechanical stress states, Mater. Sci. Eng. A 534 (2012) 384–393. https://doi.org/10.1016/j.msea.2011.11.084.

[187] Y. Huang, A. Nakajima, A. Nishikata, T. Tsuru, Effect of Mechanical Deformation on Permeation of Hydrogen in Iron, ISIJ Int. 43 (2003) 548–554. https://doi.org/10.2355/isijinternational.43.548.

[188] M. Nagumo, K. Ohta, H. Saitoh, Deformation induced defects in iron revealed by thermal desorption spectroscopy of tritium, Scr. Mater. 40 (1999) 313–319. https://doi.org/10.1016/S1359-6462(98)00436-9.

[189] T. Enomoto, R. Matsumoto, S. Taketomi, N. Miyazaki, First-Principles Estimation of Hydrogen Occupancy around Lattice Defects in Al, J. Soc. Mater. Sci. Jpn. 59 (2010) 596–603. https://doi.org/10.2472/jsms.59.596.

[190] W.A. Counts, C. Wolverton, R. Gibala, First-principles energetics of hydrogen traps in α-Fe: Point defects, Acta Mater. 58 (2010) 4730–4741. https://doi.org/10.1016/j.actamat.2010.05.010.

[191] S. Frappart, A. Oudriss, X. Feaugas, J. Creus, J. Bouhattate, F. Thébault, L. Delattre, H. Marchebois, Hydrogen trapping in martensitic steel investigated using electrochemical permeation and thermal desorption spectroscopy, Scr. Mater. 65 (2011) 859–862. https://doi.org/10.1016/j.scriptamat.2011.07.042.

[192] S. Frappart, Des éléments de compréhension sur les mécanismes de transport et de ségrégation de l'hydrogène dans les aciers martensitiques trempés et revenus à haute limite d'élasticité, phdthesis, Université de La Rochelle, 2011. https://theses.hal.science/tel-01016688 (accessed August 8, 2025).

[193] Y. Xu, H. Toda, K. Shimizu, Y. Wang, B. Gault, W. Li, K. Hirayama, H. Fujihara, X. Jin, A. Takeuchi, M. Uesugi, Suppressed hydrogen embrittlement of high-strength Al alloys by Mn-rich intermetallic compound particles, Acta Mater. 236 (2022) 118110. https://doi.org/10.1016/j.actamat.2022.118110.

[194] G. Alefeld, J. Völkl, eds., Hydrogen in Metals I, Springer Berlin Heidelberg, Berlin, Heidelberg, 1978. https://doi.org/10.1007/3-540-08705-2.

[195] K. Papp, E. Kovács-Csetényi, Diffusion of hydrogen in solid aluminium, Scr. Metall. 11 (1977) 921–923. https://doi.org/10.1016/0036-9748(77)90238-1.

[196] M. Safyari, M. Moshtaghi, S. Kuramoto, Environmental hydrogen embrittlement associated with decohesion and void formation at soluble coarse particles in a cold-rolled Al–Cu based alloy, Mater. Sci. Eng. A 799 (2021) 139850. https://doi.org/10.1016/j.msea.2020.139850.

[197] H. Kamoutsi, G.N. Haidemenopoulos, V. Bontozoglou, S. Pantelakis, Corrosion-induced hydrogen embrittlement in aluminum alloy 2024, Corros. Sci. 48 (2006) 1209–1224. https://doi.org/10.1016/j.corsci.2005.05.015.

[198] M. Leger, G.R. Piercy, Internal friction in hydrogen-charged aluminium alloys, Philos. Mag. A 43 (1981) 377–385. https://doi.org/10.1080/01418618108239416.

[199] M. Safyari, M. Moshtaghi, T. Hojo, E. Akiyama, Mechanisms of hydrogen embrittlement in high-strength aluminum alloys containing coherent or incoherent dispersoids, Corros. Sci. 194 (2022) 109895. https://doi.org/10.1016/j.corsci.2021.109895.

[200] T.P. Perng, J.K. Wu, A brief review note on mechanisms of hydrogen entry into metals, Mater. Lett. 57 (2003) 3437–3438. https://doi.org/10.1016/S0167-577X(03)00095-8.

[201] A. Züttel, Materials for hydrogen storage, Mater. Today 6 (2003) 24–33. https://doi.org/10.1016/S1369-7021(03)00922-2.

[202] L.A. Arbuzova, K.I. Slovetskaya, A.M. Rubinshtein, L.L. Kunin, V.A. Danilkin, Chemisorption of hydrogen on aluminum oxide, Bull. Acad. Sci. USSR Div. Chem. Sci. 20 (1971) 148–149. https://doi.org/10.1007/BF00849340.

[203] A. Takasaki, High-pressure hydrogen charging of TiAl-based titanium aluminides, Scr. Mater. 38 (1998) 687–692. https://doi.org/10.1016/S1359-6462(97)00506-X.

[204] T. Košová Altnerová, D. Rudomilova, P. Novák, T. Prošek, The Role of Precipitates in Hydrogen Embrittlement of Precipitation-Hardenable Aluminum Alloys, Metals 14 (2024) 1287. https://doi.org/10.3390/met14111287.

[205] A.R. Troiano, R. Gibala, R.F. Hehemann, Hydrogen Embrittlement and Stress Corrosion Cracking: A Troiano Festschrift, ASM International, 1984.

[206] H. Suzuki, D. Kobayashi, N. Hanada, K. Takai, Y. Hagihara, Existing State of Hydrogen in Electrochemically Charged Commercial-Purity Aluminum and Its Effects on Tensile Properties, Mater. Trans. 52 (2011) 1741–1747. https://doi.org/10.2320/matertrans.M2011035.

[207] A.T. Gee, B.E. Hayden, C. Mormiche, T.S. Nunney, The role of steps in the dynamics of hydrogen dissociation on Pt(533), J. Chem. Phys. 112 (2000) 7660–7668. https://doi.org/10.1063/1.481360.

[208] E.P. Georgiou, V.P. Cevallos, T. Van Der Donck, D. Drees, J. Meersschaut, C.N. Panagopoulos, J.-P. Celis, Effect of cathodic hydrogen charging on the wear behavior of 5754 Al alloy, Wear 390–391 (2017) 295–301. https://doi.org/10.1016/j.wear.2017.08.013.

[209] L. Shen, H. Chen, X. Che, L. Xu, Hydrogen embrittlement of the 7B05-T5 aluminum alloy for high-speed trains, Mater. Corros. 71 (2020) 70–76. https://doi.org/10.1002/maco.201910975.

[210] W.J. Qi, R.G. Song, X. Qi, H. Li, Z.X. Wang, C. Wang, J.R. Jin, Hydrogen Embrittlement Susceptibility and Hydrogen-Induced Additive Stress of 7050 Aluminum Alloy Under Various Aging States, J. Mater. Eng. Perform. 24 (2015) 3343–3355. https://doi.org/10.1007/s11665-015-1616-9.

[211] M.-L. De Bonfils-Lahovary, C. Josse, L. Laffont, C. Blanc, Influence of hydrogen on the propagation of intergranular corrosion defects in 2024 aluminium alloy, Corros. Sci. 148 (2019) 198–205. https://doi.org/10.1016/j.corsci.2018.12.019.

[212] Gaseous Hydrogen Embrittlement of Materials in Energy Technologies, 2012. https://shop.elsevier.com/books/gaseous-hydrogen-embrittlement-of-materials-in-energy-technologies/gangloff/978-0-85709-536-7 (accessed August 9, 2025).

[213] N. Narita, Embrittlement of Fe□Si alloy crystals by hydrogen glow discharge, Scr. Metall. 18 (1984) 985–988. https://doi.org/10.1016/0036-9748(84)90274-6.

[214] H. Kimura, H. Matsui, Mechanism of hydrogen-induced softening and hardening in iron, Scr. Metall. 21 (1987) 319–324. https://doi.org/10.1016/0036-9748(87)90221-3.

[215] Removal of Carbon Contamination using Hydrogen with Low-Power Downstream Plasma Cleaning, Evactron® (n.d.). https://evactron.com/pdf/removal-carbon-contamination-using-hydrogen-low-power-downstream-plasma-cleaning/ (accessed August 9, 2025).

[216] Effect of second phase precipitation behavior on
mechanical properties of casting Al-Cu alloys - TNMSC, (n.d.).

http://tnmsc.csu.edu.cn/paper/paperView.aspx?id=paper_14902&_d_id=fedbafed57f492433209a6a14beaf0 (accessed August 18, 2025).

[217] W. Wei, R. Zuo, D. Xue, S. Wen, Y. Wu, W. Shi, X. Zhou, H. Huang, X. Wu, K. Gao, L. Rong, Z. Nie, Effect of Aging Treatment on the Precipitation Behavior of a Novel Al-Cu-Zr Cast Alloy, Materials 15 (2022) 8163. https://doi.org/10.3390/ma15228163.

[218] P.P. Ma, C.H. Liu, C.L. Wu, L.M. Liu, J.H. Chen, Mechanical properties enhanced by deformation-modified precipitation of θ′-phase approximants in an Al-Cu alloy, Mater. Sci. Eng. A 676 (2016) 138–145. https://doi.org/10.1016/j.msea.2016.08.068.

[219] X.Q. Zhao, M.J. Shi, J.H. Chen, S.B. Wang, C.H. Liu, C.L. Wu, A facile electron microscopy method for measuring precipitate volume fractions in AlCuMg alloys, Mater. Charact. 69 (2012) 31–36. https://doi.org/10.1016/j.matchar.2012.04.009.

[220] R.P. Gangloff, ed., Gaseous hydrogen embrittlement of materials in energy technologies. V. 2: Mechanisms, Modelling and Future Developments / ed. by Richard P. Gangloff, in: Woodhead Publishing Ltd, Cambridge, 2012.

[221] H. Liu, M. Bouchard, Evaluation of interaction coefficient in Al-Cu-H alloy, Metall. Mater. Trans. B 28 (1997) 625–632. https://doi.org/10.1007/s11663-997-0035-1.

[222] J. Kim, D. Hall, H. Yan, Y. Shi, S. Joseph, S. Fearn, R.J. Chater, D. Dye, C.C. Tasan, Roughening improves hydrogen embrittlement resistance of Ti-6Al-4V, Acta Mater. 220 (2021) 117304. https://doi.org/10.1016/j.actamat.2021.117304.

[223] A. Policicchio, E. Maccallini, G.N. Kalantzopoulos, U. Cataldi, S. Abate, G. Desiderio, R.G. Agostino, Volumetric apparatus for hydrogen adsorption and diffusion measurements: Sources of systematic error and impact of their experimental resolutions, Rev. Sci. Instrum. 84 (2013) 103907. https://doi.org/10.1063/1.4824485.

[224] Y. Chen, Z. Zhang, Z. Chen, A. Tsalanidis, M. Weyland, S. Findlay, L.J. Allen, J. Li, N.V. Medhekar, L. Bourgeois, The enhanced theta-prime (θ′) precipitation in an Al-Cu alloy with trace Au additions, Acta Mater. 125 (2017) 340–350. https://doi.org/10.1016/j.actamat.2016.12.012.

[225] D.B. Williams, C.B. Carter, Transmission Electron Microscopy, Springer US, Boston, MA, 2009. https://doi.org/10.1007/978-0-387-76501-3.

[226] thermionic-emission gun | Glossary | JEOL Ltd., Thermion.-Emiss. Gun Gloss. JEOL Ltd (n.d.). https://www.jeol.com/words/semterms/20121024.071558.php (accessed September 24, 2025).

[227] S. Uhlemann, M. Haider, Residual wave aberrations in the first spherical aberration corrected transmission electron microscope, Ultramicroscopy 72 (1998) 109–119. https://doi.org/10.1016/S0304-3991(97)00102-2.

[228] S.J. Pennycook, P.D. Nellist, eds., Scanning Transmission Electron Microscopy, Springer New York, New York, NY, 2011. https://doi.org/10.1007/978-1-4419-7200-2.

[229] Understanding Chromatic & Spherical Aberration of Lenses - Digital Photography Live, (2020). http://digitalphotographylive.com/chromatic-spherical-aberration/ (accessed August 15, 2025).

[230] nanoScience instruments, Transmission Electron Microscopy, (n.d.). https://www.nanoscience.com/.

[231] Miroslav KARLÍK, Bernard JOUFFREY, Etude des métaux par microscopie électronique en transmission, (Techniques de l'ingénieur p. METTI.).

[232] J.I. Goldstein, D.E. Newbury, J.R. Michael, N.W.M. Ritchie, J.H.J. Scott, D.C. Joy, Scanning Electron Microscopy and X-Ray Microanalysis, Springer New York, New York, NY, 2018. https://doi.org/10.1007/978-1-4939-6676-9.

[233] M. Haider, H. Rose, S. Uhlemann, E. Schwan, B. Kabius, K. Urban, A spherical-aberration-corrected 200kV transmission electron microscope, Ultramicroscopy 75 (1998) 53–60. https://doi.org/10.1016/S0304-3991(98)00048-5.

[234] T. Malis, S.C. Cheng, R.F. Egerton, EELS log-ratio technique for specimen-thickness measurement in the TEM, J. Electron Microsc. Tech. 8 (1988) 193–200. https://doi.org/10.1002/jemt.1060080206.

[235] A. Bardal, K. Lie, Measuring the Thickness of Aluminium Alloy Thin Foils Using Electron Energy Loss Spectroscopy, Mater. Charact. 44 (2000) 329–343. https://doi.org/10.1016/S1044-5803(99)00072-8.

[236] T.C. Isabell, P.E. Fischione, C. O'Keefe, M.U. Guruz, V.P. Dravid, Plasma Cleaning and Its Applications for Electron Microscopy, Microsc. Microanal. 5 (1999) 126–135. https://doi.org/10.1017/S1431927699000094.

[237] H.G. Merkus, Particle size measurements: fundamentals, practice, quality, Springer Netherlands, Dordrecht, 2009.

[238] W. Lefebvre, Atom probe tomography: put theory into practice, Academic Press, London, 2016.

[239] B. Gault, Atom Probe Microscopy, 1st ed, Springer New York, New York, NY, 2012.

[240] A.D. Smith, J. Donoghue, A. Garner, B. Winiarski, E. Bousser, J. Carr, J. Behnsen, T.L. Burnett, R. Wheeler, K. Wilford, P.J. Withers, M. Preuss, On the Application of Xe+ Plasma FIB for Micro-fabrication of Small-scale Tensile Specimens, Exp. Mech. 59 (2019) 1113–1125. https://doi.org/10.1007/s11340-019-00528-w.

[241] J.R. Famelton, G.M. Hughes, C.A. Williams, C. Barbatti, M.P. Moody, P.A.J. Bagot, Xenon plasma focussed ion beam preparation of an Al-6XXX alloy sample for atom probe tomography including analysis of an α-Al(Fe,Mn)Si dispersoid, Mater. Charact. 178 (2021) 111194. https://doi.org/10.1016/j.matchar.2021.111194.

[242] P. Felfer, B. Ott, N. Vorlaufer, Specimen preparation for atom probe tomography, Pract. Metallogr. 61 (2024) 848–864. https://doi.org/10.1515/pm-2024-0075.

[243] Y.-S. Chen, P.-Y. Liu, R. Niu, A. Devaraj, H.-W. Yen, R.K.W. Marceau, J.M. Cairney, Atom Probe Tomography for the Observation of Hydrogen in Materials: A Review, Microsc. Microanal. 29 (2023) 1–15. https://doi.org/10.1093/micmic/ozac005.

[244] Q. He, J. Jiang, X. Wang, J. Chen, W. Shao, L. Zhen, Insight into Intergranular Corrosion of the Aluminum Alloy 2024-T3: Effect of Pre-Charged Hydrogen, J. Electrochem. Soc. 170 (2023) 041501. https://doi.org/10.1149/1945-7111/acc7d1.

[245] S.-H. Gong, J.-Y. Lee, Y.-J. Kim, Atom-Probe Tomographic and Electron Microscopic Analyses of a High Strength 7075-T4 Aluminum Alloy, J. Nanosci. Nanotechnol. 19 (2019) 4182–4187. https://doi.org/10.1166/jnn.2019.16143.

[246] R. Parvizi, R.K.W. Marceau, A.E. Hughes, M.Y. Tan, M. Forsyth, Atom Probe Tomography Study of the Nanoscale Heterostructure around an Al_{20} Mn_3 Cu_2 Dispersoid in Aluminum Alloy 2024, Langmuir 30 (2014) 14817–14823. https://doi.org/10.1021/la503418u.

[247] P. Kesten, A. Pundt, G. Schmitz, M. Weisheit, H.U. Krebs, R. Kirchheim, H- and D distribution in metallic multilayers studied by 3-dimensional atom probe analysis and secondary ion mass spectrometry, J. Alloys Compd. 330–332 (2002) 225–228. https://doi.org/10.1016/S0925-8388(01)01596-1.

[248] R. Gemma, T. Al-Kassab, R. Kirchheim, A. Pundt, Visualization of deuterium dead layer by atom probe tomography, Scr. Mater. 67 (2012) 903–906. https://doi.org/10.1016/j.scriptamat.2012.08.025.

[249] R. Gemma, T. Al-Kassab, R. Kirchheim, A. Pundt, Studies on hydrogen loaded V–Fe8at% films on Al2O3 substrate, J. Alloys Compd. 446–447 (2007) 534–538. https://doi.org/10.1016/j.jallcom.2007.01.099.

[250] R. Gemma, T. Al-Kassab, R. Kirchheim, A. Pundt, Analysis of deuterium in V–Fe5at.% film by atom probe tomography (APT), J. Alloys Compd. 509 (2011) S872–S876. https://doi.org/10.1016/j.jallcom.2010.11.122.

[251] K. Verbeken, Analysing hydrogen in metals: bulk thermal desorption spectroscopy (TDS) methods, in: Gaseous Hydrog. Embrittlement Mater. Energy Technol., Elsevier, 2012: pp. 27–55. https://doi.org/10.1533/9780857095374.1.27.

[252] M.H. Mendelsohn, D.M. Gruen, Temperature-programmed desorption (TPD) studies of ZrV1.6Fe0.4Hy and ZrV1.2Cr0.8Hy, Mater. Res. Bull. 16 (1981) 1027–1034. https://doi.org/10.1016/0025-5408(81)90146-X.

[253] W.Y. Choo, J.Y. Lee, Thermal analysis of trapped hydrogen in pure iron, Metall. Trans. A 13 (1982) 135–140. https://doi.org/10.1007/BF02642424.

[254] S.V. Merzlikin, S. Borodin, D. Vogel, M. Rohwerder, Ultra high vacuum high precision low background setup with temperature control for thermal desorption mass spectroscopy (TDA-MS) of hydrogen in metals, Talanta 136 (2015) 108–113. https://doi.org/10.1016/j.talanta.2015.01.014.

[255] A. Oudriss, Influence des hétérogénéités métallurgiques sur les processus de diffusion et de piégeage de l'hydrogène dans le nickel, (n.d.).

[256] S.W. Smith, J.R. Scully, The identification of hydrogen trapping states in an Al-Li-Cu-Zr alloy using thermal desorption spectroscopy, Metall. Mater. Trans. A 31 (2000) 179–193. https://doi.org/10.1007/s11661-000-0064-8.

[257] T. Izumi, G. Itoh, Thermal Desorption Spectroscopy Study on the Hydrogen Trapping States in a Pure Aluminum, Mater. Trans. 52 (2011) 130–134. https://doi.org/10.2320/matertrans.L-M2010825.

[258] J. Yvon, Hydrogen Analysis in Steel and Metals, (n.d.).

[259] F. Martin, X. Feaugas, A. Oudriss, D. Tanguy, L. Briottet, J. Kittel, State of Hydrogen in Matter: Fundamental Ad/Absorption, Trapping and Transport Mechanisms, in: Mech. - Microstruct. - Corros. Coupling, Elsevier, 2019: pp. 171–197. https://doi.org/10.1016/B978-1-78548-309-7.50008-9.

[260] C.E. Buckley, H.K. Birnbaum, J.S. Lin, S. Spooner, D. Bellmann, P. Staron, T.J. Udovic, E. Hollar, Characterization of H defects in the aluminium–hydrogen system using small-angle scattering techniques, J. Appl. Crystallogr. 34 (2001) 119–129. https://doi.org/10.1107/S0021889800018239.

[261] M. Elsayed, T.E.M. Staab, J. Čížek, R. Krause-Rehberg, Monovacancy-hydrogen interaction in pure aluminum: Experimental and ab-initio theoretical positron annihilation study, Acta Mater. 248 (2023) 118770. https://doi.org/10.1016/j.actamat.2023.118770.

[262] J.P. Chateau, D. Delafosse, T. Magnin, Numerical simulations of hydrogen–dislocation interactions in fcc stainless steels. Part I: hydrogen–dislocation interactions in bulk crystals, (n.d.).

[263] P.A. Burr, S.T. Murphy, S.C. Lumley, M.R. Wenman, R.W. Grimes, Hydrogen solubility in zirconium intermetallic second phase particles, J. Nucl. Mater. 443 (2013) 502–506. https://doi.org/10.1016/j.jnucmat.2013.07.060.

[264] T. Dorin, S. Babaniaris, L. Jiang, A. Cassel, A. Eggeman, J. Robson, Precipitation sequence in Al-Sc-Zr alloys revisited, Materialia 26 (2022) 101608. https://doi.org/10.1016/j.mtla.2022.101608.

[265] W. Lefebvre, N. Masquelier, J. Houard, R. Patte, H. Zapolsky, Tracking the path of dislocations across ordered Al3Zr nano-precipitates in three dimensions, Scr. Mater. 70 (2014) 43–46. https://doi.org/10.1016/j.scriptamat.2013.09.014.

[266] M.S. Zedalis, M.E. Fine, Precipitation and ostwald ripening in dilute AI Base-Zr-V alloys, Metall. Trans. A 17 (1986) 2187–2198. https://doi.org/10.1007/BF02645917.

[267] I. Mouton, A.J. Breen, S. Wang, Y. Chang, A. Szczepaniak, P. Kontis, L.T. Stephenson, D. Raabe, M. Herbig, T.B. Britton, B. Gault, Quantification Challenges for Atom Probe Tomography of Hydrogen and Deuterium in Zircaloy-4, Microsc. Microanal. 25 (2019) 481–488. https://doi.org/10.1017/S143192761801615X.

[268] A.J. Breen, I. Mouton, W. Lu, S. Wang, A. Szczepaniak, P. Kontis, L.T. Stephenson, Y. Chang, A.K. Da Silva, C.H. Liebscher, D. Raabe, T.B. Britton, M. Herbig, B. Gault, Atomic scale analysis of grain boundary deuteride growth front in Zircaloy-4, Scr. Mater. 156 (2018) 42–46. https://doi.org/10.1016/j.scriptamat.2018.06.044.

[269] D. Mayweg, J. Eriksson, O. Bäcke, A.J. Breen, M. Thuvander, Focused Ion Beam induced hydride formation does not affect Fe, Ni, Cr-clusters in irradiated Zircaloy-2, J. Nucl. Mater. 581 (2023) 154444. https://doi.org/10.1016/j.jnucmat.2023.154444.

[270] I. Mouton, Y. Chang, P. Chakraborty, S. Wang, L.T. Stephenson, T. Ben Britton, B. Gault, Hydride growth mechanism in zircaloy-4: Investigation of the partitioning of alloying elements, Materialia 15 (2021) 101006. https://doi.org/10.1016/j.mtla.2021.101006.

[271] D. Bardel, M. Perez, D. Nelias, A. Deschamps, C.R. Hutchinson, D. Maisonnette, T. Chaise, J. Garnier, F. Bourlier, Coupled precipitation and yield strength modelling for non-isothermal treatments of a 6061 aluminium alloy, Acta Mater. 62 (2014) 129–140. https://doi.org/10.1016/j.actamat.2013.09.041.

[272] S. Harada, S. Yokota, Y. Ishii, Y. Shizuku, M. Kanazawa, Y. Fukai, A relation between the vacancy concentration and hydrogen concentration in the Ni–H, Co–H and Pd–H systems, J. Alloys Compd. 404–406 (2005) 247–251. https://doi.org/10.1016/j.jallcom.2005.02.077.

[273] R.B. McLellan, Z.R. Xu, Hydrogen-induced vacancies in the iron lattice, Scr. Mater. 36 (1997) 1201–1205. https://doi.org/10.1016/S1359-6462(97)00015-8.

[274] D. Connétable, P. Maugis, Effect of stress on vacancy formation and diffusion in fcc systems: Comparison between DFT calculations and elasticity theory, Acta Mater. 200 (2020) 869–882. https://doi.org/10.1016/j.actamat.2020.09.053.

[275] M. Mantina, Y. Wang, R. Arroyave, L.Q. Chen, Z.K. Liu, C. Wolverton, First-Principles Calculation of Self-Diffusion Coefficients, Phys. Rev. Lett. 100 (2008) 215901. https://doi.org/10.1103/PhysRevLett.100.215901.

[276] Y. Fukai, The metal-hydrogen system: basic bulk properties, 2nd rev. and updated ed, Springer, Berlin ; New York, 2005.

[277] N.Z. Carr, R.B. McLellan, The thermodynamic and kinetic behavior of metal–vacancy–hydrogen systems, Acta Mater. 52 (2004) 3273–3293. https://doi.org/10.1016/j.actamat.2004.03.024.

[278] J.-P. Du, W.T. Geng, K. Arakawa, J. Li, S. Ogata, Hydrogen-Enhanced Vacancy Diffusion in Metals, J. Phys. Chem. Lett. 11 (2020) 7015–7020. https://doi.org/10.1021/acs.jpclett.0c01798.

[279] Y. Wang, D. Connétable, D. Tanguy, Hydrogen influence on diffusion in nickel from first-principles calculations, Phys. Rev. B 91 (2015) 094106. https://doi.org/10.1103/PhysRevB.91.094106.

[280] R.W. Cahn, P. Haasen, Physical Metallurgy, North-Holland Physics Pub., 1983.

[281] X. Sauvage, F. Wetscher, P. Pareige, Mechanical alloying of Cu and Fe induced by severe plastic deformation of a Cu–Fe composite, Acta Mater. 53 (2005) 2127–2135. https://doi.org/10.1016/j.actamat.2005.01.024.

[282] S.P. Ringer, K. Hono, T. Sakurai, The effect of trace additions of sn on precipitation in Al-Cu alloys: An atom probe field ion microscopy study, Metall. Mater. Trans. A 26 (1995) 2207–2217. https://doi.org/10.1007/BF02671236.

[283] L. Cheng, M. Enomoto, Effects of Specimen Shape, Size and Initial Occupancy on the Thermal Desorption Spectrum of Hydrogen, in: Energy Mater. 2014, Springer International Publishing, Cham, 2014: pp. 687–692. https://doi.org/10.1007/978-3-319-48765-6_83.

[284] P. Chao, R.A. Karnesky, Hydrogen isotope trapping in Al–Cu binary alloys, Mater. Sci. Eng. A 658 (2016) 422–428. https://doi.org/10.1016/j.msea.2016.02.003.

[285] E.L. Hall, J.B. Vander Sande, Defects formed during quenching in Al-4 pct Cu, Metall. Trans. 5 (1974) 987–990. https://doi.org/10.1007/bf02644309.

[286] G. Mrówka-Nowotnik, J. Sieniawski, Analysis of Intermetallic Phases in 2024 Aluminium Alloy, Solid State Phenom. 197 (2013) 238–243. https://doi.org/10.4028/www.scientific.net/SSP.197.238.

[287] Li X.-M., M.J. Starink, Effect of compositional variations on characteristics of coarse intermetallic particles in overaged 7000 aluminium alloys, Mater. Sci. Technol. 17 (2001) 1324–1328. https://doi.org/10.1179/026708301101509449.

[288] A. Lervik, E. Thronsen, J. Friis, C.D. Marioara, S. Wenner, A. Bendo, K. Matsuda, R. Holmestad, S.J. Andersen, Atomic structure of solute clusters in Al–Zn–Mg alloys, Acta Mater. 205 (2021) 116574. https://doi.org/10.1016/j.actamat.2020.116574.

[289] A. Rodríguez-Veiga, B. Bellón, I. Papadimitriou, G. Esteban-Manzanares, I. Sabirov, J. LLorca, A multidisciplinary approach to study precipitation kinetics and hardening in an Al-4Cu (wt. %) alloy, J. Alloys Compd. 757 (2018) 504–519. https://doi.org/10.1016/j.jallcom.2018.04.284.

[290] J. Berlin, T. Stegmüller, F. Haider, Observation of in-plane oriented Guinier-Preston zones in Al-Cu, Micron 173 (2023) 103504. https://doi.org/10.1016/j.micron.2023.103504.

[291] T.-F. Chung, Y.-L. Yang, C.-N. Hsiao, W.-C. Li, B.-M. Huang, C.-S. Tsao, Z. Shi, J. Lin, P.E. Fischione, T. Ohmura, J.-R. Yang, Morphological evolution of GP zones and nanometer-sized precipitates in the AA2050 aluminium alloy, Int. J. Lightweight Mater. Manuf. 1 (2018) 142–156. https://doi.org/10.1016/j.ijlmm.2018.06.002.

[292] U. Bansal, M.P. Singh, S.K. Sinha, D.K. Sahu, S. Mondol, S.K. Makineni, A. Paul, K. Chattopadhyay, Strength and stability through variable micro segregation behaviour of Ta and Zr solutes at intermetallic interfaces in Al-Cu alloys, Acta Mater. 259 (2023) 119254. https://doi.org/10.1016/j.actamat.2023.119254.

[293] L. Bourgeois, C. Dwyer, M. Weyland, J.-F. Nie, B.C. Muddle, Structure and energetics of the coherent interface between the θ′ precipitate phase and aluminium in Al–Cu, Acta Mater. 59 (2011) 7043–7050. https://doi.org/10.1016/j.actamat.2011.07.059.

[294] C. Liu, Z. Ma, P. Ma, L. Zhan, M. Huang, Multiple precipitation reactions and formation of θ′-phase in a pre-deformed Al–Cu alloy, Mater. Sci. Eng. A 733 (2018) 28–38. https://doi.org/10.1016/j.msea.2018.07.039.

[295] U. Bansal, M.P. Singh, S.K. Sinha, D.K. Sahu, S. Mondol, S.K. Makineni, A. Paul, K. Chattopadhyay, Strength and stability through variable micro segregation behaviour of Ta and Zr solutes at intermetallic interfaces in Al-Cu alloys, Acta Mater. 259 (2023) 119254. https://doi.org/10.1016/j.actamat.2023.119254.

[296] J.F. Nie, B.C. Muddle, Microstructural design of high-strength aluminum alloys, J. Phase Equilibria 19 (1998) 543–551. https://doi.org/10.1361/105497198770341734.

[297] C.V. Singh, D.H. Warner, Mechanisms of Guinier–Preston zone hardening in the athermal limit, Acta Mater. 58 (2010) 5797–5805. https://doi.org/10.1016/j.actamat.2010.06.055.

[298] J. Zander, R. Sandström, One parameter model for strength properties of hardenable aluminium alloys, Mater. Des. 29 (2008) 1540–1548. https://doi.org/10.1016/j.matdes.2008.02.001.

[299] J. Da Costa Teixeira, D.G. Cram, L. Bourgeois, T.J. Bastow, A.J. Hill, C.R. Hutchinson, On the strengthening response of aluminum alloys containing shear-resistant plate-shaped precipitates, Acta Mater. 56 (2008) 6109–6122. https://doi.org/10.1016/j.actamat.2008.08.023.

[300] B. Milligan, D. Ma, L. Allard, A. Clarke, A. Shyam, Dislocation-θ′ (Al2Cu) interactions during creep deformation of an Al-Cu alloy, Scr. Mater. 217 (2022) 114739. https://doi.org/10.1016/j.scriptamat.2022.114739.

[301] B. Bellón, S. Haouala, J. LLorca, An analysis of the influence of the precipitate type on the mechanical behavior of Al-Cu alloys by means of micropillar compression tests, (2020). https://doi.org/10.48550/ARXIV.2005.07426.

[302] R. Santos-Güemes, L. Capolungo, J. Segurado, J. LLorca, Dislocation dynamics prediction of the strength of Al–Cu alloys containing shearable θ ′ ′ precipitates, J. Mech. Phys. Solids 151 (2021) 104375. https://doi.org/10.1016/j.jmps.2021.104375.

[303] V.S. Krasnikov, A.E. Mayer, V.V. Pogorelko, F.T. Latypov, A.A. Ebel, Interaction of dislocation with GP zones or θ" phase precipitates in aluminum: Atomistic simulations and dislocation dynamics, Int. J. Plast. 125 (2020) 169–190. https://doi.org/10.1016/j.ijplas.2019.09.008.

[304] J.D. Boyd, R.B. Nicholson, The coarsening behaviour of θ″ and θ′ precipitates in two Al-Cu alloys, Acta Metall. 19 (1971) 1379–1391. https://doi.org/10.1016/0001-6160(71)90076-9.

[305] Z. Zhu, M.J. Starink, Age hardening and softening in cold-rolled Al–Mg–Mn alloys with up to 0.4wt% Cu, Mater. Sci. Eng. A 489 (2008) 138–149. https://doi.org/10.1016/j.msea.2007.12.019.

[306] A.S. Argon, Strengthening mechanisms in crystal plasticity, Oxford university press, Oxford, 2008.

[307] B. Milligan, D. Ma, L. Allard, A. Clarke, A. Shyam, Crystallographic orientation-dependent strain hardening in a precipitation-strengthened Al-Cu alloy, Acta Mater. 205 (2021) 116577. https://doi.org/10.1016/j.actamat.2020.116577.

[308] I.M. Hutchings, The contributions of David Tabor to the science of indentation hardness, J. Mater. Res. 24 (2009) 581–589. https://doi.org/10.1557/jmr.2009.0085.

[309] D. Bardel, M. Perez, D. Nelias, A. Deschamps, C.R. Hutchinson, D. Maisonnette, T. Chaise, J. Garnier, F. Bourlier, Coupled precipitation and yield strength modelling for non-isothermal treatments of a 6061 aluminium alloy, Acta Mater. 62 (2014) 129–140. https://doi.org/10.1016/j.actamat.2013.09.041.

[310] O. Myhr, Modelling of the age hardening behaviour of Al–Mg–Si alloys, Acta Mater. 49 (2001) 65–75. https://doi.org/10.1016/S1359-6454(00)00301-3.

[311] E. Mondou, A. Proietti, C. Charvillat, C. Berziou, X. Feaugas, D. Sinopoli, C. Blanc, Understanding the mechanisms of intergranular corrosion in 2024 Al alloy at the polycrystal scale, Corros. Sci. 221 (2023) 111338. https://doi.org/10.1016/j.corsci.2023.111338.

[312] H. Kamoutsi, G.N. Haidemenopoulos, H. Mavros, C. Karantonidis, P. Floratos, Z. Alhosani, P. Cho, D.H. Anjum, F. Ravaux, K. Polychronopoulou, Effect of precipitate coherency on the corrosion-induced hydrogen trapping in 2024 aluminum alloy, Int. J. Hydrog. Energy 46 (2021) 34487–34497. https://doi.org/10.1016/j.ijhydene.2021.08.005.

[313] H. Zheng, J. Liu, S. Muraishi, Optimal Arrangements and Local Anisotropy of {100} Guinier–Preston (GP) Zones by Parametric Dislocation Dynamics (PDD) Simulations, Materials 17 (2024) 5076. https://doi.org/10.3390/ma17205076.

[314] X.-H. Zhu, Y.C. Lin, Q. Wu, Y.-Q. Jiang, Effects of aging on precipitation behavior and mechanical properties of a tensile deformed Al–Cu alloy, J. Alloys Compd. 843 (2020) 155975. https://doi.org/10.1016/j.jallcom.2020.155975.

[315] H. Wang, Y. Yi, S. Huang, Influence of pre-deformation and subsequent ageing on the hardening behavior and microstructure of 2219 aluminum alloy forgings, J. Alloys Compd. 685 (2016) 941–948. https://doi.org/10.1016/j.jallcom.2016.06.111.

[316] A. Pundt, S. Wagner, Hydrogen Interactions with Defects in Materials, Chem. Ing. Tech. 96 (2024) 182–191. https://doi.org/10.1002/cite.202300235.

[317] A. Penlington, B. Diak, H.O. Jin, Application of the Nes Model for Static Recovery of the Dislocation Density in Cold Rolled AA6XXX, Mater. Sci. Forum 794–796 (2014) 605–610. https://doi.org/10.4028/www.scientific.net/msf.794-796.605.

[318] R. Nazarov, T. Hickel, J. Neugebauer, *Ab initio* study of H-vacancy interactions in fcc metals: Implications for the formation of superabundant vacancies, Phys. Rev. B 89 (2014) 144108. https://doi.org/10.1103/PhysRevB.89.144108.

Influence of hydrogen on precipitation in Al-Cu and Al-Zr aluminum alloys

ABSTRACT

Most models proposed to describe hydrogen embrittlement rely primarily on the interactions between hydrogen and crystalline defects. However, these interactions remain not fully understood, as it is challenging to experimentally localize hydrogen within metallic alloys. Given that the kinetics of phase transformations and resulting microstructures are mostly controlled by crystalline defects, it is hypothesized that hydrogen should affect the mechanisms of such transformations. We therefore investigated experimentally the influence of hydrogen on thermal stability and precipitation in Al-Cu and Al-Zr model alloys. Transmission electron microscopy was used to characterize precipitate size, morphology, distribution, and volume fraction. Hydrogen uptake was quantified by thermal desorption spectroscopy (TDS), while atom probe tomography was used to measure solute concentration in the matrix at different conditions. In the Al-Zr system, hydrogen was found to accelerate the growth of Al_3Zr precipitates. The measured Zr concentration in the matrix was systematically lower in hydrogen-aged samples, confirming an enhanced decomposition of the supersaturated solid solution. Based on a classical growth model, hydrogen increases the diffusion coefficient of Zr by a factor of two. This enhancement is attributed to hydrogen-vacancy interactions, which reduce vacancy formation or migration energies by approximately 0.04 eV. By contrast, in the Al-Cu system aged at 140 °C, hydrogen significantly delayed the growth kinetics of GP zones. Prior to the GP→ θ″ transformation, GP zones were found to be larger in the hydrogen-charged samples, suggesting a stabilizing effect of hydrogen. This also affected the mechanical response of the alloy, which exhibited lower hardness with hydrogen. TDS measurements confirmed that GP zones act as significant hydrogen traps, thus altering the transformation path to θ″. Additionally, in pre-deformed Al-Cu alloy, hydrogen was shown to slow down defect recovery, indicating a strong interaction with dislocations.

Keywords: Hydrogen, Precipitation, Diffusion, Growth kinetics, Aluminium alloy, crystalline defects, microscopie électronique en transmission

RÉSUMÉ

Les modèles proposés pour décrire la fragilisation par l'hydrogène reposent principalement sur les interactions entre l'hydrogène et les défauts cristallins. Cependant, ces interactions demeurent incomplètement comprises, car il est difficile de localiser expérimentalement l'hydrogène au sein des structures métalliques. Étant donné que la cinétique des transformations de phase et les microstructures qui en résultent sont principalement contrôlées par les défauts cristallins, notre hypothèse était que l'hydrogène pouvait influencer les mécanismes de ces transformations. Les alliages modèles Al-Cu et Al-Zr ont été choisis pour étudier expérimentalement l'influence de l'hydrogène sur la stabilité thermique et la précipitation. La microscopie électronique en transmission a été utilisée pour caractériser la taille, la morphologie, la distribution et la fraction volumique des précipités. L'absorption d'hydrogène a été quantifiée par spectroscopie de désorption thermique (TDS), tandis que la sonde atomique tomographique a permis de mesurer la concentration en soluté dans la matrice. Dans le système Al-Zr, l'hydrogène accélère la croissance des précipités Al_3Zr. Les mesures de concentration en Zr dans la matrice, ont montré des valeurs systématiquement plus faibles pour les échantillons vieillis sous hydrogène, confirmant une décomposition accrue de la solution solide. D'après le modèle classique de croissance, l'hydrogène augmente le coefficient de diffusion du Zr d'un facteur deux. Cette augmentation est attribuée aux interactions hydrogène–lacune, qui réduisent les énergies de formation ou de migration des lacunes d'environ 0.04 eV. En revanche, dans le système Al-Cu vieilli à 140 °C, l'hydrogène ralentit significativement la cinétique de croissance des zones GP. Avant la transformation GP → θ″, les zones GP apparaissent plus grandes dans les échantillons chargés en hydrogène, ce qui suggère un effet stabilisant. Ce phénomène se traduit également par une modification du comportement mécanique de l'alliage, qui présente une dureté plus faible en présence d'hydrogène. Les mesures de TDS ont confirmé que les zones GP piègent significativement l'hydrogène, modifiant ainsi la transformation vers la phase θ″. De plus, dans l'alliage Al-Cu pré-déformé, l'hydrogène ralentit la restauration des défauts, indiquant une forte interaction entre l'hydrogène et les dislocations.

Mots clés : Hydrogène, Précipitation, Diffusion, Cinétique de croissance, Alliage d'aluminium, Défauts cristallins, microscopie électronique en transmission